ANAEROBIC HYDROCARBON OXIDATION IN MARINE COLD SEEPS.

by

RYAN J. SIBERT

(Under the Direction of Samantha B. Joye)

ABSTRACT

The Gulf of Mexico is one of the most prolific oil and gas producing basins in the world and is host to some of the most dynamic seafloor environments next to hydrothermal spreading centers. Repeated cycles of flooding, first from the Pacific and then from the Atlantic, generated kilometer thick salt deposits at the seafloor. These buried salt sheets flow and fracture under the weight of kilometers of sediment overburden to produce a highly variable landscape that includes carbonate hardgrounds, brine flows, brine lakes, and hydrocarbon seeps. These environments host unique assemblages of animal and microbial life that influence biogeochemical cycling on a large scale. This dissertation explores the geochemistry of the anaerobic oxidation of methane, hexadecane, and naphthalene over a range of Gulf seafloor environments, including oil and gas seeps, brine pools, mud volcanoes, and large brine lakes.

INDEX WORDS: Anaerobic oxidation of methane, Sulfate reduction, Hydrocarbon oxidation, Cold seeps, Brine pools, Gulf of Mexico, Anaerobic metabolism, Orca Basin

ANAEROBIC HYDROCARBON OXIDATION IN MARINE COLD SEEPS.

by

RYAN J. SIBERT

B.S., Western Michigan University, 2010

M.S., Western Michigan University, 2012

A Dissertation Submitted to the Graduate Faculty of the
University of Georgia in Partial Fulfillment of the Requirements for the
Degree

DOCTOR OF PHILOSOPHY

ATHENS, GEORGIA

2021

ANAEROBIC HYDROCARBON OXIDATION IN MARINE COLD SEEPS.

by

RYAN J. SIBERT

Major Professor:	Samantha B. Joye
Committee:	Patricia Medeiros Christof Meile Christopher Martens Andreas Teske

Electronic Version Approved:

Ron Walcott
Dean of the Graduate School
The University of Georgia
May 2021

DEDICATION

For EAW, EES, HDS, and DLP.

Acknowledgements

So many people made this journey possible. First, there are my friends and family: Mom, Dad, Emily, Drake, Matt, Joe, Jason, Lindsey, Anna, Ben, Porkchop, Taters, Ming, Kathy, Brent, and Ludo. Then there are those directly involved in shaping my scientific career: Mandy Joye, Kim Hunter, Vladimir Samarkin, Joe Montoya, Christof Meile, Patricia Medeiros, Andreas Teske, Chris Martens, Renato, Daniella, Carla Koretsky, graduate students of the Joye Lab (past, present, and probably future), the numerous postdocs that have graced the lab (especially Melitza and Matt), and the captain and crew of the RV ENDEAVOR, RV PELICAN, RV ATLANTIS, RV WESTERN FLYER, EV NAUTILUS, and the RV METEOR.

Finally, I would like to thank the following agencies for their financial support: 1) Ecosystem Impacts of Oil and Gas Inputs to the Gulf (ECOGIG), 2) The Gulf of Mexico Research Initiative (GOMRI), 3) Center for Dark Energy Biosphere Investigations (C–DEBI), and 4) The National Science Foundation (NSF) Emerging Frontiers Program (grant EF- 0801741). This work would not have been possible without them and the work of their talented staff.

TABLE OF CONTENTS

LIST OF FIGURES

List of Tables

CHAPTER 1

INTRODUCTION AND BACKGROUND

1.1 INTRODUCTION

The metabolic activity of microorganisms influences geochemical cycling in every imaginable habitat and at nearly every conceivable scale. The first three billion years of life on Earth reflect the Age of Microorganisms [1]. Today, microbial life is abundant across Earth's habitats, in population numbers that dwarf other organisms, and with enough metabolic diversity such that no element of significance is left untouched. Prokaryotes can survive across an extreme range of environmental conditions. Species have been found living between -15 to 122 °C, at pressures from approximately 3 kPa to 0.1 GPa, salinities up to NaCl saturation, and from pH conditions between 0 and 12 [2–8]. Microbes have colonized numerous environments, including forests, lakes, rivers, soils, sediments, seawater, caves, hot springs, the atmosphere including clouds, ice, hydrothermal vents, brine pools, hydrocarbon reservoirs, deeply buried rocks crust, animal tissue, nuclear reactors, and even the International Space Station [5, 9–14].

At best approximation, the prokaryotic population of Earth is between $9.0–31.7 \times 10^{29}$ cells, potentially representing a trillion different species [15, 16]. Conservatively, the amount of carbon contained within this population is between 614 – 827 Pg C, of which 3.6 – 4.9 Pg C resides in the subseafloor [16]. The matter and energy required by microbial biomass is harvested from the local environment. The chemical and energetic feedbacks from microbial activity have profound impacts on the environment, on timescales ranging from minutes to billions of years [17–20]. Understanding Earth's biogeochemical cycles, particularly in extreme environments that challenge the limits of life, offers a blueprint for searching for life on extraterrestrial and extrasolar bodies [21, 22]. Extreme environments include habitats that are characterized by conditions well outside the average range for environmental variables. Microbes are able withstand extremes in pH (pH <5 = acidophiles; pH >9 = alkaliphiles), salinity (salinity > 8.8%=halophiles), temperature (T <20 °C = psychrophiles; T >45 °C = thermophiles), pressure (pressure between 10 – 50 MPa = piezophile), or water activity ($a_w < 0.7$ = xerophile) can thrive in these habitats [22]. Some microorganisms are 'polyextremophiles', organisms that can tolerate extremes in more than one of these parameters [23]. Studying the microorganisms found in extreme environments and their metabolisms has tremendous potential for advancing biotechnology [24].

This thesis focuses on key microbial processes that occur in deep sea extreme environments in the Gulf of Mexico, including brine basins, brine seeps, and hydrocarbon seeps. The Gulf of Mexico is a unique ecosystem [25]. It is an easily accessible sea on a continental margin that supports remarkable biodiversity and high rates of productivity and one that is impacted by a number of industries, from tourism to fisheries to oil exploration [25]. The Gulf of Mexico plays a vital role in the regional and national economy. The Northern Gulf is underlain by extensive hydrocarbon reservoirs and thus petroleum exploration, extraction and refinement industries are the economic backbones of the Gulf: ca. 25% of the oil and 14% of the gas used in the US is produced in the Gulf and refined in adjacent coastal states. The economic impact of Gulf commercial fisheries exceeded $19 billion in 2011 [26], and this industry is still recovering from the 2010 DWH blowout [27]. The Gulf of Mexico system is influenced by terrigenous inputs from the largest river in North America, the Mississippi, that vary seasonally and interannually. The Gulf's biota therefore experience ephemeral exposure to diverse and variable energy regimes [28, 29]. Thousands of hydrocarbon seeps discharge oil and gas into the Gulf and the system is influenced by complex large- and small-scale circulation patterns that distribute oil in the system.

Anaerobic microbial processes dominated the biogeochemistry of Archean environments [30] and these processes thrive today in the northern Gulf today, largely in permanently anoxic basins and marine sediments. The first chapter of this thesis focuses on microbial processes along the chemocline of a brine basin, while the two subsequent chapters (Chapters 2, 3) focus on microbial processes in sediments, with a common focus on understanding how microbial processes cycle hydrocarbons and on how hydrocarbon oxidation is coupled to terminal metabolic processes, such as sulfate reduction.

Marine sediments are a complex mixture of biological materials (*e.g.,* organic matter, shells, etc.), terrigenous clastics (*e.g.,* sand, clays, etc.), inorganic authigenic precipitates (*e.g.,* pyrite, carbonates, etc.), and pelagic mineral assemblages (*e.g.,* calcareous and siliceous shell material [31, 32]. Once deposited at the seabed, sediments are further altered by exposure to discharging fluids (brines, oil, gas; [28]), through secondary sedimentation of oil-derived materials (Chapter 3), through bioturbation and bioirrigation of surficial sediments [33], and through repeated processes of remobilization and mineralization [34]. Individual components of sediments are altered at different rates prior to lithification, typically in accordance with age, prevailing geologic conditions, burial rate, and microbial activity. These early diagenetic processes link the relatively fast acting components of the carbon cycle to the geologically slow CO_2-rock cycle [32]. Importantly, modern atmospheric oxygen and CO_2 levels are modulated by sedimentary processes, either locally via a complex balance between oceanic primary productivity, sedimentation rate, oxidation of organic matter, and burial rates, or on geologic timescales through the formation of kerogen, petroleum, and the diagenetic alteration of sedimentary pyrite [32, 35].

1.2 Hydrocarbon Production

Nearly 191 Tmol of photosynthetically derived organic carbon is delivered to the seafloor annually as particles (POC) and marine snow [36–38]. Approximately 34% of the POC flux is buried ($\approx$65 Tmol C y^{-1} [39]), of which approximately 50% is remineralized by a diverse group of sulfate-reducing bacteria (SRB; [40, 41]). A fraction of this buried POC has been repeatedly exhumed and reburied probably over thousands of years, an observation supported by depleted POC radiocarbon signatures [42, 43]. Final burial of POC therefore likely occurs following extended periods of exposure and reworking at or near the sediment surface [42–44].

Early diagenetic transformation and eventual burial of POC results in the formation of kerogen [45]. When heated to extreme temperatures, kerogen decomposes into liquid and gaseous hydrocarbons compounds such as short- to long-chain alkanes (e.g. methane, ethane, hexadecane, etc.), and polyaromatic compounds (e.g. naphthalene, phenanthrene, etc. [45–47]). Elevated geothermal temperature from continued burial transforms kerogen into structurally distinct, liquid pools of hydrocarbons, or crude oil [45]. Often, crude oil is defined according to methods of analysis and separated into four main pools that vary in reactivity largely based on structure: 1) Saturated compounds, 2) Aromatic compounds, 3) Resins, and 4) Asphaltenes (*i.e.,* SARA fractions [45]). Of these, saturated and aromatic compounds dominate sedimentary hydrocarbon reservoirs (80% by mass [48]). The saturated fraction includes short chain light hydrocarbons gases (e.g. methane, ethane, propane and butane), long chain alkanes (e.g. n-hexadecane), branched alkanes, and cyclic compounds. The aromatic fraction includes benzene, toluene, naphthalene and phenanthrene. All of these are viable substrate for microbial metabolism. The migration of these substances into overlying sedimentary deposits drives microbial production, population diversity, and ultimately early diagenetic processes that occur over geologically long (10^7 yr) time scales [28].

In shallow, sulfate-depleted sediments, inorganic carbon, alcohols, and volatile fatty acids are converted to methane by a diverse group of methanogenic archaea [49, and references therein]. This biogenic methane constitutes the dominant fraction of methane in some environments (*e.g.,* brines, [28, 50]), but in many cases, biogenic methane comingles with thermogenic [51] or geogenic [52, 53] methane, making it difficult to track its origin and fate. Methane is the most abundant hydrocarbon in the modern atmosphere, and it is approximately 21 times more effective at trapping heat than CO_2 [54]. The concentration of methane in the atmosphere is increasing [55], driven largely by increases from agricultural and fossil fuel sectors [56]. Tracking and understanding the fate of methane in the environment is important, given its critical role in regulating Earth's climate.

1.3 Anaerobic Methane Oxidation

More than 90% of methane produced in anoxic seafloor sediments is consumed by ANaerobic MEthanotrophs (ANME [57]). Anaerobic methanotrophy is a longstanding microbial conundrum that has been putatively linked to sulfate reduction [58–60], denitrification [61–63], and metal oxide reduction [64]. Current estimates suggest that ANME remove between 45 and 61 Tg CH4 annually from anoxic seafloor sediments [65]. Globally integrated sulfate removal through microbial reduction processes in seafloor sediments is estimated at ≈11.3 Tmol or 1.1 Pg $SO_4{}^{2-}$ y^{-1} [41]. Under the simplifying assumption that electron acceptors other than sulfate play a negligible role in the anaerobic oxidation of methane (AOM), approximately 5.3 Tmol $SO_4{}^{2-}$ y^{-1} (47% of the total) has been associated with AOM along the sulfate methane transition zone (SMTZ), the majority of which occurs along continental margins [65].

Potential syntrophic mechanisms for AOM, including reverse methanogenesis, intermediate electron transfer compounds (zero valent sulfur, denitrification [61, 66, 67]), and direct contact via nanowires and multi-heme cytochromes ([68]), have captured much attention. However, the potential for anaerobic methanotrophy in one organism via denitrification (Methylomirabilis oxyfera, [61, 69]) is well documented. There are numerous unanswered questions surrounding AOM in the environment, including the microorganisms responsible and the metabolic pathways involved [57]. Most research efforts regarding AOM are focused on a putative consortium of ANME archaea and sulfate reducing bacteria (SRB [59]) that live in clusters or aggregates [60]. In the simplest case, ANME are thought to use methanogenic pathways in reverse, first activating methane via methyl coenzyme M reductase (e.g. mcrA) [70], then passing the generated reducing equivalents to SRB, where they are then presumably routed into canonical dissimilatory sulfate reducing machinery (see Equation 1.1). The energetics of sulfate-coupled methane oxidation are favorable [59] but approach the energetic limit of life (ΔG_r° between -30 kJ $mol^{-1}$and-40 kJ mol^{-1}, depending on *in situ* conditions).

Sulfate-coupled AOM purportedly dominates anaerobic methanotrophy in marine environments, as evidenced by geochemical and isotopic data [58, 59, 71, 72]. In anoxic sediments, methane concentrations tend to diminish together with the disappearance of sulfate within the SMTZ. Methane oxidation and sulfate reduction consistently occur together at depth, but rates of the two processes rarely match each other [73]. To date however, no definitive connection between AOM and SR has been established. Further still, no definitive connection between ANME and methanotrophy has been revealed, leaving open the possibility that SRB are the lone heterotrophs in the consortium [74, 75]. Recent papers [76] have challenged this assumption, arguing that multiple, contemporaneous modes of AOM are possible and even likely.

$$CH_4 + {SO_4}^{2-} \longrightarrow {HCO_3}^{-} + HS^{-} + H_2O \tag{1.1}$$

ANME organisms are notoriously difficult to enrich in pure culture which makes distinguishing metabolic linkages between ANME and SRB difficult [77]. The comprehensive modeling efforts of Alperin and Hoehler [78] suggests two possibilities: 1) that ANME/SRB consortia are methanogenic at methane-rich seep sites, and 2) that ANME/SRB aggregates contain groups of hydrogen-producing, methanotrophic archaea and hydrogenotrophic SRB at non-seep sites. Additionally, recent reports provide compelling arguments in favor of AOM coupled to alternate electron acceptors, most notably nitrate [67, 79], nitrite [61, 66, 80, 81], and the metal oxides of iron and manganese [64, 82]. The fact that Bowles et al. (2019) [76] document significant decoupling of AOM and SR under environmentally realistic methane concentrations provides strong evidence that AOM is coupled energetically to processes other than SR.

1.4 Complex Hydrocarbon Oxidation

Crude oil is a complex mixture of organic compounds generated from geothermal catagenesis of deeply buried kerogen and bitumen [83, 84]. Crude oils is comprised of many thousands of different compounds spanning four main structural groups, the so-called SARA fractions: Saturated hydrocarbons, Aromatics, Resins, and Asphaltenes [83]. The saturated hydrocarbons are the simplest and most abundant fraction in mature, unweathered crude oil (up to 60% by weight [83]) and include short linear alkanes (*e.g.,* methane, ethane, and propane), longer linear alkanes (*e.g.,* hexadecane, n-octadecane, etc.), branched alkanes (*e.g.,* isobutane), and cyclic alkanes (*e.g.,* cyclopropane, cyclobutane and cyclohexane). The aromatic fraction (typically 20-45% by weight [83]) contains the economically valuable BTEX quartet (i.e., benzene, toluene, ethylbenzene, and xylene) and polycyclic aromatic hydrocarbons (PAHs) like naphthalene, phenanthrene and anthracene. Oil and gas seeps occur along both passive and active continental margins, including those along the passive margins of the eastern US Atlantic seaboard (gas only [85]) and throughout the Gulf of Mexico (oil and gas; hereafter Gulf [28, 50, 86]), and along active margins, like the Eel River Margin in the Pacific. The Gulf contains over 1000 known cold seeps of mixed geochemical providence [28, 50, 86]. The mobilization of oil and gas through marine sediments establishes unique metabolic niches for microorganisms and impacts local biogeochemical cycling.

1.5 OBJECTIVES

1.5.1 CHAPTER 2

Chapter 2 explores methane oxidation along the chemocline of Orca Basin, Gulf of Mexico, a deep-sea hypersaline anoxic basin. Deep-sea hypersaline anoxic basins are localized seafloor environments that contain energy- and nutrient- rich brines capable of supporting extensive microbial communities. This chapter reports the first rates of microbial methane oxidation and sulfate reduction across the chemocline of Orca basin, Gulf of Mexico, one of the world's largest submarine brine basins. Multiple pathways of methane oxidation occurred across the chemocline of Orca that creates an effective sink for methane. We hypothesized that (1) anaerobic methanotrophy would predominantly control methane flux from the gas-charged brine, (2) sulfate reduction would co-occur with anaerobic methanotrophy and be a dominant terminal metabolism across the chemocline, as observed in other deep marine hypersaline systems, and (3) microbial metabolism would be salinity-inhibited within the core of the brine.

Our results indicate that both aerobic and anaerobic methanotrophy occur along the chemocline, both confirming and refining our first hypothesis. Our hypothesis that sulfate reduction would be the dominant terminal metabolism was not only disproven, but sulfate reduction was shown to be either completely absent, or below our ability to detect with conventional radiotracer assays. Anaerobic methane oxidation was more important than aerobic methanotrophy, but rapid uptake of methane tracer along a suboxic, mildly salty horizon indicates a robust community of aerobic methanotrophic scavengers. To our surprise, not only did we find active AOM within the brine, but experimental additions of oxidized iron minerals stimulated AOM rates at full brine salinity (>250 g kg^{-1}). Iron-coupled AOM has been demonstrated in controlled laboratory settings, but this study reports the first occurrence of this in brine fluids and work with additional electron acceptors such as nitrite suggests a dynamic community of anaerobic hydrocarbon degraders.

1.5.2 Chapter 3

Chapter 3 reports naphthalene and hexadecane oxidation rates in Gulf sediments across nine sites of different water depth and hydrocarbon loading rates in the context of datasets describing porewater and solid phase geochemistry, microbial sulfate reduction and AOM, and extractable hydrocarbons. Sediment cores were sectioned and incubated with labile ^{35}S–sulfate and ^{14}C–labeled methane, hexadecane, and naphthalene to assess the coupling of sulfate reduction with short-chain alkane, long-chain alkane, and PAH degradation. We hypothesized that (1) sulfate reduction rates would be a good predictor for presence and magnitude of alkane and PAH degradation, (2) that the relative magnitude of oil oxidation would follow thermodynamic predictions, *i.e., n*-alkanes would be oxidized before PAHs, and (3) exposure to oil would prime the sediment microbial community for hydrocarbon metabolism and further predict the magnitude of hydrocarbon oxidation rates at a given site.

The hypotheses that rates of hydrocarbon oxidation would correlate - or at least scale to - rates of sulfate reduction was disproven. Sulfate reduction rates did not broadly correlate to either hexadecane or naphthalene oxidation across site types, in general, though the site with the highest rates of sulfate reduction (MC118) also exhibited the highest rates of oil oxidation. The second hypothesis, that n-alkanes would be degraded faster than PAHs, was also disproven. Though alkane degradation yields more energy than PAH degradation, the inherent insolubility of n-alkanes like hexadecane limits their biodegradation substantially. The idea that sites impacted by oil and gas would express the highest rates of activity was proven correct. While oil loading did correlate with the potential for oil degradation, this relationship was not robust. Finally, we discovered a surprising connection between sedimented oil and microbial activity at the seabed at sites impacted by both natural oil and anthropogenic oil sedimentation. The amount and relative reactivity of sedimented oil determines the relative extent to which the material stimulates anaerobic terminal metabolism. Finally, some of these data (GC767) provides tantalizing evidence of the importance of oil fermentation (methanogenesis), even in the presence of sulfate.

1.5.3 CHAPTER 4

Chapter 4 presents the first systematic assessment of microbial activity under quasi in situ conditions in sediments of mixed hydrocarbon and brine impact along the northern continental slope of the Gulf of Mexico. The northern continental slope of the Gulf of Mexico is host to thousands of cold seeps each with unique sedimentary biogeochemical signatures driven in some part by variable inputs of oil, gas and brine. Sulfate reduction and anaerobic methanotrophy were used to assess variability between four different kinds of sites: i) sites containing quiescent abyssal sediments, ii) sites impacted by oil and gas, iii) sites in proximity to methane hydrates, and iv) sites influenced by brine seepage. The purpose of this study was to (1) compile one of the most expansive spatial-temporal datasets of biogeochemistry and microbial activity within Gulf of Mexico cold seep sediments, (2) to expand the availability of rate data collected under an improved method that approximates conditions found at the seafloor, and (3) to highlight the variability inherent in cold seep systems.

1.5.4 CHAPTER 5

The broader conclusions of the work presented in this dissertation are summarized in Chapter 5, along with proposed directions for future work.

Bibliography

1. Bertrand, J.-C., Brochier-Armanet, C., Gouy, M. & Westall, F. in *Environmental Microbiology: Fundamentals and Applications: Microbial Ecology* (eds Bertrand, J.-C. *et al.*) 75–106 (Springer Netherlands, Dordrecht, 2015).
2. Mykytczuk, N. C. S. *et al.* Bacterial growth at -15 °C; molecular insights from the permafrost bacterium Planococcus halocryophilus Or1. *The ISME Journal* **7,** 1211–1226 (2013).
3. Sorokin, D., Kuenen, J. & Muyzer, G. The Microbial Sulfur Cycle at Extremely Haloalkaline Conditions of Soda Lakes. *Frontiers in microbiology* **2,** 44 (Mar. 2011).
4. Nicholson, W. L. *et al.* Exploring the Low-Pressure Growth Limit: Evolution of Bacillus subtilis in the Laboratory to Enhanced Growth at 5 Kilopascals. *Applied and Environmental Microbiology* **76,** 7559–7565 (2010).
5. Daly, M. J. A new perspective on radiation resistance based on Deinococcus radiodurans. *Nature Reviews Microbiology* **7,** 237–245 (2009).
6. Takai, K. *et al.* Cell proliferation at 122 °C and isotopically heavy methane under high-pressure cultivation. *Proceedings of the National Academy of Sciences of the United States of America* **105,** 10949–54 (Sept. 2008).
7. Edwards, K. J., Bond, P. L., Gihring, T. M. & Banfield, J. F. An archaeal iron-oxidizing extreme acidophile important in acid mine drainage. *Science* **287,** 1796–1799 (2000).
8. Yayanos, A. A., Dietz, A. S. & Van Boxtel, R. Obligately barophilic bacterium from the Mariana trench. *Proceedings of the National Academy of Sciences* **78,** 5212–5215 (1981).

9. Singh, N. *et al.* Multi-drug resistant Enterobacter bugandensis species isolated from the International Space Station and comparative genomic analyses with human pathogenic strains. *BMC Microbiology* **18** (Dec. 2018).
10. Orcutt, B. N. *et al.* Carbon fixation by basalt-hosted microbial communities. *Frontiers in Microbiology* **6,** 904 (2015).
11. DeLeon-Rodriguez, N. *et al.* Microbiome of the upper troposphere: species composition and prevalence, effects of tropical storms, and atmospheric implications. *Proceedings of the National Academy of Sciences* **110,** 2575–2580 (2013).
12. Joye, S. B. *et al.* Metabolic variability in seafloor brines revealed by carbon and sulphur dynamics. *Nature Geoscience* **2,** 349 (2009).
13. Macalady, J. L. *et al.* Dominant Microbial Populations in Limestone-Corroding Stream Biofilms, Frasassi Cave System, Italy. *Applied and Environmental Microbiology* **72,** 5596–5609. ISSN: 0099-2240 (2006).
14. Whitman, W. B., Coleman, D. C. & Wiebe, W. J. Prokaryotes: The unseen majority. *Proceedings of the National Academy of Sciences* **95,** 6578–6583. ISSN: 0027-8424 (1998).
15. Locey, K. J. & Lennon, J. T. Scaling laws predict global microbial diversity. *Proceedings of the National Academy of Sciences* **113,** 5970–5975 (2016).
16. Kallmeyer, J., Pockalny, R., Adhikari, R. R., Smith, D. C. & D'Hondt, S. Global distribution of microbial abundance and biomass in subseafloor sediment. *Proceedings of the National Academy of Sciences* **109,** 16213–16216 (2012).
17. Falkowski, P., Fenchel, T. & Delong, E. The Microbial Engines That Drive Earth's Biogeochemical Cycles. *Science* **320,** 1034–9 (2008).
18. Finzi, A. C., Cole, J. J., Doney, S. C., Holland, E. A. & Jackson, R. B. Research frontiers in the analysis of coupled biogeochemical cycles. *Frontiers in Ecology and the Environment* **9,** 74–80 (2011).

19. Hoehler, T. M. & Jørgensen, B. B. Microbial life under extreme energy limitation. *Nature Reviews Microbiology* **11,** 83–94 (2013).

20. Jelen, B., Giovannelli, D. & Falkowski, P. The Role of Microbial Electron Transfer in the Coevolution of the Biosphere and Geosphere. *Annual Review of Microbiology* **70** (2016).

21. Chopra, A. & Lineweaver, C. The Case for a Gaian Bottleneck: The Biology of Habitability. *Astrobiology* **16,** 7–22 (2016).

22. Merino, N. *et al.* Living at the Extremes: Extremophiles and the Limits of Life in a Planetary Context. *Frontiers in Microbiology* **10,** 780 (2019).

23. Capece, M. *et al.* in, 3–59 (2013). ISBN: 978-94-007-6487-3.

24. Anitori, R. P. *Extremophilesmicrobiology and biotechnology* **579.19 E9** (2012).

25. Joye, S. *et al.* The Gulf of Mexico Ecosystem, six years after the Macondo Oil Well Blowout. *Deep Sea Research Part II: Topical Studies in Oceanography* **129** (2016).

26. Oceanic, N. & Service, A. A. N. M. F. *Fisheries Economics of the United States, 2009.* Technical Memorandum (U.S. Department of Commerce. National Marine Fisheries Service., 2010).

27. Sumaila, R. *et al.* Impact of the Deepwater Horizon well blowout on the Economics of U.S. Gulf fisheries. *Canadian Journal Fisheries and Aquatic Sciences* **69,** 499–510 (2012).

28. Joye, S. B. The Geology and Biogeochemistry of Hydrocarbon Seeps. *Annual Review of Earth and Planetary Sciences* **48,** 205–231 (2020).

29. Macdonald, I. *et al.* Natural and unnatural oil slicks in the Gulf of Mexico. *Journal of Geophysical Research* **120** (2015).

30. Knoll, A. H., Bergmann, K. D. & Strauss, J. V. Life: the first two billion years. *Philosophical Transactions of the Royal Society B: Biological Sciences* **371,** 20150493 (2016).

31. Seibold, E. & Berger, W. H. *The Seafloor: An Introduction to Marine Geology* 3rd ed. (Springer–Verlag Berlin Heidelberg, 1996).

32. Burdige, D. J. *Geochemistry of marine sediments* (Princeton University Press, 2006).

33. Fossing, H., Ferdelman, T. G. & Berg, P. Sulfate reduction and methane oxidation in continental margin sediments influenced by irrigation (South-East Atlantic off Namibia). *Geochimica et Cosmochimica Acta* **64,** 897–910 (2000).

34. Diercks, A.-R. *et al.* Scales of seafloor sediment resuspension in the northern Gulf of Mexico. *Elementa: Science of the Anthropocene* **6** (2018).

35. Berner, R. A. Biogeochemical cycles of carbon and sulfur and their effect on atmospheric oxygen over Phanerozoic time. *Global and Planetary Change* **1,** 97–122 (1989).

36. Suess, E. Particulate organic carbon flux in the oceans - Surface productivity and oxygen utilization. *Nature* **288,** 260–263 (1980).

37. Lutz, M., Caldeira, K. & Dunbar, R. Regional variability in the vertical flux of particulate organic carbon in the ocean interior. *Global Biogeochemical Cycles* **16** (2002).

38. Omand, M., Govindarajan, R., He, J. & Mahadevan, A. Sinking flux of particulate organic matter in the oceans: Sensitivity to particle characteristics. *Scientific Reports* **10** (2020).

39. Dunne, J., Sarmiento, J. & Gnanadesikan, A. A synthesis of global particle export from the surface ocean and cycling through the ocean interior and on the seafloor. *Global Biogeochemical Cycles* **21** (Dec. 2007).

40. Jørgensen, B. Mineralization of organic matter in the sea bed—the role of sulphate reduction. *Nature* **296,** 643–645 (1982).

41. Bowles, M. W., Mogollón, J. M., Kasten, S., Zabel, M. & Hinrichs, K.-U. Global rates of marine sulfate reduction and implications for sub–sea-floor metabolic activities. *Science* **344,** 889–891 (2014).

42. Eglinton, T. I. *et al.* Variability in Radiocarbon Ages of Individual Organic Compounds from Marine Sediments. *Science* **277,** 796–799 (1997).

43. Masiello, C. & Druffel, E. Black Carbon in Deep-Sea Sediments. *Science (New York, N.Y.)* **280,** 1911–3 (1998).

44. Berner, R. A. Burial of organic carbon and pyrite sulfur in the modern ocean; its geochemical and environmental significance. *American Journal of Science* **282,** 451–473 (1982).

45. Tissot, B. P. & Welte, D. H. *Petroleum Formation and Occurrence. A new Approach to Oil and Gas Exploration.* 2nd ed. (Springer-Verlag Berlin Heidelberg, 1984).

46. Kharaka, Y. K., Carothers, W. W. & Rosenbauer, R. J. Thermal decarboxylation of acetic acid: Implications for origin of natural gas. *Geochimica et Cosmochimica Acta* **47,** 397–402 (1983).

47. Philp, R. in *Hydrocarbons, Oils and Lipids: Diversity, Origin, Chemistry and Fate. Handbook of Hydrocarbon and Lipid Microbiology.* (ed H., W.) (Springer, Cham., 2020).

48. Widdel, F. & Rabus, R. Anaerobic biodegradation of saturated and aromatic hydrocarbons. *Current Opinion in Biotechnology* **12,** 259–276. ISSN: 0958-1669. `http://www.sciencedirect.com/science/article/pii/S0958166900002093` (2001).

49. Ferry, J. G. How to make a living by exhaling methane. *Annual Review of Microbiology* **64,** 453–473 (2010).

50. Joye, S. B., Bowles, M. W., Samarkin, V. A., Hunter, K. S. & Niemann, H. Biogeochemical signatures and microbial activity of different cold-seep habitats along the Gulf of Mexico deep slope. *Deep Sea Research Part II: Topical Studies in Oceanography* **57,** 1990–2001 (2010).

51. Claypool, G. & Kvenvolden, K. Methane and other Hydrocarbon Gases in Marine Sediment. *Annual Review of Earth and Planetary Sciences* **11,** 299–327 (2003).

52. Etiope, G. & Lollar, B. Abiotic methane on Earth. *Reviews of Geophysics* **51** (2013).

53. Etiope, G. & Ionescu, A. Low-temperature catalytic CO2 hydrogenation with geological quantities of ruthenium: A possible abiotic CH4 source in chromitite-rich serpentinized rocks. *Geofluids* **15** (2014).

54. Reeburgh, W. S. Oceanic Methane Biogeochemistry. *Chemical Reviews* **107,** 486–513 (2007).

55. Saunois, M. *et al.* The Global Methane Budget 2000–2017. *Earth System Science Data* **12,** 1561–1623 (2020).

56. Jackson, R. *et al.* Increasing anthropogenic methane emissions arise equally from agricultural and fossil fuel sources. *Environmental Research Letters* **15,** 071002 (2020).

57. Knittel, K. & Boetius, A. Anaerobic oxidation of methane: progress with an unknown process. *Annual review of microbiology* **63,** 311–334 (2009).

58. Martens, C. S. & Berner, R. A. Methane Production in the Interstitial Waters of Sulfate-Depleted Marine Sediments. *Science* **185,** 1167–1169 (1974).

59. Hoehler, T., Alperin, M., Albert, D. & Martens, C. Field and laboratory studies of methane oxidation in an anoxic marine sediment: Evidence for a methanogen-sulfate reducer consortium. *Global Biogeochemical Cycles* **8,** 451–464 (1994).

60. Boetius, A. *et al.* A marine microbial consortium apparently mediating anaerobic oxidation of methane. *Nature* **407,** 623–6 (2000).

61. Ettwig, K. *et al.* Nitrite-driven anaerobic methane oxdation by oxygenic bacteria. *Nature* **464,** 543–8 (2010).

62. Dekas, A. E., Poretsky, R. S. & Orphan, V. J. Deep-sea archaea fix and share nitrogen in methane-consuming microbial consortia. *Science* **326,** 422–426 (2009).

63. Raghoebarsing, A. *et al.* A microbial consortium couples anaerobic methane oxidation to denitrification. *Nature* **440,** 918–21 (May 2006).

64. Beal, E., House, C. & Orphan, V. Manganese- and Iron-Dependent Marine Methane Oxidation. *Science (New York, N.Y.)* **325,** 184–7 (2009).

65. Egger, M., Riedinger, N., Mogollón, J. M. & Jørgensen, B. B. Global diffusive fluxes of methane in marine sediments. *Nature Geoscience* **11,** 421–425 (2018).

66. Raghoebarsing, A. *et al.* A microbial consortium couples anaerobic methane oxidation to denitrification. *Nature* **440,** 918–21 (2006).

67. Vaksmaa, A. *et al.* Enrichment of anaerobic nitrate-dependent methanotrophic 'Candidatus Methanoperedens nitroreducens' archaea from an Italian paddy field soil. *Applied Microbiology and Biotechnology* **101,** 7075–7084 (2017).

68. Wegener, G., Krukenberg, V., Riedel, D., Tegetmeyer, H. E. & Boetius, A. Intercellular wiring enables electron transfer between methanotrophic archaea and bacteria. *Nature* **526,** 587–590 (2015).

69. Expanding the repertoire of electron acceptors for the anaerobic oxidation of methane in carbonates in the Atlantic and Pacific Ocean. *ISME J* (2021).

70. Hallam, S. J. *et al.* Reverse methanogenesis: testing the hypothesis with environmental genomics. *Science* **305,** 1457–1462 (2004).

71. Alperin, M. J. & Reeburgh, W. S. Inhibition Experiments on Anaerobic Methane Oxidation. *Applied and Environmental Microbiology* **50,** 940–945 (1985).

72. Hinrichs, K.-U., Hayes, J. M., Sylva, S. P., Brewer, P. G. & DeLong, E. F. Methane-consuming archaebacteria in marine sediments. *Nature* **398,** 802–805 (1999).

73. Joye, S. B. *et al.* The anaerobic oxidation of methane and sulfate reduction in sediments from Gulf of Mexico cold seeps. *Chemical Geology* **205,** 219–238 (2004).

74. Alperin, M. J. & Hoehler, T. M. Anaerobic methane oxidation by archaea/sulfate-reducing bacteria aggregates: 1. Thermodynamic and physical constraints. *American Journal of Science* **309,** 869–957 (2009).

75. Alperin, M. J. & Hoehler, T. M. Anaerobic methane oxidation by archaea/sulfate-reducing bacteria aggregates: 2. Isotopic constraints. *American Journal of Science* **309,** 958–984 (2009).

76. Bowles, M. *et al.* Remarkable Capacity for Anaerobic Oxidation of Methane at High Methane Concentration. *Geophysical Research Letters* **46,** 12192–12201 (2019).

77. Laso-Pérez, R., Krukenberg, V., Musat, F. & Wegener, G. Establishing anaerobic hydrocarbon-degrading enrichment cultures of microorganisms under strictly anoxic conditions. *Nature Protocols* **13,** 1310–1330 (2018).

78. Alperin, M. J. & Hoehler, T. M. Anaerobic methane oxidation by archaea/sulfate-reducing bacteria aggregates: 1. Thermodynamic and physical constraints. *American Journal of Science* **309,** 869–957 (2009).

79. Haroon, M. F. *et al.* Anaerobic oxidation of methane coupled to nitrate reduction in a novel archaeal lineage. *Nature* **500,** 567–570 (2013).

80. Ettwig, K. *et al.* Denitrifying bacteria anaerobically oxidize methane in the absence of Archaea. *Environmental microbiology* **10,** 3164–73 (2008).

81. Ettwig, K., Alen, T., Pas-Schoonen, K., Jetten, M. & Strous, M. Enrichment and Molecular Detection of Denitrifying Methanotrophic Bacteria of the NC10 Phylum. *Applied and environmental microbiology* **75,** 3656–62 (2009).

82. Leu, A. O. *et al.* Anaerobic methane oxidation coupled to manganese reduction by members of the Methanoperedenaceae. *The ISME journal* **14,** 1030–1041 (2020).

83. Tissot, B. & Welte, D. *Petroleum Formation and Occurrence: A New Approach to Oil and Gas Exploration* ISBN: 9783642964466 (Springer Berlin Heidelberg, 1978).

84. Seewald, J. Organic-Inorganic interactions in petroleum-producing sedimentary basins. *Nature* **426,** 327–33 (2003).

85. Skarke, A., Ruppel, C., Kodis, M., Brothers, D. & Lobecker, E. Widespread methane leakage from the sea floor on the northern US Atlantic Margin. *Nature Geosci* (2014).

86. Macdonald, I. R. *et al.* Asphalt Volcanism and Chemosynthetic Life in the Campeche Knolls, Gulf of Mexico. *Science* **304,** 1002–999 (2004).

Chapter 2

Dynamics and diversity of methanotrophy across the chemocline of the deep hypersaline Orca Basin.[1]

---

[1] Sibert, R. J., Pena-Montenegro, T., Hunter, K., Montoya, J., Teske, A. P., Joye, S. B. To be submitted to *Nature Geoscience.*

2.1 Abstract

Deep-sea hypersaline anoxic basins (DHABs) are localized seafloor environments that contain energy- and nutrient- rich brines capable of supporting extensive microbial communities. Seafloor brines are hypersaline, devoid of molecular oxygen, and contain elevated concentrations of reduced solutes. Energy-rich compounds, *e.g.,* hydrogen sulfide, ammonium, and methane, diffuse across the seawater-brine interface, generating steep geochemical gradients that fuel unique halotolerant microbial communities. Here, we report the first rates of microbial methane oxidation and sulfate reduction across the chemocline of Orca basin, Gulf of Mexico, one of the world's largest submarine brine basins. Methane turnover was fastest via aerobic microbial methanotrophy in the sub-oxic zone above the chemocline. The highest rates of methane oxidation, however, occurred within the anoxic brine. Though aerobic and anaerobic methane oxidation were documented, dissimilatory sulfate reduction was not, and anaerobic methanotrophy was instead coupled to iron, and possibly nitrite reduction. In Orca Basin, successive metabolisms moderate methane oxidation, creating an effective sink for methane in this extreme environment.

2.2 Introduction

The Orca Basin is a semi-enclosed seafloor depression in the northern Gulf of Mexico (Gulf) that is filled with more than 10 km^3 of 8000-year-old anoxic brine. The predominantly halite brine is over eight times the salinity of the overlying seawater (see Fig 2.1 A; Table A.1 and A.2); the two endmembers are separated by a stable isopycnal horizon that reduces mixing between the endmember fluids. Numerous shallow brine pools, fluidized muds, and flows have been reported in the Gulf since the discovery of Orca Basin in the late 1970s, most only a few meters deep [1–5]. In contrast, the Orca Basin covers approximately 225 km^2 and is more than 200 meters deep [6, 7] making it the largest known deep-sea hypersaline anoxic brine basin (DHAB) in the Gulf. Brine lakes of this size occur in seafloor depressions elsewhere, particularly in the Mediterranean [8–11] and Red Sea [12–16]. Brines form either through the tectonic uplift and re-dissolution of buried evaporites as they interact with seawater (*e.g.,* Mediterranean and Gulf), or through interactions with hydrothermal fluids in the subsurface (*e.g.,* Red Sea). In the Mediterranean, brines of Messinian origin accumulate within depressions along the accretionary wedge complex at the convergent intersection of the African plate and the Aegean arc [17]. In the Red Sea, active rifting produces interactions between hydrothermal fluids and Miocene evaporites to produce warm, metalliferous brines [13]. Gulf brines are formed from the dissolution of Jurassic-aged evaporites [13] which occurs as buried salt sheets are deformed (i.e., salt tectonics) and interact with seawater and with fluids generated via clay dewatering through sediment compaction [18].

The chemistry of deep-sea brines is exotic. The relative habitability of brines depends on the dominant host salt and its concentration. NaCl-saturated brines exhibit lower microbial diversity than seawater but contain representatives of every domain of life that are capable of mediating almost any biogeochemical process [19, 20]. NaCl-saturated brines (5M NaCl) have a water activity (A_w) of ca. 0.755 (*e.g.,* Orca Basin [20]) which is far above the A_w that limits life, ca. 0.585. However, this A_w is substantially below that of seawater (A_w ca. 0.98) making these brines extreme environments.

While all brine fluids are hypersaline, each brine is unique with a distinct cocktail of major and minor ions, organic and inorganic nutrients, and dissolved organic matter; sometimes brines even contain petroleum [21, 22]. Most brines do share one common feature – the fluids are enriched in methane, a recognized greenhouse gas [4, 5, 15, 16, 23, 24]. Methane is approximately 26 times more effective at trapping heat than carbon dioxide, and the second most abundant greenhouse gas in the atmosphere [25]. This study was designed to estimate rates and pathways of methane oxidation across the Orca Basin chemocline to constrain the modes of methane oxidation in this unique hypersaline extreme environment. The focus on methane assures broad relevance of the work since methane is one of the most abundant electron donors in reducing environments generally, and in DHABs, specifically. These deep-sea extreme environments offer the opportunity to advance the understanding early conditions and early life on Earth [4] and Mars [26], and may advance our ability to predict the likelihood of extraterrestrial life [27, 28].

Vertical stratification of redox zones is an emergent property that is found in any habitat where diffusion limits the flux of reductant (*i.e.,* energy rich substrate) and oxidant (*i.e.,* electron acceptor). The vertical scale of redox zones varies tremendously, from the microscale (μm to mm in microbial mats [29]), to the macroscale (tens of meters in organic matter poor habitats like sediments in the South Pacific Gyre [30]) depending on the relative influx of organic matter [18]. Differential supply of electron donor and electron acceptor create unique metabolic niches for microorganisms along a predictable sequence of respiratory processes. Deep sea brine environments offer an ideal locale to study the dynamics of microbial populations along redox interfaces, as they are characterized by dramatic gradients in dissolved oxygen and redox metabolites such as methane and nitrate. Chemical gradients of reduced species and nutrients derived from the brine intersect with layers of accumulated particles and electron acceptors derived from the overlying seawater [7] creating a cascade of niches that are exploited by microbial communities.

The geometry and geology of Orca Basin (see Figure 2.1) creates an optimal situation for formation of a broad and extensive chemocline (see Figure 2.2) that spans over 100 meters. Among DHABs, Orca Basin is an ideal environment to explore microbial dynamics since the 110 m thick chemocline offers an opportunity to assess different metabolisms using traditional sampling approaches (*e.g.,* CTD rosette and Niskin bottles). The interface is cm to m at best in some other well-studied brines – such as the Bannock Basin [23] and Urania Basin [31] in the Mediterranean, and the shallow brines in the Gulf of Mexico [4] – which requires specialized equipment to capture key transformations across the interface [3]. The ability to capture specific niches across a wide salinity range using standard seagoing equipment makes Orca Basin an opportune place to advance the understanding of DHAB biogeochemistry.

Many deep-sea brines are nutrient-rich kosmotropic halite brines, energy-rich oases that make ideal habitat for microorganisms with competent strategies for dealing with salinity stress [20]. Increased salinity selects for specialized microbial populations that can thrive at high salinity [32] and there is typically an inverse relationship between microbial diversity and salinity [19]. Brine chemistry creates a series of niches and selects for unique microbes/microbial communities that able to exploit local conditions; these populations thrive and achieve substantial biomass accumulation at discrete depths of the chemocline [19]. In some extreme cases (*e.g.,* solar salterns), salinity selects for true halophiles and water activity acts as a selective force [20, 33, 34]. Microbial population numbers in brine fluids can exceed that of typical seawater by 100 or more times despite salinities an order of magnitude higher than seawater [4, 23]. There are three reasons for this: 1) the chemocline acts as a trap for nutrient-rich particles and organic matter [7], 2) variable salinity promotes the separation of distinct niches based on salinity tolerance, thereby reducing interspecies competition[23], and 3) steep geochemical gradients supply energy and reducing power for metabolic processes [20, 35].

Rates and patterns of microbial activity in deep sea brines are poorly constrained [19]. Initial reports speculated that deep sea brines were dominated by heterotrophic processes [31]. Available data suggests instead that these systems support high rates of chemoautotrophy [35]. Yakomov et al. (2007 [35]) reported high rates of dark carbon dioxide fixation rates along the chemocline, perhaps through metal oxidation [38] and sulfide oxidation ([33, 37, 39]. Methanogenesis ([4, 36, 37]) may also be important in brines, but the significance of other chemoautotrophic processes – e.g. ammonia oxidation – remains unclear [35, 40].

Previous work on microbial activity in brines has focused on dissimilatory sulfate reduction [4, 5, 23, 37]. Microbial activity has been inferred from genomics studies but direct measurement of metabolic rates using sensitive radiotracer approaches [41] is less common. Sulfate-reducing bacteria and concomitant sulfate reduction activity are common in DHABs [16, 23, 32, 37, 42]. Many other sulfur cycling microbes capable of *e.g.* thiosulfate and elemental sulfur cycling [43, 44] are also present in DHABs. While methanogenesis has been a focus of previous studies (see Merlino et al. 2018 for review [19]), information on methane oxidation in DHABs is lacking. Methane oxidation has been described in brine-impacted sediments [45] and groundwater [46], but it has not been documented in hypersaline brine fluids so far [4]. The activity of AOM, if present, was below detection in shallow brines in the Gulf [4] as predicted by thermodynamic limitations [75].

This study presents the first detailed assessment of methane oxidation across the chemocline in a deep-sea hypersaline brine environment. We hypothesized that both aerobic and anaerobic modes of methanotrophy would occur across the brine and that activity would be limited by methane availability at the upper parts of the chemocline and by abundance of electron acceptors at the lower parts. Over several research expeditions, we assessed the presence and magnitude of methane oxidation and sulfate reduction across the Orca Basin chemocline using sensitive radiotracer assays. We explored the coupling of anaerobic oxidation of methane to other processes, *e.g.,* metal oxide reduction and nitrogen reduction, in manipulative experiments. Consistent results reveal that microbial methane oxidation in Orca Basin is unique compared to previous results from other DHAB ecosystems.

2.3 Methods

2.3.1 Sampling

Samples were collected during four separate expeditions: expedition AT18-02 in 2010 and AT26-13 in 2014 aboard the R/V Atlantis, and expeditions EN586 and EN600 in 2016 and 2017, respectively, aboard the R/V Endeavor (see Figure 2.1). Target depths were selected based on data from repeated full water column hydrographic casts. The selected suite of depths encompassed the seawater-brine transition zone, and included at least one depth at normal seawater salinity, one within the core of the deep, anoxic brine, and a range of depths that captured major transitions in oxygen, salinity, and particle density (Sea-Bird Electronics, SBE 911+ CTD, SBE 25 Sealogger, and Wet Labs C-Star 25 cm transmissometer; see Figure 2.2). Unlike normal seawater sampling, Niskin bottles were fired on the downcast to avoid contaminating overlying seawater samples with viscous, methane-rich Orca brine. Sub-samples were collected immediately following recovery of the CTD rosette for assessment of rates and collection of sub-samples for microbial community composition (nucleic acids), brine chemistry, and alkane concentration quantification.

Orca Basin brine is saturated with low molecular weight alkanes and degases quickly at surface pressure. To minimize gas loss, alkane sub-samples were collected immediately upon opening

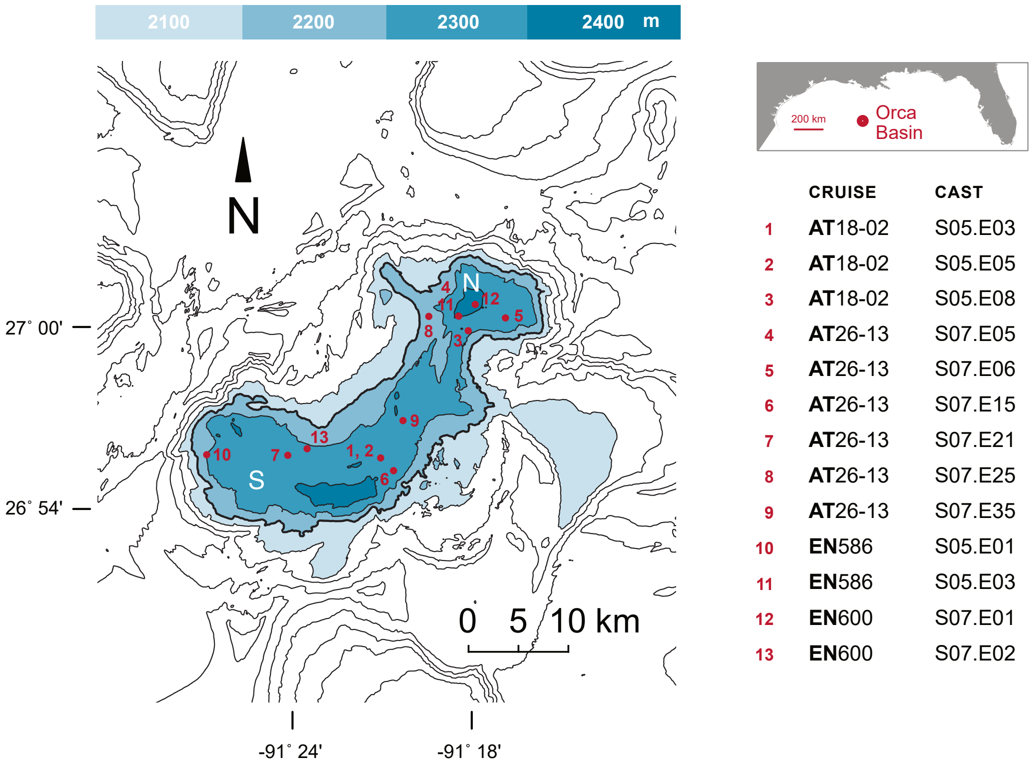

	CRUISE	CAST
1	**AT**18-02	S05.E03
2	**AT**18-02	S05.E05
3	**AT**18-02	S05.E08
4	**AT**26-13	S07.E05
5	**AT**26-13	S07.E06
6	**AT**26-13	S07.E15
7	**AT**26-13	S07.E21
8	**AT**26-13	S07.E25
9	**AT**26-13	S07.E35
10	**EN**586	S05.E01
11	**EN**586	S05.E03
12	**EN**600	S07.E01
13	**EN**600	S07.E02

Figure 2.1: Sampling locations at Orca basin, Gulf of Mexico. Bathymetry dataset courtesy of the U.S. Bureau of Ocean Energy Management: https://www.boem.gov/Gulf-of-Mexico-Deepwater-Bathymetry. Isobaths in 100 m increments.

Niskin bottles into combusted 160 mL serum vials containing two NaOH pellets to halt microbial activity. The samples were sealed headspace-free and prepared for analysis within 1 hour of collection [47, 48]. Bulk water was collected for shipboard radiotracer rates into 2 L glass media bottles, sealed headspace-free with base-boiled butyl rubber stoppers, and processed within 1 hour of collection. Additional sub-samples were collected for nucleic acids and brine chemistry in acid-washed, sample-rinsed, 1 L polyethylene terephthalate glycol bottles (PETGs) sealed headspace-free, and stored at 4 °C. Nucleic acid sub-samples (1L of fluid) were pumped immediately through 0.2 μm Sterivex filters, flash frozen in liquid nitrogen, and stored at −80 °C until extraction [49]. The molecular data is forthcoming and will be presented at the time of publication (*i.e.,* after May 2021). The remaining chemistry splits were either sampled directly or passed through sample-rinsed 0.2 μm nylon filters using acid-washed 60 mL syringes, collected in 125 mL HDPE bottles, and divided further for various chemical analyses.

2.3.2 CHEMISTRY

A combination of filtered and unfiltered sub-samples were obtained for chemical analysis, and either analyzed at sea (ammonium) or preserved for shore-based analysis. Unfiltered 2 mL sub-samples were fixed with 500 μL of 20% zinc acetate for colorimetric determination of sulfide (H_2S) using a standard method [47, 50]. Ammonium ($NH_4{}^+$) concentrations were determined at sea using an indophenol blue method on filtered, 2 mL aliquots preserved with 200 μL phenol reagent [51]. Additional 1 mL sub-samples were collected for dissolved inorganic carbon (DIC) in crimp-sealed, He-purged, 6 mL serum vials, and then acidified with 100 μL concentrated phosphoric acid. The acidified samples were shaken vigorously to drive DIC into the headspace, a subsample of which was analyzed using a gas chromatograph [47].

Filtered 1.5 mL sub-samples were preserved with concentrated, trace metal grade nitric acid (10 μL mL^{-1} HNO_3) and analyzed for anions ($SO_4{}^{2-}$, Cl^-), and cations (Na^+, K^+, Mg^{2+}, and Ca^{2+}) by ion chromatography [47]. Approximately 100 mL of the remaining filtrate was frozen at −20 °C for shore-based nutrient analysis ($NO_3{}^-$, $NO_2{}^-$, and $PO_4{}^{3-}$) using automated colorimetric methods [47]. A portion of the nutrient splits were quantified for dissolved organic carbon content on a Shimadzu TOC analyzer following methods described elsewhere [47]. Particles were collected by passing 1 – 20 L of sample directly from the CTD-rosette through pre-combusted GF/F filters (47 mm x 0.7 μm) under gentle pump pressure, dried for 24 hours at 60 °C, and stored at −20 °C. The abundance of carbon stable isotopes was measured by continuous-flow isotope ratio mass spectrometry [52, 53]. The results were standardized to the Pee Dee Belemnite and reported as $\delta^{13}C$ values (‰) according to equation 2.1, where R_{SAMPLE} is the $^{13}C{:}^{12}C$ ratio of the sample, and R_{PDB} the $^{13}C{:}^{12}C$ ratio of the Pee Dee Belemnite standard.

$$\delta^{13}C = \left[\frac{R_{SAMPLE}}{R_{PDB}} - 1 \right] \times 1000‰ \tag{2.1}$$

Headspace sub-samples were analyzed for short-chain alkanes (C_1 – C_5) by standard gas chromatography (SRI 8610C; 3.2mm x 1.8 m packed hayecep–d column, and flame ionization detector). Additional gas splits were analyzed for the stable carbon isotopes of methane ($^{13}CH_4$) and carbon dioxide ($^{13}CO_2$) using a Picarro G2201-*i* cavity ringdown spectrometer (CRDS), coupled to the Picarro Small-Sample Introduction Module (SSIM2). Similar to particle isotope values, abundances were reported as $\delta^{13}C$ (‰) using equation 2.1 above. The CRDS was standardized using a methane/CO_2 span gas with known $\delta^{13}C$ isotopic composition relative to the Pee Dee Belemnite. The span gas was measured at the Center for Applied Isotope Studies (University of Georgia) on a Thermo Gas Bench coupled to a Delta V IRMS.

Methane diffusion across the halocline was calculated using Fick's first law (equation2.2) where J is the flux, D is the diffusion coefficient (10^{-3} cm^2 s^{-1} to 10^{-2} cm^2 s^{-1}; calculated below), dc is the difference in methane concentration between brine and overlying seawater (see Table 2.4), and dz the width of the halocline (here, 15 m). The diffusion coefficient was calculated from temperature using equation 2.3, where F_{geo} is the geothermal heat flux (30 mW m^{-2}; [54]), T is temperature, z is depth, c_p is heat capacity and ρ is calculated density. Here, we adopted a diffusion coefficient of 10^{-3} cm^2 s^{-1} across the halocline (see Figure A.1).

$$J = -D_z \left(\frac{dc}{dz} \right) \tag{2.2}$$

$$D_z = F_{geo} \left(\frac{\partial T}{\partial z} c_p \rho \right)^{-1} \tag{2.3}$$

The conductivity sensor of the CTD may underestimate salinity when the salt content is greater than approximately >125 g kg^{-1}, as noted previously see Figs. 2.2 and A.2 [7]. To compensate for this, we adopt a similar strategy to Diercks et al. [7] and report the salinity output of the CTD for values <100 g kg^{-1} but thereafter report values obtained by refractometer.

2.3.3 Radiotracer Rate Measurements

Sub-samples for methane oxidation (MO) and sulfate reduction (SR) rates were distributed in triplicate from 2 L media bottles into 28 mL Balch tubes using anoxic techniques. To minimize contamination from atmospheric oxygen during transfer, media bottle stoppers were exchanged for lab-made transfer assemblies, similar to that of a Widdel flask (described in [55]). Briefly, each transfer assembly consisted of two 4 mm ID glass tubes, one short (4 cm) and one long (25 cm), both friction-fit through the holes of a boiled, two-hole, GL45 rubber stopper. The short glass tube was adjusted to about 1 mm past the bottom of the stopper and plumbed externally to a supply of UHP argon. The long tube was adjusted to within 1 cm above the bottom of the bottle and connected to sterile silicone outflow tubing. The media bottles were then sealed and pressurized to 1.2 bar to begin displacing sample through the apparatus and into Balch tubes. The tubes were filled from the bottom up, sealed headspace-free with boiled rubber stoppers, crimp-sealed and stored at 4 °C until tracer injection.

Methane oxidation rates were determined using either ^{14}C–labeled methane during expeditions AT18-02 and AT26–13, or tritiated methane during expeditions EN586 and EN600. Samples for tritium-based rates were injected with 33.3 kBq (900 fmol) C^3H_4, incubated in the dark at 4 °C for 24–48 hours, and killed with formaldehyde additions to 3.5% final concentration. Tritiated samples were purged with air for 45 minutes to strip residual C^3H_4 from solution and then a 7 mL sub-sample was analyzed for ^3H_2O with a scintillation counter. Similarly, samples for rates derived from ^{14}C–labeled methane were injected with 11.6 kBq (6 nmole) $^{14}CH_4$, incubated for 24–48 hours, and killed with 3 mL additions of 2 M NaOH. Samples were acid-distilled and processed as described elsewhere [47]. Two controls per cast were collected and killed approximately 5 hours before tracer injection by adding either formaldehyde for tritiated samples or NaOH for ^{14}C–labeled samples as described above. Both samples and kill controls were processed immediately using previously described methods [47, 56].

During expeditions EN586 and EN600, two additional sets of samples for methane oxidation rates were collected for experimental manipulation in parallel with the standard suite. During EN586, one set was amended with 3.6 mmol L-1 ferrihydrite, the other with 12.2 mmol L-1 goethite, both solid phases of oxidized iron to assess the impact of iron oxide availability on anaerobic MO. These amendments were first synthesized in the lab (see below), then weighed and distributed to tubes prior to sampling [57]. Parallel MO experiments were also conducted during expedition EN600, this time with 1 mM nitrate and 1 mM nitrite amendments to assess the impact of oxidized nitrogen species availability on anaerobic MO. No other modifications were made to the sample processing protocol or rate derivations and were otherwise treated identically to the incubations described above.

Methane oxidation rates were calculated according to equation 2.4, where $[CH_4]$ is the methane concentration in nmol L^{-1}, t is the incubation time in days, and R_{mox} is the ratio of activities between either $^{14}CO_2$:$^{14}CH_4$, or $^{3}H_2O$:$C^{3}H_4$, depending on which isotope was used. Rates derived from experimental iron incubations are calculated identically but reported as the relative difference in rates of methane oxidation ($\Delta\textsc{mox}$) between samples treated with iron oxides ($\textsc{mox}_t$) and samples with no treatment (MOx; $\textsc{mox}$), as in equation 2.6 (2.5).

$$\textsc{mox} = [CH_4] \times \frac{R_{mox}}{t} \tag{2.4}$$

$$\Delta\textsc{mox} = \textsc{mox}_t - \textsc{mox} \tag{2.5}$$

Sub-samples for sulfate reduction rates were injected with between 33 kBq (147 fmol) and 167 kBq (734 fmol) Na_2SO_4, incubated between 24–48 hours at 4 °C, and killed with a 5 mL 20% Zn acetate solution to halt microbial activity and trap evolved ^{35}S–sulfide as particulate $Zn^{35}S$. Fixed samples were vacuum-filtered through 0.22 µm Millipore nitrocellulose filters to capture particulate $Zn^{35}S$, rinsed 3 times with 10 mL of 1% zinc acetate solution (ca. pH 8) to remove residual ^{35}S–sulfate, and then counted in 7 mL scintillation fluid. This procedure quantifies ^{35}S associated with acid volatile sulfide (AVS: H_2S, FeS), chromium-reducible sulfide (CRS: S°, FeS_2), and any reduced ^{35}S species (e.g. cysteine) incorporated into microbial biomass. To determine the fraction of counts resulting from dissimilatory sulfate reduction (DSR; AVS + CRS), the scintillation fluid and filters were decanted into round-bottom flasks and distilled using the one-step hot HCl:Cr^{2+} procedure of Fossing and Jørgensen (1989 [58]). Prepared laboratory standards containing known activities of Zn^{35}S emulsified in scintillation fluid were treated as process controls to determine recovery efficiency (ca. 95%). Rates of DSR were calculated using equation 2.6 below, where [$SO_4{}^{2-}$] is the sulfate concentration in mmol L^{-1}, α is the fractionation factor for sulfur (1.06), "t" is incubation time in days, and R_{srr} is the ratio between the activities between evolved ^{35}S–sulfide and injected $^{35}SO_4$ [58–60]. SRR reported in units of µmol L^{-1} d^{-1}.

$$\text{SRR} = \left[SO_4{}^{2-}\right] \times \frac{\alpha}{t} \times R_{srr} \times 1000 \tag{2.6}$$

2.3.4 Mineral Synthesis

Two-line ferrihydrite and goethite were synthesized by precipitation using well-described procedures [57, 61]. Briefly, 20 g of $Fe(NO_3)_3 \cdot 9\,H_2O$ was dissolved in 250 mL double-deionized water (DDI) and gradually brought to pH 7–8 by dropwise titration of 1 M KOH. The resulting slurry was centrifuged and the supernatant discarded. The pellet was then rinsed in fresh DDI, vortexed and centrifuged again. This procedure was repeated until the salinity of the supernatant fell below 10 ppm as measured using a benchtop conductivity sensor. The slurry was then centrifuged one last time, frozen, freeze-dried for approximately 10 hours, ground to uniformity with a mortar and pestle, and stored in argon-flushed Falcon tubes at −20 °C until use. Goethite was synthesized by aging two-line ferrihydrite for 60 hours at 70 °C in 2 M KOH. The mineral slurry was frozen, freeze-dried, and stored at −20 °C until use [57].

2.4 Results

2.4.1 Oxygen and Salinity

Four distinct chemical zones across the 110 m chemocline of Orca were defined by down-profile changes in salinity and oxygen concentrations (see Figure 2.2). These zones corresponded to changes in major parameters, including particle abundance and concentration of oxygen, light hydrocarbon gases (see Figures 2.2 and A.3), dissolved carbon (see Figures A.5, A.3, and A.7), major ions (see Figures 2.3 and 2.4), nutrients (see Figures A.4 and A.8), and microbial activity (see

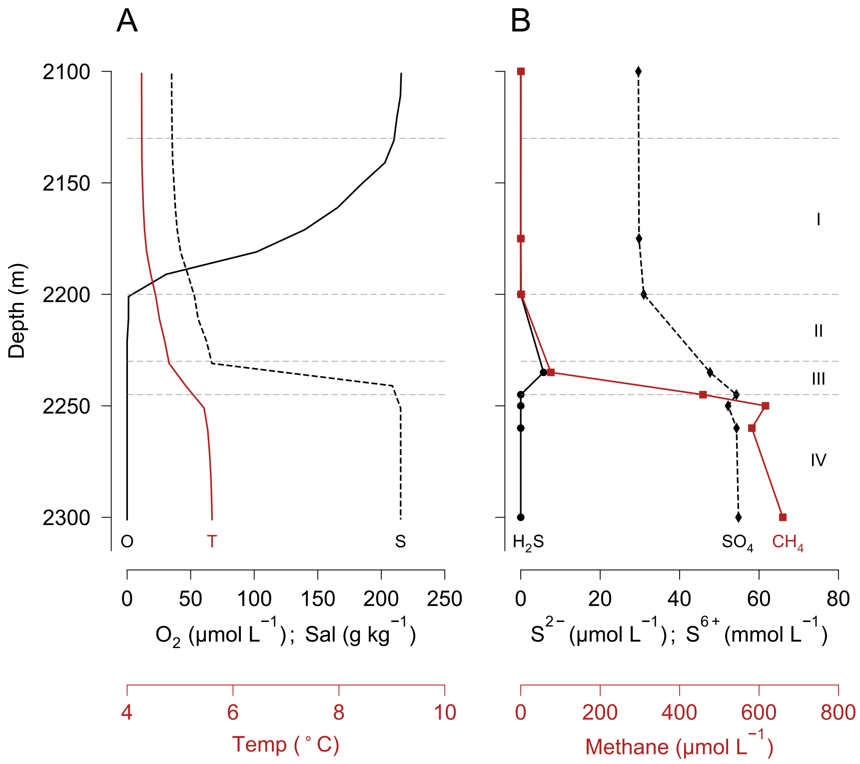

Figure 2.2: Typical hydrographic profiles of A) salinity (dashed black), oxygen (black), temperature (red), and B) methane (red), sulfate (S^{6+}; dashed black), and sulfide (S^{2-}; solid black) across the chemocline of Orca basin. Horizon abbreviations: I = oxycline, II = suboxic, III = halocline, and IV = brine. Data from Orca S., cruise EN586, 2016.

Figures 2.7). Figure 2.2 is a typical hydrocast across the 110 m seawater-brine transition (chemocline) of Orca basin, illustrating stepwise chemical zonation similar to other brines systems [11, 37, 42, 62], here defined by major shifts in oxygen and salinity. The first two zones (I and II; see Figure 2.2) were notable due to the almost complete depletion of oxygen and a doubling of the salinity. Zone I contained a steep 70 m oxycline between 2130 m and 2200 m (zone I; see Figure 2.2A), where oxygen concentrations diminished from 220 µmol L^{-1} to <10 µmol L^{-1} O_2, and salinity decreased by 12 g kg^{-1}. The second horizon remained sub-oxic below 2200 m (<5 µmol L^{-1} O_2) and oxygen concentration diminished to below detection at 2230 m and 67 g kg^{-1} salinity (zone II; see Figure 2.2).

Oxygen was below detection past 2230 m to the bottom of the basin, so the remaining two zones were defined entirely by changes in salinity. Zone III contained a sharp 15 m thick halocline

Expedition	Cast	Basin	$g\,kg^{-1}$	CH_4	SO_4^{2-}	H_2S	Cl	Na	K	Mg	Ca	NO_3^-	NH_4^+	PO_4^{3-}	DIC	DOC
AT26–13	S07.E15	S	270	565.4	42.7	0.0	4517.2	5180.4	24.7	48.2	39.7	0.6	289.7	18.5	4.7	312.8
	S07.E21	S	255	476.5	47.1	0.0	4982.9	5110.3	24.6	48.6	38.8	0.3	315.7	17.8	5.4	309.8
	S07.E25	N	273	509.5	43.3	0.0	4726.3	4942.1	24.2	47.8	37.9	1.9	434.2	18.7	5.0	298.8
	S07.E35	S	270	650.1	44.0	0.0	4448.7	5249.1	24.3	47.7	40.2	12.2	412.2	18.2	4.7	301.0
	S07.E36	S	285	487.5	42.7	0.0	4545.4	5080.4	24.8	48.3	38.6	0.3	330.9	18.7	4.3	300.0
EN586	S05.E01	S	–	666.5	54.8	5.7	4989.9	4629.6	20.0	44.0	34.0	0.7	489.6	25.1	4.4	307.8
	S05.E03	N	–	687.6	56.5	3.0	4967.2	4667.7	20.0	51.0	35.0	21.2	500.4	20.9	4.3	278.3
EN600	S07.E01	S	–	922.4	55.0	1.5	–	–	–	–	–	1.8	498.1	57.1	5.0	280.8
	S07.E02	N	–	936.4	57.0	1.5	–	–	–	–	–	1.6	498.8	58.8	4.8	300.2

Table 2.1: Orca brine chemistry. Methane, sulfide, nitrate, ammonium, phosphate, and DOC in $\mu mol\,L^{-1}$. Sulfate, chloride, sodium, potassium, magnesium, calcium, and DIC in $mmol\,L^{-1}$. Salinity values in $g\,kg^{-1}$ measured by refractometer on diluted samples

between 2230 m and 2245 m where salinity increased nearly four-fold to >250 $g\,kg^{-1}$ at 2245 m depth, transitioning into an essentially homogenous brine in zone IV (zone III; see Figure 2.2; Tables 2.2, 2.3). These trends were stable between the four expeditions presented here and have been noted since the discovery of Orca in the mid-1970s [38, 41, 63, 64].

2.4.2 MAJOR IONS AND NUTRIENTS

The Orca basin is filled with thalassahaline halite brine, which is reflected in the proportions of chloride, sodium, potassium, calcium, and magnesium (see Figures 2.3, 2.4; Tables 2.2, 2.3). Compared to normal seawater, the concentrations of every major ion, aside from magnesium, was elevated in the brine, particularly those of chloride and sodium. Chloride and sodium comprised between 48% to 50% of the ionic composition of the brine, similar to seawater (48% Cl and 43% Na; see Table 2.3), but concentrations approached those expected from halite saturation (see Tables 2.2, 2.3). Chloride concentrations varied between 4.1 to 4.7 M Cl, and sodium concentrations varied from 3.9 to 4.8 M Na, an increase of between seven and eight times the concentrations expected in seawater (see Figure 2.2, 2.3 and Table 2.2).

Calcium, potassium, and sulfate were minor components of the brine but concentrations increased across the chemocline between 1.7 and 3.4 times, yielding average brine concentrations of 34.8 mM Ca, 21.7 mM K, and 48.5 mM SO_4^{2-}, respectively (see Tables 2.1, 2.2). In contrast, magnesium concentrations diminished within the brine (zone III; see Figure 2.4), decreasing from

Sample	**$[Cl^-]$**	**$[Na^+]$**	**$[Ca^{2+}]$**	**$[K^+]$**	**$[Mg^{2+}]$**	**$[SO_4^{\ 2-}]$**
Orca N	4077.8(1936)	3889.3(1993)	31.5(12)	17.7(7)	46.0(4)	46.6(12)
Orca S	4690.8(427)	4856.9(355)	34.8(5)	21.7(3)	46.5(3)	48.5(7)
Seawater*	549	469	10.4	10.2	52.8	28.2

Table 2.2: Bulk composition of Orca brine and seawater. Concentrations reported as bootstrapped means ($n=10^4$) in mmol L^{-1}, where ± values represent a 99% confidence interval in tenths. Orca data from EN586. *Seawater composition following [65].

Sample	**Cl^-**	**Na^+**	**Ca^{2+}**	**K^+**	**Mg^{2+}**	**$SO_4^{\ 2-}$**	**Salinity**
Orca N	49.69	48.58	0.38	0.22	0.56	0.57	270
Orca S	48.36	50.08	0.36	0.22	0.48	0.50	270
Seawater*	47.87	43.25	0.91	0.91	4.96	2.46	35

Table 2.3: Bulk composition of Orca brine and seawater, in percent. Orca data from EN586. *Seawater composition following [65].

the typical seawater value of 52 mM Mg to around 46 mM Mg (zone III; see Figure 2.4; Tables 2.2, 2.3). Despite the increase in calcium, potassium and sulfate within the brine, chloride and sodium dominated the brine composition, reducing the overall proportion of other major ions relative to seawater (see Tables 2.2, 2.3).

The deepest sample (2300 m) collected during EN586 in the north basin was significantly less salty than the brine directly above it. In this sample, nitrate, sulfate, ammonium, DIC, DOC, and all major ion concentrations reflected those of seawater. However, methane and ethane concentrations were not depleted (ca 680 µmol L^{-1} CH_4 and 1.2 µmol L^{-1} ethane; see Figures 2.2, A.3), and oxygen concentrations were below detection, consistent with deep brine values found elsewhere in the basin (see Figure 2.2). LaRock et al. (1979 [41]) reported a deep-water freshening of the brine at 2338 m depth some 40 years ago. They observed as a 45% decrease in phosphate (56 µmol L^{-1} to 31 µmol L^{-1}, 78% increase in ATP (<3.4 to 15.41 ng L^{-1}), a 14,300 dpm per 100 mL d^{-1} increase in uridine uptake, and a doubling of total direct cell counts (1.4×10^5 cells mL^{-1} to 2.9×10^5 cells mL^{-1} [41]). This suggests that this unusual layer is a recurring feature of Orca brine, perhaps due to dewatering of slumped blocks of sediment sourced from above the brine [7, 66].

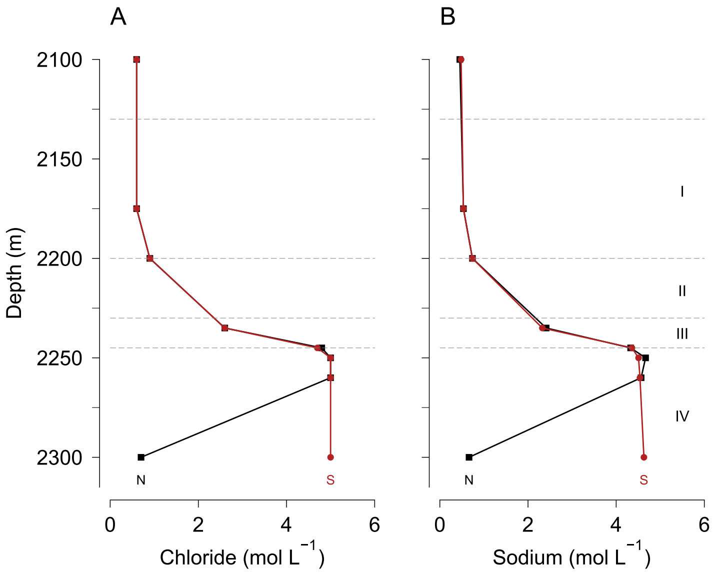

Figure 2.3: Chloride (A) and sodium (B) profiles for Orca N (black squares) and Orca S (red circles). Horizon abbreviations: I = oxycline, II = suboxic, III = halocline, and IV = brine. Data from cruise EN586.

The high-stability density interface between seawater and brine [7, 38] reduces the settling speed of particles and marine snow aggregates to <1% that of seawater (540 to 1100 m d^{-1}) and between 35% to 45% that of the brine below (180 – 400 m d^{-1} [7]). As such, it could take particles 11 – 35 days to traverse the chemocline of Orca Basin. As a result, particulate organic matter is retained along the halocline (see Figures A.6 and A.7) and undergoes heavy degradation, releasing iodine [67] and nutrients until the particles eventually dewater, increase in density, and pass into the brine [7]. It is likely that some of the particulate load is produced in situ as a consequence of increased microbial density ([41, 68]). Classic biogeochemical redox zonation results from this dynamic: Nitrate concentrations mirrored oxygen concentrations and diminished to below detection across the chemocline, concomitant with increases in ammonium (290 µmol L^{-1} to 500 µmol L^{-1}) and phosphate (18 µmol L^{-1} to 58 µmol L^{-1}; see Figure A.4 and 2.1), similar to profiles found within sediments porewater during early diagenesis [18, 21]. Dissolved inorganic nitrogen (DIN; NO_3^- + NO_2^- + NH_4^+) increased to a maximum of ca 500 µmol L^{-1}, a concentration driven almost entirely by the abundance of ammonium ions in the deep brine. The concentration of nitrous oxide (N_2O; see Figure A.4) was extremely elevated within and above

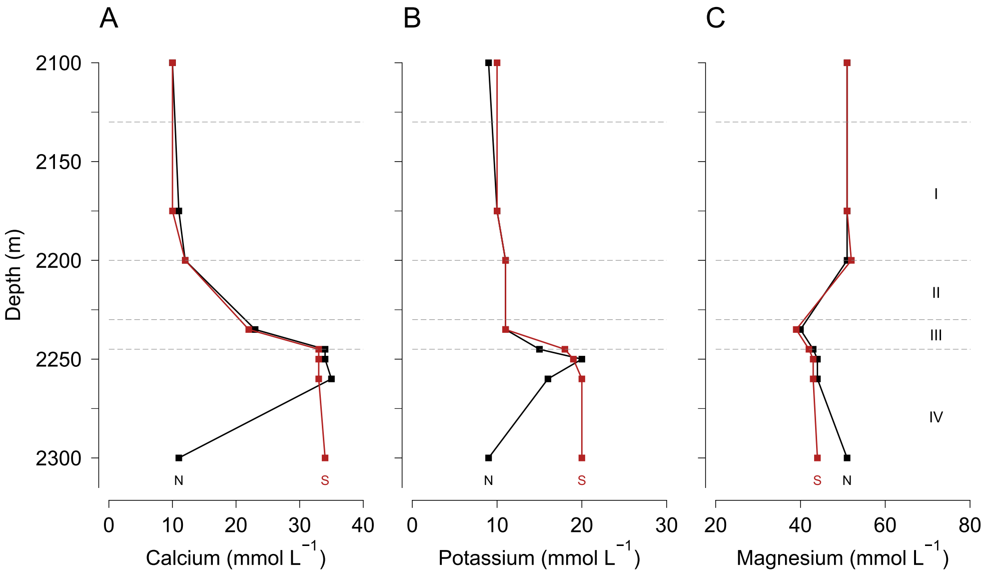

Figure 2.4: Calcium (A), potassium (B), and magnesium (C) profiles for Orca N (black squares) and Orca S (red circles). Horizon abbreviations: I = suboxic, II = suboxycline, III = halocline, and IV = brine. Data from cruise EN586.

the chemocline (5.3 µmol L^{-1} max). To our knowledge, these are the highest recorded N_2O values in any marine environment.

2.4.3 METHANE AND SULFATE

Major shifts in methane, sulfate, and sulfide corresponded with changes in salinity and oxygen (see Figures 2.2 and 2.5). For expeditions EN586 and EN600, the oxic waters between 2100 m and 2175 m contained between 15 nmol L^{-1} and 528 nmol L^{-1} CH_4, values many times higher than those reported in the surface ocean (ca 2–6 nmol L^{-1} CH_4 [69]), but similar to deepwater values observed near cold-seeps in the Gulf of Mexico (see Figure 2.2). Methane increased first to about 1 µmol L^{-1} near the base of the oxycline at 2200 m (zone I – II), and again near the middle of the halocline at 2235 m to between 69 µmol L^{-1} CH_4 (EN600) and 77 µmol L^{-1} CH_4 (EN586) in the south basin, and between 73 µmol L^{-1} CH_4 (EN586) and 82 µmol L^{-1} CH_4 (EN600) in the north basin (zone III; see Figure 2.2). Methane increased almost ten-fold through zones III and IV, to local maxima of between 667 µmol L^{-1} CH_4 (EN586) and 936 µmol L^{-1} CH_4 (EN600), depending on basin and expedition (see Figure 2.2, Table 2.1).

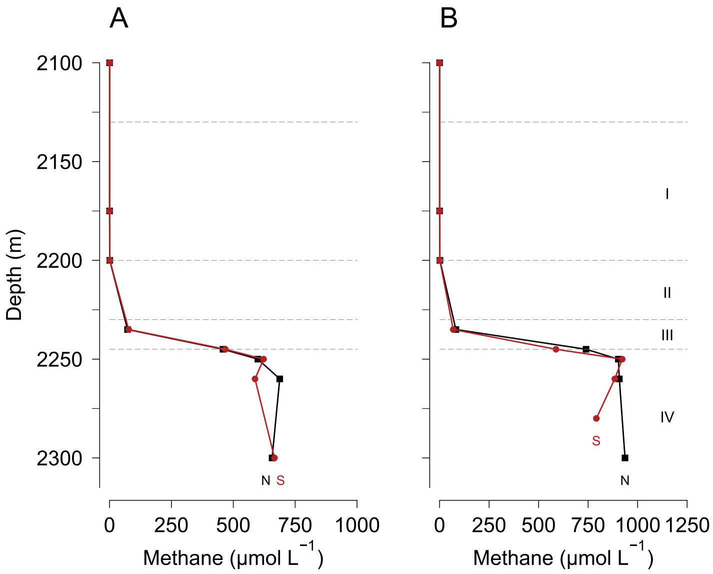

Figure 2.5: Methane profiles for expeditions EN586 (A) and EN600 (B). Orca N profiles in black squares, and Orca S in red circles. Horizon abbreviations: I = suboxic, II = suboxycline, III = halocline, and IV = brine. Data from cruise EN586.

The relative changes in sulfate concentration were modest compared the observed changes in methane concentration and salinity. Still, concentrations nearly doubled across the chemocline from 29 mmol L^{-1} $SO_4{}^{2-}$ in oxic seawater at 2130 m (zone I), to 57 mmol L^{-1} $SO_4{}^{2-}$ in the brine below 2245 m (zone IV; see Figure 2.2; Table). Consistent with previous observations, sulfide was below detection nearly everywhere except in a narrow lens near the top of the halocline at 2230 m (5.7 µmol L^{-1} H_2S max; zone III; see 2.2 and 2.1 [63, 70]). Orca brine contained over 5 orders of magnitude more methane than background Gulf seawater, but maximum values reported for expeditions AT26-13 (650 µmol L^{-1} CH_4 maximum) and EN586 (688 µmol L^{-1} CH_4 maximum) likely undershoot the true methane concentration by at least 100 µmol L^{-1} (see 2.2 [63, 71]). Previous studies reported between 780 and 830 µmol L^{-1} CH_4 in the brine, and values reported from expedition EN600 were higher still at 936 µmol L^{-1} CH_4 (see Table 2.1).

2.4.4 STABLE ISOTOPES

Major shifts in the stable carbon isotopic values for methane, dissolved inorganic carbon (DIC), and particulate organic carbon (POC) indicate methane remineralization to DIC and incorpo-

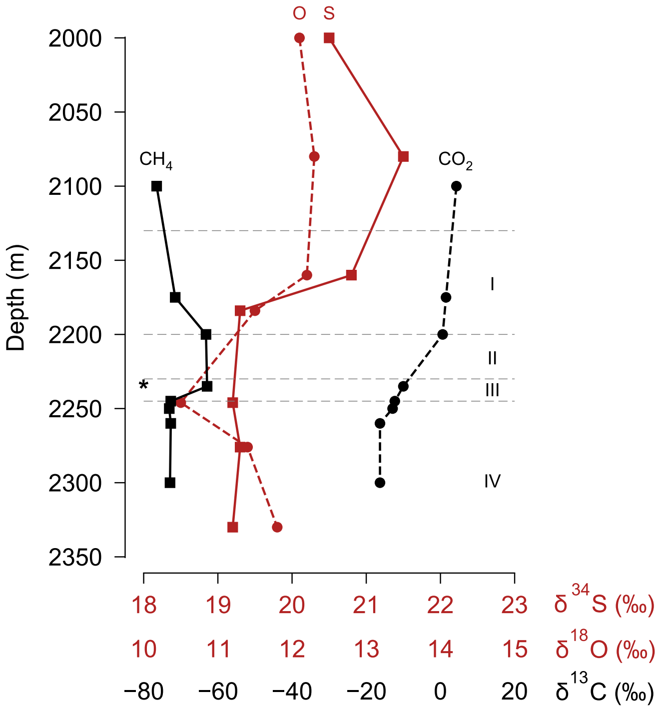

Figure 2.6: Stable isotopes of sulfate, methane, and DIC. Sulfate isotopes modified from [70]. Methane and DIC data are from EN586-S. *Indicates depth of sulfide, ASR, and particle maximum, coincident with major inflection points in salinity and methane. Oxygen, sulfur, and carbon isotope values relative to SMOW, CDT, and PDB, respectively.

rated of methane into POC (see Figures 2.6, A.6). Orca Basin methane was significantly depleted in ^{13}C–carbon (−73 to −76.5‰ δ^{13}C) and therefore of likely microbial origin, perhaps produced within the brine [68], the underlying sediment [40], or both. In general, microbial methane oxidation selects for lighter 12C-methane, leaving the residual methane pool enriched in 13C and the DIC pool depleted. Consistent with methane oxidation across the 35 m sub-oxic/anoxic horizon between 2200 m and 2235 m depth, δ^{13}C$_{\mathrm{CH_4}}$ values were enriched (13.6‰) and δ^{13}C$_{\mathrm{DIC}}$ values depleted (20.6‰) relative to seawater (zones II and III; see Fig. 2.4). Isotopically light carbon from methane and/or DIC was incorporated into the POC pool at 2200 m where methane turnover time was fastest, and to a lesser extent at 2250 m where methane oxidation rates were highest (see Figures 2.7 and A.6). Above 2175 m, δ^{13}C–POC values ranged from -24.5 to -26.4 ‰, similar to typical background deep water Gulf values of −21.7 ± 2.6 ‰ [53].

2.4.5 Microbial Activity

Both aerobic (Z < 2230 m) and anaerobic (Z > 2230 m) methane oxidation activity was observed across the chemocline of Orca Basin, but dissimilatory sulfate reduction was not (see Figure 2.7A). While the magnitude of methane oxidation rates varied from year to year, down-profile trends in activity were similar across casts (see Figures 2.7, 2.9, A.9). During expedition EN586 in 2016, MO rates were highest across a 15 m anoxic, particle-rich halocline in the north basin and within the deep brine in the south basin (zones III and IV; see Figures 2.2, 2.7A). During expedition EN600 in 2017, maximum MO rates were observed within the anoxic brine for both basins and were nearly an order of magnitude higher compared to those from EN586 (zone IV; see Figures 2.2 and 2.9).

Addition of particulate iron, nitrate, and nitrite to MO samples collected during EN586 and EN600 altered the magnitude of MO rates, particularly within the anoxic brine. Nitrite additions nearly doubled the MO rate in the anoxic brine whereas nitrate additions either had no effect or suppressed MO entirely (see Figure 2.9). Ferrihydrite amendments stimulated anaerobic methanotrophy within both the north and south basin brine (zone IV; see Figure 2.8), but addition of goethite had mixed effect, stimulating anaerobic methanotrophy in the north basin and suppressing it in the south basin (zone IV; see Figure 2.8). Sulfate reduction was below detection at all times and sites, indicating that sulfate-coupled MO was not an important sink for CH_4 in Orca Basin.

2.4.6 Methane Oxidation Rates

During expedition EN586, methane oxidation rates between N and S basins were similar above 2235 m but diverged across the halocline (see Fig. 2.3). In the north basin, MO rates were low through the majority of the oxycline (5 to 10 pmol L^{-1} d^{-1}). However, MO rates increased nearly 35 times to 350 pmol L^{-1} d^{-1} at 2200 m to where oxygen concentrations are low but not below detection (<10 μmol L^{-1} O_2; zone II; see Figure 2.7). Methane oxidation rates increased again by an order of magnitude to 3.7 μmol L^{-1} d^{-1} through the anoxic halocline but were not detected in

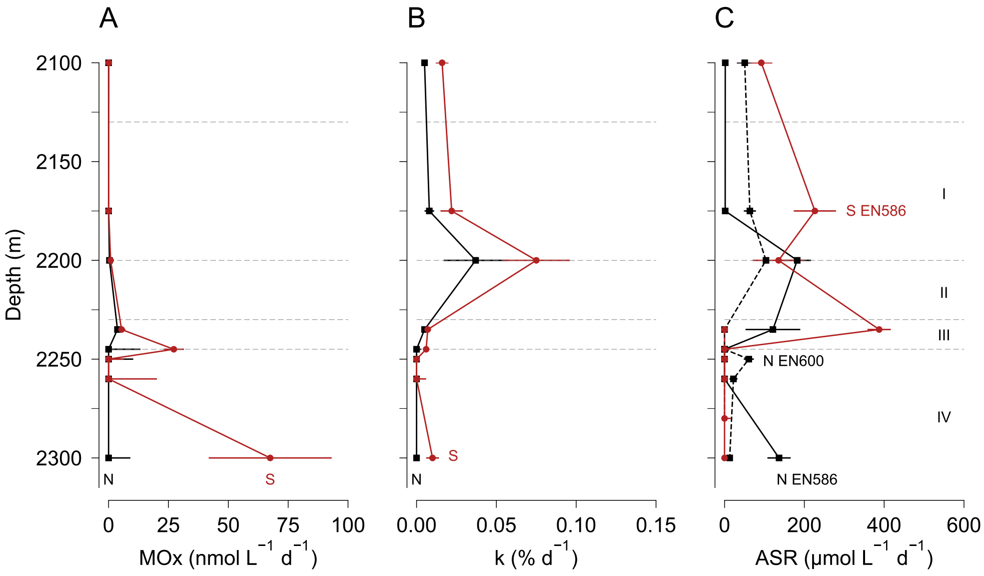

Figure 2.7: Representative profiles of A) methane oxidation rates at Orca N (black circles) and Orca S (red squares), B) ^{3}H methane tracer turnover rates at Orca N (black circles) and Orca S (red squares), and C) assimilatory sulfate reduction rates for Orca N (black circles) and Orca S (red squares), cruise EN586 (solid lines) and EN600 (dashed lines).

the brine below 2235 m (see Figure 2.7). Methane oxidation rates in the south basin were similar to those of the north basin in the oxic/sub-oxic zones but differed across the halocline and into the brine (see Figure 2.7). Below the sub-oxic zone (zone II; 2235 m), MO rates were detected in only two places, first at 2245 m (27 μmol L^{-1} d^{-1}) and again at 2300 m (67 μmol L^{-1} d^{-1}; see Figure 2.7). As with the MO rates of EN586, maximum rates during expedition EN600 occurred either at the base of the halocline (zone III; 2245 m) or within the brine. Some variability was observed between basins. In the south basin, MOx rates reached a maximum of 642 nmol L^{-1} d^{-1} at 2250, whereas in the north, rates were above 600 nmol L^{-1} d^{-1} in two locations, one at 2245 m (606 nmol L^{-1} d^{-1}) and one at 2260 m (627 nmol L^{-1} d^{-1}), both in the anoxic brine.

General trends in MO rate profiles were similar across all three expeditions, but absolute rates varied in magnitude (see Figures 2.7, 2.8 and 2.9). The MO rates in the sub-oxic water column above 2200 m (zone I) spanned over four orders of magnitude, between 3 pmol L^{-1} d^{-1} (EN600) and 112 nmol L^{-1} d^{-1} (AT26-13; see Figures 2.2 and 2.9). Rates of MO within this interval were highest around the base of the oxycline (112 nmol L^{-1} d^{-1}; AT26-13–S07.E35) at 2200 m where O_2 concentrations were <10 μmol L O_2. These MO rates were higher than those measured in typical

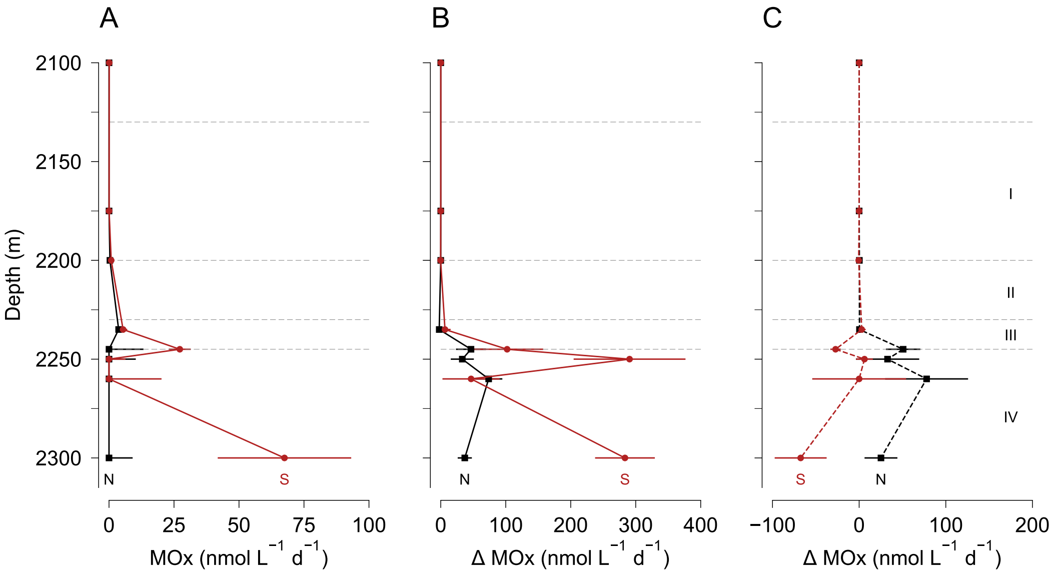

Figure 2.8: Methane oxidation rates A) for Orca N (black squares) and Orca S. (red squares), B) the difference between ferrihydrite-amended and standard MO rates (ΔMO) for Orca N (black squares) and Orca S (red circles), and C) difference between goethite-amended and standard MO rates for Orca N (black squares) and Orca S (red circles). Horizon abbreviations: I = oxycline, II = suboxic, III = halocline, and IV = brine. Data from cruise EN586.

Gulf surface waters (0 – 6 pmol L^{-1} d^{-1} [5]), similar to those in the water column around cold seeps (10's of pmol L^{-1} d^{-1} to 100 pmol L^{-1} d^{-1} [72]) but lower than those measured within the brine (see Figures 2.7, 2.8, 2.9, and 2.4). Aerobic methanotrophy is effective and efficient at low oxygen concentrations (e.g., ca 2 µmol L^{-1} O_2 [73]); the horizon at the base of the oxycline (2200 m; <10 µmol L^{-1} O_2; zone II; see Figure 2.2) is an ideal habitat for aerobic methanotrophs with modest salinity tolerance. Without exception, MO rates increased within the halocline of Orca Basin and maximal activity was present in highly saline samples (zone III; see Figures 2.7, 2.8 and 2.9).

While methane oxidation rates were generally highest through the halocline or in the deep brine, turnover constants (k) were significantly higher at the base of the oxycline (2200 m) across all expeditions (see Figures 2.7, 2.9). As with MO rates, the turnover constant, k was lower for expedition EN586 than it was for EN600 by at least a factor of 4, but still reached a maximum value at 2200 m. Additionally, turnover constants were slightly higher in the south basin as compared to those in the north basin for both EN586 (0.075 % per day max) and EN600 (2.4 % per d).

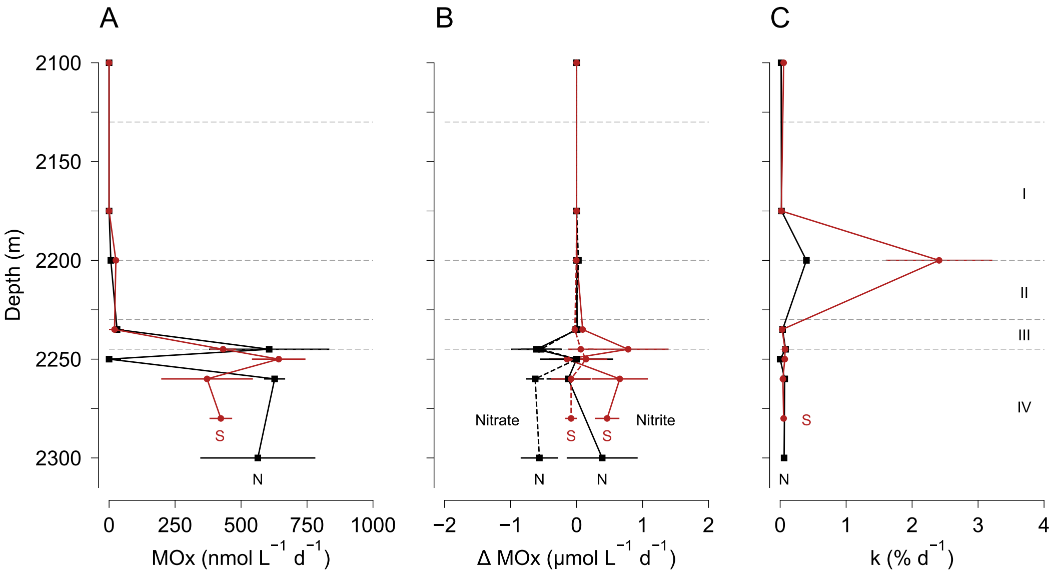

Figure 2.9: Methane oxidation (MO) rates (A), MO response to nitrate and nitrite amendments (1 mmol L^{-1} each) (B), and turnover constants (C) for Orca N (black squares) and Orca S (red circles). ΔMO calculated as $MO_{treatment} - MO$. Horizon abbreviations: I = oxycline, II = suboxic, III = halocline, and IV = brine. Data from cruise EN600.

Methane oxidation rates were measured across six CTD casts during expedition AT26-13 using two different techniques, one with ^{14}C–methane and one with ^{3}H—methane. The average MO rates using ^{14}C–methane were lower than those measured with ^{3}H–methane by at least an order of magnitude for every cast but those of EN586 (see Table 2.4). One explanation for this discrepancy is that ^{14}C—derived methane oxidation rate techniques reflect only net CO_2 production, rather than direct methane assimilation, the assimilation of ^{14}C-DIC into biomass, or backflux reactions [74]. The tritiated methane technique tracks labeled hydrogen into water – rather than carbon – and so it captures both methane oxidation and assimilation. Average MO rates across the chemocline of Orca during expeditions AT26-13 and EN600 generally agree with each other 214 and 292 nmol L^{-1} d^{-1}, generally in agreement with each other (see Table 2.4). In contrast, average MO rates for EN586 were between 1 and 13 nmol L^{-1} d^{-1}, one to two orders of magnitude lower than tritium derived MO rates reported for AT26-13 and EN600. These rates were of similar magnitude to the values obtained from ^{14}C–derived MO rates during AT26-13 (see Table 2.4).

To ground-truth our rates – especially give the variability between cruises - integrated MO rates from each cruise were compared to calculated methane fluxes (see Table 2.4). Many of the casts on expedition AT26-13 were partial casts and focused either on the brine or the overlying seawater. For tritium-derived MO rates from expeditions AT26-13, cast AT26-13–S07.E35 is the only one that encompasses both the seawater and brine. For ^{14}C–derived rates from AT26-13, casts AT26-13–S07.E15 and AT26-13–S07.E21 were full casts. The MO rates for cast AT26-13–S07.E35 (tritium MO) show two maxima, one in the suboxic zone at 2215 m (zone II; 579 nmol L^{-1} d^{-1}) and one at the base of the halocline at 2245 m (zone III; 1019 nmol L^{-1} d^{-1}; see Table 2.4). The two profiles of ^{14}C–derived MO rates (AT26-13–S07.E15 and AT26-13–S07.E21) have maxima either at the base of the halocline (2243 m; 57 nmol L^{-1} d^{-1}; AT26-13–S07.E21; see Table 2.4) or within the brine itself at 2276 m (zone IV; AT26-13–S07.E15; see Table 2.4).

Figure 2.8 shows the relative change in methane oxidation rates (ΔMO) between standard assays (see Figure 2.7), and those conducted with additions of particulate ferrihydrite and goethite. To varying degrees, additions of both goethite and ferrihydrite stimulated methanotrophy across the chemocline in both basins (see Figure 2.8). Ferrihydrite amended methane oxidation rates increased between 35% to more than 250% within the oxic and sub-oxic horizons of both basins (2100 m – 2200 m; see Figure 2.8). In the anoxic brine below 2235 m, MO rates increased by up to 290 nmol L^{-1} d^{-1} (2250 m) in the south basin, and to 74 nmol L^{-1} d^{-1} (2260 m) in the north (see Fig. 2.5B). In both cases, ferrihydrite stimulated anaerobic methanotrophy was observed in the brine relative to unamended rates. In contrast, goethite amendment inhibited methanotrophy in almost every sample from the south basin, except for an increase of 3 nmol L^{-1} d^{-1} at 2235 m depth (see Figure 2.8C) and through the oxic and sub-oxic horizons of both basins. Samples from the North basin produced a nearly identical response of methane oxidation to the ferrihydrite amendment. Here again, the largest response was 78 nmol L^{-1} d^{-1} at 2260 m (see Fig 2.5C). However, goethite essentially suppressed methane oxidation in the North Basin.

2.4.7 DISCUSSION

This work documents the first direct measurements of methane oxidation and sulfate reduction rates across the chemocline of Orca basin. Both aerobic and anaerobic methane oxidation were active across a wide range of salinities, and anaerobic methanotrophy was coupled to a variety of electron acceptors. Aerobic methanotrophy was maximal under hypoxic conditions. While anaerobic methanotrophy is typically coupled to sulfate reduction in sediments, we found no evidence of sulfate-coupled MO in Orca Basin. Anaerobic MO was stimulated by addition of electron acceptors of varying redox capacity: ferrihydrite and goethite, both particulate phases of oxidized iron, and of nitrite. Nitrate addition suppressed methanotrophy in both basins. The extreme salinity of Orca Basin does not appear to inhibit methanotrophy, in contrast to the predictions based on thermodynamic considerations [75]. Methanotrophic communities across the Orca Basin chemocline oxidize methane using oxygen, nitrite, and iron oxides as electron acceptor, allowing these microorganisms to exploit ecological niches despite the challenge of increasing salinity.

Methane concentrations varied by roughly 30% across samples collected from the deep anoxic brine. Though this represents substantial variability, such differences could result from spatial or temporal variability or sampling artifacts (poor seals on the Niskin bottles). Despite the potential for sampling related artifacts, it is possible, if not likely, that the differences reflect spatial and temporal variability. Orca basin is very large system (225 sq km at the depth of the chemocline) and it was sampled at different locations across three different expeditions that spanned the summers of 2014, 2015, and 2016. Samples were collected from both the middle of the basin as in AT26-13–S07.E21 (see Figure 2.1 and Table 2.1) and closer to edge of the brine basin for cast EN600–S05.E01 (see Figures 2.1, 2.2, Table 2.1) where the influence of sediment geochemistry is more likely. As a result, average brine methane values were bootstrapped from brine samples collected below 2245 m across all three expeditions (AT26-13, EN586, and EN600), yielding an average brine methane concentration of 736 ± 21 μmol L^{-1} (99% CI; $n = 10^4$) in the north basin and 691 ± 20 μmol L^{-1} (99% CI; $n = 10^4$). This value is in line with values reported previously [63].

The disparity between the magnitude of methane oxidation rates between cruises is either a consequence of temporal variability, choice of tracer assay (*i.e.,* ^{14}C versus ^{3}H tracer), or both (see Figure A.9). The relatively high average rates of 214 – 229 nmol L^{-1} d^{-1} measured using tritiated tracer during the better part of the Atlantis expeditions match well with the tracer experiments during the EN600 expedition. However, the average tritiated rates from EN586 just the year prior, are lower by about one order of magnitude (see Table 2.4), and broadly fall in line with the average rates obtained using the ^{14}C assays of the 2014 Atlantis cruise. We performed a simple methane flux calculation between 2235 and 2250 m depth and compared this value of methane oxidation rates integrated over the same horizon. This 15 m zone (zone III) is the location where rates are highest and the concentration gradient of methane the steepest. Here, the methane flux across the chemocline must be greater than or equal to the integrated rate of methane oxidation to sustain our observed rates. Only the integrated MO rates estimated from tritiated tracer during EN586 and from ^{14}C methane during expedition AT26-13 are well supported by calculated diffusive methane fluxes (see Table 2.4). Cumulative MO estimated from tritiated methane during AT26-13 and EN600 are at least 35 times higher than the calculated flux. Additional sources of methane are clearly required to sustain these elevated rates. Methanogenesis within the Zone III halocline has not been measured but may play a major role in DIC cycling. The chemocline of Orca acts as a significant particle trap [7, 64] and multiple studies indicate significant particle degradation at the brine-seawater interface [64, 67]. The depleted ^{13}C signature above the halocline (see Figure 2.6) suggests a possible flux of depleted methane, produced in the halocline, into the oxic water column above. Methylotrophic methanogenesis is a possibility here [40] and it should be assessed in the future.

We assumed originally that Orca Basin system was essentially homogenous, but available data revealed substantial spatial, and possibly temporal, differences in methane dynamics. Seasonal differences in the vertical flux of labile organic matter may drive subsequent changes in rates of heterotrophic metabolism and methanogenesis. Despite consistent vertical trends across the chemocline year to year (*e.g.,* O_2 and salinity profiles), the Orca chemocline contains sub-meter scale

Expedition	Cast	Basin	Flux	ΔCH_4	Avg ^3H–MO	Avg ^{14}C–MO	$\sum$ ^3H–MO	$\sum$ ^{14}C–MO
AT26-13	S07.E15	S	324.8	564	–	18(9)	–	327(116)
	S07.E21	S	273.6	475	214(119)	20(9)	8659(1341)	413(156)
	S07.E25	N	292.6	508	215(109)	–	12801(2710)	2(17)*
	S07.E35	S	373.6	649	292(144)	8(8)	10386(448)	2(13)*
	S07.E36	S	279.9	486	–	6(3)	–	121(39)
EN586	S05.E01	S	383.0	665	13(9)	–	381(88)	–
	S05.E03	N	395.2	686	0.5(5)	–	90(136)	–
EN600	S07.E01	S	530.4	921	239(91)	–	5763(1597)	–
	S07.E02	N	538.5	935	229(109)	–	5344(2156)	–

Table 2.4: Calculated methane flux (μmol m^{-2} d^{-1}), change in methane across the halocline (ΔCH_4; μmol L^{-1}), average methane oxidation rate (MO; nmol L^{-1} d^{-1}) and integrated methane oxidation rates (μmol m^{-2} d^{-1}) across the N and S halocline ($\delta z = 15$ m), for both tritiated methane and ^{14}C–methane. Flux calculated with diffusion coefficient = 10^{-3} cm^2 s^{-1}. Standard error of the mean in parenthesis. * = incomplete profile.

structure, visible predominantly as thin, heterogenous lenses of accumulated particulates and cm to tens of cm-long marine snow aggregates distributed vertically according density [7]. Particles and aggregates have high surface area and the residence time of these materials along layers of the chemocline is protracted, providing an opportunity microorganisms to colonize unique environmental niches. Furthermore, variability in the fluxes of solid phase electron acceptors (iron) through the anoxic layers could stimulate AOM periodically (see below). It is likely that the variability we see from year to year is a temporal pattern rather than a pure sampling artifact.

Methane dynamics within Orca are also strongly influenced by microbial respiration, particularly across the seawater-brine interface. Isotopically light methane (-72‰$\delta^{13}CH_4$) within the sediments and brine document accumulation of biogenic methane that is produced actively in the underlying sediments via methylotrophic processes ([40]). The isotopic composition of methane and DIC within the brine is very close to values reported for Orca basin sediments [40, 68]. This methane likely diffuses into the overlying brine, accumulates to nearly millimolar levels; deeply-sourced methane fluxes across the chemocline and is consumed by halotolerant methanotrophs. A localized increase in $\delta^{13}CH_4$ (maximum -60‰) and decrease in $\delta^{13}C$—DIC between 2175 m and 2240 m depth (see figure 2.6) suggests increased methane oxidation through the particle-rich, brine-seawater interface, and this pattern is corroborated by radiotracer assays presented here (see Figures 2.7, 2.8 and 2.9).

Aerobic and anaerobic methanotrophy occur sequentially across the Orca Basin chemocline. The water column above at least 2200 m, and likely down to 2235 m, contains sufficient oxygen to support aerobic microbial methanotrophy. Aerobic methanotrophic bacteria are distributed across 26 genera of Bacteria, primarily within the Alpha and Gamma subunits of the Proteobacteria [76], as well as three thermoacidophilic members of Verrucomicrobia [76, 77]. Aerobic methanotrophs thrive under low oxygen conditions[73]; in fact, rates of aerobic methanotrophy are often maximal at low oxygen levels (<0.5 μmol L^{-1} O_2). Aerobic methanotrophy along the Orca Basin chemocline also operates effectively at low methane concentration (<10 μmol L^{-1} O_2), serving as a cap that consumes methane escaping the anaerobic methane biofilter and reaching the upper portion of the chemocline, as evidenced by the persistent increase in tracer scavenging around 2200 m depth (see Figures 2.7, 2.9). Maximal tracer turnover within the microaerophilic lens at 2200 m indicates that methane oxidation is supported by a highly active, mildly halotolerant, aerobic methanotrophic bacterial community. Methane oxidation rates reach a local minimum at 2230 m, nearly coincident with the observed particle maximum [7]. Known and potentially novel aerobic methane-oxidizing bacteria possessing alkane monooxygenases occur at the upper portion of oxygen gradients of other brines, e.g., Atlantis II Deep and Kebrit Deep [78, 79]. These measurements represent the first documentation of aerobic methane oxidation in a DHAB environment.

Thermodynamic energy yields predict the following series of metabolisms proceed in series following exhaustion of molecular oxygen: nitrate/nitrite reduction, metal (Fe, Mn) oxide reduction, sulfate reduction, and finally methanogenesis [18]. In marine sediments because sulfate is the dominant available electron acceptor, anaerobic methanotrophy is thought to proceed primarily through the cooperative metabolism of archaeal ANaerobic MEthanotrophs (ANME) and sulfate reducing bacteria [80–83]. It is increasingly clear that other metabolic couplings also may be coupled anaerobic MO [84]. Thus, we began by assuming that dissimilatory sulfate reduction was coupled to anaerobic MO in the Orca Basin brine. Other workers have speculated that DSR at Orca Basin occurs predominantly through the seawater-brine interface based on the stable isotopic composition of the sulfate pool ($\delta^{18}O$ and $\delta^{34}S$ [70, 85]). Sheu, et al. [70] reported stable isotopes of sulfate through the Orca seawater-brine interface (see fig. 2.6). Elevated sulfate within the Orca brine results from lateral infiltration of fluids containing dissolved, Jurassic-aged Louanne evaporites rich in ^{34}S-depleted sulfate (+16.5 ± 1.0‰ca.[86]), sourced predominantly from breaching diapirs of gypsum and anhydrite at the surrounding slopes [6, 70].

Sulfate is abundant within the brine (ca. 50 mmol L^{-1}, but hydrogen sulfide concentrations in the deep brine and across the chemocline are low (typically only a few µmol L^{-1} and only present at 2235 m, as in Figure 2.2. Analysis of the oxygen isotopes in sulfate suggest reoxidation of sulfide along the 15 m halocline, nearly coincident with a lens of low-level sulfide. Sulfide only accumulates to approximately 5.7 µmol L^{-1} within a narrow lens near the base of the seawater-brine transition at 2235 m depth, despite the abundance of free sulfate throughout (see Figure 2.2, Table 2.1). Many DHABs contain abundant sulfide including Kebrit Deep in the Red Sea (>10 mmol L^{-1} [16, 87]), and Urania basin in the Mediterranean (16 mmol L^{-1} [31, 37]) and sulfate reduction is consider a key process in deep sea brines [4, 5, 19, 37].

Dissimilatory sulfate reduction was not detected either through the seawater-brine interface or within the core of the brine using traditional ex situ ^{35}S-sulfate radiotracer assays. We suspect that sulfate reduction is confined to vanishingly narrow spatial window between the suboxic conditions above 2230 m and high salinity conditions that dominate below 2245 m. The lack of dissimilatory sulfate reduction in the Orca Basin brine fluids is very surprising, since sulfate reduction is known to occur in other brines of comparable salinity [4, 37] as well as in Orca Basin hypersaline sediments [40, 85]. Potential explanations for low dissimilatory sulfate reduction rates and low sulfide concentration in Orca Basin generally fall into two categories: 1) SR rates are exceedingly slow due to salinity stress, or 2) SR proceeds as expected but evolved sulfide precipitates as particulate iron-sulfide minerals (e.g. mackinawite, pyrite, etc. [85, 88, 89]). Unusually high concentrations of particulate and dissolved iron found within the brine [38, 70], and large fractions of accumulated pyrite found in the underlying sediments within both sub-basins suggests sustained reaction between free sulfide by the relatively large pool of reduced, unreacted iron [85]. However, if option (2) was important, we would have recovered produced FeS minerals in our rate assays and we did not. It is possible that, over time, persistent rates at a level below the detection limit of the method we used (<1 pmol L^{-1} d^{-1}), could, potentially, generate such a sedimentary signal of sulfate reduction, though in situ DSR/pyrite formation in sediments seem likely. The apparent lack of sulfate reduction in the Orca Basin system warrants further study focusing on the depths between 2230 and 2245 m and conducting some long term (7-14 day) incubations to address the possibility that rates are extremely low.

Given the absence of sulfate reduction supported anaerobic MO in the Orca Basin system, we explored the potential for nitrogen oxide and iron oxide supported anaerobic MO. Nitrate additions to Orca Basin brine suppressed anaerobic methane oxidation, which argues against nitrate coupling to methane oxidation by organisms like ANME-2d ('Methanoperedens nitroreducens' ANME-2d [90, 91]). Nitrite, by contrast, stimulated anaerobic MO in anoxic brine from both basins (see Figure 2.9). It is possible that nitrate is consumed via classic denitrification while nitrite fuels anaerobic MO [92]. Even though no nitrite was detected in our profiles, that could reflect instantaneous consumption rather than reflect its unimportance. It is also possible a nitrite maximum was simply missed by our bottle sampling.

Nitrous oxide increases towards the base of the oxycline, coincident with nitrate drawdown. The presence of substantial N_2O - over 5 μmol L^{-1} – above the Orca Brine could reflect denitrification or perhaps nitrate reduction [93] coupled to methane oxidation, which in some microorganisms produces only nitrous oxide. However, nitrate inhibited methane oxidation in our experiments (see Figure 2.9). Given the abundance of particles, sub-oxic conditions (<5 μmol L^{-1} O_2; see Figure 2.2), and the proximity of N_2O production to nitrate depletion, we propose that N_2O is produced as a byproduct of incomplete denitrification [94]. The Orca Basin chemocline is thus characterized by diverse modes of active cycling of nitrogen oxides, resulting in complete drawdown of the NOx pool by a depth of 2200 m (see Figure A.4).

The most likely mode of nitrogen coupled methanotrophy in Orca Basin is nitrite-fueled methanotrophy, as described for Methylomirabilis-like bacteria in the NC10 phylum [95–98]. Unlike anaerobic methane oxidizers that oxidize methane using the reverse methanogenesis pathway to activate methane, the Methylomirabilis-like bacteria have a novel particulate methane monooxygenase that is very similar to those employed by aerobic methane oxidizing microorganisms. Relatives of NC10 bacteria have been documented in oceanic oxygen minimum zones and are believed to be active participants in methane oxidation there [97]. So far, these microorganisms have not been identified in hypersaline brine ecosystems, but the data presented here suggests they may play a role in anaerobic methane oxidation in Orca Basin.

The Orca Basin brine is enriched in manganese and iron oxides [38, 99]. Previous reports [38] showed extremely high concentrations of reduced manganese (Mn(II)) and suggested the oxidation of organic matter was coupled to dissimilatory manganese reduction. The same authors suggested that the primary sink for Fe-oxides was reaction with hydrogen sulfide [99]; coupling of organic matter to dissimilatory iron-oxide reduction was considered unimportant. Dissimilatory sulfate reduction was considered to be an active and important process. Metal oxides have not been considered potential, or important, electron acceptors to support anaerobic methane oxidation in brine ecosystems in general or in the Orca Basin. The importance of metal oxide reduction coupling to anaerobic methane oxidation in other systems is well documented [100–102].

When anoxic Orca Basin brine samples from depths below 2235 m were amended with ferrihydrite, rates in the Northern basin increased from essentially zero to almost 75 nmol L^{-1} d^{-1} (see Figure 2.8). Similarly, in the Southern Basin, rates increased significantly – from near zero to up to nearly 300 nmol L^{-1} d^{-1} in response to increased ferrihydrite addition. Additions of goethite generated mixed results but by and large rates were not as responsive to goethite addition (see Figure 2.8). The fact that ferrihydrite stimulated anaerobic methane oxidation so strongly shows that a microbial population capable of coupling ferrihydrite reduction to anaerobic methane oxidation exists in the Orca Basin brine and that these microorganisms are, at least sometimes, limited by availability of ferrihydrite.

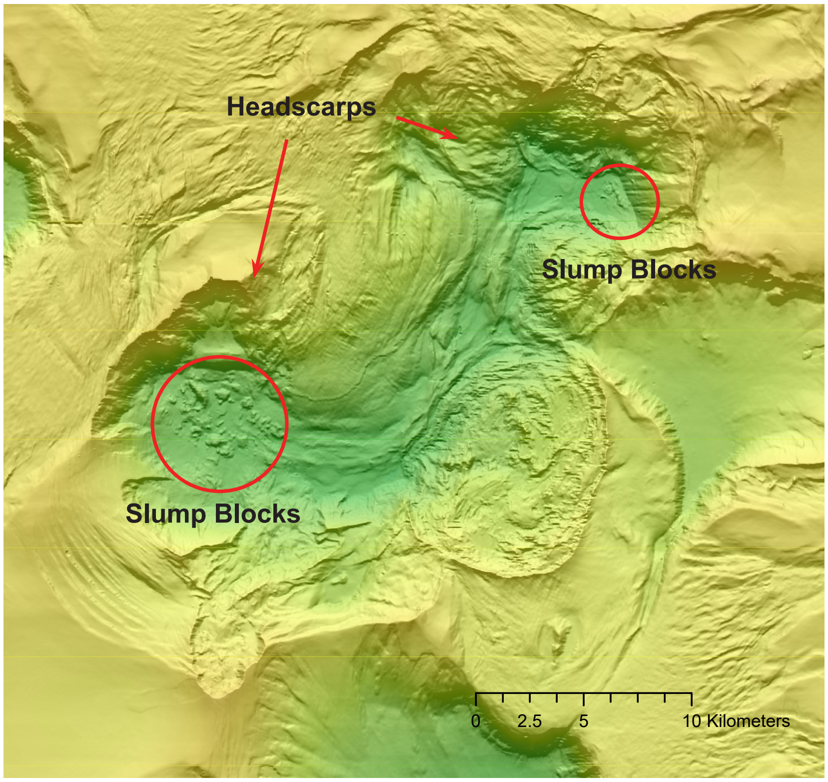

Figure 2.10: Evidence for mass wasting at Orca Basin, Gulf of Mexico. Hillshaded bathymetry dataset courtesy of the U.S. Bureau of Ocean Energy Management: https://www.boem.gov/Gulf-of-Mexico-Deepwater-Bathymetry.

The fact that iron oxide mediated AOM is clearly metal oxide limited could help explain the substantial differences in rates of anaerobic methane oxidation in the brine observed across the data set. Metal oxides could be introduced to the deep Orca Basin laterally by slumping, a phenomenon that is known to occur regularly in the system [66]. Sawyer et al. (2019) present voluminous evidence of slumping and landslides disturbing the brine by causing internal waves and depositing oxidized sediments into the deep brine. Figure 2.10 shows the proposed headscarps and slump blocks as interpreted from new high-resolution hillshade bathymetry from the Bureau of Ocean Energy Management (BOEM). This mechanism also been suggested by Diercks et al. (2019 [7]) to explain the rich nepheloid layer atop the brine. Diercks, et al. proposed that these slumping events delivered fresh particulate matter at the seawater brine interface as a mechanistic explanation for the presence of a particle maximum at 2230 m depth [7]. Other evidence suggest that metal oxides are introduced to the Gulf of Mexico through Mississippi River discharge of clastic sediments and via the deposition of Saharan dust, which occurs generally at rates around 28 – 78 mg Fe m^{-2} per 6 months [103]. Such periodic inputs of oxidized sediments could lead to pulsed delivery of iron-rich sediments, thereby stimulating iron-oxide coupled anaerobic methane oxidation in the deep Orca brine.

This is the first time that iron reduction coupled to anaerobic methane oxidation has been shown in a deep-sea brine. Metal oxide coupled AOM is known to be important in marine sediments [100] and there is no inherent reason why this process would not occur in Orca Basin. Aromokeye et al. (2020 [102]) showed that sediment slurries enriched with iron minerals lepidochrocite, hematite, and magnetite became enriched in the anaerobic methanotrophs ANME-1b and ANME-2a/2b, but not ANME-2c/2d. These slurries oxidized methane anaerobically at high rates when sulfate reduction was inhibited by molybdate addition. Interestingly, addition of manganese oxides did not stimulate anaerobic methane oxidation. In some years [103], like 2020, however, transport and deposition of Saharan dust is much higher; so extreme that it generates "brown rain" and can be seen from space [104]. So, variability in vertical flux of iron rich particles – through river inputs or Saharan dust flux – may also contribute to variability in iron-oxide availability in the deep Orca Brine. In the case of Saharan dust, this unexpected biogeochemical teleconnection would constitute remarkable connectivity and reveal an unanticipated consequence of Saharan dust input to the Gulf of Mexico system.

2.5 Conclusions

Methane oxidation in the Orca Basin is fueled by aerobic and anaerobic processes. Surprisingly, sulfate reduction coupled anaerobic oxidation of methane is not important in the Orca Basin. Instead, nitrite and iron-oxide coupled anaerobic oxidation of methane dominate. We document for the first time, substantial rates of anaerobic methane oxidation at high salinity. This discovery suggests that anaerobic methane oxidation may occur in other brine ecosystems, but availability of electron acceptors may limit activity. Extensive spatial and temporal variability in anaerobic methane oxidation are likely driven by differences in the availability of iron oxides as a function of basin location and over time. Sediment slumping, terrestrial inputs via the Mississippi River, and possibly iron inputs from Saharan dust could all contribute to variable iron delivery to the deep Orca Basin. The anaerobic microbial community in Orca Basin is primed and able to respond instantaneously to iron-oxide inputs. So, pulsed delivery of iron oxides to the deep Orca Basin likely modulates the fate of methane in the deep anoxic brine.

BIBLIOGRAPHY

1. Shokes, R. F., Trabant, P. K., Presley, B. J. & Reid, D. F. Anoxic, hypersaline basin in the northern Gulf of Mexico. *Science* **196,** 1443–1446 (1977).
2. MacDonald, I. R. *et al.* Chemosynthetic mussels at a brine-filled pockmark in the northern Gulf of Mexico. *Science* **248,** 1096–1099 (1990).
3. Joye, S. B., MacDonald, I. R., Montoya, J. P. & Peccini, M. Geophysical and geochemical signatures of Gulf of Mexico seafloor brines. *Biogeosciences* **2,** 295–309 (2005).
4. Joye, S. B. *et al.* Metabolic variability in seafloor brines revealed by carbon and sulphur dynamics. *Nature Geoscience* **2,** 349 (2009).
5. Wankel, S. *et al.* New constraints on methane fluxes and rates of anaerobic methane oxidation in a Gulf of Mexico brine pool via in situ mass spectrometry. *Deep Sea Research Part II: Topical Studies in Oceanography* **57,** 2022–2029 (2010).
6. Pilcher, R. S. & Blumstein, R. D. Brine volume and salt dissolution rates in Orca Basin, northeast Gulf of Mexico. *AAPG bulletin* **91,** 823–833 (2007).
7. Diercks, A., Ziervogel, K., Sibert, R., Joye, S. B. & Asper, V. Vertical Marine Snow Distribution in the Stratified Hypersaline, and Anoxic Orca Basin (Gulf of Mexico). *Elementa: Science of the Anthropocene* **7,** 1 (2019).
8. Jongsma, D. *et al.* Discovery of an anoxic basin within the Strabo Trench, eastern Mediterranean. *Nature* **305,** 795 (1983).
9. Cita, M. B. *et al.* Gypsum precipitation from cold brines in an anoxic basin in the eastern Mediterranean. *Nature* **314,** 152 (1985).

10. Consortium, M. Three brine lakes discovered in the seafloor of the eastern Mediterranean. *Eos, Transactions American Geophysical Union* **76,** 313–318 (1995).

11. Hallsworth, J. E. *et al.* Limits of life in $MgCl_2$-containing environments: chaotropicity defines the window. *Environmental Microbiology* **9,** 801–813 (2007).

12. Charnock, H. Anomalous bottom water in the Red Sea. *Nature* **203,** 591–591 (1964).

13. Brewer, P., Riley, J. & Culkin, F. *The chemical composition of the hot salty water from the bottom of the Red Sea* in *Deep Sea Research and Oceanographic Abstracts* **12** (1965), 497–503.

14. Swallow, J. C. & Crease, J. Hot salty water at the bottom of the Red Sea. *Nature* **205,** 165–166 (1965).

15. Faber, E. *et al.* Methane in Red Sea brines. *Organic Geochemistry* **29,** 363–379 (1998).

16. Antunes, A., Ngugi, D. K. & Stingl, U. Microbiology of the Red Sea (and other) deep-sea anoxic brine lakes. *Environmental Microbiology Reports* **3,** 416–433 (2011).

17. Suess, E., Westbrook, G., Winckler, G., Westbrook, M., Della Vedova, B., *et al.* Salty brines on the Mediterranean sea floor. *1997* **387,** 31–32 (1997).

18. Joye, S. B. The Geology and Biogeochemistry of Hydrocarbon Seeps. *Annual Review of Earth and Planetary Sciences* **48,** 205–231 (2020).

19. Merlino, G., Barozzi, A., Michoud, G., Ngugi, D. K. & Daffonchio, D. Microbial ecology of deep-sea hypersaline anoxic basins. *FEMS microbiology ecology* **94,** fiy085 (2018).

20. Lee, C. *et al.* NaCl-saturated brines are thermodynamically moderate, rather than extreme, microbial habitats. *FEMS microbiology reviews* **42** (2018).

21. Joye, S. B., Bowles, M. W., Samarkin, V. A., Hunter, K. S. & Niemann, H. Biogeochemical signatures and microbial activity of different cold-seep habitats along the Gulf of Mexico deep slope. *Deep Sea Research Part II: Topical Studies in Oceanography* **57,** 1990–2001 (2010).

22. Bowles, M., Hunter, K. S., Samarkin, V. & Joye, S. Patterns and variability in geochemical signatures and microbial activity within and between diverse cold seep habitats along the lower continental slope, Northern Gulf of Mexico. *Deep Sea Research Part II: Topical Studies in Oceanography* **129,** 31–40 (2016).

23. Daffonchio, D. *et al.* Stratified prokaryote network in the oxic-anoxic transition of a deep-sea halocline. **440** (2006).

24. Steinle, L. *et al.* Life on the edge: active microbial communities in the Kryos MgCl 2-brine basin at very low water activity. *The ISME journal* **12,** 1414 (2018).

25. Shukla, P. *et al.* IPCC, 2019: Climate Change and Land: an IPCC special report on climate change, desertification, land degradation, sustainable land management, food security, and greenhouse gas fluxes in terrestrial ecosystems (2019).

26. Cooper, Z. S. *et al.* Distinctive microbial communities in subzero hypersaline brines from Arctic coastal sea ice and rarely sampled cryopegs. *FEMS Microbiology Ecology* **95** (2019).

27. Zolotov, M. Y. & Shock, E. L. Composition and stability of salts on the surface of Europa and their oceanic origin. *Journal of Geophysical Research: Planets* **106,** 32815–32827 (2001).

28. McCord, T. B. & Sotin, C. Ceres: Evolution and current state. *Journal of Geophysical Research: Planets* **110** (2005).

29. Klatt, J. *et al.* Versatile cyanobacteria control the timing and extent of sulfide production in a Proterozoic analog microbial mat. *The ISME Journal* **14,** 1–14 (2020).

30. D'Hondt, S. *et al.* Distributions of Microbial Activities in Deep Subseafloor Sediments. *Science* **306,** 2216–2221 (2004).

31. Sass, A. M., Sass, H., Coolen, M. J., Cypionka, H. & Overmann, J. Microbial communities in the chemocline of a hypersaline deep-sea basin (Urania basin, Mediterranean Sea). *Appl. Environ. Microbiol.* **67,** 5392–5402 (2001).

32. Microbial ecology and biogeochemistry of hypersaline sediments in Orca Basin. *PLoS ONE* **15,** 1–25 (2020).

33. Pachiadaki, M. G., Yakimov, M. M., Lacono, V., Leadbetter, E. & Edgcomb, V. Unveiling microbial activities along the halocline of Thetis, a deep-sea hypersaline anoxic basin. *ISME Journal* **8,** 2478–2489 (2014).

34. Cono, V. L. *et al.* The discovery of Lake Hephaestus, the youngest athalassohaline deep-sea formation on Earth. *Scientific Reports* **9,** 1679 (2019).

35. Yakimov, M. M. *et al.* Primary producing prokaryotic communities of brine, interface and seawater above the halocline of deep anoxic lake L'Atalante, Eastern Mediterranean Sea. *The ISME journal* **1,** 743–755 (2007).

36. Van der Wielen, P. *et al.* The Enigma of Prokaryotic Life in Deep Hypersaline Anoxic Basins. *Science (New York, N.Y.)* **307,** 121–3 (2005).

37. Borin, S. *et al.* Sulfur cycling and methanogenesis primarily drive microbial colonization of the highly sulfidic Urania deep hypersaline basin. *Proceedings of the National Academy of Sciences* **106,** 9151–9156 (2009).

38. Van Cappellen, P. *et al.* Biogeochemical cycles of manganese and iron at the oxic- anoxic transition of a stratified marine basin (Orca Basin, Gulf of Mexico). *Environmental Science & Technology* **32,** 2931–2939 (1998).

39. Van Der Wielen, P. W. J. J. Diversity of ribulose-1,5-bisphosphate carboxylase/oxygenase large-subunit genes in the MgCl2-dominated deep hypersaline anoxic basin discovery. *FEMS Microbiology Letters* **259,** 326–331 (2006).

40. Zhuang, G.-C. *et al.* Multiple evidence for methylotrophic methanogenesis as the dominant methanogenic pathway in hypersaline sediments from the Orca Basin, Gulf of Mexico. *Geochimica et Cosmochimica Acta* **187,** 1–20 (2016).

41. LaRock, P. A., Lauer, R. D., Schwarz, J. R., Watanabe, K. K. & Wiesenburg, D. A. Microbial biomass and activity distribution in an anoxic, hypersaline basin. *Appl. Environ. Microbiol.* **37,** 466–470 (1979).

42. Yakimov, M. M. *et al.* Microbial community of the deep sea brine Lake Kryos seawater–brine interface is active below the chaotropicity limit of life as revealed by recovery of mRNA. *Environmental Microbiology* **17,** 364–382 (2015).

43. Sorokin, D. Y. *et al.* Elemental sulfur and acetate can support life of a novel strictly anaerobic haloarchaeon. *The ISME journal* **10,** 240–252 (2016).

44. Sorokin, D. *et al.* Discovery of anaerobic lithoheterotrophic haloarchaea, ubiquitous in hypersaline habitats. *The ISME journal* **11** (2017).

45. Lloyd, K. G., Lapham, L. & Teske, A. An Anaerobic Methane-Oxidizing Community of ANME-1b Archaea in Hypersaline Gulf of Mexico Sediments. *Applied and Environmental Microbiology* **72,** 7218–7230 (2006).

46. Avrahamov, N. *et al.* Anaerobic oxidation of methane by sulfate in hypersaline groundwater of the Dead Sea aquifer. *Geobiology* **12** (2014).

47. Joye, S. B. *et al.* The anaerobic oxidation of methane and sulfate reduction in sediments from Gulf of Mexico cold seeps. *Chemical Geology* **205,** 219–238 (2004).

48. Magen, C. *et al.* A simple headspace equilibration method for measuring dissolved methane. *Limnology and Oceanography: Methods* **12,** 637–650 (2014).

49. Diverse, rare microbial taxa responded to the Deepwater Horizon deep-sea hydrocarbon plume. *ISME Journal* **10,** 400–415 (2016).

50. Cline, J. D. Spectrophotometric Determination of Hydrogen Sulfide in Natural Waters. *Limnology and Oceanography* **14,** 454–458 (1969).

51. Solórzano, L. Determination of Ammonia in Natural Waters by the Phenolhypochlorite Method. *Limnology and Oceanography* **14,** 799–801 (1969).

52. Fernández-Carrera, A., Rogers, K. L., Weber, S. C., Chanton, J. P. & Montoya, J. P. Deep Water Horizon oil and methane carbon entered the food web in the Gulf of Mexico. *Limnology and Oceanography* **61,** S387–S400 (2016).

53. Rogers, K. L. *et al.* Sources of carbon to suspended particulate organic matter in the northern Gulf of Mexico. *Elem Sci Anth* **7,** 51 (2019).

54. Epp, D., Gnim, P. J. & Langseth, M. G. Heat flow in the Caribbean and Gulf of Mexico. *Journal of Geophysical Research* **75,** 5655–5669 (1970).

55. Laso-Pérez, R., Krukenberg, V., Musat, F. & Wegener, G. Establishing anaerobic hydrocarbon-degrading enrichment cultures of microorganisms under strictly anoxic conditions. *Nature Protocols* **13,** 1310–1330 (2018).

56. Valentine, D. L., Blanton, D. C., Reeburgh, W. S. & Kastner, M. Water column methane oxidation adjacent to an area of active hydrate dissociation, Eel River Basin. *Geochimica et Cosmochimica Acta* **65,** 2633–2640 (2001).

57. Das, S., Hendry, M. J. & Essilfie-Dughan, J. Transformation of two-line ferrihydrite to goethite and hematite as a function of pH and temperature. *Environmental science & technology* **45,** 268–275 (2011).

58. Fossing, H. & Jørgensen, B. B. Measurement of bacterial sulfate reduction in sediments: evaluation of a single-step chromium reduction method. *Biogeochemistry* **8,** 205–222 (1989).

59. Jørgensen, B. & Fenchel, T. The sulfur cycle of a marine sediment model system. *Marine Biology* **24,** 189–201 (1974).

60. Iversen, N. & Blackburn, T. H. Seasonal rates of methane oxidation in anoxic marine sediments. *Appl. Environ. Microbiol.* **41,** 1295–1300 (1981).

61. Schwertmann, U. & Cornell, R. M. *Iron oxides in the laboratory: preparation and characterization* (John Wiley & Sons, 2008).

62. Yakimov, M. *et al.* Microbial life in the Lake Medee, the largest deep-sea salt-saturated formation. English (US). *Scientific Reports* **3** (2013).

63. Wiesenburg, D. A., Brooks, J. M. & Bernard, B. B. Biogenic hydrocarbon gases and sulfate reduction in the Orca Basin brine. *Geochimica et Cosmochimica Acta* **49,** 2069–2080 (1985).

64. Tribovillard, N. *et al.* Does a strong pycnocline impact organic-matter preservation and accumulation in an anoxic setting? The case of the Orca Basin, Gulf of Mexico. *Comptes Rendus - Geoscience* **341,** 1–9 (2009).

65. Schijf, J. Alkali elements (Na, K, Rb) and alkaline earth elements (Mg, Ca, Sr, Ba) in the anoxic brine of Orca Basin, northern Gulf of Mexico. *Chemical Geology* **243,** 255–274 (2007).

66. Sawyer, D., Mason, R., Cook, A. & Portnov, A. Submarine Landslides Induce Massive Waves in Subsea Brine Pools. *Scientific Reports* **9** (2019).

67. Wong, G. T., Takayanagi, K. & Todd, J. F. Dissolved iodine in waters overlying and in the Orca Basin, Gulf of Mexico. *Marine Chemistry* **17,** 177–183 (1985).

68. Shah, S., Joye, S., Brandes, J. & McNichol, A. Carbon isotopic evidence for microbial control of carbon supply to Orca Basin at the brine-seawater interface. *Biogeosciences Discussions* **9** (2013).

69. Reeburgh, W. S. Oceanic Methane Biogeochemistry. *Chemical Reviews* **107,** 486–513 (2007).

70. Sheu, D.-D. *et al.* Sulfur and oxygen isotopic compositions of dissolved sulfate in the Orca Basin: Implications for origin of the high-salinity brine and oxidation of sulfides at the brine-seawater interface. *Marine Geology* **78,** 303–310 (1988).

71. Solomon, E. A., Kastner, M., MacDonald, I. R. & Leifer, I. Considerable methane fluxes to the atmosphere from hydrocarbon seeps in the Gulf of Mexico. *Nature Geoscience* **2,** 561–565 (2009).

72. Rogener, M.-K., Bracco, A., Hunter, K., Saxton, M. & Joye, S. Long-term impact of the Deepwater Horizon oil well blowout on methane oxidation dynamics in the northern Gulf of Mexico. *Elem Sci Anth* **6,** 73 (2018).

73. Steinle, L. *et al.* Effects of low oxygen concentrations on aerobic methane oxidation in seasonally hypoxic coastal waters. *Biogeosciences* **14,** 1631–1645 (2017).

74. Holler, T. *et al.* Carbon and sulfur back flux during anaerobic microbial oxidation of methane and coupled sulfate reduction. *Proceedings of the National Academy of Sciences* **108,** E1484–E1490 (2011).

75. Oren, A. Thermodynamic limits to microbial life at high salt concentrations. *Environmental microbiology* **13,** 1908–23 (2011).

76. Carere, C. R. *et al.* Mixotrophy drives niche expansion of verrucomicrobial methanotrophs. *The ISME Journal* **11,** 2599–2610 (2017).

77. Van Teeseling, M. C. *et al.* Expanding the verrucomicrobial methanotrophic world: description of three novel species of Methylacidimicrobium gen. nov. *Applied and environmental microbiology* **80,** 6782–6791 (2014).

78. Bougouffa, S. *et al.* Distinctive Microbial Community Structure in Highly Stratified Deep-Sea Brine Water Columns. *Applied and environmental microbiology* **79** (2013).

79. Abdallah, R. Z. *et al.* Aerobic methanotrophic communities at the Red Sea brine-seawater interface. *Frontiers in Microbiology* **5,** 487 (2014).

80. Boetius, A. *et al.* A marine microbial consortium apparently mediating anaerobic oxidation of methane. *Nature* **407,** 623–6 (2000).

81. Orphan, V., House, C., Hinrichs, K.-U., Mckeegan, K. & DeLong, E. Methane-consuming Archaea revealed by directly coupled isotopic and phylogenetic analysis. *Science* **293,** 484–487 (2001).

82. Laso-Pérez, R. *et al.* Thermophilic archaea activate butane via alkyl-coenzyme M formation. *Nature* **539,** 396–401 (2016).

83. Wegener, G., Krukenberg, V., Riedel, D., Tegetmeyer, H. E. & Boetius, A. Intercellular wiring enables electron transfer between methanotrophic archaea and bacteria. *Nature* **526,** 587–590 (2015).

84. Bowles, M. *et al.* Remarkable Capacity for Anaerobic Oxidation of Methane at High Methane Concentration. *Geophysical Research Letters* **46,** 12192–12201 (2019).

85. Hurtgen, M. T., Lyons, T. W., Ingall, E. D. & Cruse, A. M. Anomalous enrichments of iron monosulfide in euxinic marine sediments and the role of H 2 S in iron sulfide transformations; examples from Effingham Inlet, Orca Basin, and the Black Sea. *American Journal of Science* **299,** 556–588 (1999).

86. Claypool, G. E., Holser, W. T., Kaplan, I. R., Sakai, H. & Zak, I. The age curves of sulfur and oxygen isotopes in marine sulfate and their mutual interpretation. *Chemical Geology* **28,** 199–260 (1980).

87. Backer, H. & Schoell, M. New deeps with brines and metalliferous sediments in the Red Sea. *Nature Physical Science* **240,** 153–158 (1972).

88. Sheu, D.-D. & Presley, B. Formation of hematite in the euxinic Orca Basin, northern Gulf of Mexico. *Marine Geology* **69,** 309–321 (1986).

89. Sheu, D.-D. Sulfur and organic carbon contents in sediment cores from the Tyro and Orca basins. *Marine Geology* **75,** 157–164 (1987).

90. Raghoebarsing, A. *et al.* A microbial consortium couples anaerobic methane oxidation to denitrification. *Nature* **440,** 918–21 (2006).

91. Haroon, M. F. *et al.* Anaerobic oxidation of methane coupled to nitrate reduction in a novel archaeal lineage. *Nature* **500,** 567–570 (2013).

92. Ettwig, K. *et al.* Denitrifying bacteria anaerobically oxidize methane in the absence of Archaea. *Environmental microbiology* **10,** 3164–73 (2008).

93. Kits, K. D., Klotz, M. G. & Stein, L. Y. Methane oxidation coupled to nitrate reduction under hypoxia by the Gammaproteobacterium Methylomonas denitrificans, sp. nov. type strain FJG1. *Environmental Microbiology* **17,** 3219–3232 (2015).

94. Stein, L. & Yung, Y. Production, isotopic composition, and atmospheric fate of biologically produced nitrous oxide. *Annual Review of Earth and Planetary Sciences* **31,** 329–56 (2003).

95. Ettwig, K., Alen, T., Pas-Schoonen, K., Jetten, M. & Strous, M. Enrichment and Molecular Detection of Denitrifying Methanotrophic Bacteria of the NC10 Phylum. *Applied and environmental microbiology* **75,** 3656–62 (2009).

96. Ettwig, K. *et al.* Nitrite-driven anaerobic methane oxdation by oxygenic bacteria. *Nature* **464,** 543–8 (2010).

97. Padilla, C. *et al.* NC10 bacteria in marine oxygen minimum zones. *The ISME Journal* **10,** 2067–2071 (2016).

98. Guerrero-Cruz, S. *et al.* Key Physiology of a Nitrite-Dependent Methane-Oxidizing Enrichment Culture. *Applied and Environmental Microbiology* **85** (ed Liu, S.-J.) (2019).

99. Trefry, J. H., Presley, B. J., Keeney-Kennicutt, W. L. & Trocine, R. P. Distribution and chemistry of manganese, iron, and suspended particulates in Orca Basin. *Geo-Marine Letters* **4,** 125–130 (1984).

100. Beal, E., House, C. & Orphan, V. Manganese- and Iron-Dependent Marine Methane Oxidation. *Science (New York, N.Y.)* **325,** 184–7 (2009).

101. Bar-Or, I. *et al.* Iron-Coupled Anaerobic Oxidation of Methane Performed by a Mixed Bacterial-Archaeal Community Based on Poorly Reactive Minerals. *Environmental Science & Technology* **51** (2017).

102. Aromokeye, D. A. *et al.* Rates and Microbial Players of Iron-Driven Anaerobic Oxidation of Methane in Methanic Marine Sediments. *Frontiers in Microbiology* **10,** 3041 (2020).

103. Lenes, J., Prospero, J., Landing, W., Virmani, J. & Walsh, J. A model of Saharan dust deposition to the eastern Gulf of Mexico. *Marine Chemistry* **134-135,** 1–9 (2012).

104. NASA. *NASA-NOAA's Suomi NPP Satellite Analyzes Saharan Dust Aerosol Blanket* `https://www.nasa.gov/feature/goddard/2020/nasa-noaa-s-suomi-npp-satellite-analyzes-saharan-dust-aerosol-blanket`. (accessed: 03.29.2021).

CHAPTER 3

MICROBIAL HYDROCARBON OXIDATION IN SEDIMENTS FROM ACROSS THE NORTHERN GULF OF MEXICO.[1]

---

[1] Sibert, R. J., McKenna, A. M., Rogers, R. P., Hunter, K. S., and Joye, S. B. To be submitted to *Geophysical Research Letters*.

3.1 ABSTRACT

The presence of oil derivatives in marine sediments initiates an environmentally relevant chain of alterations in the local biogeochemical cycles of carbon, sulfur, oxygen, and nitrogen. The quantity, quality, composition, and distribution of hydrocarbons over sediment depth influences microbial population dynamics as well as the dominant mode of microbial metabolism. In turn, metabolic processes related to oil degradation accelerates local sedimentary diagenesis, which ultimately influences the linkages between sediment and seawater biogeochemical cycles. We determined hydrocarbon oxidation rates at nine sites across a spectrum of natural and anthropogenic oil impact using two compounds – hexadecane and naphthalene – that are representative proxies for the oxidation of two major oil fractions, the saturates (hexadecane) and the aromatics, specifically, polycyclic aromatic hydrocarbons (PAH) (*i.e.,* naphthalene). We present the first rates of oxidation for saturates and PAHs in Gulf of Mexico sediments determined using sensitive radiotracer techniques. Integrated naphthalene oxidation rates were highest at two sites: 1) MC118 (921 ± 75 nmol m^{-2} d^{-1}), a prolific natural hydrocarbon seep, and 2) the Taylor Energy site (283 ± 15 nmol m^{-2} d^{-1}), a shallow-water site impacted by anthropogenic discharge of oil. Average and integrated naphthalene oxidation rates were consistently higher than hexadecane oxidation rates by several orders of magnitude. Hydrocarbon oxidation rates were poorly correlated with sulfate reduction rates. In fact, some sites exhibited measurable hydrocarbon oxidation in the absence of sulfate reduction, underscoring the coupling of alternate anaerobic metabolisms, including fermentation and methanogenesis, for supporting hydrocarbon oxidation.

3.2 INTRODUCTION

Crude oil is a complex mixture of organic compounds generated from geothermal catagenesis of deeply buried kerogen and bitumen [1, 2]. In special cases, oil-like substances are produced through rapid hydrothermal cracking of autochthonous organic matter in organic-rich marine sediments (*e.g.,* Guaymas Basin, Escanaba Trough, etc. [3]). Crude oils contain tens of thousands of different compounds but are often described according to the proportion of four main structural types, the so-called SARA fractions: saturated hydrocarbons (S), aromatics (A), resins (R), and asphaltenes (A [1]). The saturated hydrocarbons are the simplest and most abundant fraction in mature, unweathered crude oil (up to 60% by weight [1]) and include short linear alkanes (*e.g.,* methane, ethane, and propane), longer linear alkanes (*e.g.,* hexadecane, n-octadecane, etc.), branched alkanes (*e.g.,* isobutane), and cyclic alkanes *e.g.,* cyclopropane, cyclobutane and cyclohexane. The aromatic fraction (typically 20-45% by weight [1]) contains the economically valuable BTEX quartet (*i.e.,*, benzene, toluene, ethylbenzene, and xylene) and polycyclic aromatic hydrocarbons (PAHs) like naphthalene, phenanthrene and ovalene.

The saturated and aromatic fractions comprise over 80% of most mature crude oils [1]. These fractions are degraded preferentially over the resins and asphaltenes and are therefore considered to constitute the most labile components and the ones most prone to biological oxidation. Heavily degraded oils, therefore, tend to contain greater and more complex fractions of resins, asphaltenes, and accumulated succinates [4, 5]. The reactivity of the saturates and aromatics is evidenced by the sequential disappearance of n-alkanes (C_6+) and aromatics (up to C_{40} [4–6]), and the appearance of an unresolved complex mixture (UCM) in gas chromatographic analysis. Significant evidence suggests that biodegradation of oils occurs predominantly through anaerobic metabolism in subsurface reservoirs [5–7], and may also proceed through secondary methanogenesis whereby n-alkanes are converted to methane ([5–8]). The rate of biodegradation, whether through oxidative processes or secondary methanogenesis, appears to decrease with increasing carbon number [6, 9].

The mobilization of oil and gas through surficial marine sediments establishes unique metabolic niches for microorganisms and impacts local biogeochemical cycling. Many seep systems are classified according to fluid flow regime: the mobilization of cold seep fluids can either be fast (mud volcanoes) or slow (oil seeps), and depending on reservoir characteristics, emit any combination of oil, gas, and brine, each with different biogeochemical consequences [10]. Mud volcanoes are areas of ephemeral high fluid flow; the fluids contain a mix of seawater, brine, fluidized mud, and/or gas, but rarely support complex benthic communities (*e.g.*,, bivalves, tube worms, etc.) because of the turbidity imparted by fluidized mud discharge [10–12]. Sites of more moderate seepage can discharge a combination of oil, gas and/or brine [10].

Oil and gas seeps occur along both passive and active continental margins, including those along the passive margins of the eastern US Atlantic seaboard (gas only [13]) and throughout the Gulf of Mexico (oil and gas; hereafter Gulf [10, 11, 14]), and along active margins, like the Eel River Margin in the Pacific. The Gulf contains over 1000 known cold seeps [10] of mixed geochemical providence. Some are brine seeps both small (GC600) or localized (NR-1 [15]) while others are large (*i.e.,* Orca basin [16, 17]). Some are oil-dominated seeps like those of GC600 [18], some are gas-dominated seeps like those of the Garden Banks area (mud volcanoes [19]), and some are a mix of both, like those at MC118, etc. [20]. Natural gas stocks at gassy seeps often have biogenic sources [14, 21], but where gas and oil co-occur, low molecular weight alkanes can be of mixed biogenic / thermogenic origin [19].

Sediments in the northern Gulf overlay massive, deeply buried, Jurassic-aged salt sheets, which, in turn, overlay massive oil and gas reservoirs [22]. Salt becomes plastic and ductile when overpressured; it is more buoyant than the overlying sediment. As result, salt forces its way upward through the sediment, in some places ballooning into salt diapirs (salt domes), and/or fracturing and faults that are ideal conduits for oil, gas, and brine migration ([10]). Marine cold seeps are surface expressions of hydrocarbon reservoirs sourced from deeper, porous strata. Upward migration of oil, gas and brine delivers carbon and nutrients into shallow sediments, and along with it, microbial species from the source reservoir [23]. Movement of deeply buried salt below the sediment column creates complex and dynamic bathymetry (see Figure 3.1). The resulting seabed along the northern Gulf is a network of fractures and faults and basin and range topography generated by 'salt tectonics'. Cold seeps of all sorts pepper the seabed in the Gulf, creating a biogeochemical cornucopia that supports diverse and active microbial communities.

Extensive interest in microbial oxidation of petroleum stems from the role that microbial degradation has on the economic value of oil reserves (*e.g.*,, souring of reserves [24]) and from the fundamental role that microbial processes play in recycling oil and natural gas within the global carbon cycle. Microbial processes modulate the flux of deeply buried, ancient carbon as it moves into the active carbon cycle. Microbial oxidation of oil products serves as a gatekeeper on this ancient carbon, controlling the reentry of ancient carbon into the active carbon cycle. For example, anaerobic methane oxidation (AOM) converts methane to DIC and alkalinity. The increase in alkalinity and DIC drives the precipitation of solid carbonate hardgrounds [10]. The AOM process essentially converts methane into rock [25]. The process of oil consumption and concomitant alkalinity degradation also contribute directly to the formation of carbonate hardgrounds. Microbial oxidation of oil products closes the loop on millions of years of carbon transformations, from the fixation of carbon dioxide into biomass, to oil and back, a natural cycle that occurs on timescales of 10^7 years ([10]).

The upward migration of hydrocarbons from the deep subsurface infuses shallow seafloor sediments with labile carbon in "reverse" biogeochemical order ([10, 23]). Oil first passes through the zone of methanogenesis, then sulfate reduction, then metal oxide reduction, nitrate reduction and may ultimately reach the surface oxic zone where it can be oxidized through coupling to oxygen reduction. Oil can be oxidized in each of these zones, and at different rates, which ultimately impacts biogeochemical zonation ([10, 23]). However, very little data are available describing patterns of microbial oil metabolism in the environment([26–29]). Most often, oil oxidation rates are inferred from data on sulfate reduction, or other rates of anaerobic metabolism [29]. While numerous studies have shown hydrocarbon oxidation potential using radiolabeled substrates in mesocosm experiments (*e.g.,* [29, 30]), no previous studies have assessed hydrocarbon oxidation rates directly because such measurements are extremely difficult to make.

The anaerobic biodegradation of petroleum hydrocarbons in subsurface marine sediments is one of the primary processes controlling the formation of heavy oil. Microbial oil metabolism also impacts the flow of deeply buried carbon through seafloor sediments [4, 6, 31–33]). For the most part, anaerobic processes govern the degradation of petroleum hydrocarbons in deep sedimentary environments over a wide range of environmental conditions including nitrate-reducing

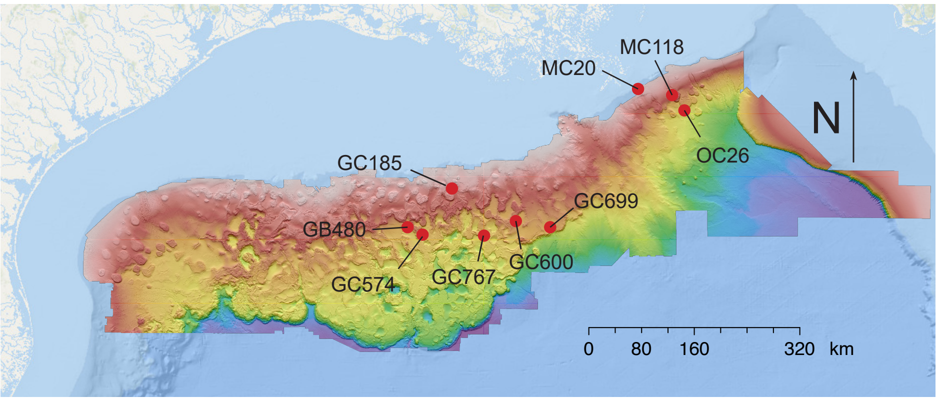

Figure 3.1: Sampling locations in the Gulf of Mexico. Bathymetry dataset courtesy of the U.S. Bureau of Ocean Energy Management: https://www.boem.gov/Gulf-of-Mexico-Deepwater-Bathymetry

([34–36]), sulfate-reducing ([26, 29, 37–41]), metal-reducing ([42–44]), and methanogenic conditions ([4, 6, 8, 39, 45]). In particular, sulfate reduction in marine sediments is coupled to the oxidation of organic matter, accounting for up to 29% of the global carbon flux to the deep ocean ([46]). Sulfate reducing microorganisms have been linked to the oxidation of methane ([31]), ethane, propane, and butane ([41, 47]), hexadecane ([29]), and PAHs ([29, 48]). Many sulfate reducing microorganisms have the metabolic machinery necessary to oxidize hydrocarbons across the structural spectrum, from methane to complex aromatics, including PAHs [49, 50].

Here we report naphthalene and hexadecane oxidation rates in Gulf sediments across nine sites of different water depth and hydrocarbon loading rates. Each of these sites were characterized for porewater and solid phase geochemistry, microbial activity, and extractable hydrocarbons. Sediment cores were sectioned and incubated with ^{35}S-sulfate and ^{14}C labeled methane, hexadecane, and naphthalene to assess the coupling of sulfate reduction with short-chain alkane, long-chain alkane, and PAH degradation. We hypothesized that i) sulfate reduction rates would be a good predictor for presence and magnitude of alkane and PAH degradation, ii) that n-alkanes would be oxidized faster than PAHs based on energetics, and iii) that known exposure to oil would prime the sediment microbial community for hydrocarbon metabolism and further predict the magnitude of hydrocarbon oxidation rates at a given site.

3.3 METHODS

3.3.1 STUDY SITES AND SAMPLE TYPES

Ten sediment cores were collected in the northern Gulf and processed for hydrocarbon oxidation rates and geochemistry during two expeditions aboard the research vessel R/V Endeavor (University of Rhode Island), expedition EN559 in 2015 and EN586 in 2016. All cores were collected using a multiple coring device (polycarbonate liners; hereafter MUC) fitted with polycarbonate liners. Study sites for experimental determination of naphthalene and hexadecane oxidation (collectively HYOx) rates were chosen based on past observations of hydrocarbon seepage and oil impact using a combination of geochemical data and visual observations (see Figure 3.1 Table 3.1). We included two "control" sites (Green Canyon lease block 699, hereafter GC699, and Garden Banks lease block 480, hereafter GB480) that lacked hydrocarbon seepage, three known vigorous oil and gas seeps (Green Canyon lease block 600, hereafter GC600; Green Canyon lease block 185, hereafter GC185; and Mississippi Canyon lease block 118, hereafter MC118), two sites previously impacted by anthropogenic oil spills (Deepwater Horizon, hereafter OC26, which was impacted by the 2010 Deepwater Horizon oil well blowout; the Taylor Energy site at Mississippi Canyon lease block 20, hereafter MC20), a site impacted by a slow but uncontrolled and significant discharge between September 2004 and April 2019 [51]; and two sites of moderate gas seepage (Green Canyon lease blocks 767 and 574, hereafter GC767 and GC574).

Utilizing a multiple corer lacking a video guidance system to try and sample areas of active hydrocarbon seepage is not ideal. Furthermore, the R/V Endeavor is not equipped with dynamic positioning, so even when targeting areas of known and intense seepage activity, movement of the ship and multicore during sampling often resulted in cores with only modest seepage signatures. Furthermore, even at areas known for oil seepage, active seeps are heterogeneously distributed, often fed by faults and fractures in the subsurface that grow, collapse, and change over time. As a result, active sites of seepage are ephemeral and difficult to sample directly with unguided multiple core technology like that utilized in this study.

Cruise	Site	Depth (m)	Lat (DDM)	Long (DDM)	Features
EN559	GB480	783	25°28.86′	−91°59.78′	Shallow control site; diffuse methane; sulfate-rich; sulfide free; undescribed benthic community
	GC767	1570	27°12.56′	−91°0.82′	Diffuse methane seepage; sulfate-rich; sulfide-free; undescribed benthic community
EN586	GC185	585	27°47.23′	−91°30.38′	Heterogeneous oil and gas seepage; carbonates; breaching hydrates; benthic community includes chemosythetic tubeworms, mussels, and *Beggiatoa* mats [52, 53]
	GC699	1372	27°17.53′	−90°2.33′	Deep control site; diffuse methane seepage; sulfate-rich; sulfide-free; undescribed benthic community
	GC574	1053	27°21.18′	−91°49.29′	Diffuse methane seepage; sulfate-rich; sulfide-free; undescribed benthic community
	GC600	1306	27°22.06′	−90°33.80′	Oil and gas seepage; authigenic carbonates; breaching gas hydrates; benthic community includes chemosythetic tubeworms, mussels, and microbial mats [14]
	GC767	1526	27°12.61′	−91°1.54′	Diffuse methane seepage; sulfate-rich; sulfide-free; undescribed benthic community
	MC118	880	28°51.20′	−88°29.50′	Oil and gas seepage; authigenic carbonates; breaching gas hydrates; benthic community includes mussels, bacterial mats, and clams [20, 54, 55]
	OC26	1634	28°41.46′	−88°22.63′	Little to no methane; Site of Deepwater Horizon oil spill; sulfate-rich; sulfide-free; undescribed benthic community
	MC20	123	28°56.63′	−88°58.07′	Little to no methane; impacted by anthropogenic oil contamination; sulfate-rich; sulfide-free

Table 3.1: Study site name, water depth, location, and features. Site abbreviations in red.

Sediment recovery in multicores varied by site (see Figure 3.2). Near-shore, shallow sediments like those found at MC20 (see Table 3.1) contained high proportions of sand-sized terrigenous clastics, which resisted penetration by gravity-driven coring devices. Sediments at sites of effusive hydrocarbon seepage, such as the active seepage areas of GC600, frequently contained authigenic carbonates, gas hydrates, shell hash, and otherwise difficult to sample components. Only cores of sufficient length (>25 cm depth) were selected for geochemistry and rate determination. At each site, three parallel MUC cores were selected following retrieval and transferred to a cold van (*ca.* 4 °C) for visual description and photographs. One core was reserved for hydrocarbon characterization and HYOx rate sampling, one for porewater geochemistry and solid-phase analysis, and one for gaseous hydrocarbons, microbial rate measurements, and metagenomic work. All cores were processed within 8 hours of retrieval.

3.3.2 PROCESSING

Sediments were collected in discrete 3 cm or 5 cm depth intervals in all cores, for all major analyses. Individual sediment horizons were extruded with a floor standing plunger assembly into a specially designed, argon-filled, polycarbonate chamber and, depending on the core, sub-sampled for hydrocarbons, gases, pore water geochemistry, solid phase analysis, rate assays, and metagenomics. Metagenomics analyses are underway through collaboration with Dr. Brett Baker's group; that work is underway and will be included in the publication but are not discussed further in this chapter. For bulk sediment geochemistry, sub-samples were collected from the center of the core using an ethanol-rinsed, stainless steel spoon, and immediately transferred into an argon-filled Delrin (polyoxymethylene) squeezer cup [56]. The samples were pressurized and the pore water discharged into acid-washed, Ar-flushed, 25 mL plastic syringes. Depending on the estimated amount of sulfide (via smell), a volume of pore water (0.5 to 2 mL) was collected immediately for sulfide analysis (H_2S). Sulfide samples were preserved in 500 μL of 20 wt% zinc acetate, and later analyzed via the methylene blue method [57].

The remaining pore water sample was filter-sterilized with a 500 μm Target filter, dispensed into a high-density polyethylene bottle (HDPE; Nalgene), and further sub-sampled for downstream geochemical analysis according to Joye et al. (2004, 2010 [14, 52]). A 2 mL sub-sample for anions (SO_4^{2-} and Cl^-) and cations (*e.g.*,, Na^+, Mg^{2+}, Ca^{2+}, K^+) were preserved by addition of nitric acid to 0.1 μmol L^{-1} final concentration and stored at room temperature until analysis. An additional 1.5 mL porewater for ammonium quantification (NH_4^+) was preserved in 100 μL phenol solution and analyzed shipboard within 24 hours by the phenol hypochlorite method [58]. The remaining sample was frozen at −20 °C until subsequent nutrient (NO_2^-, NO_3^+, and PO_4^{3-}), dissolved organic carbon (DOC), and total dissolved nitrogen (TDN) analysis. The dewatered sediment was collected in a sterile Whirl-pack bag, and the bag was then flushed with argon, sealed without headspace, and frozen at −20 °C for solid phase analysis [52].

A second core was selected for hydrocarbon quantification and microbial activity. All ^{14}C-hydrocarbon oxidation rates were conducted in triplicate at each depth interval, with two killed controls per core. Rate samples were collected in 3 mL sediment volumes in custom made, cut-end Hungate tubes, and sealed headspace-free. Controls were immediately injected with 3 mL of 2 M NaOH solution and homogenized to halt microbial activity. Live incubations and controls were left to pre-incubate at 4 degrees C for 24 hrs before tracer addition. At GC767, two cores were analyzed for hydrocarbon oxidation (see Tables 3.1, 3.2) and data were pooled for calculation of averages and integrations. For hydrocarbon quantification, approximately 100 g of the remaining sediment was collected from the center of the core using a stainless steel, ethanol-rinsed spoon, and immediately transferred into pre-combusted, argon-filled, 250 mL amber-glass jars. The jar was flushed again briefly with argon, covered in combusted foil, sealed with a Teflon-lined cap, and frozen at −20 °C until hydrocarbon quantification. Care was taken to avoid sampling along the perimeter of the core to prevent contamination/adsorption of oil components from/by the polycarbonate core liner.

A third core was sectioned to determine methane and hydrogen concentrations, metagenomics, and anaerobic oxidation of methane AOM and dissimilatory sulfate reduction (DSR) rates. A 5 mL sub-sample was collected for methane using a cut-end syringe and placed into an argon-flushed 25 mL borosilicate glass serum vial containing 2 mL 2 M NaOH to stop microbial activity. The sample was sealed with a blue chlorobutyl rubber stopper, secured with an aluminum crimp seal, vortexed to slurry, and stored at room temperature until analysis by a gas chromatograph equipped with a flame ionization detector (GC-FID [52]). An additional 5 mL sub-sample for hydrogen analysis was transferred to a 25 mL borosilicate serum vial and crimp-sealed. The headspace was flushed with helium for 1 minute and the sample incubated at 4 degree C for 4 days before shipboard analysis, following the headspace equilibration technique described by Lin, et al., [59]. Similar to sample handling for HYOx rates, 3 mL of sediment were collected in cut-end Hungate tubes for AOM and SR rate assays. Sub-samples were collected in triplicate for each assay at each depth interval, with two controls carried out per core. Controls were prepared by adding either 3 mL of 2 mL 2 M NaOH for AOM, or 3 mL concentrated zinc acetate solution (20 wt.%) for DSR, to halt microbial activity before tracer injection. Both controls and live samples were pre-incubated for 24 hour at 4 °C to allow recovery of the microbial population (from the sampling disturbance) before radiotracer injection.

3.3.3 Hydrocarbon analysis

Sediment samples were characterized in 3 cm intervals for oil components by gas chromatography [20] with flame ionization detector (SRI 8610C; 3.2mm x 1.8 m packed hayecep–d column, and flame ionization detector). Sediments for hydrocarbon analysis were first thawed overnight at 4 °C, and then extracted in a 90:10 mix of HPLC-grade toluene to methanol, using a Soxhlet apparatus and 500 mL round-bottom flask. Between 5 to 25 g of thawed sediment was weighed and placed in a combusted glass thimble using a methanol-rinsed metal scoopula, and then inserted into a combusted Soxhlet unit. Approximately 300 mL of the toluene/methanol mixture was poured into the Soxhlet apparatus and allowed to siphon into the round bottom flask. A heating mantle was used to bring the contents of the round bottom flask to a gentle boil. Sediments were extracted under hot solvent for 24 hours. Following this 24–hour period, the remaining solvent in the Soxhlet was quantitatively transferred to the main extract in the round-bottom flask and reduced to approximately 5 mL by rotary evaporation. Excess water was removed by passing the extracts three times through combusted sodium sulfate columns. Excess sulfides were removed by passing the samples three times through columns packed with solvent-rinsed, HC-activated copper shot. The cleaned extracts were placed into combusted and pre-weighed, 7 mL amber glass vials, blown to dryness under a stream of UHP nitrogen gas, weighed to determine the final mass of extracted hydrocarbons, and reported in units of $\mu g\ g^{-1}$ of wet sediment.

3.3.4 Geochemistry

Porewater methane samples were vortexed to extract gas from the sample slurry and analyzed by gas chromatography using a flame ionization detector (GC-FID; SRI 8610C gas chromatograph; 1.8 m x 3.175 mm packed HayaSep–D column [14]). Certified gas mixtures (0.1% CH_4 in He) were used to calibrate the instrument prior to analysis. Porewater hydrogen concentrations were determined by headspace equilibration [59] and then injecting 1 mL of sample headspace into a Peak Performer 1 Reducing Compound Photometer (Peak Laboratories, USA [60]), calibrated with certified standards. Sample concentrations were calculated using the salinity and temperature corrected solubility constants of Crozier and Yamamoto [61]. Porewater concentrations of sodium (Na^+), potassium (K^+), magnesium (Mg^{2+}), calcium (Ca^{2+}), chloride (Cl^-), sulfate ($SO_4{}^{2-}$), and nutrients (nitrate, nitrite, phosphate) were analyzed using previously described methods [14, 20, 52]. Hydrogen sulfide was determined using standard colorimetric techniques [57]. A subsample of sediment was analyzed for porosity, dried, analyzed for carbon, nitrogen, and phosphorus content, and then combusted to determine organic matter content by loss on ignition [14].

3.3.5 Microbial Activity

Two major crude oil fractions were assessed for rates of microbial degradation using radiolabeled tracers: [1-14C] hexadecane (2.0 TBq $mmol^{-1}$; American Radiolabeled Chemicals; ARC) was used as a proxy for long-chain alkanes, and [1-14C] naphthalene (2.0 TBq $mmol^{-1}$; ARC) for polycyclic aromatic hydrocarbons (PAH). The naphthalene tracer was delivered to the laboratory dissolved in an ethanol solvent but the hexadecane was dissolved in hexane. To reduce toxicity of the hexadecane tracer, the original hexane solvent of the [1-14C] hexadecane tracer was evaporated under a stream of sterile argon and the tracer was then redissolved in ethanol to match the naphthalene carrier. Radiotracer experiments were carried out shipboard following sample collection. After a pre-incubation period of approximately 24 h, samples were injected with 20 μL of either ^{14}C–hexadecane (≈2.8 μg per sample) or ^{14}C–naphthalene (≈1.4 μg per sample) to achieve a final activity of approximately 10^6 dpm ^{14}C–hydrocarbon per sample. Rate samples were then incubated at 4 °C for 2 to 4 days. After incubation, 3 mL of 2 M NaOH solution was injected into each sample and the sample was homogenized to halt microbial activity and trap CO_2 as dissolved inorganic carbon (DIC). Preserved samples were then transferred to 50 mL Falcon tubes (including two rinses to assure quantitative transfer of product) for storage until analysis back at the UGA laboratory.

Radioactive DIC was recovered from samples using an acid digestion technique modified from Sibert, et al., 2016, for sediments [62]. Sediments were transferred into a cylindrical 250 mL glass flask and sealed with a flow-through distillation head with a ground glass joint. The distillation head directs a steady stream of argon down a central glass tube at 50 mL/min and out through a sintered frit situated just below the sample surface. 3 mL of concentrated HCl (approx. 12 M) was introduced into the argon line immediately upstream of the distillation head and allowed to bubble through the glass frit. This lowered the pH of the sample to <1, driving the ^{14}C-DIC off as $^{14}CO_2$ into the flask headspace. The headspace was then cleared through a tygon tube attached to the outlet of the distillation head and bubbled through a 1.5 mL solution of 3–methoxypropylamine and 3.5 mL scintillation fluid for 45 min to trap the purged $^{14}CO_2$. The activity of the 5 mL cocktail was then counted on a liquid scintillation counter (LSC).

Residual naphthalene tracer was removed from samples prior to distillation by the storage procedure: naphthalene in the sample was quantitatively removed via sorption onto the polycarbonate Falcon tubes. However, hexadecane was difficult to remove quantitatively from the sample matrix; additions of shredded plastic, activated charcoal, and C-18 bonded silica gel all failed to remove parent hexadecane tracer from the sample. Ultimately, we used custom glassware and Tygon tubing to extract hexadecane from the gas-phase effluent, downstream of the distillation vessel but upstream from the DIC trap. $^{14}CO_2$-DIC recovery determined via controlled additions was better than 95% and scintillation traps contained lower than 100 dpm background tracer contamination following distillation of amended process controls. Hexadecane and naphthalene oxidation rates were calculated similarly to AOM procedures in sediments, with modifications [63]. Environmental naphthalene and hexadecane concentrations could not be measured and are not known. Even if concentrations were known, the tracer addition represents a substantial substrate addition, so the measured rates reported here reflect potential activity, or apparent rates. So, concentrations available to microorganisms during the incubations were estimated from tracer additions and solubility limits. Naphthalene concentrations were calculated using the specific activity of [1-14C] naphthalene (2.0 TBq mmol^{-1}), the injected activity ($\approx 1 \times 10^6$ dpm), and sample size (3 mL). Hexadecane has a very low solubility in seawater, such that tracer injections routinely produced hexadecane concentrations 500 times the solubility limit (≈0.04 µg L^{-1}; 177 pmol L^{-1}; 25 °C; 1 atm [64]). Accordingly, [1-14C] hexadecane tracer concentrations and activity numbers (in dpm) were adjusted to reflect saturation conditions. Hexadecane and naphthalene oxidation rates were otherwise calculated the same way, again modified from Sibert et al., 2016 [62] following the equation:

$$\textsc{hyox} = [\textsc{hc}] \times \phi_{\text{sed}} \times \frac{\alpha_1}{t} \times \left[\frac{{}^{14}\text{CO}_2}{{}^{14}\text{C}-\textsc{hc}}\right] \tag{3.1}$$

where [HC] is the concentration of either naphthalene or hexadecane (derived as described above), ϕ_{sed} is sediment porosity [52], α_1 is the ^{14}C isotope fractionation factor (1.008) [65], t is incubation time in days, $^{14}CO_2$ is the recovered DIC activity in dpm, and ^{14}C–HC is the total injected hydrocarbon activity in dpm. The rates are porosity corrected to deliver a final rate in terms of volume of 'wet sediment', which are more meaningful than rates in a volume of porewater.

Rates of DSR and AOM were carried out using ^{35}S-labeled sodium sulfate ($Na_2^{35}SO_4$; American Radiolabeled Chemicals; ARC; ≈1.59 TBq $mmol^{-1}$), and ^{14}C-labeled methane ($^{14}CH_4$; ARC; ≈1.85 TBq $mmol^{-1}$) as described previously [63, 66]. Radiolabeled sulfate and methane tracers were both diluted in sterile milli-Q to yield stocks with an activity of $\approx 1 \times 10^6$ dpm per 100 µL. Samples and controls were injected with 100 µL tracer, incubated at 4 °C for 1 d at in situ pressure, and slurried with 3 mL of either 20 wt.% zinc acetate (SR), or 2 mol L^{-1} NaOH (AOM), to halt microbial activity and preserve labeled oxidation products, and then stored at room temperature until distillation and analysis.

Fixed DSR samples were processed to quantify radioactively labeled sulfide using a standard one-step chromium distillation. Briefly, sediments were transferred to a 50 mL Falcon tube, rinsed of porewater and excess tracer three times by centrifugation and resuspension with 25 mL tap water. The rinsate was transferred to a 125 mL flask and brought to 100 mL total volume, of which, 100 uL was counted by LSC to determine the total activity of unused $Na_2^{35}SO_4$ tracer. The rinsed sediment sample was then transferred to a round-bottom boiling flask, placed in a heating mantle, and distilled with a solution of hot HCl and reduced chromium under a stream of nitrogen gas, as described by Fossing and Jørgensen [66]. Evolved ^{35}S from the distillation process was trapped in 5 mL of 2% zinc acetate solution as Zn^{35}S and counted on by LSC. DSR rates (nmol cm^{-3} d^{-1}) were calculated as:

$$\textsc{srr} = \left[SO_4{}^{2-}\right] \times \phi_{\text{sed}} \times \frac{\alpha_2}{t} \times \left[\frac{\textsc{tris}}{{}^{35}SO_4{}^{2-}}\right] \times 1000 \qquad (3.2)$$

where [$SO_4{}^{2-}$] is the porewater sulfate concentration in mmol L^{-1}, ϕ the sediment porosity, α_2 the ^{35}S isotope fractionation factor (1.06) [67], TRIS the activity of the distillation trap (in dpm), and $^{35}SO_4{}^{2-}$ the total activity of injected tracer (dpm). The rates are porosity corrected to deliver a final rate in terms of volume of 'wet sediment', which are more meaningful than rates in a volume of porewater.

Preserved AOM samples were transferred to a 125 mL Erlenmeyer flask, sealed with a specially modified, gas-tight stopper, and processed using an acid digestion technique as described by Sibert, et al [63]. The stopper was designed to hold a CO_2 trap (here, an uncapped 7 ml glass scintillation vial containing 1.5 mL 3–methoxypropylamine) a few centimeters above the sample via a moldable plastic wire. Samples were acidified with 5 mL 30% H_2SO_4 (final pH <1) and digested for 4 h on a shaker table. Following digestion, the trap was removed from the flask, filled with 5.5 mL scintillation fluid, and counted by LSC. Recovery was better than 95% on process controls. AOM rates (nmol cm^{-3} d) were calculated as:

$$\textsc{aom} = [CH_4] \times \frac{\alpha_1}{t} \times \left[\frac{{}^{14}CO_2}{{}^{14}CH_4}\right] \qquad (3.3)$$

where [CH_4] is the concentration of methane in µmol L^{-1}, α_1 is the ^{14}C isotope fractionation factor (1.008) [65], $^{14}CO_2$ is the activity of the oxidation product in dpm, and $^{14}CH_4$ is the total amount of injected tracer activity in dpm. These rates are not porosity corrected as the concentration of methane is already reported in terms of 'wet sediment'.

Site	$\sum CH_4$	$\sum$ DOC	$\sum$ Alk	$\sum H_2S$	$\sum NH_4^+$	$\sum H_2$	$\sum$NaphOx	$\sum$HexOx	$\sum$AOM	$\sum$SRR
GB480	0.3(0)	58.0(39)	—	0.0(0)*	0.8(1)	36.3(25)	65.0(44)	42.7(29)	0.8(1)	0.0(0)*
GC185	0.8(1)	74.3(51)	350.6(239)	0.0(0)*	3.9(3)	49.2(33)	132.9(9)	18.2(12)	0.0(0)*	80.4(55)
GC574	3.8(3)	25.7(17)	223.2(152)	0.0(0)*	0.2(0)	205.6(140)	76.8(52)	3.2(2)	0.6(0)	52.2(36)
GC600	2.3(1)	27.6(15)	625.1(338)	1.2(1)	9.6(5)	89.2(48)	84.7(46)	—	0.5(0)	237.2(179)
GC699	1.2(2)	51.9(65)	213.0(266)	0.0(0)*	0.8(1)	336.5(561)	133.5(167)	38.2(48)	1.3(2)	4.8(6)
GC767	1.2(0)	97.0(21)	336.5(133)	0.0(0)*	3.3(1)	292.7(62)	173.7(37)	68.3(15)	0.9(0)	0.0(0)*
MC118	59.0(48)	52.3(43)	880.9(719)	26.9(22)	15.1(12)	168.8(138)	921.1(752)	85.0(69)	565.6(462)	19 115.2(1560)
OC26	0.6(0)	111.7(60)	398.3(215)	0.0(0)*	3.4(2)	3078.6(1662)	83.6(45)	1.4(1)	0.0(0)*	17.0(16)
MC20	0.9(1)	79.2(43)	667.4(360)	0.0(0)*	31.5(17)	379.1(239)	282.5(152)	42.4(23)	1.0(1)	883.0(477)

* = below detection

— = no sample

Table 3.2: Integrated methane (in µmol m^{-2}), dissolved organic carbon (DOC), alkalinity, sulfide, and ammonium (all in mmol m^{-2}), hydrogen (nmol m^{-2}), naphthalene oxidation rates (NAPHOX; nmol m^{-2} d^{-1}), hexadecane oxidation rates (HEXOX; pmol m^{-2} d^{-1}), anaerobic oxidation of methane (AOM), and sulfate reduction rates (AOM and SRR; µmol m^{-2} d^{-1}). Rates and concentrations integrated over 17 cm for consistency between cores. Values in parenthesis represent standard error in tenths. Abbreviations: Alk = alkalinity; NaphOx = naphthalene oxidation; HexOx = hexadecane oxidation; AOM = anaerobic oxidation of methane rate; and SRR = sulfate reduction rate.

3.4 RESULTS

Geochemistry data from all nine sites are summarized in Tables 3.2, 3.3. This included sites described as "control" sites (GB480 and GC699; see Table3.1). The control sites were characterized by low methane, low sulfide, and low rates of AOM and DSR (see Figures 3.3, 3.4; Table 3.2, 3.3). The three cold-seep sites, GC600, GC185, and MC118, were characterized by natural oil and gas discharge, gas hydrate formation, and chemosynthetic biological communities. Two sites impacted by anthropogenic oil release, one deep (OC26) and one shallow (MC20), were characterized by a layer of sedimented oil "fluff" at the sediment surface, sulfate-rich porewater, undetectable sulfide, and low rates of AOM (see Figures 3.3, 3.4; Table 3.2, 3.3). The remaining sites (GC767 and GC574) were characterized by diffuse methane seepage and mildly sulfidic pore fluids (see Figures 3.3, 3.4; Table 3.2, 3.3).

Sulfide accumulated to measurable levels in cores from only two sites: GC600 (262 µmol L^{-1} H_2S max) and MC118 (702 µmol L^{-1} H_2S max; see Figures 3.3, 3.4; Table 3.2, 3.3)). Both GC600 and MC118 are sites of prolific seepage of oil and gas and abundant gas hydrate mounds. Integrated naphthalene oxidation rates (between 65 and 921 nmol m^{-2} d^{-1}) were consistently higher than hexadecane oxidation rates (between 1 and 85 nmol m^{-2} d^{-1}) by over five orders of magnitude across all nine sites (see Figures 3.5, 3.6; Table 3.2, 3.3). The highest HEXOx (85 ± 7 pmol m^{-2} d^{-1}) and NAPHOx rates were observed at MC118, a site with active oil seepage, high levels of sulfide, high rates of AOM and DSR, and the highest fraction of extractable hydrocarbons (1592 μg g^{-1}; see Tables 1–4). The second highest NAPHOx rates were found at MC20 (Taylor Energy spill site), a shallow-water site historically impacted by anthropogenic oil discharge (see Figures 3.5, 3.6; Table 3.2, 3.3 [22]). However, the second highest HEXOx rates were found at a different site, GC767, which was characterized by undetectable sulfide and DSR, high DOC concentrations, and high levels of extractable hydrocarbons (see Tables 3.3 - 3.6). The highest rates of NAPHOx and HEXOx corresponded to highest DSR rates (MC118; see Figures 3.5, 3.6; Table 3.2, 3.3), but rates of DSR were very poor indicators of HYOx magnitude. Anaerobic methane oxidation rates were always significantly higher than hexadecane oxidation, perhaps due to the low solubility of hexadecane relative to methane. Even though the low DIC:DIP ratios for highly active seep sites (*e.g.,* MC118 and GC600) suggest hydrocarbon oxidation, we found no further correlation between HYOx rates and DSR, AOM, or any other geochemical parameter. Rates of HYOx were dynamic and variable.

3.4.1 Control Sediments

The control sites GC699 and GB480 were selected to assess the potential for hydrocarbon oxidation at sites lacking active seepage. The sediments at these sites contained well-oxidized argillaceous sediments, brown to gray in color, with no detectable sulfide and little methane (<11 μmol L^{-1} CH_4; see Tables 3.1 and 3.2). Sediments at both control sites contained abundant sulfate (approx. 28 mM) and no sulfide (see Tables 3.2 and 3.3). The average methane concentration at GB480 was low (2 μmol L^{-1} CH_4) (see Table 3.3), but it was five times at GC699 (11 μmol L^{-1}), of similar magnitude to some values observed at GC574 and GC600, though those cores clearly missed sites of highly active seepage.

Site	Core ID	CH_4	H_2S	SO_4^{2-}	H_2	NH_4^+	NO_2^-	NO_3^-	PO_4^{3-}	DIC	DIN	DOC
GB480	EN559-S18-E07	2.1	BDL	27.3	6.4	20.6	0.8	16.1	7.9	–	37.3	719.2
GC185	EN586-S02-E13	5.0	BDL	27.3	0.7	46.8	0.1	8.9	12.6	2.0	55.9	567.0
GC574	EN586-S15-E08	15.3	BDL	27.6	5.0	4.2	BDL	12.4	7.2	2.0	17.1	343.6
GC600	EN586-S18-E11	15.4	75.0	25.8	0.9	75.8	0.5	7.9	4.9	3.4	84.1	264.8
GC699	EN586-S07-E07	11.3	BDL	27.7	4.0	15.1	BDL	9.6	4.7	2.1	25.1	574.7
GC767	EN559-S25-E03	3.7	BDL	27.4	5.2	44.9	0.9	14.9	8.7	–	60.6	511.2
	EN586-S06-E07	3.0	BDL	27.6	1.9	10.3	BDL	20.0	6.9	2.7	30.9	450.8
MC118	EN586-S20-E03	939.5	240.5	16.3	1.8	164.5	5.5	15.5	8.3	11.4	173.7	637.2
OC26	EN586-S12-E07	2.8	BDL	27.8	29.6	30.2	0.4	6.0	8.0	2.0	36.5	732.0
MC20	EN586-S11-E04	5.1	BDL	27.2	3.5	261.0	0.1	3.0	15.2	4.1	264.0	726.4

BDL = below detection

— = no sample

Table 3.3: Geochemical parameters averaged over 40 cm. Methane, sulfide, ammonium, nitrate, nitrite, phosphate, dissolved inorganic nitrogen (DIN), dissolved inorganic phosphorus (DIP), and dissolved organic carbon (DOC) concentrations in μmol L^{-1}. Sulfate and dissolved inorganic carbon (DIC) concentrations in mmol L^{-1}. Hydrogen concentration in nmol L^{-1}.

Site	Core ID	%C	%N	%P	C:N	%OM
GB480	EN559-S18-E07	4.74	0.13	0.06	36.46	12.96
GC185	EN586-S02-E13	2.62	0.17	0.08	15.41	9.95
GC574	EN586-S15-E08	4.02	0.08	0.06	50.25	12.41
GC600	EN586-S18-E11	3.95	0.06	0.06	65.83	7.81
GC699	EN586-S07-E07	2.43	0.07	0.06	34.71	9.21
GC767	EN559-S25-E03	3.38	0.15	0.07	22.53	11.58
GC767	EN586-S06-E07	3.72	0.09	0.06	41.33	13.04
MC118	EN586-S20-E03	5.04	0.13	0.05	38.76	10.46
OC26	EN586-S12-E07	3.20	0.18	0.06	17.78	12.67
MC20	EN586-S11-E04	1.95	0.22	0.06	8.86	11.49

Table 3.4: Solid phase organic carbon (wt% C), nitrogen (wt% N), and phosphorus (wt% P), weight-percent C:N ratio (C:N), and percent organic matter by loss on combustion (wt%OM), averaged over 40 cm.

Average ammonium concentrations at GB480 were low (21 μmol L^{-1}) but nearly identical to those found at the GC699 control site (15 μmol L^{-1}; see Table 3.3). These values are between 1.5 and 5 times higher than those at GC574 and GC767, sites previously determined to have moderate seepage. However, integrated ammonium was lowest at the control sites, 0.8 mmol m^{-2} at both GB480 and GC699. The lowest integrated alkalinity of all the sites was observed at GC699 (213 mmol m^{-2}; see Table 3.2), essentially no different than values at GC574 and consistent with lower rates of heterotrophic metabolism. Porewater alkalinity values were not available for GB480. Integrated DOC values were similar between control site sediments, 58 mmol m^{-2} at GB480 and 52 mmol m^{-2} at GC699 (see Table 3.2). These values are similar to those of MC118, our most active seep site, nearly double those of GC600 and GC574, but about half those of GC767 and OC26.

Sediments of GB480 contained a higher percentage of organic matter (12.96%; see Table 3.4) than every site but GC767, and similar to those reported in the past for active GC600 seep sediments ([14]). The carbon content of GB480 sediments was 4.74%, second only to the active MC118 seep site (see Table 3.4), similar again to previous reports from GC600 sediments, this value drove a high C:N ratio (36.75; [14, 52, 68]). The high carbon content combined with low sulfate reduction and methane oxidation rates suggests the presence of recalcitrant carbon in these sediments. The carbon and nitrogen content of GC699 sediments (2.43% C and 0.07% N) were nearly half that of GB480 (4.74% C and 0.07% N; see Table 3.4). The sediment carbon content of both control sites in this study are higher than those found at other control sites reported in the Gulf (see Tables 3.2 and 3.4 [52, 68]).

Integrated sulfate reduction rates were undetectable at GB480 and only 4.8 μmol m^{-2} d^{-1} at GC699, much lower than every other site except GC767 (also undetectable; see Table 3.2). Rates of AOM were similarly low at GB480 (0.8 μmol m^{-2} d^{-1}) and only a little higher for GC699 (1.3 μmol m^{-2} d^{-1}; see Table 3.2). Microbial activity at GB480 was extremely low and resembled that of GC767 most closely, so much so, that GC767 could easily be considered another control site in the absence of hydrocarbon data (see Table 3.2).

Site	Core ID	AOM	SRR	NAPHOX	HEXOX
GB480	EN559-S18-E07	0.004	BDL	0.283	0.267
GC185	EN586-S02-E13	0.001	0.327	0.745	0.090
GC574	EN586-S15-E08	0.002	0.193	0.538	0.012
GC600	EN586-S18-E11	0.005	1.235	0.506	–
GC699	EN586-S07-E07	0.004	0.017	0.480	0.315
GC767	EN559-S25-E03	0.003	BDL	0.870	0.267
GC767	EN586-S06-E07	BDL	BDL	0.558	0.140
MC118	EN586-S20-E03	19.851	187.483	4.176	0.477
OC26	EN586-S12-E07	BDL	0.126	0.394	0.005
MC20	EN586-S11-E04	0.006	4.669	1.560	0.253

Table 3.5: Average rates of anaerobic methane oxidation (AOM; nmol cm^{-3} d^{-1}), dissimilatory sulfate reduction (SRR; nmol cm^{-3} d^{-1}), naphthalene oxidation (NAPHOX; pmol cm^{-3} d^{-1}), and hexadecane oxidation (HEXOX; fmol cm^{-3} d^{-1}). BDL = below detection

Down-core trends in hexadecane and naphthalene oxidation rates were similar between control sites but differed in magnitude. Naphthalene oxidation was confined to the upper 15 cm of sediment at both GB480 and GC699 (see Figures 3.7 and 3.8; Table 3.3) and given the sulfate-rich, sulfide-free porewater of both control cores, may have been linked to aerobic rather than to anaerobic metabolism. Maximum NAPHOx rates at GB480 and GC699 were were nearly identical: 1.41 pmol cm^{-3} d^{-1} and 1.96 pmol cm^{-3} d^{-1}, respectively. There were differences in the cumulative rate, despite initial similarities. Integrated NAPHOx rates at GC699 (133.5 nmol m^{-2} d^{-1}) were double those of GB480 (65 nmol m^{-2} d^{-1}; see Figures 3.7 and 3.8; Table 3.2).

Depth profiles of HEXOx rates were bimodal at both sites, with a peak of activity concomitant with NAPHOx within the first 10 cm and another deeper peak in the sediment column below 25 cm (0.769 fmol cm^{-3} d^{-1} for GB480 and 0.542 fmol cm^{-3} d^{-1} for GC699). Hexadecane oxidation rates diminished between 15 and 25 cm depth but increased slightly with depth down to 40 cmbsf. Methane concentrations were low at both sites. However, the increase in hexadecane oxidation rate below 25 cm depth corresponded to higher concentrations of methane at deeper depths (see Figures 3.7 and 3.8).

3.4.2 Sediments of Moderate Seepage

The sediments from GC574 and GC767 were visually similar to control core sediments of GB480 and GC699. The top 10 cm of each core contained flocculent, well-oxidized brown sediments but transitioned to gray, argillaceous muds below that. As with the control sediments of GB480 and GC699, porewaters were sulfate-rich (27-28 mmol L^{-1} SO_4^{2-}; see Table 3.3), contained moderate to low methane (3 – 4 μmol L^{-1} CH_4 at GC767 and 15 μmol L^{-1} CH_4 at GC574), and sulfide was below detection. Sediments of core EN559-S25-E03 at GC767 contained approximately double the average ammonium and DIN concentration of GC574 or any of the control sites (see Table 3.3), and nearly triple the integrated amount of ammonium (3.3 mmol m^{-2}; see Table 3.2). The sediments of GC767 contain more total DOC (97 mmol m^{-2}) than GC574 or either of the control sites (see Table 3.2). However, average DOC values for both GC574 (244 μmol L^{-1}) and GC767 (451 – 511 μmol L^{-1}) are lower than those of the control sites (*e.g.*, 719 μmol L^{-1} DOC for GB480). Integrated hydrogen concentrations for both GC574 (205.6 nmole/m^2) and GC767 (292.7 nmol m^{-2}) were elevated compared to the GB480 control (36.3 nmol m^{-2}) but lower than that of the GC699 control core (336.5 nmol m^{-2}; see Table 3.2).

On average, the sediments of GC574 and GC767 contain high amounts of organic matter, elevated particulate carbon, and low to moderate levels of nitrogen (see Table 3.4). Sediments at both sites contain >10% organic matter (12.41% OM for GC574 and between 11.58% and 13.04% for GC767), more than either of the known seep sites and similar to the control sites. This is perhaps indicative of low rates of microbial metabolism. Both sites contained an abundant percentage of carbon, over 4% for GC574 and between 3.38 and 3.72% for GC767. This combined with the relatively low nitrogen content of the sediments, generate C:N ratios of between 43 (GC767) and 49 (GC574), second only to the oil seep at GC600 (see Table 3.4). Maximum rates of sulfate reduction and AOM were low at these sites (see Figures 3.12, 3.10). There was no detectable sulfate reduction at GC767 and only pmol cm^{-3} d^{-1} levels of AOM (10 pmol cm^{-3} d^{-1}; see Table 3.5). Maximum sulfate reduction rates at GC574 were about 1 nmol cm^{-3} d^{-1} and maximum AOM was double that of GC767 (10 pmol cm^{-3} d^{-1}). Integrated SR rates are below detection for GC767 but considerably higher for GC574 at 52 µmol m^{-2} d^{-1} (see Table 3.2). Integrated AOM rates were higher for GC767 (0.9 µmol m^{-2} d^{-1} than either GC574 or the GB480 control site, but lower than rates reported for many other control and seep sites previously in the Gulf (see Table 3.2 [68]).

In general, sediments from GC767 were more active than those from GC574 (see Figures 3.12 and 3.10; see Tables 3.3 and 3.2, 3.5). Integrated NAPHOx rates for GC767 (173.7 nmol m^{-2} d^{-1}) were 2.6 times higher than those of the shallow control site at GB480 and 1.3 times higher than the GC699 (133 nmol m^{-2} d^{-1}) deep control. Integrated NAPHOx rates at GC574 (76.8 nmol m^{-2} d^{-1}) were similar to those of GB480 (65 nmol m^{-2} d^{-1}; see Table 3.2). While the integrated rates at GC767 were high compared to the controls, it is worth noting that the maximum NAPHOx rate for GC767 (1.48 pmol cm^{-3} d^{-1}) was nearly identical to that of GB480 (1.41 pmol cm^{-3} d^{-1}; see Figures 3.12 and 3.10). Integrated HEXOx rates were low at GC574 (3.2 pmol m^{-2} d^{-1}), lower even than the controls, and 21 times lower than integrated HEXOx rates at GC767 (68.3 pmol m^{-2} d^{-1}). Naphthalene oxidation rates for both sites remained relatively low in the first 20 cm but reached a maximum at 22 cm (see Figures 3.12 and 3.10). Maximum NAPHOx rates were nearly three times higher at GC767 (3.89 pmol cm^{-3} d^{-1}) than at GC574 (1.34 pmol cm^{-3} d^{-1}). As opposed to the trends in NAPHOx rates, profiles of HEXOx were generally highest within the uppermost 20 cm of each core. Here, maximum HEXOx rates were five times higher at GC767 (0.575 fmol cm^{-3} d^{-1}) than at GC574 (0.107 fmol cm^{-3} d^{-1}; see Figures 3.12 and 3.10).

3.4.3 ANTHROPOGENIC OIL IMPACTED SITES

Sediments from OC26 [69] and MC20 [22] were both impacted by previous anthropogenic releases of oil. The OC26 site received oil sedimentation for about a year [70] while the MC20 site has received semi-continuous oil sedimentation for almost 15 years [22]. The sediment in the cores were topped with a 2 – 5 cm cap of dark brown weathered oil layer that was called "oil fluff" because of its inherent loose-knit, easily disturbed character and the presence of small tar balls (S. Joye, visual observation). This layer was consistent with sedimented marine oil snow [71]. Below the oil fluff layer, sediments graded from brown and well-oxidized near the surface to gray clay-rich sediments below 10 cmbsf. Sediment porewaters were sulfate-rich (27 - 28 mM SO_4^{2-}), contained similar concentrations of methane as the control cores (3-5 µmol L^{-1} CH_4 average), and were sulfide-free (see Tables 3.2 and 3.3). The OC26 sediments contained the highest amount of both integrated porewater DOC (111.7 mmol m^{-2}) and hydrogen (3078 nmol m^{-2} H_2). In contrast, the MC20 sediments contained moderate amounts of integrated DOC (79.2 mmol m^{-2}), similar to values at GC185 and lower than the GC767 core. Integrated porewater alkalinity was elevated at MC20 (668.4 mmol m^{-2}), similar to values found at the GC600 and MC118 seep sites (see Table 3.2).

The average DOC values at MC20 (726 µmol L^{-1}) and OC26 (732 µmol L^{-1}) were the highest of any site, including the high DOC GB480 control site. The MC20 sediments contained the highest values for average (261 µmol L^{-1}) and integrated ammonium values (31.5 mmol m^{-2}) of any of the sites (see Tables 3.2 and 3.3). Both the MC20 and OC26 sites contained low average nitrate concentrations. Average dissolved inorganic nitrogen concentrations at MC20 was the highest of any site assessed (DIN 291 µmol L^{-1}; see Figure 3.6); this was not surprising since this site is near shore and receives terrigenous input from the Mississippi River, as well as oil sedimentation from the Taylor Energy Spill.

Sediments at MC20 and OC26 contained over 11% organic matter (see Table 3.4), more so than our sites of active seepage. Carbon content for OC26 (3.2% C) was and 1.95% C for MC20. Both sites contained the highest fraction of solid phase nitrogen of any of the sites under consideration (0.18% for OC26 and 0.22% for MC20). The MC20 site is in shallow water (see Figure 3.1, Table 3.1) and situated at the mouth of the Mississippi River, so the low carbon content could indicate a larger fraction of terrigenous clastics. The MC20 cores were the shortest of all the cores collected, in part due to the higher sand content; the efficiency of the Multiple Corer is significantly reduced in sandy sediments. The low percentage of carbon (1.95%) and high percentage of nitrogen (0.22%) at MC20 produced the lowest solid phase C:N ratio of all the sites, indicating that this site was not nitrogen limited.

Integrated AOM rates were either below detection (OC26) or very low (MC20) similar to those at the control sites (1 μmol m^{-2} d^{-1}; see Table 3.2). These rates are at least an order of magnitude lower than those observed elsewhere in the Gulf. Integrated rates of SR were higher in OC26 sediments (17.0 μmol m^{-2} d^{-1}) than in either the GB480 or GC699 control cores but lower than those found at GC574 or the seep sites GC185, GC600, and MC118. At MC20, however, integrated SR rates were 883 μmol m^{-2} d^{-1}, second only to integrated SR rates at MC118, our most active site (see Table 3.2). Maximum SR rates at MC20 were 6.5 nmol cm^{-3} d^{-1}, higher than maximum rates observed at GC600 (see Figures 3.15, 3.13). Maximum SR rates at OC26 were 0.65 nmol cm^{-3} d^{-1} (see Figure 3.14), significantly higher than those found in the GB480 (see Figure 3.8) and GC699 (see Figure 3.7) control sites, but only occurred within a thin lens at 5 cm depth, along the interface between sedimented Macondo oil and the previous sediment/seawater interface. Integrated rates of NAPHOx were moderate at OC26 (83.6 nmol m^{-2} d^{-1}), similar to rates observed at GC574, GB480, and GC600 (see Table 3.2). However, integrated rates of NAPHOx at MC20 were 282.5 nmol m^{-2} d^{-1}, higher than rates from any other site in this study, but MC118 (see Table 3.2). Similarly, integrated HEXOx rates were about 40 times higher at MC20 (42.4 nmol m^{-2} d^{-1}) than at OC26 (1.4 nmol m^{-2} d^{-1}). In the water column above MC20, rates of hexadecane oxidation were higher than naphthalene oxidation [51].

3.4.4 NATURAL SEEP SEDIMENTS

Generally speaking, the cores from active seep sites contained abundant sulfide, authigenic carbonates, bivalve shell hash, and have visible oil staining, though cores from MC118, GC185, and GC600 varied in physical appearance and geochemistry between sites. The MC118 core was the most active of any investigated during this study and showed activity levels typical of cores from active oil and gas seeps in the Gulf collected using visually targeted methods, *i.e.,* an ROV or submersible, [14, 68]. The sediments at MC118 were black to gray in color, heavily stained with oil, sulfidic (700 μmol L^{-1} H_2S max), methane-rich (max 2.7 μmol L^{-1} CH_4) and contained chunks of smooth carbonate (see Figure 3.2). In contrast, the sediments at both GC600 and GC185 resembled those of our control sediments: well-oxidized, brown to gray in color, with no visible oil staining, low sulfide (GC600 core only), and little methane (see Table 3.2 and Figure 3.11, 3.15). Of all the sites considered for this study, only GC600 (262 μmol L^{-1} max) and MC118 (702 μmol L^{-1} max) contained appreciable sulfide (see Tables 3.2, 3.3), and the observed values that were low compared to those reported at these sites in the past (see discussion below).

Porewater DOC, DIC, and alkalinity were variable across the seep sites. Integrated porewater DOC concentrations at MC118 (52.3 mmol m^{-2}) and GC600 (27.6 millimol/m^2) were either comparable to or lower than those of the control sites (see Table 3.2). Average DOC concentrations at MC118 (637 μmol L^{-1}), GC600 (265 μmol L^{-1}) and GC185 (567 μmol L^{-1}) were lower than values at control sites (see Table 3.3). Compared to MC118 and GC600, the sediments of GC185 contained higher integrated porewater DOC concentrations (74.3 mmol m^{-2}), but the lowest overall average DOC of the seep sites (567 μmol L^{-1} DOC; see Table 3.3). Given the high methane content of MC118 sediments (59.0 μmol m^{-2}; 940 μmol L^{-1} average CH_4; see Tables 3.2, 3.3), it is unsurprising that porewater alkalinity at MC118 (880.9 mmol m^{-2}) was greater than at any other site assessed here. Integrated alkalinity at GC600 was also elevated (625.1 mmol m^{-2}) compared to the control sites, but was similar to values at MC20 (see Table 3.2). Integrated alkalinity at GC185 was 350.6 mmol m^{-2}, similar to values observed in OC26 sediments but higher than that of the GC699 control site. Average DIC values of 11.4 mmol L^{-1} at MC118 were the highest observed at any of the sites, indicative of microbial oxidation of organic carbon. The DIC values at GC600 (3.4 mmol L^{-1} 3.4 mM) are less dramatic than those of MC118, but still suggest microbial oxidation within the sediments. The DIC values of GC185 (2.0 mmol L^{-1} 2.0 mM) are comparable to concentrations found at other Green Canyon sites such as GC767, GC574, and the GC699 control (see Table 3.3).

The sediments of all three seep sites contained elevated concentrations of ammonium and phosphate and were depleted in nitrate. Among the seep sites, the sediments of MC118 contained the highest integrated ammonium (15.1 mmol m^{-2}), the highest average ammonium (165 µmol L^{-1}), the highest concentration of nitrate (16 µmol L^{-1}), and was the only site with significant nitrite (6 µmol L^{-1}; see Table 3.3 and Figure 3.4). Sediments at the GC600 site contained less overall ammonium (76 µmol L^{-1} average NH_4^+; 79 µmol L^{-1} average DIN) than MC118 and MC20, but more than any of the remaining sites (see Table 3.3). Average ammonium values at GC185 (47 µmol L^{-1} average NH_4^+) were double the GB480 control, triple that of the GC699 control, but similar to those of GC767 (see Table 3.3). Integrated hydrogen concentrations were 168.8 nmol m^{-2} for MC118, 89.2 nmol m^{-2} for GC600, and 49.2 nmol m^{-2} for GC185 (see Table 3.2). These values are significantly lower than every other site but the GB480 control, likely indicating a decreased roll for fermentation at the active seep sites ([60]).

The percentage by weight of carbon and nitrogen in the seep site sediments was variable (see Table 3.4). The active seep sediments at MC118 contained the highest proportion of carbon (5.04 wt%C) of all the sites in this study, but similar amounts of nitrogen (0.13 wt%N) as the GB480 control site (see Table 3.4). The sediments at MC118 contained about 10.5 wt% organic matter, similar to GC185 (9.95 wt%). Sediments at GC600 contained the lowest fraction of organic matter of any of the sites (7.81 wt%; see Table 3.4). In general, the amount of organic matter in these seep site sediments were lower than nearly every other site except for the GC699 control site. The C:N ratios of these sediments were well above Redfield ratios, 15.51 for GC185, 62.47 for GC600 and 38.54 for MC118, indicating these sediments are probably nitrogen limited (see Table 3.4).

The highest rates of microbial activity by far were observed at MC118 (see Table 3.2). The prolific MC118 seep had the highest SR rates (19.12 mmol m^{-2} d^{-1}) of the study. The MC118 sediments had the highest NAPHOx rates (921.1 nmol m^{-2} d^{-1}), highest HEXOx rates (85.0 pmol m^{-2} d^{-1}), and was the only site with appreciable AOM rates (556.6 µmol m^{-2} d^{-1}; see Table 3.2; Figures 3.4 and 3.5). The cumulative SR rate at MC118 was at least 21 times that of the next highest rate (MC20), and AOM rate at MC118 was over 500 times that of any other site (see Table 3.2). Such high rates of microbial activity at MC118 were not unusual and our estimates broadly align with those of other studies ([20]). In contrast, the AOM rates at GC185 and GC600 were indistinguishable from any other site in this study (see Table 3.2), and in both cases were lower than those in our control sediments (GB480 and GC699; see Table 3.2).

Sulfate reduction rates at GC600 and GC185 were 237.2 μmol m^{-2} d^{-1} and 80.4 μmol m^{-2} d^{-1}, respectively, higher than all other sites but MC118 and MC20 (see Table 3.2). However, these rates are much lower than those observed at these locations previously [14, 52]. At GC185, NAPHOx rates were 132.9 nmol m^{-2} d^{-1} and HEXOx rates were 18.2 pmol m^{-2} d^{-1} (see Table 3.2). NAPHOx rates were 84.7 nmol m^{-2} d^{-1} at GC600, similar to those at the low activity OC26 site (see Table 3.2). Hexadecane oxidation rates were not available for GC600.

3.4.5 HYDROCARBONS

Table 6 shows the amount of total petroleum hydrocarbons (TPH) extracted from raw sediments using toluene and methanol (90:10 mix), pooled across specific depth horizons. Sediments from the two most active seep sites, GC600 and MC118, contained the greatest concentrations of extractable hydrocarbons (see Table 6). Sediments at MC118 contained the highest fraction of TPH (1592 μg g^{-1} wet sediment) and was also the only core to have visible oil staining. There was no noticeable oil staining on the GC600 core but sediments still contained about 40% the total hydrocarbon concentrations (625 μg g^{-1} wet sediment) of MC118.

Hydrocarbon concentrations in excess of 1000 μg g^{-1} have been reported at oily MC118 sites previously ([20]), but gassy sites with no visible oil within the same site contained a much lower concentration of hydrocarbons (approx 120 μg g^{-1} wet sediment; [20]). The hydrocarbon concentration at GC185 (176 μg g^{-1} wet sediment) was similar to the amount extracted from MC20 (187 μg g^{-1} wet sediment) and the GC699 control sediments (115 μg g^{-1} wet sediment). Sediments at OC26 contained the least amount of extractable petroleum hydrocarbons (5.9 μg g^{-1} wet sediment), only about 20% that of the GB480 control core (28.9 μg g^{-1} wet sediment). Surprisingly, GC767 sediments contained nearly twice the amount of extractable hydrocarbons (340 μg g^{-1}) than that of GC185 seep sediments (176 μg g^{-1}; see Table 6). The GB480 and GC699 controls had a hydrocarbon concentration of 29 μg g^{-1} and 117 μg g^{-1}, respectively (see Table 6).

Site	Core ID	TPH
GB480	EN559-S18-E07 (3–20 cm)	28.9
GC185	EN586-S02-E13 (6–20 cm)	176.4
GC574	EN586-S15-E08 (3–20 cm)	51.2
GC600	EN586-S18-E11 (0–15 cm)	625.6
GC699	EN586-S07-E07 (0–20 cm)	114.5
GC767	EN559-S25-E03 (0–20 cm)	340.1
MC118	EN586-S20-E03 (0–20 cm)	1592.3
OC26	EN586-S12-E07 (0–20 cm)	5.9
MC20	EN586-S11-E04 (0–20 cm)	186.9

Table 3.6: Total petroleum hydrocarbons ($\mu g\, g^{-1}$) from toluene:methanol sediments extracts (90:10) pooled along select depth horizons. Sediment depth range (cm) shown in parenthesis.

Relative to GC600 crude oil, extracts from seep sites show a chromatographic shift in the low molecular weight n-alkanes with short elution times ($t < 15$ minutes) toward higher carbon numbers with longer elution times and higher column temperatures (between 5 and 10 minutes; see Figure 3.17). Both GC600 and MC118 chromatograms display an unresolved complex mixture (UCM) at greater than 25 minutes (see Figure 3.17). The disappearance of n-alkanes and the appearance of UCMs was indicative of subsurface weathering processes ([4, 6, 39]). As indicated by the elevated concentration of extractable hydrocarbons shown in Table 3.6 (340 $\mu g\, g^{-1}$ wet sediment), GC767 extracts contained weathered petroleum hydrocarbons, similar to the chromatographic signature of GC600 extracts. Sediments were extracted with a mixture of toluene and methanol - rather than with a mixture containing dichloromethane - for downstream Fourier Transform Ion Cyclotron Resonance Mass Spectrometry. This extraction is not ideal for GC-FID analysis and is reflected in the relatively flat chromatograms.

3.5 DISCUSSION

This work aimed to measure rates of sulfate reduction, methane oxidation, and hydrocarbon oxidation directly at sites spanning a spectrum of hydrocarbon influence across the Northern Gulf of Mexico. As noted previously, the Gulf if home to over a thousand natural hydrocarbon seeps that drive a large natural flux of oil into the Gulf system ($2.5–9.4 \times 1 \times 10^4$ m^3 of oil yr^{-1} [72–74]). Previous work has shown that in the Gulf of Mexico, sulfate reduction and AOM are loosely coupled, pointing to the role of other low molecular weight alkanes [72] and oil [74] in fueling sulfate reduction, though the latter study did not quantify rates of oil oxidation directly.

3.5.1 ASSESSING DEGRADATION RATES FOR COMPLEX HYDROCARBONS

Advancing the understanding of the fate of hydrocarbons at cold seeps has been a focus of the scientific community for decades [10]. Sulfate reduction is a dominant electron acceptor in marine sediments [75] because of its high abundance in seawater [76] and because a diverse array of sulfide oxidizing bacteria are able to recycle the sulfide produced by sulfate reduction (Pellerin et al. 2015), promoting and accelerating sulfate reduction in organic rich sediments. Measuring sulfate reduction rates is straightforward using ^{35}S sulfate tracers [75], so many studies have focused on quantifying sulfate reduction rates and then inferring the cooperative metabolism of hydrocarbon oxidizing microorganisms. For example, [31] quantified rates of sulfate reduction and used these data to estimate rates of anaerobic methane oxidation, assuming 1:1 stoichiometry of the two processes. However, other studies have shown that sulfate reduction is coupled largely to the oxidation of non-methane hydrocarbons under some circumstances [52]. There is no straightforward way to translate sulfate reduction rates to rates of anaerobic methane oxidation or to rates of non-methane hydrocarbon oxidation [10].

In fact, determining the oxidation rates of oil components is inherently difficult. Most hydrocarbons have high octanol-water partition coefficients (K_{ow}), meaning that they readily partition into organic phases and have poor solubility in water. Thus, in the natural world, hydrocarbons partition largely in the organic (oil) phase and only a small fraction is available in aqueous solution.

Solubility of hydrocarbons may thus play a key role in limiting microbial hydrocarbon oxidation in the environment [77]; many hydrocarbon degraders thrive at the organic-aqueous interface where hydrocarbons steadily exchange into the aqueous realm. The poor solubility of hydrocarbons – especially the saturated hydrocarbons, like hexadecane – can hinder their biodegradation and complicate assessment of biodegradation rates. Given these inherent considerations, the most common approach for assessing hydrocarbon breakdown potential has been to amend sediments with high hydrocarbon concentrations and then to track the change in bulk concentration over time to estimate biodegradation rates [29, 78, 79].

There are some fundamental problems with such approaches – most importantly, the concentrations of added hydrocarbons are often extreme – g/L levels [29]. In such experiments, an inert carrier, such as 2,2,4,4,6,8,8-heptamethylnonane (HMN) is sometimes used to constantly source hydrocarbons to the aqueous phase. It is unlikely that this is a reasonable representation of background environmental conditions. In the natural environment, polar compounds like hexadecane are partitioned in the organic (oil) phase. As oil moves through sediments, hexadecane may slowly be exchanged with the surrounding aqueous phase. However, the high concentrations used in enrichment experiments [29] are poor proxies for this natural process and almost certainly generate higher dose regimes for the microbial populations.

Rates of hexadecane oxidation determined in such experiments - 10's to 100's nmol cm^{-3} d^{-1} - likely overestimate in situ environmental rates, given the high loading rates of hydrocarbons in those experiments (11.32 g L^{-1}; the solubility limit is 177 pmol L^{-1}). We took a different approach that aimed to obtain more realistic rates under environmental conditions. We selected two hydrocarbons – naphthalene and hexadecane – that are representative of two important hydrocarbon classes, the aromatics and saturates. We conducted ex situ hydrocarbon oxidation rate assays at in situ pressure and temperature in parallel with rates of sulfate reduction and AOM, so that we could evaluate how hydrocarbons contributed to anaerobic metabolism in these sediments.

3.5.2 Spatial variability in biogeochemical signatures

Given the widespread nature of hydrocarbon seepage in the Gulf of Mexico, it is extremely difficult to identify a control site that is not impacted by seepage to some degree. At the same time, it is likewise difficult to capture seepage signatures when sampling "blind", *i.e.,* with a multiple corer. As such, most of the sediment cores recovered during the two cruises were not heavily impacted by hydrocarbons, despite working at several sites, like GC600, that are known for active seepage and from which sulfidic, gassy, oily, and very active cores have been recovered with visually-guided sampling via submersible or ROV (see Chapter 4). Nonetheless, this collection of cores offers an opportunity to assess the potential for naphthalene and hexadecane activity across a wide range of habitats in the Gulf of Mexico, including so-called controls that lie some distance from known sites of hydrocarbon seepage.

Sediments from prolific natural oil seeps – GC600 and MC118 – contained the highest amounts of total petroleum hydrocarbons (TPH) (see Table 3.6). Sediments from MC118 contained 1592 μg TPH g^{-1} wet sediment. Even though the GC600 core had no visible oil staining, it contained 625 μg TPH g^{-1} wet sediment. TPH concentrations in excess of 1000 μg g^{-1} are not unusual for cores with visible oil staining. Hydrocarbon concentrations at GC185 and MC20 (176 and 187 μg TPH g^{-1} wet sediment, respectively) were similar, and the "control" site GC699 also contained a surprising amount of TPH (115 ug TPH/g wet sediment). The lowest amount of TPH was observed at OC26, but is should be noted that this value was for the bulk core and did not reflect concentrations in the oil fluff layer, which are known to be elevated compared to deeper sediments. The GB480 control core (28.9 μg TPH g^{-1} wet sediment) contained the second lowest amount of TPH, underscoring that this site was more of a true control than GC699 (see below). The biggest surprise in TPH content was GC767, which contained nearly twice the amount of TPH (340 μg g^{-1}) than that the GC185 natural seep site (176 μg g^{-1}; see Table 3.6). The TPH data show that all of the sites are impacted by hydrocarbons, albeit to differing degrees. Relative to GC600 reservoir oil, oil extracts from these sites show a shifts consistent with microbial weathering, including the disappearance of alkanes and the appearance of unresolved complex mixture

(UCM; at *e.g.,*, GC600 and MC118). Notably, the MC118 TPH is most similar to unweathered oil, reflecting a higher flux of hydrocarbons through this site.

Sediments from control sites exhibited all of the characteristics of deepwater marine sediments: brown to gray color, oxidized appearance and no detectable sulfide, and little to no methane. Nutrient and alkalinity inventories were low (Table 3.2), reflecting low rates of metabolism. Inventories of DOC were between 50-60 mmol m^{-2}, reflecting active fermentation in the sediments. The sedimentation rates offshore in the Gulf are around 6 cm/1000 years [80]; such a low sedimentation rate supports only modest rates of sediment metabolism [52]. However, during the Deepwater Horizon oil spill it became clear that some of the discharged oil was returned to the seafloor as 'sedimented oil' [70, 71, 81]. Oil sedimentation also occurs at natural seeps, with some of the discharged oil returning to the seafloor as oil floc [81].

The occurrence of natural seepage and the importance of naturally sedimented oil is important in the context of interpreting the particulate carbon inventories at the control sites. The content of organic carbon varied substantially between the control sites, while the organic nitrogen was the same: GB480 contained 2.4% C and 0.07% N and GC699 contained 4.7% C and 0.07% N (Table 3.2) and it is possible that oil discharged from lease block GC600 later sedimented naturally to the seabed, contributing excess sediment organic carbon relative to organic nitrogen at GC699. The GC600 site is roughly 10 km west of GC699. The GC699 control core pore fluids also contained higher than expected dissolved hydrogen 336.5 nmol m^{-2}; see Table 3.2, which could suggest the presence of more labile organic matter at this site. A hydrocarbon source to the particulate organic carbon pool could explain both observations, particularly since organic carbon is elevated but organic nitrogen is not.

The sites GC574 and GC767 were selected for inclusion in this study based on the presence of persistent oil slicks (I. MacDonald, pers. com.), suggesting at least intermittent oil seepage at the sites. However, GC574 and GC767 sediments looked similar to sediments from control sites and contained oxidized sediments with no obvious visual marks of seepage (*i.e.,*, there was no oil staining). Sediment pore fluids from these sites showed no sulfate depletion, contained only a few um (15 μmol L^{-1} max) methane, and were sulfide free. Sediment nitrogen inventories at these sites were generally higher than the controls and, in particular, the GC767 sediments more substantially more DOC (97 mmol m^{-2}) than GC574 or the control sites (see Table 3.2). Integrated pore water hydrogen concentrations at these sites (GC574 = 205.6 nmol m^{-2} and GC767 = 292.7 nmol m^{-2}) were elevated significantly compared to the GB480 control (36.3 nmol m^{-2}). The elevated levels of organic matter in these sediments (12.41% OM for GC574 and between up to 13.04% for GC767) were among the highest documented in the data set and the percentage of sedimentary organic carbon, over 4% for GC574 and between up to 3.72% for GC767 coupled with the low nitrogen content suggest hydrocarbon input (see Table 3.4).

The discovery of marine "oil snow" and oil snow "sedimentation" was one of the most important scientific advances resulting from the Deepwater Horizon oil spill [70, 71, 81, 82]). Two of the sites included in this study were impacted by anthropogenic oil sedimentation; there are important differences between the sites. The OC26 site is about 2 miles from the epicenter of the Deepwater Horizon oil spill. This area received extensive sedimentation for more than a year as a direct result of the oil spill [70]. The MC20 site is closer to shore, more shallow, and is impacted by Mississippi River discharge. The Taylor Energy oil spill began in the aftermath of Hurricane Ivan, which toppled a production platform at the site. Extensive oil discharge occurred between 2004 and 2019 [22].

Sediments at both OC26 and MC20 were marked by visible 2 – 5 cm 'oil fluff' layers [71]. Sediments from both MC20 and OC26 were organic rich, containing >11% organic matter (see 3.4), 3.2% (OC26) and 1.95% C (MC20) organic carbon, and roughly 0.2% organic nitrogen (0.18% at OC26, 0.22% at MC20). The proximity of the MC20 site to the mouth of the Mississippi River likely accounts for the slightly lower carbon content, which likely reflects terrigenous clastics. The high organic nitrogen content (0.22%) resulted in a lower C:N ratio and indicated that this site was nitrogen replete. This was a stark contrast to all of the other sites, which were nitrogen limited.

Without the oil fluff layer, the sediments resembled normal offshore sediments, being brown and oxidized in color with pore fluids that were sulfate-rich and methane-poor. Clearly these sites are not typically impacted by seepage from depth in the sediment column (Tables 3.2, 3.3). However, oil sedimentation led to extremely high sediment inventories of DOC (111.7 mmol m^{-2}) and hydrogen (3078 nmol m^{-2} H_2) at OC26; this signature likely reflected the fermentation of deposited Macondo oil (see below). The retrieved MC20 sediments were different - they contained only modest amounts of DOC (79.2 mmol m^{-2}) but showed higher integrated porewater alkalinity (668.4 mmol m^{-2}) (see Table 3.2). The high alkalinity levels at this sites may reflect remineralization of sedimented oil. Since MC20 is a much shallower site (about 1400 m shallower than OC26), oxidation of oil components in the water column during sedimentation was less extensive, meaning that the pool of sedimented oil at this site could be more labile.

Some of the cores recovered from areas known for persistent natural seepage contained hallmark signatures of oil discharge, including, abundant sulfide, authigenic carbonates, shell hash, and visible oil staining, though the intensity of the seep signature varied across sites. The MC118 site is one of the most consistently active natural seeps in the Gulf of Mexico and may well be the most active seep field east of the Mississippi. The cores recovered from MC118 had the strongest seep signature and were the most active (see below) of all those sampled during this study: MC118 sediments were black to gray, heavily oil stained, contained carbonates, and were sulfide and methane rich (see Figure 3.2). The sediments at both GC600 and GC185 lacked strong seepage signatures and instead resembled control cores. Those cores were oxidized, brown, lacked oil staining as well as highly elevated sulfide and methane (see Table 3.2).

The amount of organic matter and of organic carbon and nitrogen in the solid phase varied in seep sediments (Table 3.4). The elevated C:N ratios above that expected from the Redfield ratio indicated nitrogen limitation at the seep sites (Table 3.4). This is not surprising and has been reported previously [52]. Understanding the source of nutrients fueling microbial activity at seeps remains an important line of inquiry. Inventories of DOC were low at MC118 (52.3 mmol m^{-2}) and GC600 (27.6 mmol m^{-2}) (see Table 3.2) and only slightly higher at GC185 (74.3 mmol m^{-2}). Average DOC concentrations at all sites, includeing the seep sites of MC118 and GC600 were below 1 mmol L^{-1} (see Figure 3.3). Such low DOC inventories were not expected from active seeps. Porewater DOC at seep sites is commonly influenced by deeply-sourced, DOC-rich fluids, especially those in the Gulf, as indicated by previous studies from oil and gas impacted sites such as GC185 [52] and MC118 [20]. Porewater alkalinity at MC118 (880.9 mmol m^{-2}) was greater than at any other site assessed here and values of integrated alkalinity at GC600 were also elevated (625.1 mmol m^{-2}); this elevated alkalinity at GC600 could reflect a signature of a previous active period. Integrated alkalinity at GC185 (350.6 mmol m^{-2}) was similar to values at OC26 and higher than the GC699. Integrated hydrogen concentrations were lower at the active seep sites compared to the other sites (Table 3.2), likely indicating a dominance of terminal metabolism instead of fermentation ([60]).

Biogeochemical signatures at these sites are consistent with intermittent hydrocarbon inputs at all sites except GB480. All offshore sites were nitrogen limited; only the nearshore (MC20) site was characterized by nitrogen replete conditions. Most sites had biogeochemical signatures consistent with low rates of terminal metabolism, but MC118 and GC600 clearly support high rates of metabolism (though the GC600 site was not so active at the time of sampling). The importance of fermentation at some of the sites (OC26, GC767) suggests consistent aspects of hydrocarbon degradation that differ from traditional expectations (see below).

3.5.3 Microbial Activity

Rates of microbial sulfate reduction were undetectable at GB480 and GC767 and activity was very low (5 μmol m^{-2}) at GC699 and GC574. Rates of AOM were similarly low at these sites. In the absence of hydrocarbon, DOC and hydrogen data, both GC767 and GC574 could be mistaken for a control site (Table 3.2). Sulfate reduction activity was a poor indicator of hydrocarbon – methane, naphthalene, or hexadecane – oxidation at these sites. Hexadecane and naphthalene oxidation rates were detectable, but low, at both GC699 and GB480. It is possible that this activity may have been coupled to aerobic metabolism, rather than anaerobic metabolisms like sulfate reduction, given the bulk characteristics of the sediments. At GC767, substantial rates of naphthalene and hexadecane oxidation occurred in the absence of sulfate reduction.

Rates of naphthalene oxidation consistently exceeded rates of hexadecane oxidation. This pattern is almost certainly driven by differences in solubility, and hence bioavailability. Naphthalene is much more soluble than hexadecane and this increased availability results in its more rapid consumption. It appears that solubility is the main factor limiting and regulating hydrocarbon oxidation rates at these sites and the low estimated rates lie in stark contrast to the exceedingly high rates presented in recent papers (*e.g.,*, Shin et al. 2019 [29]). Rates of hydrocarbon oxidation determined under such extreme and enriched conditions do not at all represent the patterns present in nature (see below).

Of these four offshore, low activity sites, the most interesting observation with respect to hydrocarbon oxidation was the possibility that hexadecane oxidation is achieved through methanogenesis [83]. At GC699, there is a deep increase in hexadecane oxidation that correlates with increased methane concentrations. At GC767, integrated hexadecane oxidation rates were high ($68.3\,\mathrm{pmol\,m^{-2}\,d^{-1}}$) and showed a similar loosely positive relationship to methane concentration at depth. This observation is extremely interesting since this occurred in sulfate-rich sediments that was documented to lack sulfate reduction activity. As oil seeps upward through sediments from deep reservoirs, it encounters methanogenic sediments first. Crude oil degradation via methanogenesis is widely recognized in oil reservoirs, leading to the removal of n-alkanes and the production of dry gas [6]. Similar processes almost certainly in seep-impacted sediments, though this process is not well studied or well understood in those habitats [83]. Exploring the role of methanogenic alkane metabolism at natural seeps is an important avenue for future research.

Rates of SR and AOM at the sites impacted by anthropogenic oil, OC26 and MC20, were low compared to the control sites assessed here and to other sites in the Gulf. Though integrated rates of SR at OC26 ($17.0\,\mathrm{\mu mol\,m^{-2}\,d^{-1}}$) were higher than those at GB480 or GC699 they were far lower than those present at MC20 (see below). Rates of SR at OC26 are low given the high carbon content of those sediments, consistent with other activity measurements since 2010, in the wake of the Deepwater Horizon oil spill (Storo et al. in preparation).

Maximum SR rates at OC26 – 0.65 nmol cm^{-3} d^{-1} – occurred in a thin layer at 5 cm depth, along the interface between sedimented Macondo oil and the original sediment/seawater interface (see Figure 3.14). The lack of SR activity in the sedimented oil layer could stem from an ill-equipped microbial community (Storo et al. in preparation), from inhibition due the chemical dispersant load in this layer, or because the carbon in this layer is recalcitrant. Despite low rates of SR, the OC26 site had the highest average and integrated DOC and H2 concentrations of any of the sites explored in this study, suggesting robust rates of fermentation at this site but inefficient consumption of this DOC via terminal metabolism.

The rates of SR at MC20 (883 µmol m^{-2} d^{-1}) were second only to integrated SR rates at MC118, the most active site (Table 3.2). In fact, maximum SR rates at MC20 were higher than those observed at GC600 (see Figures 3.16, 3.15). The fact that sediments at MC20 supported such high SR rates suggests that sedimented oil at that site is inherently bioavailable. This difference could stem from a lack of chemical dispersant residue in MC20 sediments, because the MC20 site is much more shallow and more nutrient rich, or it could reflect the substantially higher hydrocarbon load at MC20 compared to OC26.

In fact, integrated rates of NAPHOx – 282.5 nmol m^{-2} d^{-1} were extremely high at MC20. The only site with higher activity was MC118 (Table 3.2, see below). Likewise, integrated HEXOx rates were 40 times higher at MC20 (42.4 nmol m^{-2} d^{-1}) than OC26 (1.4 nmol m^{-2} d^{-1}). Clearly the microbial community at MC20, fueled by a substantial hydrocarbon load that exhibits clear signs of biological weathering, is well equipped to oxidize hydrocarbons. The poor quality and recalcitrant nature of hydrocarbons at OC26 compared to MC20 appear to be unable to stimulate a response in the anaerobic microbial community with respect to SR and hydrocarbon oxidation.

Unsurprisingly, sediments with prior and sustained oil exposure display higher rates of hydrocarbon oxidation. In this respect, the observations of Shin et al. (2019 [29]) warrants more discussion. Shin et al. estimated hydrocarbon oxidation rates from sulfide accumulation in enrichment slurries that were amended with phenanthrene (8.91 g L^{-1}) or hexadecane (11.32 g L^{-1}). They observed nearly identical rates of hexadecane and phenanthrene oxidation (ca. 50 nmol cm^{-3} d^{-1}) in sediment slurries constructed from Gulf of Mexico sediments. In their experiments, both substrates were provided to sediment microbial communities in excess using an inert carrier, HMN. Furthermore, slurries were incubated at 30 °C. Their samples were collected from the 56 m deep site about 90 miles NW of the Deepwater Horizon wellhead (there was no evidence for oil sedimentation at this site when the sediments were collected in 2013). Field temperatures for the site were not provided but [84] report bottom water temperatures of 20 °C at 60 m along the Louisiana shelf, substantially lower than those used in the incubations of Shin et al (2019 [29]).

Using the HMN delivery system, the microbial population is constantly supplied with hydrocarbon substrates. Under in situ conditions, hydrocarbon bioavailability is almost certainly limited. The high incubation temperatures (in Celsius) used by Shin et al. (2019) [29] are about 7.5 times higher than in situ temperatures at our deepwater sites and about double the bottom water temperature of our most shallow site. The high temperatures used in the Shin et al. experiments almost certainly elevated their hydrocarbon oxidation rates. If we compare the rates of Shin et al. (50 nmol cm^{-3} d^{-1}) to the rates at our most similar site (MC20, pmol cm^{-3} d^{-1} or less), it is clear that while the excessive concentrations used in their experiments allowed them to enrich organisms responsible for hydrocarbon metabolism, the reported rates may be unrealistic.

Sulfate reduction rates at MC118 were the highest of any site (19.12 mmol m^{-2} d^{-1}; see Table 3.2). The MC118 site also had the highest rates of AOM (565.6 µmol m^{-2} d^{-1}), naphthalene oxidation (921.1 nmol m^{-2} d^{-1}), and hexadecane oxidaiton (85 pmol m^{-2} d^{-1}; see Table 3.2). The level of activity observed at MC118 is consistent with previous studies ([20]). Activity at the other natural seep sites was lower than anticipated (Table 3.2). Even though the integrated sulfate reduction rates at GC600 (237.2 µmol m^{-2} d^{-1}) and GC185 (80.4 µmol m^{-2} d^{-1}) were higher than the control and offshore sites (except MC118 and MC20) (Table 3.2), rates were far below the extremely high levels of activity published previously ([14, 52]). Both the GC600 ([14]) and GC185 ([52]) sites host highly active oil and gas seeps, but seepage is known to be extremely patchy. Past studies show that rates of AOM and SR at these sites [14, 20] are comparable to, or higher than, the rates observed at MC118 in this study. Unfortunately, the sediments recovered from GC600 and GC185 in this study were well-oxidized, methane-poor, only mildly sulfidic, and contained no visible oil. These observations combined with the comparatively low rates of AOM and hydrocarbon oxidation (see Table 3.2) at both sites points to the fact that we missed locations of active seepage with the multiple core.

3.5.4 Conclusions

We report the first apparent degredation rates of microbial naphthalene and hexadecane oxidation in Gulf of Mexico sediments in the context of biogeochemical signatures and of rates of sulfate reduction and anaerobic oxidation rates of methane. Our initial hypotheses that rates of hydrocarbon oxidation would correlate - or at least scale to - rates of sulfate reduction was not supported (see Figures 3.18 and 3.19). Sulfate reduction rates did not broadly correlate to either HEXOx or NAPHOx across site types, but observed the highest rates of sulfate reduction concomitantly to the highest rates of NAPHOx and HEXOx at the extremely active, oil- and gas-charged MC118 site. This suggests involvement from sulfate reducing communities at a site already primed for hydrocarbon oxidation due to the presence of oil. Our secondary hypothesis, that n-alkanes would be degraded faster than PAHs, was also disproven. Though alkane degradation yields more energy than PAH degradation, the inherent insolubility of n-alkanes like hexadecane limits their biodegradation substantially. The idea that sites impacted by oil and gas would express the highest rates of activity was supported by our observations. We discovered a surprising connection between sedimented oil and microbial activity at the seabed at sites impacted by both natural oil and anthropogenic oil sedimentation. The amount and relative reactivity of sedimented oil determines the relative extent to which the material stimulates anerobic terminal metabolism. Finally, some of these data (GC767) provides tantalizing evidence of the importance of fermentative (methanogenic) metabolism of oil in the presence of sulfate. Further assessment of the potential for methanogenic metabolism of oil in Gulf of Mexico sediments is warranted.

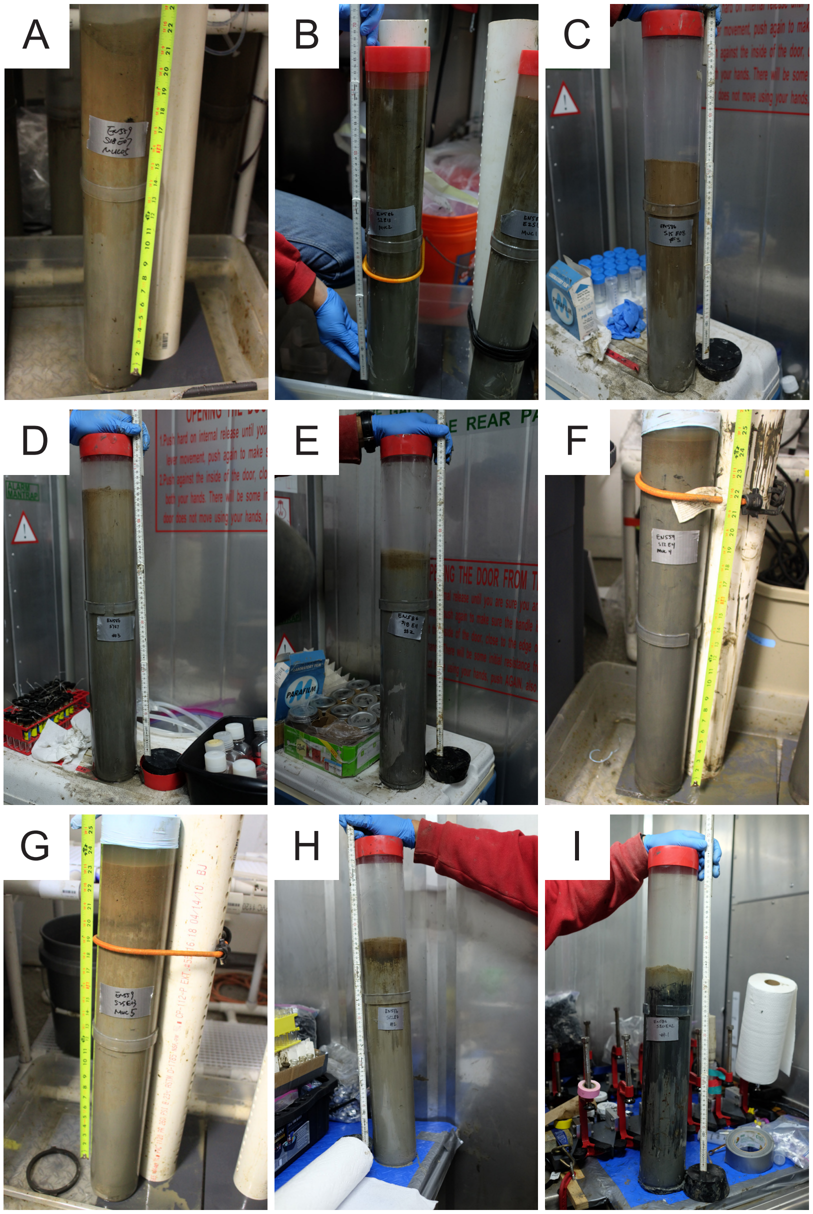

Figure 3.2: Core photographs at A) GB485 (EN559), B) GC185 (EN586), C) GC574 (EN586), D) GC699 (EN586), E) GC600 (EN586), F) MC20 (EN559), G) GC767 (EN559), H) OC26 (EN586), and I) MC118 (EN586).

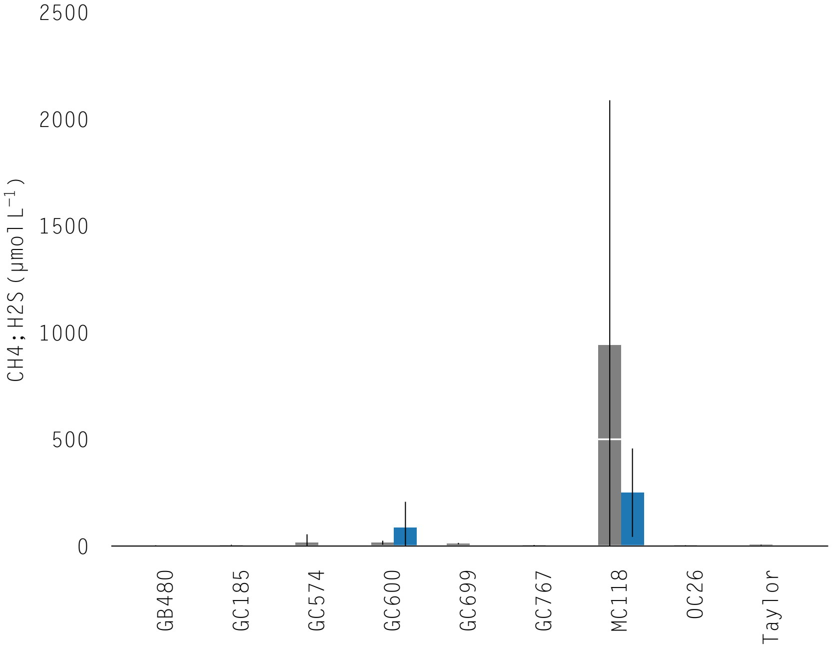

Figure 3.3: Average methane (gray) and sulfide (blue) concentrations, by site. Error bars represent one standard deviation

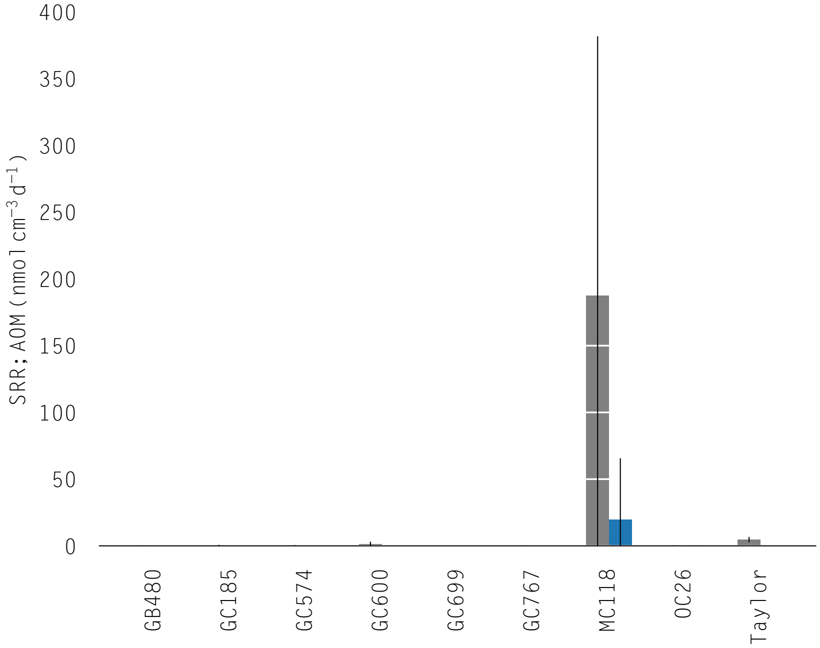

Figure 3.4: Average sulfate reduction (gray) and anaerobic oxidation of methane rates (blue), by site. Error bars represent one standard deviation.

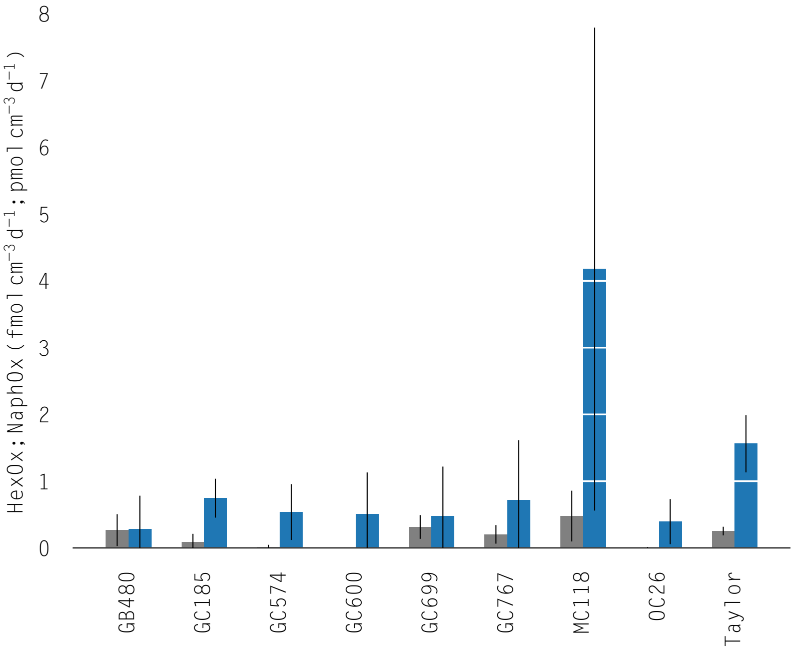

Figure 3.5: Average hexadecane (gray) and naphthalene (blue) oxidation rates, by site. Error bars represent one standard deviation.

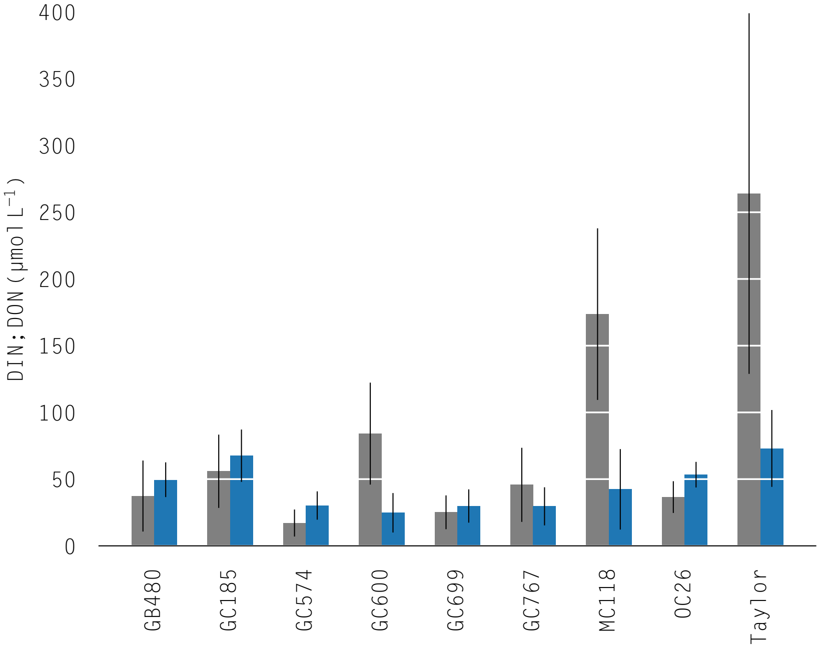

Figure 3.6: Average dissolved inorganic (gray) and organic (blue) nitrogen, by site. Error bars represent one standard deviation.

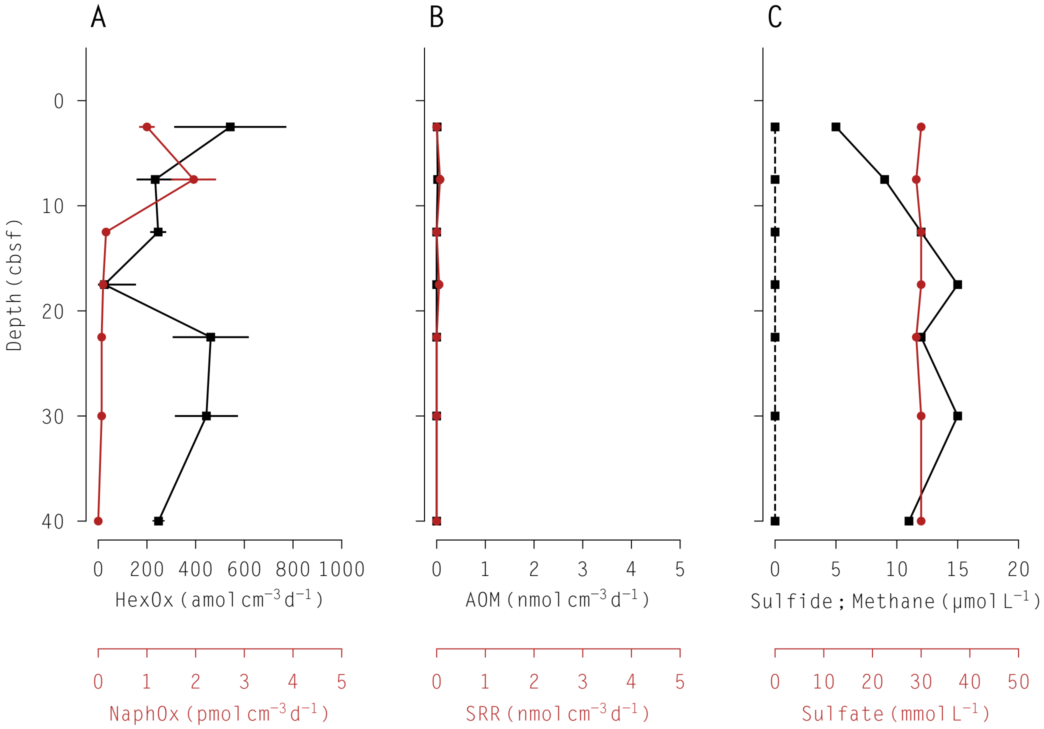

Figure 3.7: Sediment depth profiles of A) HexOx (black), NaphOx (red), B) SRR (black), AOM (red), C) sulfide (dashed black), methane (solid black), and sulfate (red), Gulf of Mexico, lease block GC699. Error bars represent standard error about the mean.

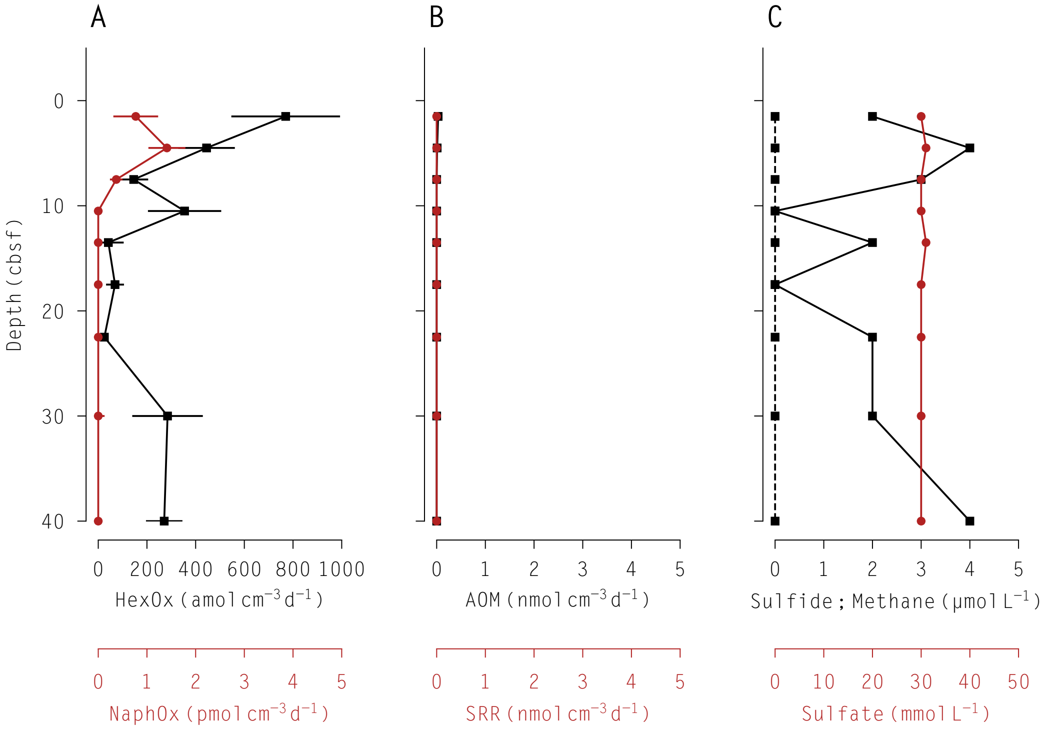

Figure 3.8: Sediment depth profiles of A) HexOx (black), NaphOx (red), B) SRR (black), AOM (red), C) sulfide (dashed black), methane (solid black), and sulfate (red), Gulf of Mexico, lease block GB480. Error bars represent standard error about the mean.

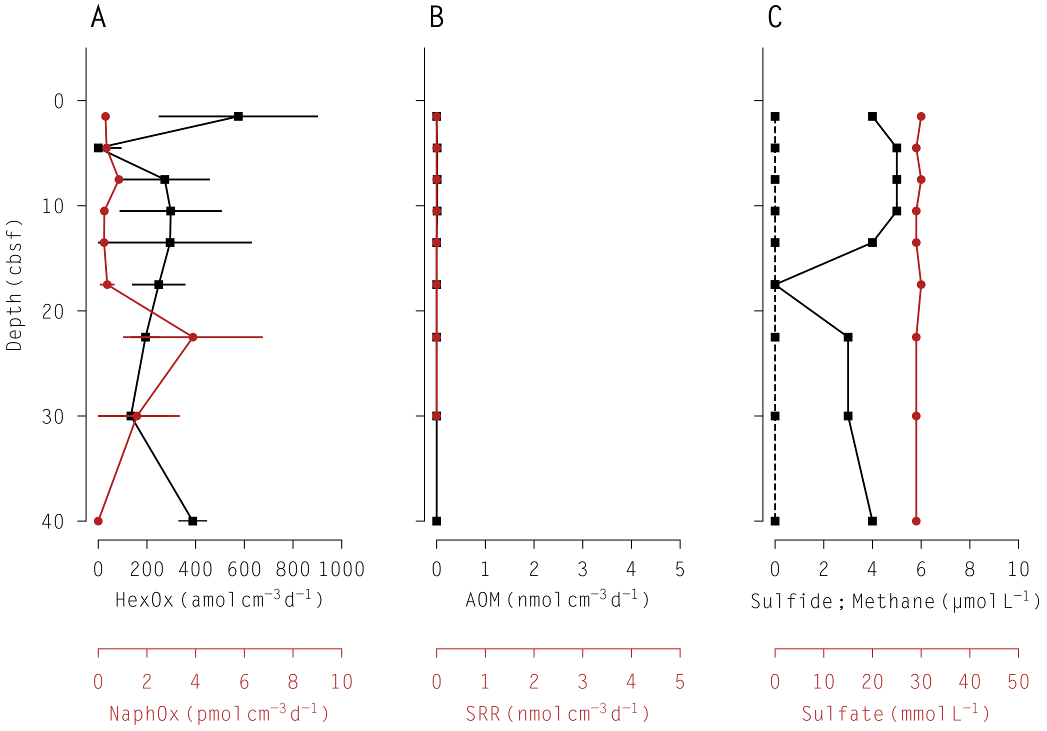

Figure 3.9: Sediment depth profiles of A) HexOx (black), NaphOx (red), B) SRR (black), AOM (red), C) sulfide (dashed black), methane (solid black), and sulfate (red), Gulf of Mexico, lease block GC767. Error bars represent standard error about the mean.

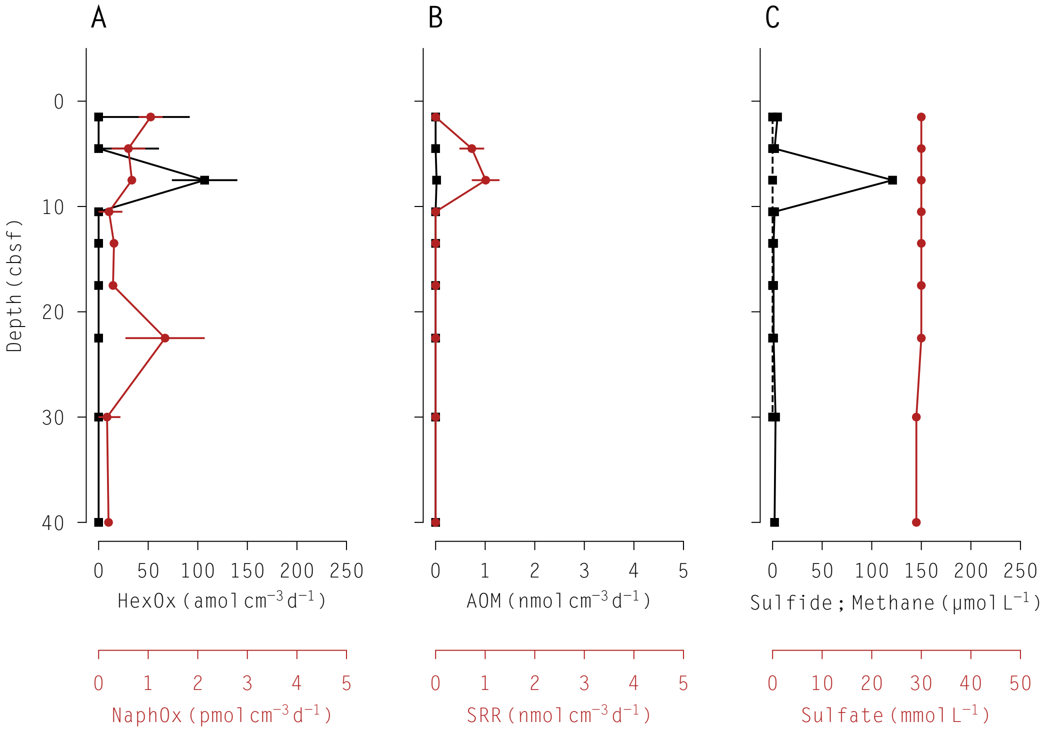

Figure 3.10: Sediment depth profiles of A) HexOx (black), NaphOx (red), B) SRR (black), AOM (red), C) sulfide (dashed black), methane (solid black), and sulfate (red), Gulf of Mexico, lease block GC574. Error bars represent standard error about the mean.

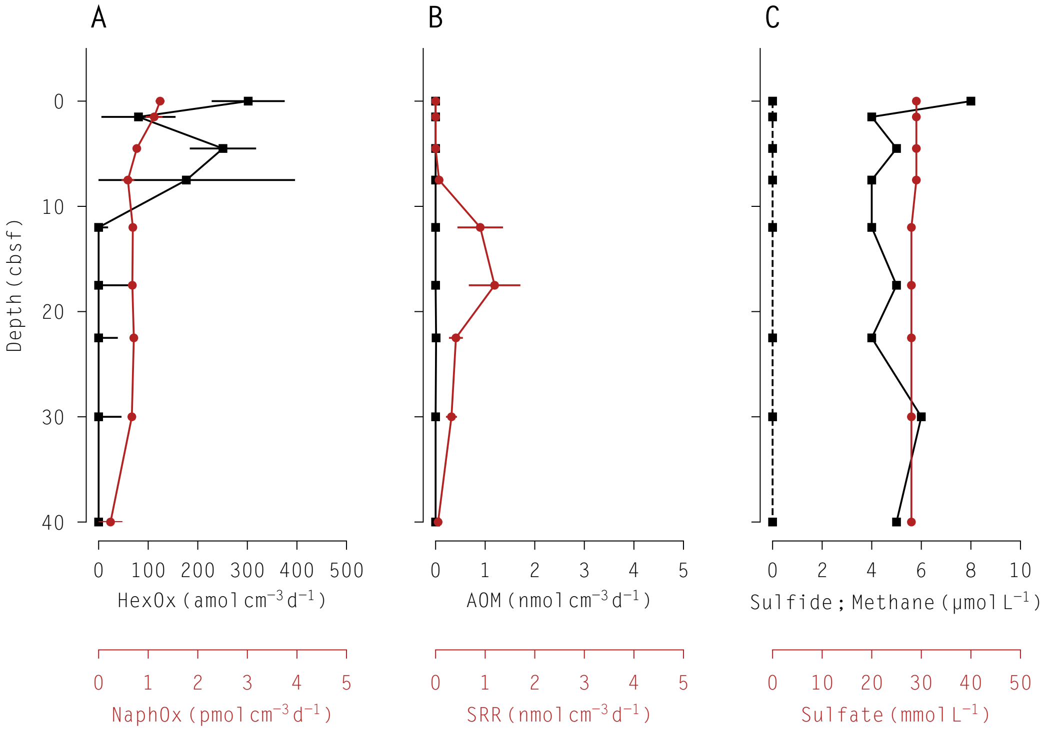

Figure 3.11: Sediment depth profiles of A) HexOx (black), NaphOx (red), B) SRR (black), AOM (red), C) sulfide (dashed black), methane (solid black), and sulfate (red), Gulf of Mexico, lease block GC185. Error bars represent standard error about the mean.

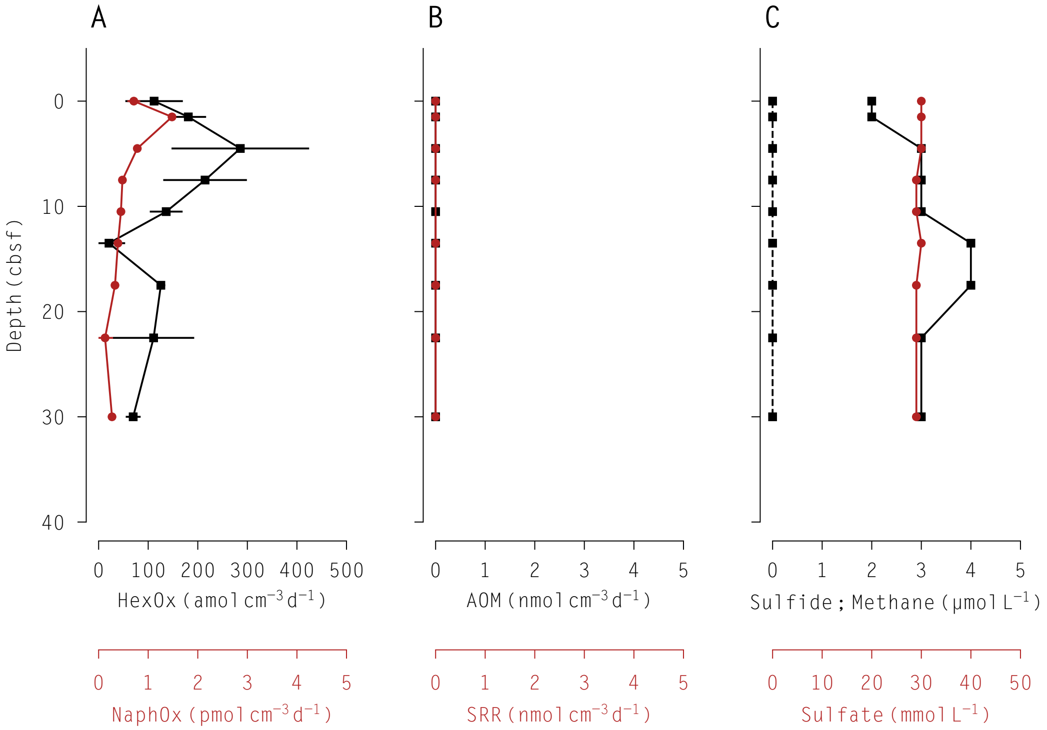

Figure 3.12: Sediment depth profiles of A) HexOx (black), NaphOx (red), B) SRR (black), AOM (red), C) sulfide (dashed black), methane (solid black), and sulfate (red), Gulf of Mexico, lease block GC767. Error bars represent standard error about the mean.

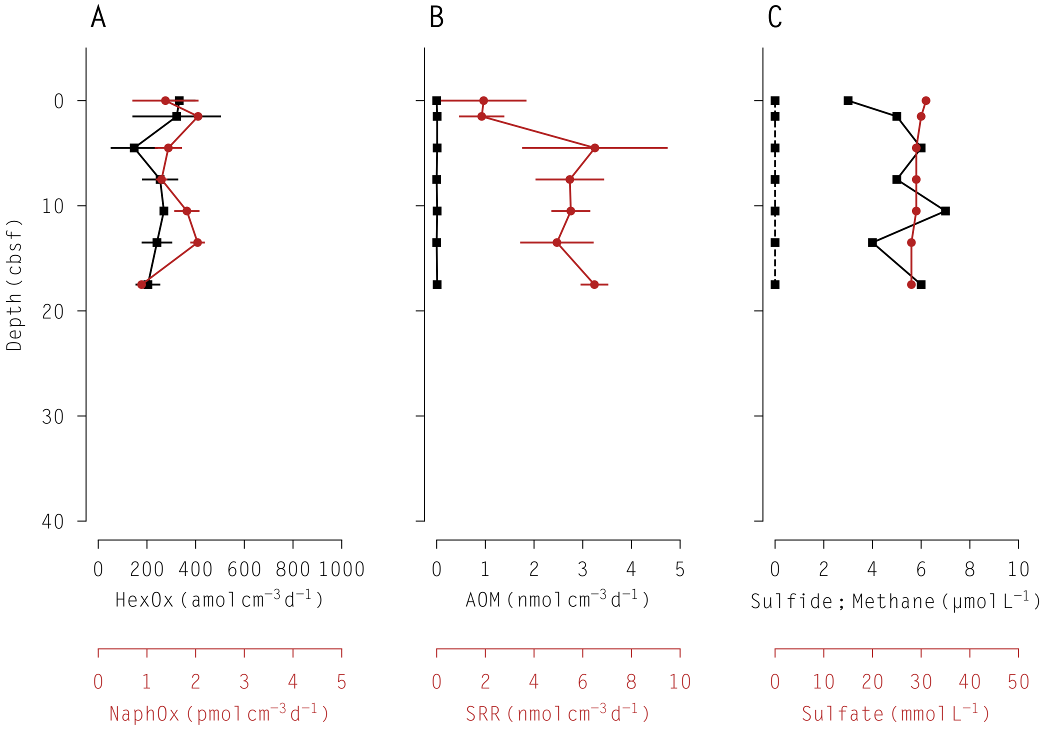

Figure 3.13: Sediment depth profiles of A) HexOx (black), NaphOx (red), B) SRR (black), AOM (red), C) sulfide (dashed black), methane (solid black), and sulfate (red), Gulf of Mexico, Taylor Energy site. Error bars represent standard error about the mean.

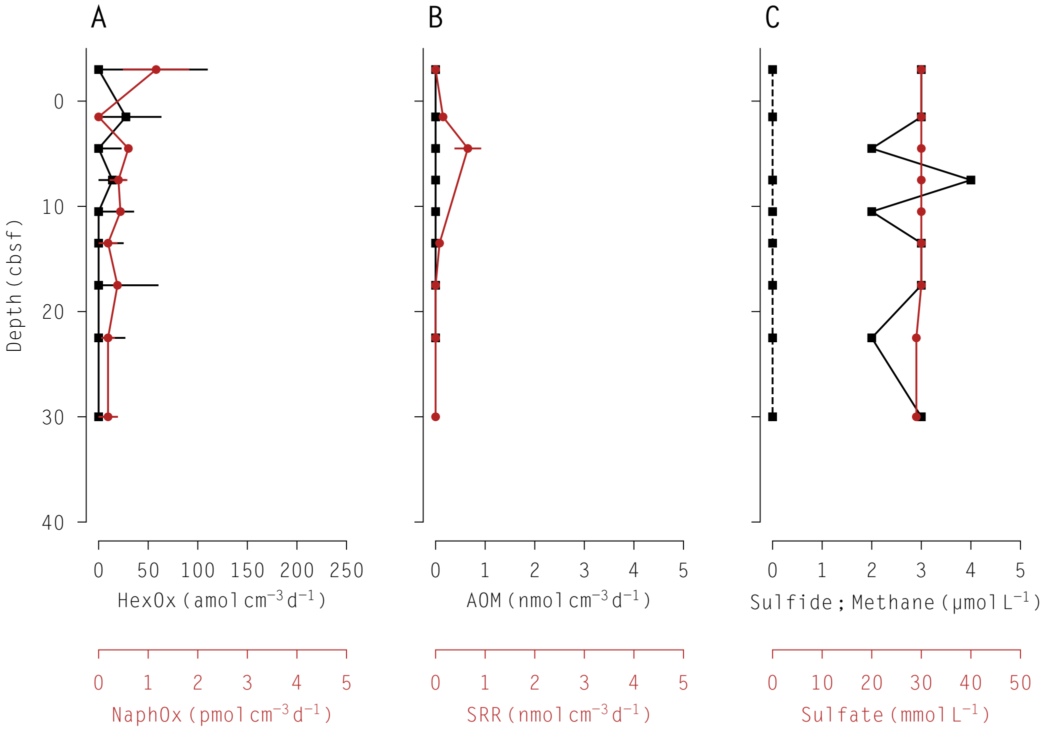

Figure 3.14: Sediment depth profiles of A) HexOx (black), NaphOx (red), B) SRR (black), AOM (red), C) sulfide (dashed black), methane (solid black), and sulfate (red), Gulf of Mexico, OC26. Error bars represent standard error about the mean.

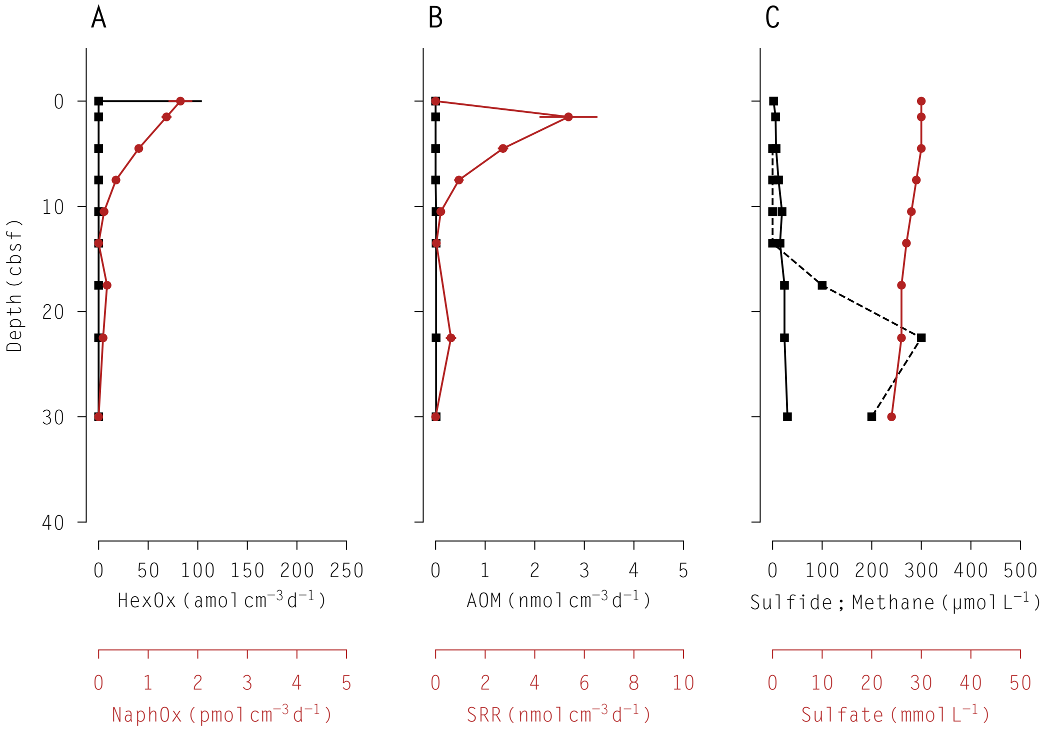

Figure 3.15: Sediment depth profiles of A) HexOx (black), NaphOx (red), B) SRR (black), AOM (red), C) sulfide (dashed black), methane (solid black), and sulfate (red), Gulf of Mexico, lease block GC600. Error bars represent standard error about the mean.

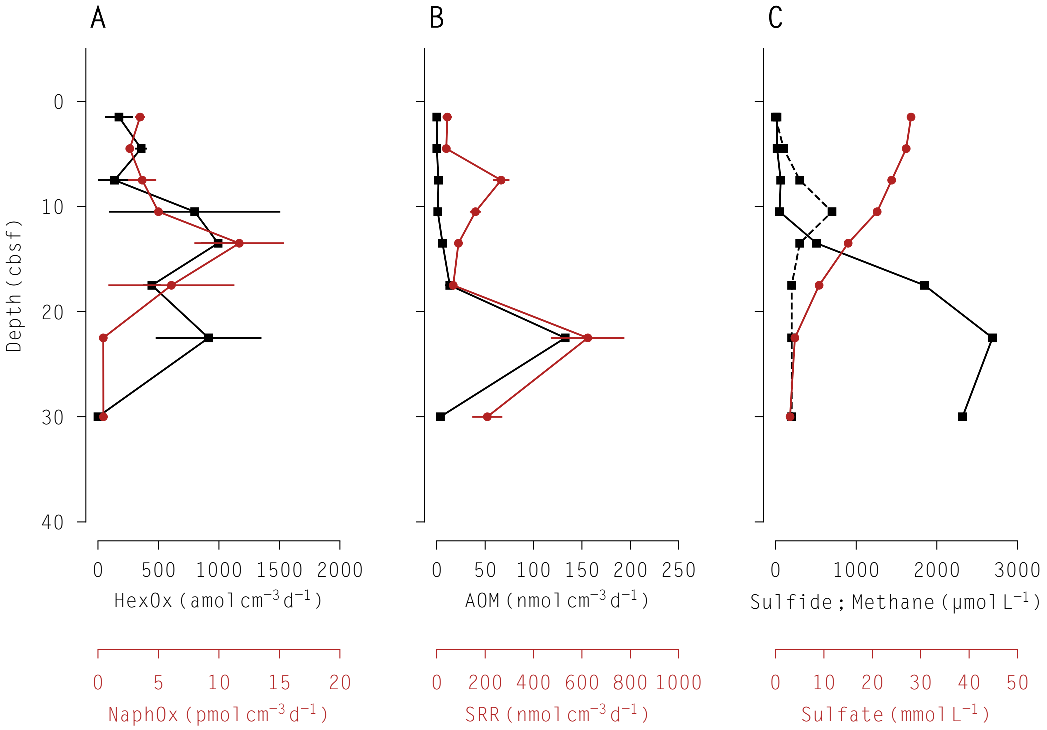

Figure 3.16: Sediment depth profiles of A) HexOx (black), NaphOx (red), B) SRR (black), AOM (red), C) sulfide (dashed black), methane (solid black), and sulfate (red), Gulf of Mexico, lease block MC118. Error bars represent standard error about the mean.

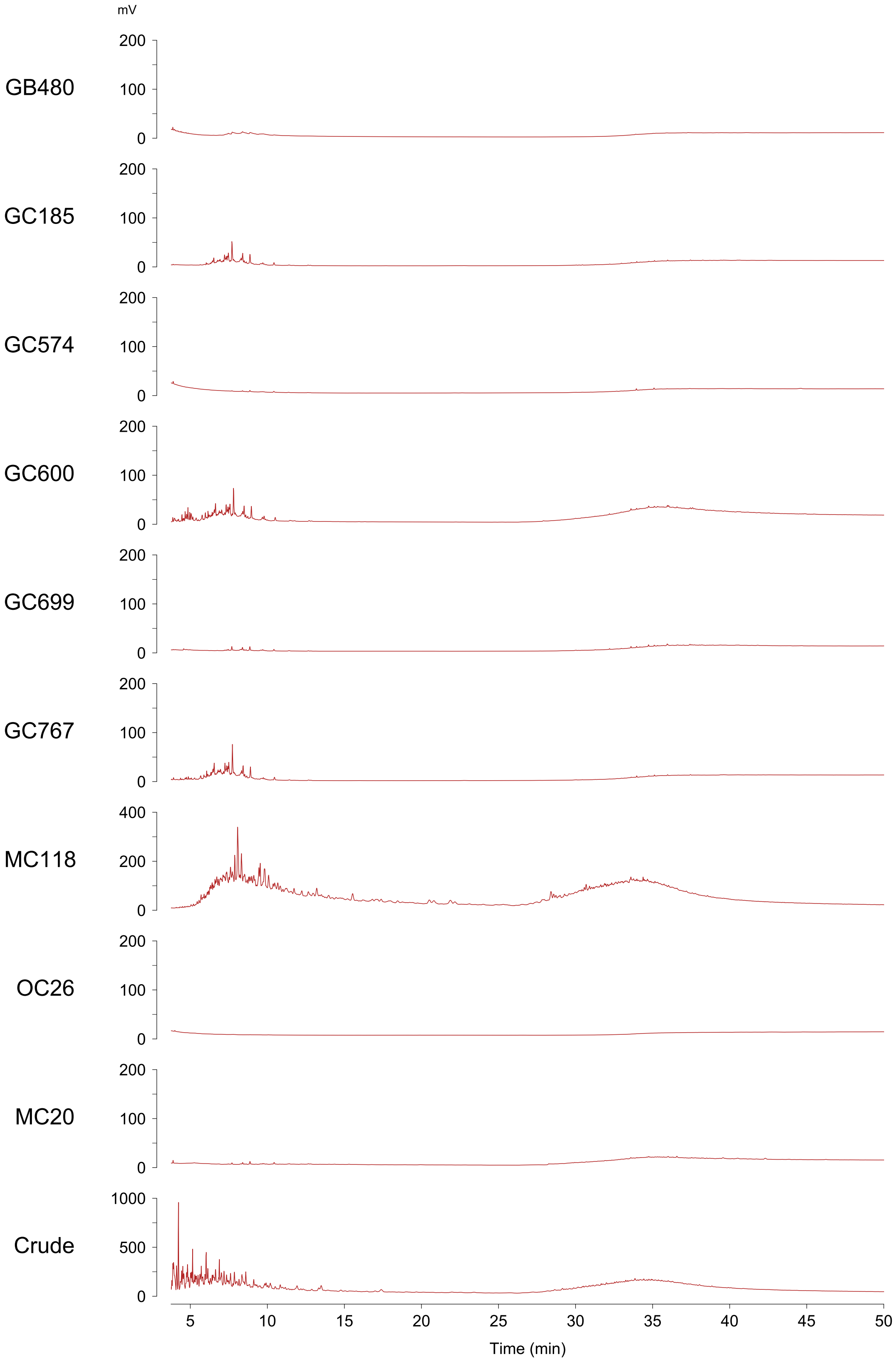

Figure 3.17: Chromatographic characterization of extractable hydrocarbons. Samples extracted with 90:10 mixture of toluene to methanol and analyzed by GC–FID.

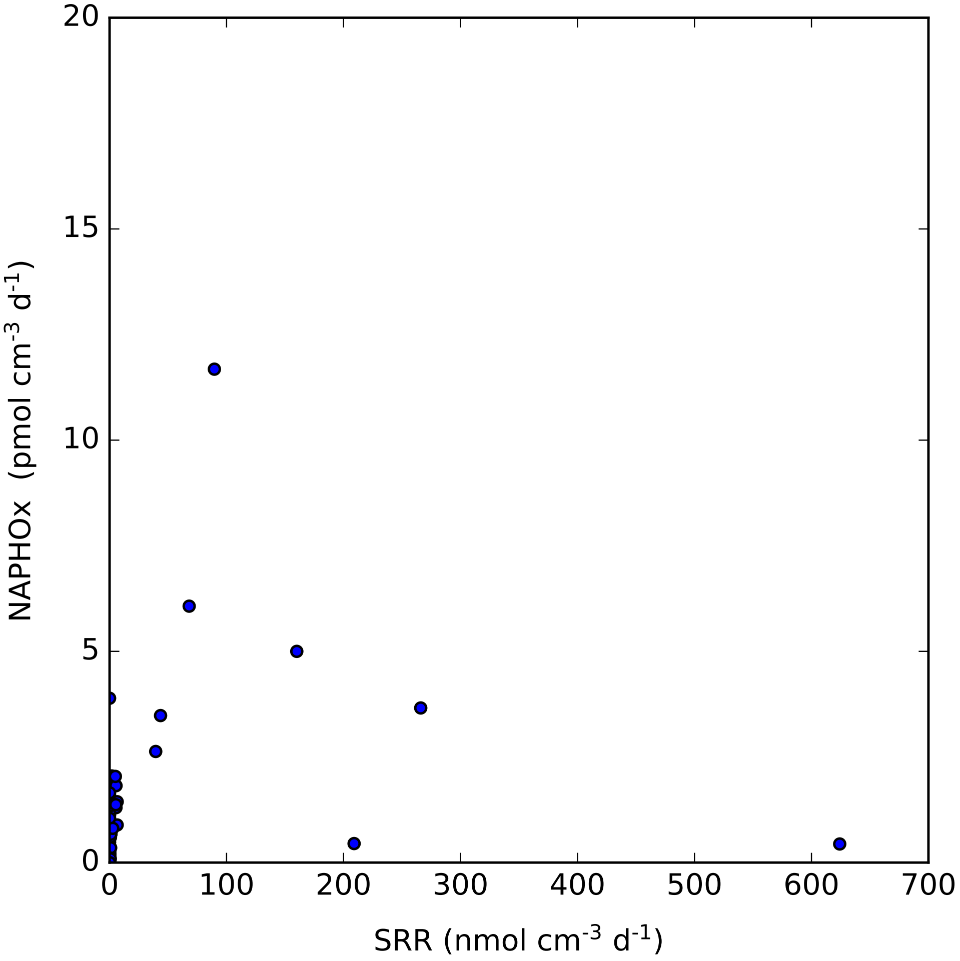

Figure 3.18: Sulfate reduction rates versus naphthalene oxidation rates.

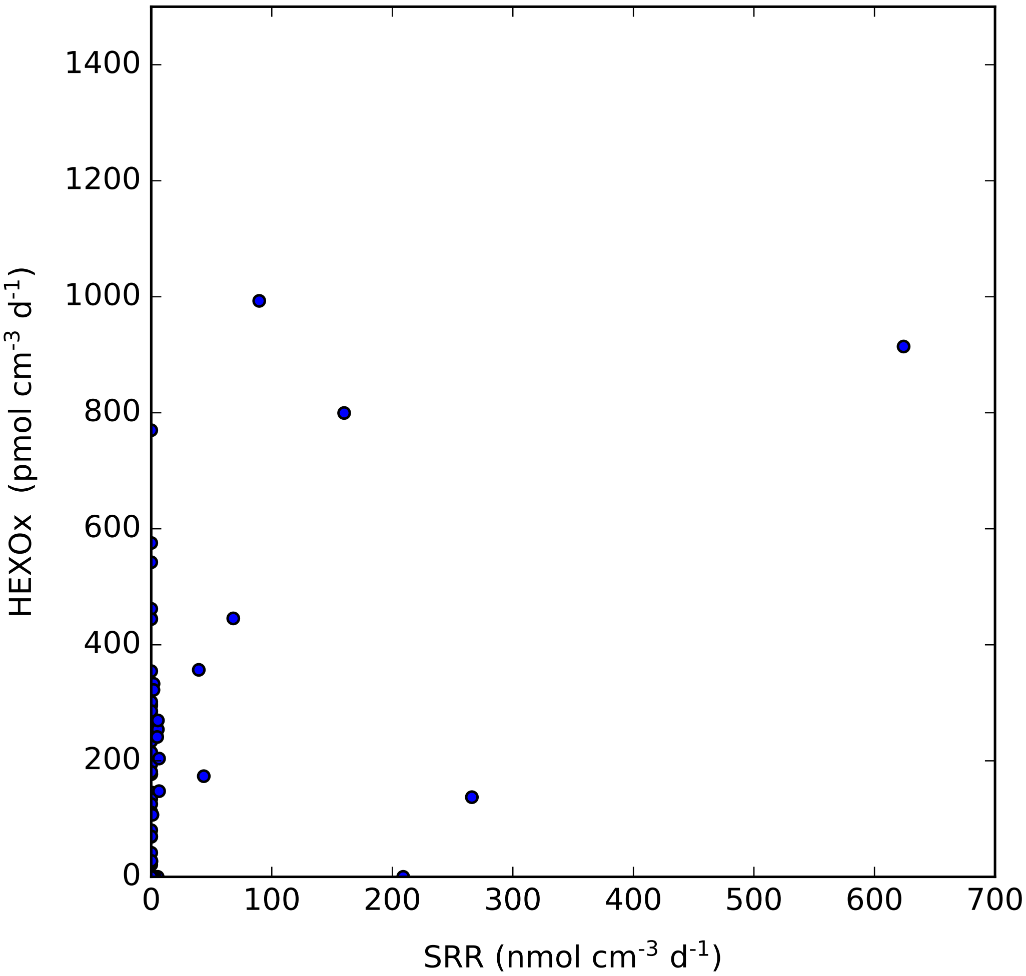

Figure 3.19: Sulfate reduction rates versus hexadecane oxidation rates.

BIBLIOGRAPHY

1. Tissot, B. & Welte, D. *Petroleum Formation and Occurrence: A New Approach to Oil and Gas Exploration* ISBN: 9783642964466 (Springer Berlin Heidelberg, 1978).
2. Seewald, J. Organic-Inorganic interactions in petroleum-producing sedimentary basins. *Nature* **426,** 327–33 (2003).
3. Simoneit, B. R. Petroleum generation, an easy and widespread process in hydrothermal systems: an overview. *Applied Geochemistry* **5,** 3–15 (1990).
4. Head, I., Jones, D. & Larter, S. Head IM, Jones DM, Larter SR.. Biological activity in the deep subsurface and the origin of heavy oil. *Nature* **426,** 344–52 (2003).
5. Philp, R. in *Hydrocarbons, Oils and Lipids: Diversity, Origin, Chemistry and Fate. Handbook of Hydrocarbon and Lipid Microbiology.* (ed H., W.) (Springer, Cham., 2020).
6. Jones, D. *et al.* Crude-oil biodegradation via methanogenesis in subsurface petroleum reservoirs. *Nature* **451,** 176–80 (2008).
7. Dolfing, J., Larter, S. & Head, I. Thermodynamic constraints on methanogenic crude oil biodegradation. *The ISME journal* **2,** 442–52 (2008).
8. Zengler, K., Richnow, H., Rossello-Mora, R., Michaelis, W. & Widdel, F. Methane formation from long-chain alkanes by anaerobic microorganisms. *Nature* **401,** 266–9 (1999).
9. Volkman, J. K., Alexander, R., Kagi, R. I., Rowland, S. J. & Sheppard, P. N. Biodegradation of aromatic hydrocarbons in crude oils from the Barrow Sub-basin of Western Australia. *Organic Geochemistry* **6,** 619–632 (1984).

10. Joye, S. B. The Geology and Biogeochemistry of Hydrocarbon Seeps. *Annual Review of Earth and Planetary Sciences* **48,** 205–231 (2020).
11. Macdonald, I. R. *et al.* Asphalt Volcanism and Chemosynthetic Life in the Campeche Knolls, Gulf of Mexico. *Science* **304,** 1002–999 (2004).
12. Joye, S. B. *et al.* Metabolic variability in seafloor brines revealed by carbon and sulphur dynamics. *Nature Geoscience* **2,** 349 (2009).
13. Skarke, A., Ruppel, C., Kodis, M., Brothers, D. & Lobecker, E. Widespread methane leakage from the sea floor on the northern US Atlantic Margin. *Nature Geosci* (2014).
14. Joye, S. B., Bowles, M. W., Samarkin, V. A., Hunter, K. S. & Niemann, H. Biogeochemical signatures and microbial activity of different cold-seep habitats along the Gulf of Mexico deep slope. *Deep Sea Research Part II: Topical Studies in Oceanography* **57,** 1990–2001 (2010).
15. MacDonald, I. R. *et al.* Chemosynthetic mussels at a brine-filled pockmark in the northern Gulf of Mexico. *Science* **248,** 1096–1099 (1990).
16. Pilcher, R. S. & Blumstein, R. D. Brine volume and salt dissolution rates in Orca Basin, northeast Gulf of Mexico. *AAPG bulletin* **91,** 823–833 (2007).
17. Zhuang, G.-C. *et al.* Multiple evidence for methylotrophic methanogenesis as the dominant methanogenic pathway in hypersaline sediments from the Orca Basin, Gulf of Mexico. *Geochimica et Cosmochimica Acta* **187,** 1–20 (2016).
18. Johansen, C. *et al.* Hydrocarbon migration pathway and methane budget for a Gulf of Mexico natural seep site: Green Canyon 600. *Earth and Planetary Science Letters* **545** (2020).
19. Joye, S. B., MacDonald, I. R., Montoya, J. P. & Peccini, M. Geophysical and geochemical signatures of Gulf of Mexico seafloor brines. *Biogeosciences* **2,** 295–309 (2005).
20. Bowles, M. W., Samarkin, V. A., Bowles, K. M. & Joye, S. B. Weak coupling between sulfate reduction and the anaerobic oxidation of methane in methane-rich seafloor sediments during ex situ incubation. *Geochimica et Cosmochimica Acta* **75,** 500–519 (2011).

21. Colwell, F. *et al.* Estimates of Biogenic Methane Production Rates in Deep Marine Sediments at Hydrate Ridge, Cascadia Margin. *Applied and environmental microbiology* **74,** 3444–52 (2008).
22. Mason, A. *et al.* An Integrated Assessment of Oil and Gas Release into the Marine Environment at the Former Taylor Energy MC20 Site (2019).
23. Chakraborty, A. *et al.* Hydrocarbon seepage in the deep seabed links subsurface and seafloor biospheres. *Proceedings of the National Academy of Sciences* **117,** 11029–11037 (2020).
24. Gieg, L., Jack, T. & Foght, J. Biological souring and mitigation in oil reservoirs. *Applied microbiology and biotechnology* **92,** 263–82 (2011).
25. Jensen, P. *et al.* Bubbling reefs" in the Kattegat: Submarine landscapes of carbonate-cemented rocks support a diverse ecosystem at methane seeps. *Marine Ecology-Progress Series* **83,** 103–112 (1992).
26. Suarez-Suarez, A. *et al.* Response of sulfate-reducing bacteria to an artificial oil-spill in a coastal marine sediment. *Environmental microbiology* **13,** 1488–99 (2011).
27. Matturro, B., Cruz Viggi, C., Aulenta, F. & Rossetti, S. Cable bacteria and the bioelectrochemical snorkel: the natural and engineered facets playing a role in hydrocarbons degradation in marine sediments. *Frontiers in microbiology* **8,** 952 (2017).
28. Kleindienst, S. *et al.* Chemical dispersants can suppress the activity of natural oil-degrading microorganisms. **112,** 14900–14905 (2015).
29. Shin, B. *et al.* Anaerobic degradation of hexadecane and phenanthrene coupled to sulfate reduction by enriched consortia from northern Gulf of Mexico seafloor sediment. *Scientific Reports* **9** (Dec. 2019).
30. Anderson, R. & Lovley, D. Naphthalene and Benzene Degradation under Fe(III)-Reducing Conditions in Petroleum-Contaminated Aquifers. *Bioremediation Journal* **3,** 121–135 (1999).
31. Boetius, A. *et al.* A marine microbial consortium apparently mediating anaerobic oxidation of methane. *Nature* **407,** 623–6 (2000).

32. Orphan, V., House, C., Hinrichs, K.-U., Mckeegan, K. & DeLong, E. Methane-consuming Archaea revealed by directly coupled isotopic and phylogenetic analysis. *Science* **293,** 484–487 (2001).

33. Sun, X. & Turchyn, A. V. Significant contribution of authigenic carbonate to marine carbon burial. *Nature Geoscience* **7,** 201–204 (2014).

34. Raghoebarsing, A. *et al.* A microbial consortium couples anaerobic methane oxidation to denitrification. *Nature* **440,** 918–21 (2006).

35. Callaghan, A., Tierney, M., Phelps, C. & Young, L. Anaerobic Biodegradation of n-Hexadecane by a Nitrate-Reducing Consortium. *Applied and environmental microbiology* **75,** 1339–44 (2009).

36. Ettwig, K. *et al.* Nitrite-driven anaerobic methane oxdation by oxygenic bacteria. *Nature* **464,** 543–8 (2010).

37. Aeckersberg, F., Bak, F. & Widdel, F. Anaerobic oxidation of saturated hydrocarbons to CO 2 by a new type of sulfate-reducing bacterium. *Archives of microbiology* **156,** 5–14 (1991).

38. Musat, F. *et al.* Anaerobic degradation of naphthalene and 2-methylnaphthalene by strains of marine sulfate-reducing bacteria. *Environmental Microbiology* **11,** 209–219 (2009).

39. Gray, N. D. *et al.* The quantitative significance of Syntrophaceae and syntrophic partnerships in methanogenic degradation of crude oil alkanes. *Environmental Microbiology* **13,** 2957–2975 (2011).

40. Kleindienst, S. *et al.* Diverse sulfate-reducing bacteria of the Desulfosarcina/Desulfococcus clade are the key alkane degraders at marine seeps. *The ISME journal* **8** (2014).

41. Laso-Pérez, R. *et al.* Thermophilic archaea activate butane via alkyl-coenzyme M formation. *Nature* **539,** 396–401 (2016).

42. Coates, J. D., Anderson, R. T., Woodward, J. C., Phillips, E. J. P. & Lovley, D. R. Anaerobic Hydrocarbon Degradation in Petroleum-Contaminated Harbor Sediments under Sulfate-Reducing and Artificially Imposed Iron-Reducing Conditions. *Environmental Science & Technology* **30,** 2784–2789 (1996).

43. Beal, E., House, C. & Orphan, V. Manganese- and Iron-Dependent Marine Methane Oxidation. *Science (New York, N.Y.)* **325,** 184–7 (2009).

44. Kleemann, R. & Meckenstock, R. Anaerobic naphthalene degradation by Gram-positive, iron-reducing bacteria. *FEMS microbiology ecology* **78,** 488–96 (2011).

45. Laso-Pérez, R. *et al.* Anaerobic Degradation of Non-Methane Alkanes by "Candidatus Methanoliparia" in Hydrocarbon Seeps of the Gulf of Mexico. *mBio* **10** (eds Orcutt, B. & Newman, D. K.) (2019).

46. Bowles, M. W., Mogollón, J. M., Kasten, S., Zabel, M. & Hinrichs, K.-U. Global rates of marine sulfate reduction and implications for sub–sea-floor metabolic activities. *Science* **344,** 889–891 (2014).

47. Kniemeyer, O. *et al.* Anaerobic oxidation of short-chain hydrocarbons by marine sulphate-reducing bacteria. *Nature* **449,** 898–901 (2007).

48. Davidova, I., Gieg, L., Duncan, K. & Suflita, J. Anaerobic phenanthrene mineralization by a carboxylating sulfate-reducing bacterial enrichment. *The ISME journal* **1,** 436–42 (2007).

49. Widdel, F., Boetius, A. & Rabus, R. in *The Prokaryotes: Volume 2: Ecophysiology and Biochemistry* (eds Dworkin, M., Falkow, S., Rosenberg, E., Schleifer, K.-H. & Stackebrandt, E.) 1028–1049 (Springer New York, New York, NY, 2006). ISBN: 978-0-387-30742-8.

50. Wasmund, K., Mußmann, M. & Loy, A. The life sulfuric: Microbial ecology of sulfur cycling in marine sediments: Microbial sulfur cycling in marine sediments. *Environmental Microbiology Reports* **9** (2017).

51. Harrison, S. *Lessons from the taylor energy oil spill: history, seasonality, and nutrient limitation* 2017.

52. Joye, S. B. *et al.* The anaerobic oxidation of methane and sulfate reduction in sediments from Gulf of Mexico cold seeps. *Chemical Geology* **205,** 219–238 (2004).

53. Arvidson, R., Morse, J. & Joye, S. The sulfur biogeochemistry of chemosynthetic cold seep communities, Gulf of Mexico, USA. *Marine Chemistry* **87,** 97–119 (2004).

54. Sassen, R. *et al. The Mississippi Canyon 118 gas hydrate site: A complex natural system* in *Offshore Technology Conference* (2006).

55. Lapham, L. *et al.* Measuring Temporal Variability in Pore-Fluid Chemistry To Assess Gas Hydrate Stability: Development of a Continuous Pore-Fluid Array. *Environmental science & technology* **42,** 7368–73 (2008).

56. Reeburgh, W. S. An improved insterstitial water sampler. *Limnology and Oceanography* **12,** 163–165 (1967).

57. Cline, J. D. Spectrophotometric Determination of Hydrogen Sulfide in Natural Waters. *Limnology and Oceanography* **14,** 454–458 (1969).

58. Soloranzo, L. Determination of ammonia in natural waters by the phenolhypochlorite method. *Limnology and Oceanography* **14,** 799–801 (1969).

59. Lin, Y.-S. *et al.* Towards constraining H2 concentration in subseafloor sediment: A proposal for combined analysis by two distinct approaches. *Geochimica et Cosmochimica Acta* **77,** 186–201 (2012).

60. Hoehler, T. M., Alperin, M. J., Albert, D. B. & Martens, C. S. Thermodynamic control on hydrogen concentrations in anoxic sediments. *Geochimica et Cosmochimica Acta* **62,** 1745–1756 (1998).

61. Crozier, T. E. & Yamamoto, S. Solubility of hydrogen in water, sea water, and sodium chloride solutions. *Journal of Chemical & Engineering Data* **19,** 242–244 (1974).

62. Sibert, R., Harrison, S. & Joye, S. in *Hydrocarbon and Lipid Microbiology Protocols* (ed McGenity T. Timmis K., N. B.) (Springer, Berlin Heidelberg, 2016).

63. Sibert, R., Samarkin, V. & Joye, S. in *Hydrocarbon and Lipid Microbiology Protocols* (ed McGenity T. Timmis K., N. B.) (Springer, Berlin Heidelberg, 2016).

64. Verschueren, K. in. 4th ed., 1256 (John Wiley & Sons, New York, NY, 2001).

65. Alperin, M., Reeburgh, W. & Whiticar, M. Carbon and hydrogen isotope fractionation resulting from anaerobic methane oxidation. *Global biogeochemical cycles* **2,** 279–288 (1988).

66. Fossing, H. & Jørgensen, B. B. Measurement of bacterial sulfate reduction in sediments: evaluation of a single-step chromium reduction method. *Biogeochemistry* **8,** 205–222 (1989).

67. Jørgensen, B. B. A comparison of methods for the quantification of bacterial sulfate reduction in coastal marine sediments. *Geomicrobiology Journal* **1,** 11–27 (1978).

68. Bowles, M., Hunter, K. S., Samarkin, V. & Joye, S. Patterns and variability in geochemical signatures and microbial activity within and between diverse cold seep habitats along the lower continental slope, Northern Gulf of Mexico. *Deep Sea Research Part II: Topical Studies in Oceanography* **129,** 31–40 (2016).

69. Crespo-Medina, M. *et al.* The rise and fall of methanotrophy following a deepwater oil-well blowout. *Nature Geoscience* **7,** 423–427 (2014).

70. Yan, B. *et al.* Sustained deposition of contaminants from the Deepwater Horizon spill. *Proceedings of the National Academy of Sciences* **113** (2016).

71. Joye, S. B., Teske, A. P. & Kostka, J. E. Microbial Dynamics Following the Macondo Oil Well Blowout across Gulf of Mexico Environments. *BioScience* **64,** 766–777 (2014).

72. Bose, A., Rogers, D., Adams, M., Joye, S. & Girguis, P. Geomicrobiological linkages between short-chain alkane consumption and sulfate reduction rates in seep sediments. *Frontiers in Microbiology* **4,** 386 (2013).

73. Macdonald, I. *et al.* Natural and unnatural oil slicks in the Gulf of Mexico. *Journal of Geophysical Research* **120** (2015).

74. Orcutt, B. N. *et al.* Microbial response to oil enrichment in Gulf of Mexico sediment measured using a novel long-term benthic lander system. *Elementa: Science of the Anthropocene* **5** (2017).

75. Jørgensen, B. Mineralization of organic matter in the sea bed—the role of sulphate reduction. *Nature* **296,** 643–645 (1982).

76. Jørgensen, B., Findlay, A. J. & Pellerin, A. The Biogeochemical Sulfur Cycle of Marine Sediments. *Frontiers in Microbiology* **10,** 849 (2019).

77. Joye, S., Kleindienst, S. & Peña-Montenegro, T. SnapShot: Microbial Hydrocarbon Bioremediation. *Cell* **172,** 1336–1336.e1 (2018).

78. So, C. M. & Young, L. Y. Isolation and characterization of a sulfate reducing bacterium that anaerobically degrades alkanes. *Applied and Environmental Microbiology* **65,** 2969–2976 (1999).

79. Bacosa, H. *et al.* Hydrocarbon degradation and response of seafloor sediment bacterial community in the northern Gulf of Mexico to light Louisiana sweet crude oil. *The ISME Journal* **12,** 1 (2018).

80. Behrens, E. On sedimentation rates and porosity. *Marine Geology* **35,** M11–M16 (1980).

81. Giering, S. *et al.* The ecosystem baseline for particle flux in the Northern Gulf of Mexico. *Elementa Science of the Anthropocene* **6,** 6 (2018).

82. Passow, U. & Overton, E. B. The Complexity of Spills: The Fate of the Deepwater Horizon Oil. *Annual Review of Marine Science* **13,** 109–136 (2021).

83. Jimenez, N., Richnow, H., Vogt, C., Treude, T. & Krüger, M. Methanogenic Hydrocarbon Degradation: Evidence from Field and Laboratory Studies. *Journal of Molecular Microbiology and Biotechnology* **26,** 227–242 (2016).

84. Turner, R., Rabalais, N. & Justić, D. Trends in summer bottom-water temperatures on the northern Gulf of Mexico continental shelf from 1985 to 2015. *PLOS ONE* **12,** e0184350 (2017).

CHAPTER 4

A SURVEY OF ANAEROBIC OXIDATION OF METHANE AND SULFATE REDUCTION IN THE GULF OF MEXICO.

4.1 INTRODUCTION

The Gulf of Mexico (hereafter, Gulf) is the most prolific hydrocarbon basin in the world. The Gulf basin accounts for about 20% of US oil production, 11% of the world's proven oil reserves, roughly 200 billion barrels of oil equivalent [1, 2], and provides 5% of US gas production. The Gulf of Mexico is a true ocean basin in that it formed through sea-floor spreading between 160 and 140 million years ago [3]. Repeated cycles of flooding, first from the Pacific and then from the Atlantic, and subsequent evaporation generated thick salt deposits – at least 1.5 km and up to 4 km – across the basin that are at least upper Jurassic in age, and no older than upper Permian [1, 2]. The majority of salt in the Gulf of Mexico is Louann salt (halite), with some underlying Werner salt (anhydrite) dispersed throughout [4].

The Laramide Orogeny and uplift of the Rocky Mountains generated tremendous sediment loading into the Gulf of Mexico, between about 75 and 45 million years ago [4]. Flooding of the salt basement with up to 10 km of sediment generated substantial overpressure in the system, initiating salt tectonics and creating an ideal dynamic for petroleum formation and storage. The distribution of oil fractions reflects multiple sources fueling petroleum formation, variations in maturation of that petroleum, and post-generational modification of oil in local reservoirs [5].

The Gulf of Mexico is home to >1,000 known active hydrocarbon and brine seeps, often referred to collectively as cold seeps [6]. A cold seep is an area where oil, methane and other alkanes, and / or brine are discharged from the seabed. The fluids are typically cold, or slightly elevated (approx. 10-30 °C) in temperature for the case of mud volcanoes, in contrast to the superheated fluids (>300 degrees C>300 °C) discharged at deep sea hydrothermal vents [7]. The Gulf is the only place on place on Earth where all major classes of cold seepage – brine, gas, oil and gas, oil, gas, and brine, and asphalt – occur [7–12]. The Gulf system is large, with a surface area of ca. 1 605 792 km^2. The Northern Gulf captures the entire spectrum of seepage regimes in an area - 141 000 km^2 - that has been mapped, characterized by towed video surveys, and sampled during a number of previous projects, including the Minerals Management Service funded Chemosynthetic Ecosystems Studies programs (1999-2008 [13–16]), the Florida Escarpment Study (1980-1983 [10]), the Life Extreme Environments study [11, 12, 17], the Mississippi Canyon 118 Gas Hydrate Observatory (2003-2010 [9, 18, 19], the Brine Ecosystems Microbial Observatory (2010-2015; [20] this work), and the Ecosystem Impacts of Oil and Gas Inputs to the Gulf program (ECOGIG; 2012-2018; this work).

Cold seepage occurs through fissures and faults in the sediment column caused by salt tectonics or through clay dewatering of deep subsurface sediments [7]. Concentrated brine along with fluidized mud, oil and/or gas or just oil and gas move through deeply sourced faults and emerge at different points from the seafloor. At natural seeps, the seafloor is peppered with numerous individual discharge points, releasing fluids at different rates, over an area as small as a few meters wide and at some sites, as large as several hundred meters across [7]. In the case of brine seepage, pools of brine can form along the seafloor, where high density brine (up to 5 times the salinity of seawater) accumulates in topographic lows along the seabed due to the high density of the fluid and the slow mixing of the brine with overlying seawater [7]. Rates of fluid discharge at seeps is poorly constrained ([6, 21, 22]), but discharge is known to be patchy and variable ([23, 24]).

The Gulf of Mexico is also known for the presence of abundant seafloor breaching gas hydrate mounds, also known as "methane ice". Methane hydrates are ice-like crystalline structures comprised of water and methane that form naturally under the high pressures and saturated methane concentrations in the zone of hydrate stability in the Gulf, as well as in other deep-sea locations.

Methane hydrate systems are dynamic way stations for light hydrocarbons as they migrate through the upper few hundred meters of continental margin sediments [25, 26]. Hydrates are abundant in the Gulf [27] and their stability excerpts a strong influence on seabed oil and methane fluxes, thereby affecting biological processes in adjacent sediments and in the overlying water column [7].

Seepage of hypersaline fluids (brines) occurs along the seafloor at sites across the globe. Movement of salt bodies (diapirs) and the resulting salt-tectonics, creates fault networks that serve as conduits for the rapid transfer of oil, gas and brines from deep reservoirs through the sediments to the seafloor [28–31]). Brine expulsion generates brine pools, brine-filled basins, and mud volcanoes and two of these types of brine environments were assessed in this study. Brine pools, where brine fills surface depressions creating "lake-like" features on the seafloor [29, 30]. And, mud volcanoes, where brine, oil, gas and fluidized mud are actively expelled, inducing large temperature fluctuations and seabed alterations. Finally, we assessed a site where brines formed in response to gas hydrate formation, which generates hypersaline residual fluids. Hydrate-derived brines reflect the exclusion of seawater salts from the hydrate ice matrix, similar to the cryoconcentration of seawater ice [32]. These brines can have distinct chemistry from halite or anhydrite derived brines.

Much previous work in the Gulf has focused on the ecology and macro-ecology of chemosynthetic communities (e.g., Fisher et al. 2007 [16, 33], and many more). The purpose of this work was three-fold. First, we aimed to assemble the most extensive spatial and temporal comparative biogeochemical and microbial activity data set of Gulf of Mexico cold seeps. We carried out an exhaustive characterization of pore fluid and solid phase geochemistry and quantified rates of sulfate reduction and anaerobic oxidation of methane (see methods). Previous efforts have focused on approximately 18 cores from 10 sites examined during one research expedition ([14, 15]). Here, we examined 13 sites over 6 research expeditions between 2010 and 2016 and evaluated a total of 48 sediment cores from the Gulf of Mexico. Some individual sites (n=6) were further sampled across detailed spatial resolution and multiple expeditions. With this data set, we confirm previous observations and report new findings that advance the field. A notable difference between this work and previous efforts (e.g., Joye et al. 2004, Orcutt et al. 2004, 2005, Bowles et al. 2011, 2019 [11, 12, 17–19]) stems from the focus on ALVIN expeditions, where brine-influenced sites were targeted. The ALVIN expeditions did not focus on oil-gas seep sampling, though some samples were collected from GC600 in the second brine expedition (see below). The cores from oil and gas seeps presented here were collected mostly using a multiple-corer, an unguided device that cannot accurately target active oil and gas seepage.

Second, this is the first data set where microbial activity was examined at a wide range of sites using an improved approach that reproduces quasi-in-situ conditions. Bowles et al. (2011 [18]) reported weak coupling between anaerobic methane oxidation and sulfate reduction when methane concentrations were low (i.e., 2-4 mM). In the Gulf of Mexico, co-migration of oil and gas provide sulfate reducing bacteria a wide array of possible substrate choices and this appears to effectively decouple anaerobic methane oxidation and sulfate reduction. Subsequent work by Bowles et al. ([18, 19]) pointed out a major flaw in previous assessments of deep sea microbial activity. Previously, it was assumed that sulfate reduction and anaerobic oxidation of methane exhibit 1:1 metabolic stoichiometry [34, 35] such that sulfate reduction rates could be used as a proxy for rates of anaerobic oxidation of methane.

Pore fluid methane saturation at only 500 m water depth could be as high as 50 mM [36]. Methane concentrations documented at seafloor cold seeps – from 15 mM up to 80 mM [31, 37] – are certain to impact rates of microbial processes that cycle methane. Bowles et al. (2011 [18]) presented a new method that involved recreating in situ conditions by amending samples with pure methane gas (ca. 1 mL) to generate methane concentrations of about 20 mM during incubations. Bowles et al. discovered – unsurprisingly – that rates of anaerobic methane oxidation were profoundly underestimated using the traditional approach of conducting rates assays at 1 atmosphere using sediment that had degassed during recovery, and as such, had low (<1 mM) methane concentration. Bowles et al. (2019 [19]) went further, suggesting that multiple modes of AOM co-exist such that the reduction of sulfate and non-sulfate electron acceptors coupled to

AOM occur contemporaneously, promoting much higher rates of AOM that would occur than through coupling to sulfate reduction alone.

The present work presents the first broad survey of AOM and SR using the improved method of Bowles et al. (2011 [18]) to quantify rates. In doing so, we discovered that deep sea brines support considerable rates of AOM when methane concentrations are more realistic of in situ conditions. Sulfate reduction independent of AOM was still observed at many sites, but rates of AOM are, in general, much higher under these more realistic conditions. We did not see the extreme rates of AOM presented by Bowles et al. (2019) but none of the samples included in this analyses were as oily as those considered in that study.

Third, the nature of the data set allowed us to assess spatial and temporal variability at hydrocarbon seeps. In particular, the Green Canyon 600 which was sampled during ALVIN cruises and extensively by multiple coring, and the GC233 and GC246 brine seeps. The GC600 site exhibits striking variability in geochemistry and microbial activity within the site and over time. It is well known that seepage regimes are variable, but this variability is rarely documented so explicitly. Sediments at GC600 contained variable mixtures of oil, gas, brine, and hydrate, each with unique geochemical consequences on microbial activity, particularly with respect to the availability of nitrogen and DOC. The presence of brine generally increased the availability of DON, DOC, ammonium, and resulted in elevated rates of microbial activity.

4.2 METHODS

4.2.1 STUDY SITES AND SAMPLING SCHEME

The Gulf of Mexico (hereafter, Gulf) is a prolific, but leaky hydrocarbon basin. The study sites were chosen to encompass a range of sedimentary environments along the Northern Gulf, including quiescent abyssal sites (type I), sites of known oil and gas seepage (type II), gas hydrate-bearing sites (type III), and sites impacted by brine flows (type IV; see Figure 4.1 and Tables 4.1, 4.2). Sites for this study were chosen from among four general oil and gas lease provinces, including the: 1) Alaminos Canyon, 2) Garden Banks, 3) Green Canyon, and 4) Mississippi Canyon areas along

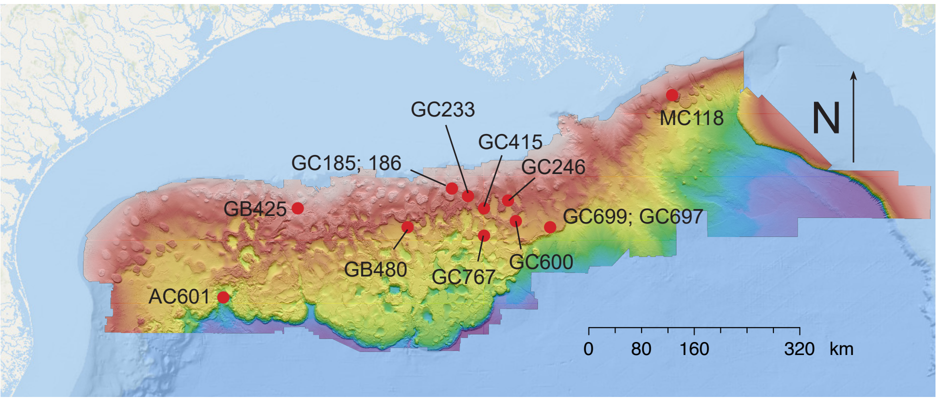

Figure 4.1: Map of sampling locations, Gulf of Mexico. Bathymetry dataset courtesy of the U.S. Bureau of Ocean Energy Management: https://www.boem.gov/Gulf-of-Mexico-Deepwater-Bathymetry.

the Northern continental shelf. The Alaminos Canyon cuts into the Sigsbee Escarpment at the base of the continental slope in the western Gulf (see Figure 4.1).

Sampling sites within lease block 601 (hereafter AC601) were located approximately in the middle of the canyon on top of a breached E-W trending anticline. The AC601 is characterized by fractures and faults that provide migration pathways for fluids and gases, between a deep anticlinal hydrocarbon reservoir and the seafloor. The AC601 site contains a brine lake, a mounded fluid and gas expulsion feature, with evidence of mudflow radiating from the crest of the mound [38]. The lake has a diameter of about 110m and a variable depth of up to 20 m. The lake is characterized by two transitional zones, a barite "swash" zone at the edge of the lake and the brine-seawater "fog" zone above the lake. The shoreline of lake is characterized by flock aggregations of various sizes floating at the interface. Next to the swash zone, moving away from the lake, was a zone characterized by heart urchins and microbial mats, Siboglinid polycheates, and clumps of mussels. On the NW edge, there is a relatively steep drop off. Along the N-NE edge, an old (higher) shoreline was visible. On the S edge, pelagic sea cucumbers were abundant.

Garden Banks lease block 425 (GB425) lies on the western edge of the Auger basin, an intraslope basin that contains economically significant hydrocarbons in the Auger, Cardamom, and Macaroni fields and is bordered to the west by tabular salt bodies. The GB425 mud volcano is situated at a small, active diatreme on the southern margin of a flat-topped mound located midway along the fault. The site is characterized by frequent and vigorous mud flows, and the fluidized brine accumulates in a centralized basin. Similar to other areas that experience frequent mud flows, chemosynthetic communities are poorly developed at this site. A tension-leg platform installed at Auger Field is producing from an estimated 100 million barrels of extractable oil, but large quantities of pressurized fluid have evidently escaped through anticline faults along the flanks of the salt diapir at the basin margin. Fluids migrating up these faults disturb surface sediments due to the formation of carbonate nodules, oil and gas pockets, and biogenic debris. Sediment cores from the area contain high-molecular weight hydrocarbons, brine, and, sometimes, thermogenic gas hydrate.

Active venting of brine, free and dissolved gases, and high molecular weight hydrocarbons sustains an expulsion crater from which gas and fluidized mud streams are frequently visible. The sediments adjacent to the south of the diatreme support chemosynthetic mussel communities and mats of free-living giant sulfur bacteria, however, the distribution of mussels and microbial mats is more patchy at GB425 compared to GC233, for example. The GB425 brine pool is physically larger than the GC233 brine pool and it supports a high rate of gas discharge and flows of fluidized muds and oil. The GB425 brine consisted of fine clay suspended in brine with a salinity of about 133 PSU. The suspended sediment load is at least 65% by volume. The mud volcano brine pH was about 7.4.

The Green Canyon 185/186 site is situated west of the Mississippi Fan in adjacent lease blocks. The first recovery of gas hydrate in the Gulf of Mexico occurred at GC185. The GC185 site is known as Bush Hill because of extensive fields of tube worm bushes all along the site. GC185 is a prominent mound aligned along a N-S antithetic fault. The mound is surrounded on all sides by a fault system, and below it there is an acoustic wipeout associated with gas-charged sediments. The faults on either side of the gas hydrate mound help move hydrocarbons from deep reservoirs to the seafloor. Sediment failure and slumping is evident along the edges of the mound. The central mound is home to a 4 m diameter and 1 m high exposed gas hydrate mound, that is covered with a thin veneer of sediment and orange Beggiatoa mats. Vigorous discharges of oil and gas from the vicinity of the gas hydrate mound is known to create persistent oil slicks at the sea surface.

The Green Canyon (GC233) site is a small brine pool (190 sq. m) situated at a depth of 650 m. The GC233 brine pool is situated on a mound, which is elevated 6 to 8 m above the surrounding seafloor and has a basal diameter of approximately 100 m. The fluid filling the pool had a salinity of 130 PSU and was supersaturated with methane. Added density due to the excess salt maintained the brine as a distinct fluid in the pool but the brine mixes with seawater by molecular and eddy diffusion. Subbottom records revealed considerable complexity at the site. On the flanks of the mound, indurate layers underlie layers with a weak seismic reflection, suggested surface flows of loosely consolidated material over hardened ground. A narrow dike, raised about 25 cm, formed a rim that surrounds three sides of the pool outside of the mussel bed. The mussels appeared as a layer distinct from the brine, which formed a level reflector. Below the brine, sediments were homogeneous and contained a large, irregular reflector near the bottom of the record. The most regular subbottom features were a sequence of layers buried under the present-day mound. Distances between these layers were greatest in the center of the mound and least around the edges. The deepest layer formed a funnel shaped base to the outline of the mound. Continuous discharge of gas through the brine leads to saturation with dissolved methane in the brine and in the surrounding sediments, which serves as a source of energy for mussels with methanotrophic symbionts that are found along the edges of the pool. Patchy mats of giant sulfur bacteria, such as Beggiatoa, Thioploca, and Thiomargarita, covered the sediments adjacent to the mussel beds.

Green Canyon lease block 246 (GC246) is located approximately 200 km SW of the Mississippi Delta on the flank of the upper-middle continental slope in the Gulf of Mexico. The GC246 block consists of featureless mud plains rising to a pockmarked bathymetric mound approximately 830 m below the surface of the Gulf. The GC246 mound is complex terrain of slopes, depressions, and plateaus, punctuated by active brine seeps and flows, brine pools, mud-flows, and massive mud volcanoes. Mottled grey sediments cover much of GC246 area, interrupted occasionally by carbonate outcrops, coral communities, black to milky colored brine flows, ocher mud-flows, white to orange Beggiatoa meadows, fields of spent mussel and crab carcasses, and communities of live mussels (Bathymodiolus) and snails. With the exception of these few communities of mussels, crabs, bacterial mats, and corals, GC246 is largely devoid of benthic macrofaunal life. In the central portion of the GC246 area is Dead Crab Lake (DCL), a brine lake approximately 15 to 25 cm deep. DCL is an active brine seep, ringed with orange mineral crusts, dead mussels, and dead crabs. The seascape at GC246 is peppered with small ocher-colored mineral chimneys surrounded by sulfide-oxidizing bacterial mats. Both white and orange Beggiatoa meadows are common in GC246. Small communities of soft corals (Callagorgia) and brittle stars (Ophiuroidea) inhabit the occasional carbonate hardground outcrop in GC246. Bathmodiolus mussels, snails, crabs, sea cucumbers (Benthodytes), and isopods (Bathynomus giganteous) have all been identified in varying degrees of abundance at GC 246, usually in close proximity to active seep sites.

The Green Canyon 415 (GC415) is an area of very active oil and gas seepage ([39]) as evidenced by the widespread occurrence of Beggiatoa mats, shell hash, and carbonate pavements. Though some disseminated gas hydrate have been recovered in cores, no large outcropping gas hydrate mounds, like those at Bush Hill, are present at this site. Sediments were gassy and oil-stained. The abundance of bacterial mats was highest around areas of gas flares. Bacterial mats were often associated with highly reducing sediments, suggesting subseafloor brine or gas hydrate; deep brines likely affect this site as evidenced by some elevated pore fluid salinities ([39]. In contrast to past observations at GC185, no tube worms have been documented at GC415.

Green Canyon Block 600 (GC600) is located at a depth of 1200 m approximately 260 km SW of the Mississippi Delta, on the upper-middle continental slope of the Gulf. GC600 is one of the largest natural oil seeps in the GoM, ejecting enough oil and gas into the water column to produce numerous persistent oil slicks at the surface. Active fluid-gas expulsion of hydrocarbons at GC600 supports numerous chemosynthetic communities at the seafloor. A NW-SW trending bathymetric ridge is the dominant feature at GC600. This ridge bifurcates the site into two intraslope basins. Observational data obtained through drift camera work with the DSV Alvin confirms a heterogeneous patchwork of fractured carbonate hardground outcrops and blocs, oil-laden anoxic sediments, brine pools and flows, gas hydrate mounds, barite deposits, fluid-gas discharge, and chemosynthetic communities dominating the local geology. Previous work by Roberts et al. (2010; [40]) shows that carbonate species are predominantly composed of authigenic high-magnesium calcite and aragonite. The highly fractured carbonate pavements of GC600 act as conduits for oil and gas expulsion. The flux of oil and gas through these fissures provide ideal habitat for a number of benthic chemosynthetic fauna, including tube-worms, mussels, and bacterial mats. Lamellibrachia occupy GC600 as single individuals or as small communities growing out of active fissures. Colonial cnidarians (i.e., Gorgonian), mollusks (predominantly Bathymodiolus brooksi and Calyptogena ponderosa), and bacterial mats (Thiomargarita and Beggiatoa) are also commonly observed near active seepage of oil and gas.

Mississippi Canyon Block 118 (MC118) is located approximately 80 km SE of the Mississippi Delta on the upper continental slope of Louisiana. At 880 m depth, the MC118 range supports abundant chemosynthetic fauna in a complex terrain of hydrocarbon seeps, authigenic carbonate pavements, brine flows, mud volcanoes, and exposed methane hydrate outcrops. MC118 site sits above a salt diapir, the movement of which results in a complex fault architecture that act as a conduits for oil and gas export to benthic sediments. Benthic oil and gas expulsion at MC118 gives rise to gas and oil laden sediments, providing ample substrate for chemosynthetic mussels and bacterial colonies. Seep sites and breaching hydrates at MC118 are host to fields of white Beggiatoa mats, Siboglinidae tube worms, and Hesiocaeca methanicola worms. Moderate methane flux and the persistence of bacterial Beggiatoa mats and other subsurface microbial communities have resulted in carbonate pavements and poorly cemented carbonate hardgrounds, ideal habitat for clams (Calyptogena ponderosa), corals (Gorgonacea, Chrysogaorgia sp, and Madrepora), and brittle stars (Astroschema ophiuroid). Golden crabs, hagfish, and sea cucumbers (Holothuroidae) have all been identified at MC118.

The Garden Banks 697 (GB697) is characterized by active salt tectonics and gas and oil seepage along the flanks of salt diapirs. The seafloor is characterized by numerous topographic highs, overlying shallow salt. The site is home to a small, highly active, mud volcano that discharges copious gas and fluidized mud. The fluid salinity was approximately 210‰ and the temperature was elevated substantially above the bottom water. This active brine flow is believed to be geologically young; it lies atop a strong positive amplitude anomaly. There are multiple gas and brine chimneys emanating from flank of salt along the edge of the mound and basin below. The site is characterized more by hydrocarbon flow than mud flow, though some active mud flows are present in the area. Microbial mats, animals, and active and turbulent brine flows features characterized this site.

The three other sites have never been sampled using a ROV or human occupied vehicle, and were selected based on remote sensing data, which showed the presence (GC767) or absence (GB480, GC699) of persistent surface oil slicks, a good indicator of seafloor seepage potential (Ian MacDonald, personal communication). The Green Canyon (GC767) area is suprasalt minibasin. The site is surrounded by salt diapirs and underlain by extensive hydrocarbon reservoirs. The periodic presence of sea surface oil slicks suggests at least intermittent oil discharge from the site. The Green Canyon 699 (GC699) and Garden Banks 480 (GB480) lie within the greater Green Canyon and Garden Banks lease blocks, respectively. Neither area is characterized by oil slicks and each of the sites is several km from known areas of seepage (e.g., GC600 or GB425). Thus, these two areas are considered non-seafloor-seepage-impacted control sites.

4.2.2 SAMPLING

Over 175 sediment cores were collected in the Gulf of Mexico across six expeditions between 2010 and 2016. Two research vessels were used 1) the R/V Atlantis (Woods Hole Oceanographic Institution) for expeditions AT18-02 in 2010 and AT26-13 during 2014, and 2) the R/V Endeavor (University of Rhode Island) for expeditions EN527 (2013), EN528 (2013), EN559 (2015) and EN586 (2016); see Figure 4.1;Tables 4.1, 4.2 and 4.3). Sediment cores were collected using push-cores from the deep-sea submersible, the HOV ALVIN, during the Atlantis expeditions and using a multicore device (hereafter, MUC) on the Endeavor expeditions.

On Atlantis expeditions, push-cores were targeted visually by researchers inside ALVIN and then collected using the ALVIN's robotic manipulators. The MUC was targeted to known areas of seepage, based on available mapping data, but the MUC was dropped 'blind' – without the aid of a live video feed – and the Endeavor lacked a Dynamic Positioning system, so MUC sampling did not explicitly capture sites of seepage the majority of the time. As such, though all of the study sites have recognized signatures of oil and gas seepage, some of the cores retrieved lacked such signatures. Both MUC and push-cores were constructed from machined polycarbonate liners but the MUC cores were longer (50 cm length) than the push cores (35 cm length). We refer to cores collected from areas of known seep signatures but that lacked geochemical signatures of seepage as 'inactive'.

Most of the inactive cores were recovered from our non-seafloor-seepage-impacted sites GC699 and GB480, though some were recovered from known seep sites (see Figure 4.1;Tables 4.1, 4.2 and 4.3). The control sites were characterized by low methane (<15 μmol L^{-1} CH_4), high sulfate concentrations (approx. 28 mM), undetectable sulfide, and very low rates of microbial activity. Sites of oil and gas seepage were chosen based on descriptions from previous expeditions that employed towed camera systems and autonomous vehicle surveys to identify areas of potential oil, gas or brine seepage, e.g., authigenic carbonates ([38]) and built on results from previous projects ([14, 15, 17, 18]). Sites of oil and gas seepage included locations within Mississippi Canyon (MC118) and Green Canyon (GC185, GC415, GC600, GC767) (see Figure 4.1;Tables 4.1, 4.2 and 4.3). In general, the sediments at seep sites were characterized by high methane, low sulfate, high sulfide, moderate concentrations of ammonium, and moderate to high rates of microbial activity (see Figure 4.1;Tables 4.1, 4.2 and 4.3).

Brine influenced sites were identified visually and confirmed by documented increases in porewater chloride concentration (> 600 mM; see Table 2). Numerous sites contained brines, including sites at AC601, GB425, GB697, and sites within Green Canyon across GC233, GC246, and GC600 (see Figure 4.1;Tables 4.1, 4.2 and 4.3). In addition to elevated chloride (and typically sodium), briny sediments were characterized by moderate to high methane concentrations, low sulfate, extremely variable amounts of sulfide, high ammonium, high dissolved organic carbon (DOC) and nitrogen (DON), and variable rates of microbial metabolism (see Figure 4.1;Tables 4.1, 4.2 and 4.3). Only one push-core at GC600 contained noticeable hydrate (type III) but had similar geochemical features as the oil and seep sites described above. All cores were collected immediately upon retrieval from the seafloor and stored at 4 °C until further processing. All cores were processed within 8 hours following retrieval.

4.2.3 Processing

Two parallel cores of equal length and appearance were selected (i.e., > 25 cm for MUCs and > 15 cm for push-cores), one for porewater geochemistry and one for hydrocarbon gas and rate determinations. Sediment samples were collected in 3 cm intervals (reported as average depth below seafloor, in centimeters) for geochemical and rate analysis, using aseptic techniques at in situ temperature (4 degrees C). The cores were extruded into a polycarbonate chamber under argon atmosphere using a floor standing plunger assembly. The geochemistry core was subsampled for porewater and solid phase geochemistry, the rate core for hydrocarbon gases, rate assays, and metagenomics. Sub-samples were first collected for bulk porewater geochemistry using an ethanol-rinsed, stainless steel spoon, with care taken to avoid sampling near the polycarbonate liners.

Whole sediment was transferred into argon-filled polyoxymethylene squeezer cups ([41]), and the porewater extracted under mechanical pressure into acid-washed, Ar-flushed, plastic syringes using a custom argon-purged squeezer as described by Joye et al., 2004 ([17]). After discarding the first 1 mL of fluid, the porewater sample was collected into a 25 mL plastic syringe. At the end of squeezing, 0.5 – 2 mL of unfiltered porewater was transferred immediately into a 15 mL polycarbonate Falcon tube, preserved in 20 wt.% zinc acetate and later analyzed to quantify hydrogen sulfide (H_2S) via the methylene blue method ([42]). The amount of fixative used to preserve sulfide varied based on anticipated sulfide content (via smell): 100 µL zinc acetate solution was used in cores with no perceptible sulfide, and 500 µL zinc acetate in noticeably sulfidic cores.

Salinities were measured visually on a 500 μL porewater subsample using a hand-held refractometer (Cole-Parmer RSA-BR60). Porewater pH was measured on board using a ROSS pH electrode that had been calibrated with salinity corrected buffers (pH 4, 7, and 10) chilled to in situ temperature ([18]). The remaining pore water sample was filter-sterilized with a 0.2 μm Target filter, dispensed into high-density polyethylene bottle (HDPE; Nalgene), and further sub-sampled for downstream geochemical analysis (described below). The dewatered sediment was collected in a sterile whirl-pack bag, the bag flushed with argon, sealed without headspace, and frozen at −20 °C for solid phase analysis ([17]).

Rate cores were processed under anoxic conditions using similar procedures as the geochemistry core above. First, a 5 mL sub-sample was collected for short-chain alkane analysis using a cut-end syringe and transferred to an argon-flushed, 25 mL borosilicate glass serum vial containing 2 mL of 2 M NaOH to stop microbial activity. The sample was sealed with a blue chlorobutyl rubber stopper, crimp sealed, homogenized, and stored at room temperature until analysis. Gaseous hydrocarbons were analyzed later by a gas chromatograph equipped with a flame ionization detector (GC-FID; [17]). Samples for rates of microbial activity were collected in triplicate into custom cut-end Hungate tubes and sealed headspace free with double base-boiled and twice milliQ rinsed butyl rubber stoppers. Two controls were collected for each core, immediately injected with 3 mL of 2 M NaOH solution and homogenized to halt microbial activity. Both live incubations and controls were left to pre-incubate at 4 °C for 24 hrs before tracer addition to allow the microbial community to recover from sampling and processing activities. Incubation details are described below.

4.2.4 Geochemistry

Subsamples for dissolved inorganic carbon (DIC; 2 mL) were collected into evacuated 10 ml serum vials and preserved with 1 mL saturated CuSO4 and 1 mL of 56 mM $NaMoO_4$ in 10% v/v H_3PO_4. The headspace DIC was converted to methane using a methanizer and analyzed by GC-FID [17]. A 2 mL subsample of filtered porewater was collected for ammonium determination, preserved in 100 μL phenol solution, and analyzed on board the ship using the phenolhypochlorite method of Soloranzo (1969 [43]). An additional ammonium subsample was analyzed back in the laboratory in parallel with TDN analysis, again using the method outlined by Soloranzo (1969 [43]). A 5 ml subsample for major ions (sodium, magnesium, potassium, calcium, sulfate, and chloride) was preserved with concentrated nitric acid (0.1 μmol L^{-1} final concentration) and stored at room temperature until analysis by ion chromatography [17]. The remaining nutrient subsample was frozen at −20 °C until shore-based laboratory analysis. Total dissolved nitrogen (TDN) was analyzed via the oxidative combustion-chemiluminescence technique of Salgado and Miller (1998 [44]) using a Shimadzu TOC 5000 coupled to an Antek model 7020 NO analyzer [17].

Nitrate and nitrite were analyzed on a Lachat FIA 8000 Autoanalyzer using method 31-107-04-1-A, phosphate via the molybdate blue colorometric method, total dissolved phosphate (TDP) by high-temperature combustion and hydrolysis [45], dissolved organic carbon (DOC) by oxidative combustion-infrared analysis, methane by GC-FID, and stable ^{13}C isotopes of DIC by headspace analysis using a Picarro G2201-i isotope analyzer [15, 17]. Porewater methane samples were analyzed by gas chromatography using a flame ionization detector (GC-FID; SRI 8610C gas chromatograph; (1.8 m x 3.175 mm packed HayaSep–D column; [14]). Certified gas mixtures (0.1% CH_4 in He) were used to calibrate the instrument prior to analysis. Porewater hydrogen concentrations were determined by headspace equilibration ([46]) using the salinity– and temperature–corrected H_2 solubility constants of Crozier and Yamamoto [47]. Headspace hydrogen concentrations were obtained by injecting 1 mL of sample headspace into a Peak Performer 1 Reducing Compound Photometer (Peak Laboratories, USA; [48]), calibrated with certified standards. A subsample of sediment was analyzed for porosity, dried, analyzed for carbon, nitrogen, and phosphorus content, and then combusted to determine organic matter content by loss on ignition [14].

4.2.5 Microbial Activity

Rates of dissimilatory sulfate reduction (DSR) and the anaerobic oxidation of methane (AOM) were carried out using ^{35}S-labeled sodium sulfate ($Na^{35}_2SO_4$; American Radiolabeled Chemicals; 1.59 TBq/mmol), and ^{14}C-labeled methane ($^{14}CH_4$; American Radiolabeled Chemicals; approx. 1.85 TBq/mmol) as described elsewhere [49, 50]. Radiolabeled sulfate and methane tracers were both diluted in sterile milli-Q to yield stocks with an activity of 10^6 dpm per 100 µL. Samples and controls were injected with 100 µL tracer, incubated at 4 °C for 1 day at in situ pressure and temperature, and slurried with 3 mL of either 20 wt% zinc acetate (DSR), or 2 M NaOH (AOM), to halt microbial activity and preserve labeled oxidation products. The fixed samples were then stored at room temperature until distillation and analysis. Methane can be lost from samples due to degassing during core recovery. This loss of methane can lead to inaccurate estimates of rates of microbial processes that are dependent on methane availability ([18]). Beginning in 2010, all samples for AOM and SR were amended with 20 mM methane for rate assays to generate for more robust estimates of in situ activity ([18, 50]).

Fixed DSR samples were processed to quantify radioactively labeled sulfide using a standard one-step chromium distillation. Briefly, sediments were transferred to a 50 mL Falcon tube, rinsed of porewater and excess tracer three times by centrifugation and resuspension with 25 mL tap water. The rinsate was transferred to a 125 mL flask and brought to 100 mL total volume, of which, 100 uL was counted by liquid scintillation counting (LSC) to determine the total activity of unused tracer. The rinsed sediment sample was then transferred to a round-bottom boiling flask, placed in a heating mantle, and distilled with a solution of hot HCl and reduced chromium under a stream of nitrogen gas, as described by Fossing and Jørgensen ([51]). Evolved 35S from the distillation process was trapped in 5 mL of 2% zinc acetate solution as $Zn^{35}S$ and counted by LSC. DSR rates nmol cm^{-3} d^{-1} were calculated as:

$$\text{SRR} = \left[SO_4{}^{2-}\right] \times \phi_{\text{sed}} \times \frac{\alpha_2}{t} \times \left[\frac{\text{TRIS}}{^{35}SO_4{}^{2-}}\right] \times 1000 \tag{4.1}$$

where $[SO_4{}^{2-}]$ is the porewater sulfate concentration in mmol L^{-1}, ϕ the sediment porosity, α_2 the ^{35}S isotope fractionation factor (1.06) [51], TRIS the activity of the distillation trap (in dpm), and $^{35}SO_4{}^{2-}$ the total activity of injected tracer (dpm).

Samples for AOM were processed using an acid digestion technique ([50]). First, the samples were transferred from Hungate tubes to 50 mL Falcon tubes and purged with air for 45 minutes to remove unused methane tracer. The preserved samples were then transferred to a 125 mL Erlenmeyer flask, sealed with a specially modified, gas-tight stopper. The stopper was designed to hold a carbon dioxide trap (here, an uncapped 7 mL glass scintillation vial containing 1.5 mL 3–methoxypropylamine) a few centimeters above the sample via a plastic wire. Samples were acidified with 5 mL 30% H_2SO_4 (final pH <1) to convert radiolabeled DIC to CO_2 and digested for 4 hours on a shaker table. Following digestion, the trap was removed from the flask, filled with 5.5 mL scintillation fluid, and counted by LSC. Recovery was better than 95% on process controls. AOM rates nmol cm^{-3} d^{-1} were calculated as:

$$\text{AOM} = [CH_4] \times \frac{\alpha_1}{t} \times \left[\frac{^{14}CO_2}{^{14}CH_4}\right] \tag{4.2}$$

where $[CH_4]$ is the concentration of methane in µmol L^{-1}, α_1 is the ^{14}C isotope fractionation factor (1.008) [52], $^{14}CO_2$ is the activity of the oxidation product in dpm, and $^{14}CH_4$ is the total amount of injected tracer activity in dpm.

4.3 RESULTS AND DISCUSSION

This is the first large-scale assessment of microbial activity conducted under quasi-in-situ conditions across the Northern Gulf of Mexico. Recovered sediment cores were classified and subdivided into four groups according to geochemical regime: cores were labeled as controls, i.e., quiescent abyssal sites (type I), cores from oil and gas seeps (type II), cores from gas hydrate-bearing sites (type III), or cores from brine seeps, pools, and flows (type IV; see Figure 4.1 and Tables 4.1, 4.2). Average geochemistry and integrated rate data were parsed according to expedition and habitat and are presented in Tables 4.2 and 4.3. In total, the data encompass three control cores (type

Site	Core	Type	Cl^-	CH_4	Max CH_4	DOC	SO_4^{2-}	Min SO_4^{2-}	H_2S	NH_4^+	∑AOM	∑SRR
AC601	AT18.02–4640.16	IV	1482.9	102.2	172.1	1.4	1.1	0.0	2206.4	2340.5	0.0	4.6
	AT18.02–4641.04	IV	712.4	572.1	727.0	0.9	16.2	10.9	0.0	497.6	0.1	7.3
	AT18.02–4641.07	IV	583.0	12.5	18.5	1.3	27.9	26.5	26.0	235.8	0.0	9.1
	AT18.02–4641.19	IV	666.7	29.1	72.6	0.9	21.6	6.5	10225.0	–	0.0	3.0
GB425	AT18.02–4645.04	IV	623.0	291.1	425.1	1.6	29.5	24.2	481.3	220.0	2.9	82.1
	AT18.02–4645.13	IV	587.0	347.1	463.9	1.0	10.0	3.2	10674.3	183.2	0.1	22.7
GB480	EN586–S03.E07	I	553.8	3.4	6.5	0.3	27.1	26.7	0.0	7.3	BDL	BDL
GB697	AT18.02–4646.02	IV	2883.0	347.4	632.7	1.3	15.4	1.2	209.0	826.3	0.0	0.1
	AT18.02–4646.04	IV	634.9	318.8	408.8	1.3	4.4	0.9	10556.7	82.3	1.3	10.5
GC185	EN528–S29.E06	II	544.4	6.3	7.5	0.6	28.2	27.1	0.0	31.2	BDL	0.7
	EN559–S05.E05	II	568.7	4.3	5.8	0.6	28.3	27.8	31.4	130.1	0.0	2.0
	EN586–S02.E13	II	555.8	5.0	7.6	0.6	28.2	27.8	0.0	46.8	BDL	0.1
GC186	EN559–S06.E05	II	566.4	1.7	2.3	0.7	28.0	27.6	0.0	117.6	BDL	0.0
GC233	AT18.02–4653.03	IV	990.9	9.5	13.6	0.7	17.5	9.4	7982.0	298.6	0.1	165.9
	AT18.02–4653.17	IV	755.2	466.3	687.8	0.5	7.5	1.0	14834.0	582.5	2.1	21.3

Table 4.1: Summary of average geochemistry (mmol L^{-1} for chloride, DOC, and sulfate; µmol L^{-1} for methane, sulfide and ammonium; and mmol m^{-2} d^{-1} for integrated rates of AOM and SRR), for control (type I), gas-seep (II), hydrate (III), and brine (IV) cores. Rates integrated over 20 cm to provide consistency between cores. Data from expeditions AT18–02, EN528, EN559 and EN586. Abbreviations: max = maximum concentration; min = minimum concentration; BDL = below detection limit. Values of 0.0 are smaller than the chosen order of magnitude.

I), seventeen cores broadly classified as oil and gas seeps (type II), one core associated with gas hydrate (and perhaps brine; type III), and twenty-seven cores from sites of obvious brine seepage (type IV).

4.3.1 Non-seepage Impacted Sites

There were considerable differences in sediment geochemistry between our control sites (type I), oil/gas sites (type II), hydrate site (III), and brine sites (IV; see Figures 4.2 and 4.3). The average geochemistry and microbial activity at the type I control sites were significantly different - i.e., generally lower - than every other habitat type (see Figures 4.2 and 4.3). On average, the control site sediments (GC699 and GB480) were methane poor (approx. 6.3 µmol L^{-1} CH_4), sulfide free, contained abundant sulfate, and were not influenced by brines (see Figures 4.3, 4.5, and 4.4; Tables 4.2 and 4.3). The control cores contained moderate amounts of DON (29.0 µmol L^{-1} DON), ammonium (8.4 µmol L^{-1} NH_4), and DOC (374.7 µmol L^{-1} DOC), as well as low levels of nitrite (0.2 µmol L^{-1}; see Figures 4.2 and 4.3). Average nitrate and phosphate concentrations at control sites (15.1 μmol L^{-1} NO_3 and 5.4 μmol L^{-1} $PO_4{}^{3-}$) were similar to those of the more active oil and gas seeps, although they were considerably less variable, as inferred from the smaller error associated with control averages (see Figures 4.2 and 4.3).

The quiescent abyssal type I sites at GC699 and GB480 were geochemically unremarkable and had very low rates of microbial activity, rates of anaerobic oxidation of methane were below detection and rates of sulfate reduction were approximately 15 pmol cm^{-3} d^{-1} (see Figures 4.2 and 4.3). Average chloride concentrations varied little between control cores (553 – 568 mmol L^{-1}; see Figures 4.5, 4.4). The only geochemical parameter that displayed significant differences between average and median concentrations for control cores was nitrate (see Figure 4.3). Both average and integrated rates of SR were approximately 10 pmol cm^{-3} d^{-1} and AOM rates were below detection in every core (see Tables 4.1 and 4.2). While most of the geochemistry was unremarkable, especially compared with the more active sites, down-core profiles show muted redox zonation with depth (see Figure 4.5, and 4.4). These data from non-seepage-influenced sites is consistent with previous data describing control sediments [14], namely the sites show little sulfate depletion and very low rates of sulfate reduction and anaerobic oxidation. The vast majority of sediments in the Gulf are likely similar to this.

Similar trends were observed in the control core en586—s07.e07 at GC699 (see Figure 4.5). The first 20 cm of this core was nearly sulfide free but then accumulated to nearly 10 μmol L^{-1} at 30 cmbsf. Methane concentrations were higher here than in the GB480 core, increasing steadily with depth to a maximum concentration of nearly 15 15 μmol L^{-1} CH_4. Similar to the GB480 core, ammonium accumulated in the porewater below 20 cmbsf to 35.9 μmol L^{-1} - nearly double that of the GB480 core – with a smooth decrease in nitrate concentrations from around 30 μmol L^{-1} at the seawater sediment interface to nearly below detection at 30 cm depth. Both the GC699 and GB480 control sites are probably diffusion controlled and apparently have significant oxygen penetration in the first 10 cm. These data further underscore the low rates of metabolism supported by the background sediment flux to the seabed in the Gulf [17]. The differences between average and median concentrations of geochemical species between two control cores at GC699 and

Site	Core	Type	Cl^-	CH_4	Max CH_4	DOC	$SO_4{}^{2-}$	Min $SO_4{}^{2-}$	H_2S	$NH_4{}^+$	$\sum$AOM	$\sum$SRR
GC246	AT18.02–4651.07	IV	1791.3	145.3	211.8	0.9	8.8	0.5	1600.0	555.0	0.7	1.3
	AT18.02–4651.19	IV	2914.7	608.6	845.8	0.9	3.0	0.2	1748.0	1644.5	1.1	1.9
	AT18.02–4656.03	IV	3019.5	245.9	338.6	0.6	2.1	0.2	708.3	2250.7	0.3	55.0
	AT18.02–4656.18	IV	2796.6	472.2	712.8	0.7	10.6	1.0	0.0	1947.6	0.0	3.3
	AT26.13–S06.E01A	IV	–	1457.0	2327.2	1.9	3.9	0.7	0.0	2888.7	0.7	9.5
	AT26.13–S06.E01B	IV	–	–	–	1.4	6.1	0.3	538.3	2418.4	–	–
	AT26.13–S08.E03A	IV	–	1018.5	1621.1	0.8	4.4	0.6	138.0	1881.9	–	–
	AT26.13–S08.E03B	IV	–	1226.3	1581.6	0.8	4.7	0.7	0.0	3476.6	–	
GC415	EN528–S27.E07	II	595.5	1697.5	2226.3	2.4	9.7	0.9	33.3	288.0	4.4	333.5
	EN528–S27.E15	II	583.4	10.0	15.5	0.8	26.7	22.8	0.0	76.0	BDL	1.6
GC600	AT26.13–S05.E01	III	596.7	323.2	1234.5	1.4	22.8	13.9	950.0	224.1	0.3	25.9
	AT26.13–S05.E03	IV	1438.2	1580.2	3228.1	6.9	12.4	3.7	640.0	234.7	0.2	0.2
	AT26.13–S05.E12.1	IV	620.6	1396.1	2188.6	1.7	9.3	1.3	5820.0	259.6	3.5	25.5
	AT26.13–S05.E12.2	IV	617.8	747.4	1922.5	3.3	6.4	0.7	4683.3	262.6	0.9	13.9
	AT26.13–S05.E12.3	IV	617.4	923.6	1688.8	1.6	16.7	5.4	–	111.2	0.8	1.5
	AT26.13–S05.E14	IV	615.5	2052.1	4650.7	1.4	7.7	0.8	8485.7	91.3	6.1	26.6
	AT26.13–S05.E24	IV	961.0	1014.6	2019.8	3.1	10.4	1.3	2285.7	1819.2	–	2.2
	AT26.13–S05.E25	IV	588.2	27.2	50.5	0.9	28.2	26.4	0.0	30.2	BDL	0.0
	AT26.13–S05.E33	IV	574.4	214.7	1388.8	1.0	15.8	0.7	5216.7	247.8	0.0	0.7
	AT26.13–S05.E34	IV	555.7	304.7	913.6	0.9	11.7	1.6	8700.0	93.0	1.1	21.8
	EN527–S01.E05	II	562.2	695.4	2155.1	2.3	15.6	0.7	28.6	52.0	0.5	2.5
	EN527–S01.E07	II	553.2	609.1	2241.7	1.5	21.0	10.3	44.4	36.3	0.0	2.9
	EN559–S02.E06	II	566.9	55.1	124.9	0.8	26.0	23.7	157.1	139.0	0.0	0.6
	EN559–S02.E17	II	560.2	384.6	1732.9	1.2	19.8	2.7	385.7	211.5	1.5	14.7
	EN586–S04.E11	II	560.8	384.7	915.1	1.2	15.3	7.0	428.6	92.0	0.4	26.6
	EN586–S18.E11	II	565.6	17.5	32.0	0.3	27.5	23.9	85.7	75.8	BDL	0.3
GC699	EN586–S07.E07	I	561.7	11.1	14.9	0.6	27.7	27.4	1.4	15.4	BDL	0.0
	EN586–S19.E06	I	560.6	4.1	5.9	0.2	27.8	27.0	0.0	1.6	BDL	
GC767	EN559–S25.E03	II	568.4	3.8	5.4	0.5	28.4	28.0	0.0	44.9	BDL	BDL
	EN559–S25.E17	II	566.5	3.5	4.8	0.5	28.5	28.0	–	52.1	BDL	BDL
	EN586–S06.E09	II	562.3	2.9	3.9	0.5	28.2	27.8	0.0	10.3	BDL	0.0
	EN586–S6.E06	II	560.2	3.9	8.2	0.2	28.1	27.7	0.0	18.1	BDL	BDL
MC118	EN586–S20.E02	II	555.7	939.5	2690.0	0.6	16.3	2.6	275.7	164.6	9.3	76.2

Table 4.2: Summary of average geochemistry (mmol L^{-1} for chloride, DOC, and sulfate; μmol L^{-1} for methane, sulfide and ammonium; and mmol m^{-2} d^{-1} for integrated rates of AOM and SRR), for control (type I), gas-seep (II), hydrate (III), and brine (IV) cores. Rates integrated over 20 cm to provide consistency between cores. Data from expeditions AT26–13, EN527, EN528, EN559 and EN586. Abbreviations: max = maximum concentration; min = minimum concentration; BDL = below detection limit. Values of 0.0 are smaller than the chosen order of magnitude.

GB480 were negligible. Figure 4.4 shows a suite of down-core profiles for a GB480 core. Here, sulfide accumulated to <2 uM <2 μmol L^{-1} at 12 cmbsf but diminished quickly thereafter. Average methane concentrations were generally low, but the profile shows a slight accumulation to approximately 6.5 uM 6.5 μmol L^{-1} between 15 and 30 cmbsf, just below the sulfide maximum. Ammonium reaches a maximum within this horizon as well (18 μmol L^{-1}) concomitant with a doubling of DOC concentrations below 20 cmbsf and a 20 μmol L^{-1} decrease in nitrate (see Figure 4.4), perhaps indicative of dissimilatory nitrate reduction to ammonium (DNRA), nitrate reduction coupled to sulfide oxidation, or denitrification in these cores.

4.3.2 Seepage Impacted Sites

Hotspots of activity were documented frequently in seepage-influenced sediments. The type II oil/gas sites of GC600, GC415, GC767, GC185, GC186, MC118 exhibited variable geochemical signatures, but contained moderate amounts of methane and sulfide, were microbially active, had elevated concentrations of DON, ammonium, nitrite, DOC, and moderate amounts of phosphate (see Figures 2 and 3). The single type III hydrate core was recovered from GC600 (core; at26.13-s05.e01; see Table 3) and was methane-rich, moderately sulfidic, contained elevated ammonium, nitrite, nitrate and DOC, and had moderate rates of microbial activity. This was a shallow core but the underlying sediments were likely impacted by hydrate brines. The type IV brine sites were geochemically distinct, containing the highest average amounts of methane, sulfide, DON, ammonium, and phosphate of all the sites. Elevated DOC was a consistent feature of the type IV sites, but maximum concentrations were found among the type II seeps.

More than 19 cores spanning eight sites of confirmed oil/gas seepage (type II cores) were compared for bulk sediment geochemistry and rates (GC185, GC186, GC415, GC600, GC767, and MC118; see Tables 4.1 and 4.2). These sites were characterized by elevated average methane concentrations (257.6 μmol L^{-1} CH_4; see Figure 4.2), elevated sulfide (0.7 mM; see Figure 2B), moderate to high rates of AOM (2.7 nmol/cc/d; see Figure 4.2), high average sulfate reduction rates (125 nmol L^{-1}; see Figure 4.2), moderate concentrations of ammonium and DON (92 μmol L^{-1}

Lease Block	Chloride	Methane	Sulfate	Sulfide	DOC	NH_4^+	Nitrate	Nitrite	DON	AOM	SRR
AC601	968.2	131.9	14.2	3.8	1.16	1463.3	0.0	0.0	0.0	0.5	59.7
GB425	607.5	315.6	21.2	5.2	1.32	203.9	–	–	–	7.8	240.2
GB480	553.8	3.4	27.1	0.0	0.30	7.3	12.3	0.2	31.7	0.0	0.0
GB697	1983.8	337.3	11.0	4.1	1.33	563.7	–	–	–	4.6	42.1
GC185	556.8	5.1	28.3	0.0	0.57	69.1	7.8	0.3	47.1	0.0	3.3
GC186	566.4	1.7	28.0	0.0	0.68	117.6	19.7	0.8	43.5	0.0	0.0
GC233	883.8	217.1	12.9	11.4	0.65	427.6	–	–	–	6.0	568.2
GC246	2649.1	713.2	5.4	0.6	0.95	2212.1	8.1	3.0	2444.2	5.2	200.4
GC415	589.8	659.0	17.7	0.0	1.61	188.2	29.8	6.4	466.7	10.9	859.8
GC600	609.3	615.8	17.3	2.2	1.73	254.2	14.5	1.8	165.6	6.2	68.9
GC699	561.2	7.9	27.7	0.0	0.41	9.0	16.7	0.2	27.5	0.0	0.0
GC767	564.6	3.5	28.3	0.0	0.43	32.7	14.7	0.5	26.7	0.0	0.0
MC118	555.7	939.5	16.3	0.3	0.64	164.6	15.9	5.6	42.2	19.9	212.0

Table 4.3: Average geochemistry in mmol L^{-1} for chloride, DOC, and sulfate, in µmol L^{-1} for methane, sulfide, ammonium, nitrate, nitrite, and DON, and in nmol cm^{-3} d^{-1} for rates of AOM and SRR). Abbreviations: max = maximum concentration; min = minimum concentration; BDL = below detection limit. Values of 0.0 are smaller than the chosen order of magnitude.

and 103 µmol L^{-1}, respectively; see Figure 4.3), elevated concentrations of nitrite (1.5 µmol L^{-1}; see Figure 3C), nitrate (13.6 µmol L^{-1}), DOC (878 µmol L^{-1}), and phosphate (9 µmol L^{-1}; see Figure 4.3; Tables 24.1 and 4.2). Average SR rates at these sites (125.1 nmol cm^{-3} d^{-1}; see Figure 4.2) were of similar magnitude as both those of the hydrate core (171.9 nmol cm^{-3} d^{-1}) and the brine cores (155.7 nmol cm^{-3} d^{-1}), but AOM rates were lower (2.7 nmol cm^{-3} d^{-1}) than either the hydrate or brine site (3.5 nmol cm^{-3} d^{-1} and 7.2 nmol cm^{-3} d^{-1}, respectively; see Figure 4.2). Average seep sulfide concentrations were lower than those found in the hydrate core (1.0 mM), and only 20% those observed in the brine cores (see Figure 2B). Average methane concentrations for the oil/gas seeps (257.6 µmol L^{-1}) were about 20% lower than the hydrate site at GC600 (323 µmol L^{-1}; core at26.13–s05.e01; see Table 4.1). Average type II sulfide concentrations were the lowest of all non-control cores (0.7 mM H_2S; see Figure 4.2).

The geochemistry of the one gas hydrate core (core at26.13-s05.e01) was distinct from the type I controls and type II seeps (see Tables 4.1 and 4.2). Average concentrations of methane (323 µmol L^{-1}) and sulfide (1.0 mM) were both slightly higher than those found at type II seeps, but lower than those of the type IV brines (see Figures 4.2 and 4.3). The hydrate core contained more DON, nitrite, and nitrate, but less phosphate than either the type I control or type II seep cores. Average phosphate concentrations were 4 µmol L^{-1} (versus 9 µmol L^{-1} in the seep cores), DON concentrations were 156 µmol L^{-1} (versus 100 µmol L^{-1} in the gas/oil cores), and ammonium concentrations were 224 µmol L^{-1} (see Figure 4.3). Nitrate concentrations were higher (18.8 µmol L^{-1}) than those found in any of the other seep habitats (see Figure 4.3). The hydrate core contained roughly similar amounts of DOC (1421 µmol L^{-1}) as observed in sites impacted by brines (see Figure 4.3).

Core AT2613-S05.E01 was short - only about 17 cm long - due to the presence of hydrate in the sediment that prevented the core liner from penetrating further into the sediment (see Figure 4.6). This core was collected using a MUC but the effectiveness of the MUC diminishes quickly in sandy sediments, sediments with carbonate crust or hardgrounds, and particularly in gas-hydrate bearing sediments. The down-core profile suggests that most of the activity at this site occurs below 10 cm and likely increases dramatically below 20 cmbsf (see Figure 4.6). Within the 7 cm horizon between 10 cm and 17 cm depth, sulfide increases by over 3 mM, methane concentrations increase to 1.2 mM, SR rates increase to 428 nmol cm^{-3} d^{-1} and AOM rates increase to 16 nmol cm^{-3} d^{-1} (see Figure 4.6). Ammonium values were high (224 µmol L^{-1}; 295 µmol L^{-1} max) and DOC (2.2 mM max) also becomes abundant within the first 10 cm. The average DOC concentration (1472 µmol L^{-1}) in the hydrate core was quite high, and indistinguishable from that of the type IV brine sites. The hydrate site where this core was collected was laden with oil and it is likely that the high DOC at this site resulted from this.

The type IV brine cores contained highly reduced pore fluids with the highest average sulfide (3.5 mM), ammonium (1068 µmol L^{-1}), phosphate (16 µmol L^{-1}), DON (600 µmol L^{-1}), and methane concentrations (513 µmol L^{-1}) of any other habitat (see Figures 4.2 and 4.3). Average SR rates for the type IV cores (155.7 nmol cm^{-3} d^{-1}) were comparable to those found at type II oil and gas seeps (125.2 nmol cm^{-3} d^{-1}), and most similar to that of the hydrate core (171.9 nmol cm^{-3} d^{-1}). The highest rates of anaerobic methanotrophy were recorded at brine sites (7.8 nmol cm^{-3} d^{-1}; 155.6 nmol cm^{-3} d^{-1} maximum; see Figure 4.3). However, most AOM occurred along subsurface porewater salinity gradients similar to brine pools in the area ([31]), suggesting an optimal salinity/nutrient regime for AOM in brine systems and underscoring the role of elevated methane concentration in driving high activity rates in brine sediments. Even though more reduced forms of N are abundant at the brine sites, nitrate concentrations were approximately half (7.2 μmol L^{-1} nitrate) those observed at the other sites (13.3 μmol L^{-1} to 18.9 μmol L^{-1} nitrate; see Figure 4.3), suggesting nitrogen reduction processes are active or that ammonium oxidation activity is limited by the high salinity.

Rates of sulfate reduction and AOM in the briny cores were much higher than previously reported for brine sites in the Gulf [14]. None of the briny sites sampled by Joye et al. (2010 [14]) were sampled in this study. Most of the briny sites in this data set were characterized by much more active brine flows and fluid discharges than those included in the previous study from Joye et al. Joye et al. (2010) reported findings from the Chemosynthetic Ecosystems III (CHEMO III) study, which focused on habitats with large populations of chemosynthetic animals [14]. Active brine flows and intense brine discharges, such as that observed at the GB425, GC246 or GC697 mud volcanoes, are not conducive to development of animal communities [53]. In particular, the high particle flux resulting from episodic discharges of fluidized mud inhibits chemosynthetic animals by interfering with their ability to obtain oxygen (plumes of tube worms or gills of mussels would be fouled by particles). However, the more rigorous discharge regimes at the sites included in this study likely provide more rich substrates regimes to the local microbial populations, stimulating their growth and metabolism.

Previous data was available from some of these sites, offering an opportunity to assess changes over time and/or spatial variability. The AC601 brine seep was described previously by [54] using cores collected from along the edge of the brine lake during a 2006 ALVIN expedition. The brine lake at AC601 is surrounded by a swash zone that is peppered with barite. The cores collection described by Crespo-Medina et al. (2016) documented striking variability in microbial activity in sediments from near the brine lake versus those collected some 40 m away from the lake edge [54]. Microbial activity near the brine lake was limited by sulfate availability, but in the barite swash zone where sulfate, methane and DOC were more abundant, sulfate reduction rates were high (35 to 70 mmol m^{-2} d^{-1}); rates of anaerobic oxidation of methane were low (0.1 to 0.6 mmol m^{-2} d^{-1} [54]). Cores from AC601 assessed during this study (Table 4.1) targeted the high activity swash zone and documented average rates of sulfate reduction (60 nmol cm^{-3} d^{-1}) and anaerobic oxidation of methane (0.5 nmol cm^{-3} d^{-1}). The highest rates of sulfate reduction (300 nmol cm^{-3} d^{-1}) and anaerobic oxidation of methane (2.5 nmol cm^{-3} d^{-1}) documented in this study were lower than (sulfate reduction of 2000 nmol cm^{-3} d^{-1}) or comparable to (anaerobic oxidation of methane of 15 nmol cm^{-3} d^{-1}) those reported by Crespo-Medina et al. The AC601 site exhibited fairly consistent patterns of activity between 2006 and 2010. The highest average sulfide values for some of the brine seep sites AC601 (3.8 mM) and GB425 (10.7 mM) were quite high, with the high average at AC601 resulting from the extremely sulfidic AC601 areas driven by high sulfate availability via barite dissolution [54] (see Table 4.1).

Similarly, the GC233 brine site was the focus of a 2005 paper by Orcutt et al [12]. The GC233 site – known also as the NR1 brine pool – has been a focus of study for decades; it was first described by MacDonald et al. (1990 [28]) and the first biogeochemical assessment was done by Orcutt et al. (2005 [12]). In the 1990s, the site was studied extensively by Fisher et al. [53, 55, 56] to learn how chemosynthetic animals endured the harsh conditions of the brine pool. Orcutt et al. (2005) reported extremely high rates of sulfate reduction at this site (up to 3500 nmol cm^{-3} d^{-1}) and low rates of anaerobic oxidation of methane (1 nmol cm^{-3} d^{-1}) [12]. Rates of sulfate reduction (500 nmol cm^{-3} d^{-1}) were generally much lower than those documented by Orcutt et al. while anaerobic oxidation of methane (up to 50 nmol cm^{-3} d^{-1}) were considerably higher. The visual presentation of the central brine pool changed considerably over time. Considerable rates of sulfate reduction were documented in the central brine pool during a 2002 expedition [30]. During the 2010 expedition, the brine fluid was discolored (dark instead of brown) and it was laden with particles, apparently iron sulfides. The fluid smelled of sulfide, suggesting it was much more stagnant than during previous samplings. Brine infused sediments may have received considerable sulfide loading via brine seepage, but overall, the site appeared less active in terms of fluid flow in the 2010 sampling, compared to sampling eight years earlier.

4.3.3 INTRA-SITE VARIABILITY AT OIL AND GAS SEEPS

Unlike the relatively consistent geochemistry observed in control cores, seep sediments exhibited highly variable geochemistry and rate profiles, not only between sites (e.g., GC767 vs MC118) but also from sediments located within the same site (e.g. GC415, GC600; see Tables 2 and 3). Methane concentrations averaged by site, like MC118 (940 µmol L^{-1} CH_4), GC600 (616 µmol L^{-1} CH_4), GC246 (713 µmol L^{-1} CH_4), and GC415 (660 µmol L^{-1} CH_4) were significantly higher than those at GC185 (5 µmol L^{-1} CH_4), GC186 (1.7 µmol L^{-1} CH_4), and GC767 (3.5 µmol L^{-1} CH_4; see Table 4.3), even though some of these lower activity sites were collected near locations of prolific seepage (i.e., GC185 [57]). Contrary to the implications of a predicted 1:1 stoichiometry of sulfate-coupled AOM - namely, one mole of sulfide produced per mole of methane oxidized - average sulfide concentrations did not correlate with methane (see Figure 4.14).

The geochemistry of some sampling locations (e.g., GC185, GC699, GC246, etc.) was consistent between cores, while others contained a mix (e.g., GC600, GC415, etc.). Three of the four cores from the brine site AC601 contained elevated porefluid salinity (>600 mM porewater Cl), but one did not (at18.02—4641.07 see Table 4.1), even though it was collected proximal to the main brine lake. Representative samples collected at GC600 fell into three of the four categories (i.e., types II, III, and IV). Figures 4.2and 4.3 show the average (gray bars) and median (blue bars) values for methane, sulfide, microbial activity, DOC, ammonium, nitrate, nitrite, dissolved organic nitrogen, and chloride, by site type. Table 4.3 present average values for methane, sulfide, DOC, ammonium, nitrite, nitrate, DON, chloride, and rates of AOM and SR by site name rather than by site type (discussed below).

The inherent variability present at some of the more active seep sites is reflected in differences between median and mean values for key parameters, like sulfide. The documented variability is real and it is important: extensive spatial variability within a site is a characteristic of cold seeps. The patchy and stochastic nature of seepage generates a diverse and biogeochemical mosaic that turns microbial populations on and off in response to variations in electron donor and accepter availability. The concept of biogeochemical 'hot spots and hot moments' [58] to characterize terrestrial regimes where biogeochemical reactions were accelerated applies quite well to cold seeps, as exemplified by this data set.

However, Bernhardt et al. (2017) went further and introduced the idea of "ecosystem control points" [59]. At cold seeps and in other systems, localized inputs of energy through fluid seepage exert a disproportional influence on the biogeochemical signature of an area, i.e., fluid seepage promoting the formation of Beggiatoa mats or extensive beds of chemosynthetic mussels. Bernhardt et al. (2017) underscore the fact that hot spots in the terrestrial realm are regulated by transport phenomena; the same is true for the deep sea. They considered areas of disproportional influence to be 'ecosystem control points'. In the deep sea, seepage acts as an ecosystem control point that dictates the biogeochemical signature of the system and helps modulate the composition and activity of microbial communities [60].

The geochemical variability within the GC600 site illustrates the heterogeneous nature of the seafloor surrounding prolific oil and gas seeps. Average methane values between cores ranged from 17.5 μmol L^{-1} CH_4 to >2 mM CH_4. Chloride concentrations – used as a proxy for brine input – varied from seawater values of approximately 550 mM to 1.4 M Cl (core at26.13-s05.e03; see Table 4.2). Some cores contained little sulfide (*e.g.,* at26.13-s05.e25), while others were putrid (8.7 mM average; core at26.13-s05.e34; see Table 4.2). Sediment geochemical signature and microbial activity was not necessarily predictable from the location of core collection. For example, some samples were collected from areas with microbial mats [17]. Microbial mats have long been considered a robust way to target areas of seepage. Some of the mat cores collected in this study had modest or low rates of activity.

As noted previously, seepage at a given location is highly variable in space and time. Cores with the highest rates of activity reflect the most recent and intense seepage impact, as suggested by Bowles et al. (2019 [19]). As oil and gas (or brine) move through the sediments, the local microbial population responds to that input by increasing their activity and processing the introduced material. Prolonged seepage input can lead to increased biomass and/or ingrowth of specialist organisms. For example, sulfide accumulation in the pore fluid creates ideal conditions for the proliferation of microbial mats, e.g. by Beggiatoa [9] or Thiomargarita [61], along the sediment water interface. When seepage abates, the accumulated sulfide is slowly oxidized and the microbial mat may persist, but the underlying sediments may not be as active, as one would expect from the presence of a mat. Hence, there can be a disconnect between the presence of a microbial mat – which can serves as a "bulls-eye" target high activity areas – and the rates of sulfate reduction at the site.

One of the GB425 cores (at18.02—4645.13; see Table 4.1) also had highest maximum values (18.5 mM) of all the type II seep sites. Average rates of SR varied over an order of magnitude, from below detection at GC767 and GC186, to 26 mmol m^{-2} d^{-1} at GC600, 76 mmol m^{-2} d^{-1} at MC118, and up to 333 mmol m^{-2} d^{-1} at GC415 (core en528–s27.e07; see Tables 4.2 and 4.3). This is the highest cumulative SR rates in this study, yet the companion core (en528-s27.e15) from the same MUC deployment contained only 0.5% as much methane, 33% the DOC, over double the sulfate, 26% the dissolved ammonium average, undetectable AOM rates, and cumulative SR rates of 1.6 mmol m^{-2} d^{-1}, or only 0.5% that of the sister core (see Table 4.2). The extremely active core at GC415 is not unusual for a seep site in the Gulf; the highest SR rates reported to date in the Gulf were observed at MC118 (1429 mmol m^{-2} d^{-1}; [18]).

Despite the high sulfate reduction rates observed at many seeps, a lot of the AOM rates at seep sites were below detection, including those at GC767 (all four cores), GC415 (one of two), and GC185 (all three cores). The highest rates of AOM at seep sites were observed at MC118 (9.3 mmol m^{-2} d^{-1}), GC600 (6.1 mmol m^{-2} d^{-1}; core at26.13—s05.e14), GC415 (4.4 mmol m^{-2} d^{-1}). Inter-site variability was observed at nearly every site (see Figures 2 – 6) with just as many cores showing high activity, as low. Surprisingly, methane concentrations and rates of anaerobic oxidation of methane were, on average, highest at brine seeps. Previous results [30] had that rates of anaerobic oxidation of methane were expected to be low, if not below detection, in brine-influenced samples because of the thermodynamic challenges of living at high salinity. Cores from brine seeps exhibited substantial variability vertically in the cores and in between cores from a given site (see Figures 4.8, 4.6; Supplemental Figures A.15 – A.20; Table 4.2). Though the highest AOM rates were observed at gas and oil seeps (GC415, MC118 >10 nmol cm^{-3} d^{-1}), measurable rates of approx. 5 nmol cm^{-3} d^{-1} were consistently observed in brine-influenced sites, even in extremely challenging environments such as the sediments collected in brine flows at GC246 (chloride approx 2.6 M) and GB697 (chloride ca. 1.9M).

4.3.4 Driving Factors

Examining the relationship of major parameters versus chloride help identify the factors driving differences between sites. Previous studies documented strong relationships between chloride content and other geochemical variables, including ammonium, dissolved organic carbon, phosphate and silica [14, 15]. A plot of dissolved organic carbon versus chloride builds on previous observations (see Figure 4.15). Distinct relationships between dissolved organic carbon versus chloride across brine sites (e.g. AC601, GB697, GB246) likely reflect source salt and brine history [14]. The deeply sourced brine from AC601 has a higher DOC load than the shallow sourced brines from GB697 and GC246 [14]. Sites impacted by oil and gas seepage show no relationship between chloride and dissolved organic carbon because the dissolved organic carbon is likely derived from oil.

The relationship between dissolved ammonium versus chloride was more compelling and informative (see Figure 4.16). The AC601 brine contains a higher ammonium per salt load than brines from GB697 and the chemistry of the GC246 brine exhibits a remarkable trend between ammonium and chloride. The GC246 samples were the most brine-influenced we obtained – some cores contained 4M chloride, which is roughly 7.2 times seawater. Halite saturation occurs at about 10 times seawater salinity. The GC246 brine is highly concentrated and remarkable, containing 3 mM ammonium. Unlike GB697 brine fluids, which contained much less ammonium per salt load (see Figure 4.16) or AC601, which showed a consistent stoichiometry between ammonium and salt, the GC246 fluids showed continuing and profound ammonium enrichment with increasing salt content. Ammonium in particular is a good indicator of depth to salt, with higher ammonium concentrations reflecting more deeply sourced salt [14]. Some pore fluid constituents like dissolved organic nitrogen were markedly higher at gas and oil seeps than at brine seeps (see Figure 4.17). It is unclear why oil and gas seeps – especially GC415 – have such high concentrations of dissolved organic nitrogen (1000 μmol L^{-1}) in pore fluids but two sites with gas and oil impact, GC600 and GC415, and which supported extremely high rates of microbial activity, also had high rates of dissolved organic nitrogen. The GC415 site has <500 μmol L^{-1} ammonium while at GC600, dissolved organic nitrogen concentrations were comparable to ammonium concentrations. Typically, cold seeps are considered nitrogen limited [17] but these two sites sported very high nitrogen levels, among the highest reported for Gulf cold seeps. It is possible that nitrogen fixation is active at these sites, accounting for the high N levels measured [62].

Overall, rates of anaerobic oxidation of methane were much lower than sulfate reduction rates (see Figure 4.18), consistent with previous reports from the Gulf [14, 15, 17]. We report some of the highest rates of anaerobic oxidation of methane measured at Gulf seeps and brine seeps exhibited the highest average rates of activity (see Figure 4.8, Table 4.3). Brines are generally replete in dissolved organic and inorganic nitrogen compared with oil and gas impacted sites. Each site had slightly different ammonium, DON and DOC signatures. The disconnect between rates of anaerobic oxidation of methane and sulfate reduction plus the increase in dissolved organic carbon and ammonium suggest that sulfate reduction is the terminal metabolism for dissolved organic carbon in brines.

We did not document rates of anaerobic oxidation of methane comparable to the extraordinary rates - μmol cm^{-3} d^{-1} levels - reported by Bowles et al. (2019), but this is not surprising [19]. The seeps samples from MC118 reported by Bowles et al. were collected from an active oil seep adjacent to a massive gas hydrate mound. The area was impacted by active seepage and the microbial community was clearly well-poised to support high rates of activity. While the sulfate reduction rates measured in this study aligned well with those of Bowles et al., the rates of anaerobic oxidation of methane were about ten times lower for the same methane concentration. This suggests that distinct populations of anaerobic methanotrophs with locally-poised kinetics exist across the seep spectrum in the Gulf, and underscores that observations of high activity rates from one prolific oily, gassy seepage regime cannot – and should not – be extrapolated to other sites in the system. Each seep system appears to be quite unique.

4.3.5 VARIABILITY

The distribution of geochemistry and rate data for the entire dataset show significant right skew (see Supplementary Figures A.21 - A.31), and in the case of sulfate and ammonium, are bimodal (see Supplementary Figures A.30 and A.21). Many studies routinely report average concentration and rate data for large datasets ([14, 15, 18, 63]), which is broadly applicable as a measure of central tendency for symmetrically distributed data. However, our dataset is skewed in nearly every parameter; a feature driven by the extremely variable nature of oil and gas-impacted and brine-impacted seeps. Because median values are insensitive to outliers, they are the preferred measure of central tendency with highly skewed data. Different trends emerge depending on which measure is used (see Figures 4.2, 4.3). We suggest here that median values are perhaps more meaningful than arithmetic averages for these kinds of data.

The GC185 site is known as a prolific oil and gas seep where high rates of AOM and SR have been observed ([63]). However, the geochemistry of cores obtained from GC185 and adjacent GC186 site in this study were consistently unremarkable, even over 3 separate expeditions (see Table 4.2). Rates of AOM were below detection in all but one core (EN559—s05.e05; average of 13 pmol cm^{-3} d^{-1}). This core had moderate cumulative SR rates 2 mmol m^{-2} d^{-1}, modest sulfide accumulation (31 µmol L^{-1}), and elevated ammonium (130 µmol L^{-1} NH_4). The GC185 area was long considered one of the most active seepage areas in the Gulf of Mexico, as evidenced by the long term occurrence of fields of large hydrate mounds and extensive accumulations of tube worms, hence the common name of the site, "Bush Hill" [64]. In 2016, submersible examine of the site revealed that the central area – which had always been filled with numerous, large gas hydrate mounds since the early 1990s - was free of hydrate and many of the tube worms, many more than usual, were dead. Tube worm bushes were covered with sediment (S. Joye, pers. com.). Bottom water temperature in 2016 was almost 12 °C, which would have resulted in gas hydrate dissociation. Higher bottom water temperatures does not explain why gas and oil seepages rates would decrease, but if there was a massive discharge, carbonate precipitation may have reduced flow through the subsurface, and ultimately reduced the seep signature of the site and muted microbial activity subsequently.

At brine sites, sulfate reduction reached high levels but overall sulfate reduction appeared to be limited by sulfate availability. Most of the brine-impacted samples in this study were halite derived, meaning that brine seepage reduced pore fluid sulfate concentrations. At the same time, brine seepage increases methane concentrations. Rates of anaerobic oxidation of methane declined with increasing salinity, but we documented anaerobic oxidation of methane at salinities up to 4M salt (19.6 nmol cm^{-3} d^{-1} GC246; core at18.02-4651.19), which we believe is the highest salinity at which active anaerobic oxidation of methane has been documented. Recently, Schutte et al. (2019 [65]) provide tantalizing evidence for anaerobic oxidation of methane in the deep anoxic brine from Lake Fryxell, Antarctica, which has a salinity about 10 times that of seawater but Saxton et al. (2021 [66]) were not able to document anaerobic oxidation of methane in standard radiotracer assays (though they may have missed the thin layer where the process was happening). Those data, along with the data presented herein, suggest that brines support active, potentially novel, microbial communities capable of anaerobic oxidation of methane.

4.4 CONCLUSIONS

The highest cumulative rates of AOM were found predominantly at the type II seep sites, namely at GC415, GC600, and especially MC118 (see Figure 24.2 and Tables 4.2 and 4.3). However, high cumulative rates of AOM were also documented at the GC233 and GB425 brine sites, suggesting a larger role for anaerobic methanotrophy in high salinity environments. Two of the three highest rates of SR were documented at the GC233 (4840 nmol cm^{-3} d^{-1}) and GC246 (1815 nmol cm^{-3} d^{-1} max) brine sites, yet both the highest maximum and cumulative rates of SR were recorded at the GC415 seep site (6193 nmol cm^{-3} d^{-1} max; 333 mmol m^{-2} d^{-1}; see Tables 4.2, 4.3). Some of our sampling efforts at sites of known oil and gas seepage – especially GC185 and GC186 – either missed locations of active seepage (MUCs are difficult to target samples with) or the location has become dormant.

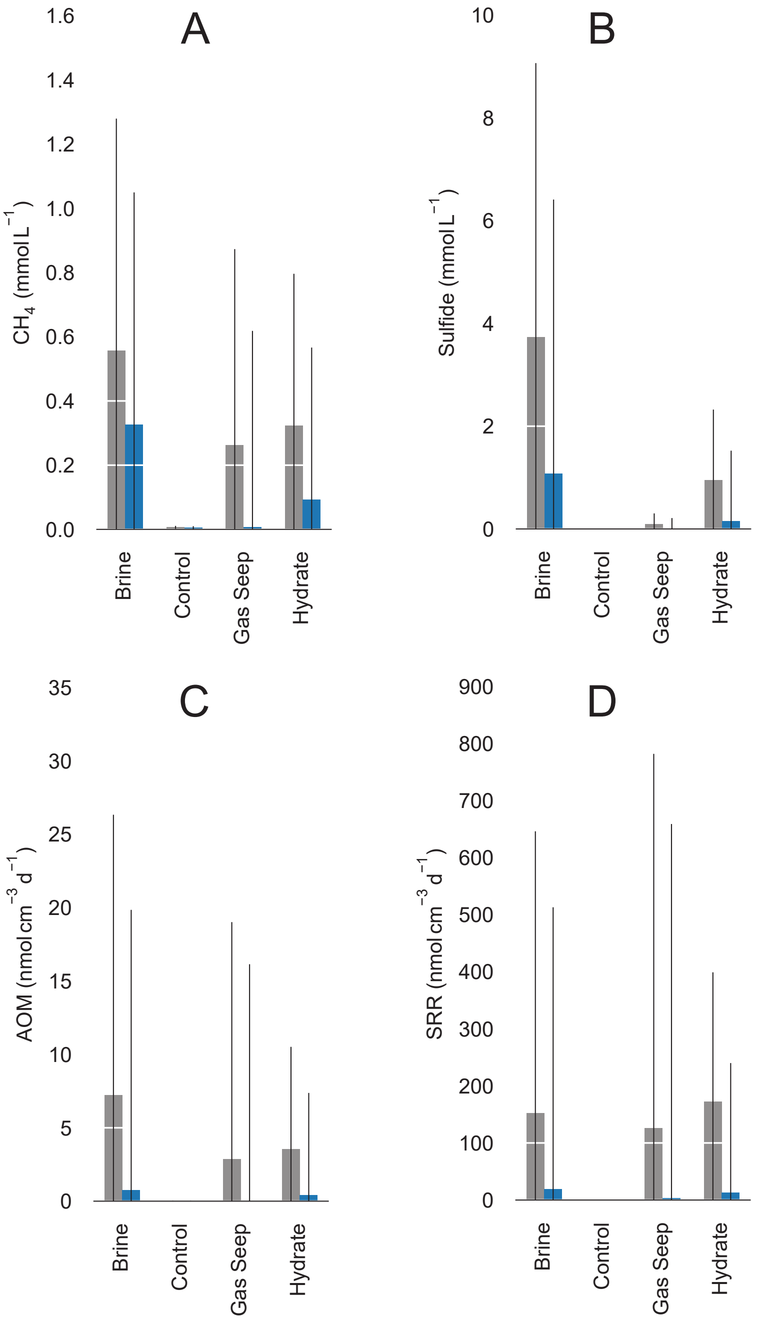

Figure 4.2: Habitat comparisons; median (blue) versus mean (gray) across numerous sites. Error bars indicate one standard deviation.

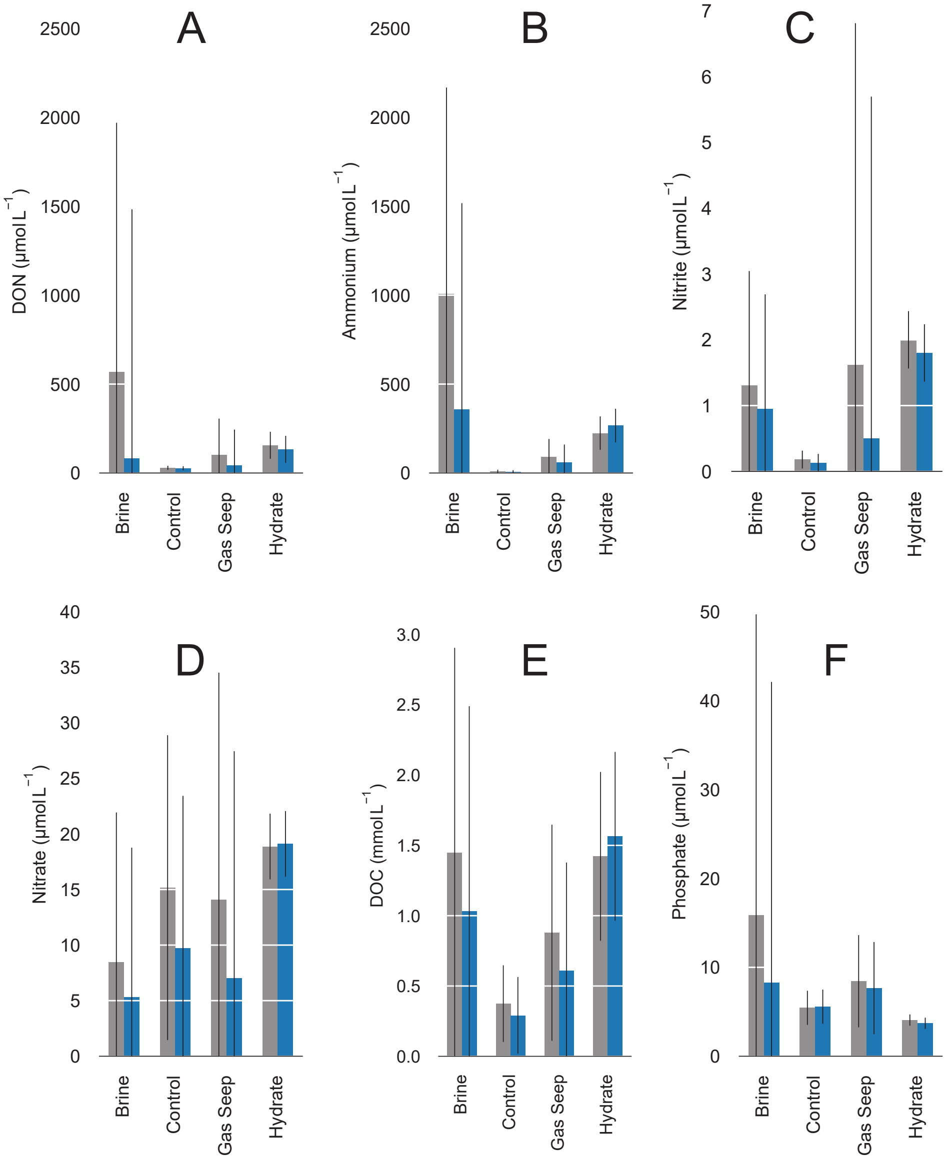

Figure 4.3: Habitat comparisons; median (blue) versus mean (gray) across numerous sites. Error bars indicate one standard deviation.

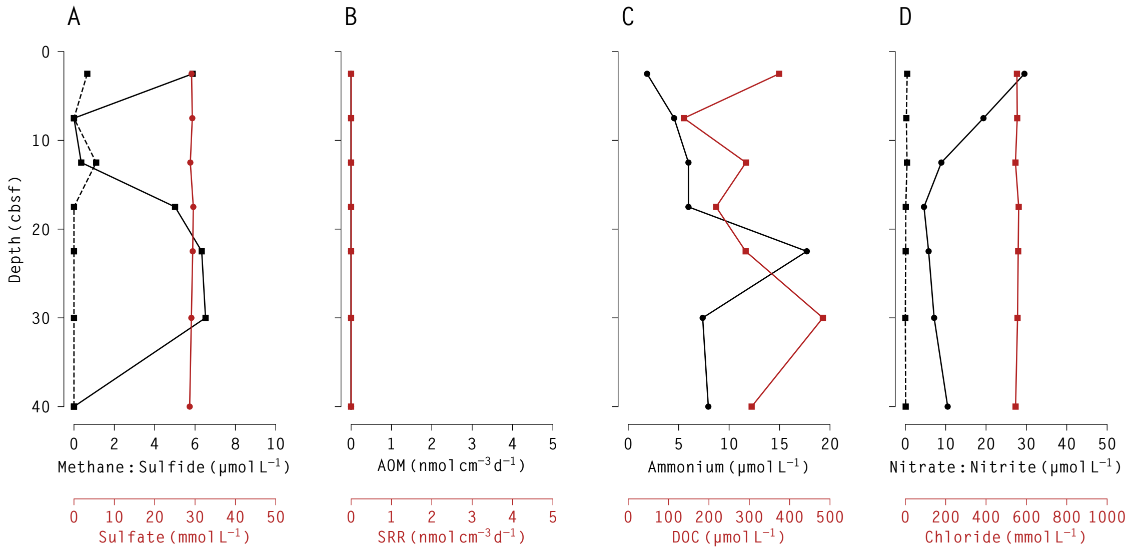

Figure 4.4: Geochemistry and rates for GB480, core EN586–S03.E07. (A) methane (solid black), sulfate (red), sulfide (dashed black), (B) AOM, SRR, (C) ammonium, DOC, and (D) nitrate (solid black), nitrite (dashed black), and chloride.

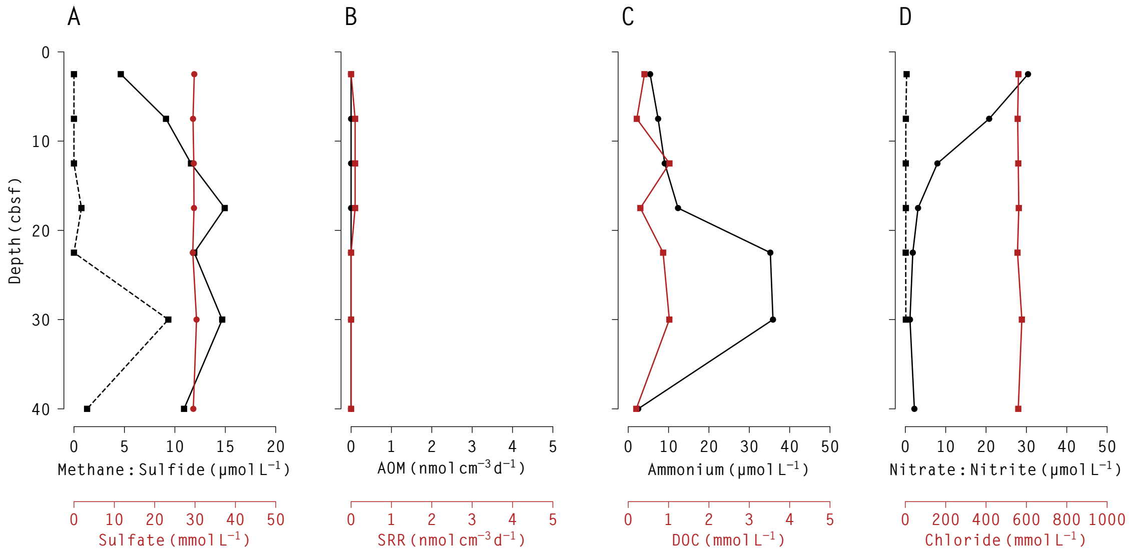

Figure 4.5: Geochemistry and rates for GC699, core EN586–S07.E07. (A) methane (solid black), sulfate (red), sulfide (dashed black), (B) AOM, SRR, (C) ammonium, DOC, and (D) nitrate (solid black), nitrite (dashed black), and chloride.

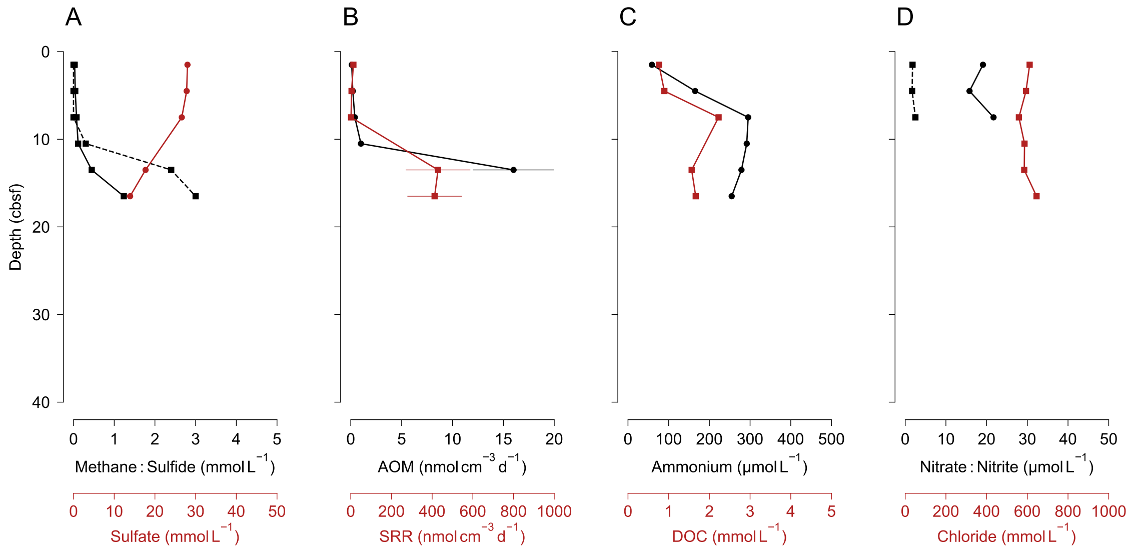

Figure 4.6: Geochemistry and rates for the hydrate (type III) GC600, core AT26.13–S05.E01. (A) methane (solid black), sulfate (red), sulfide (dashed black), (B) AOM, SRR, (C) ammonium, DOC, and (D) nitrate (solid black), nitrite (dashed black), and chloride.

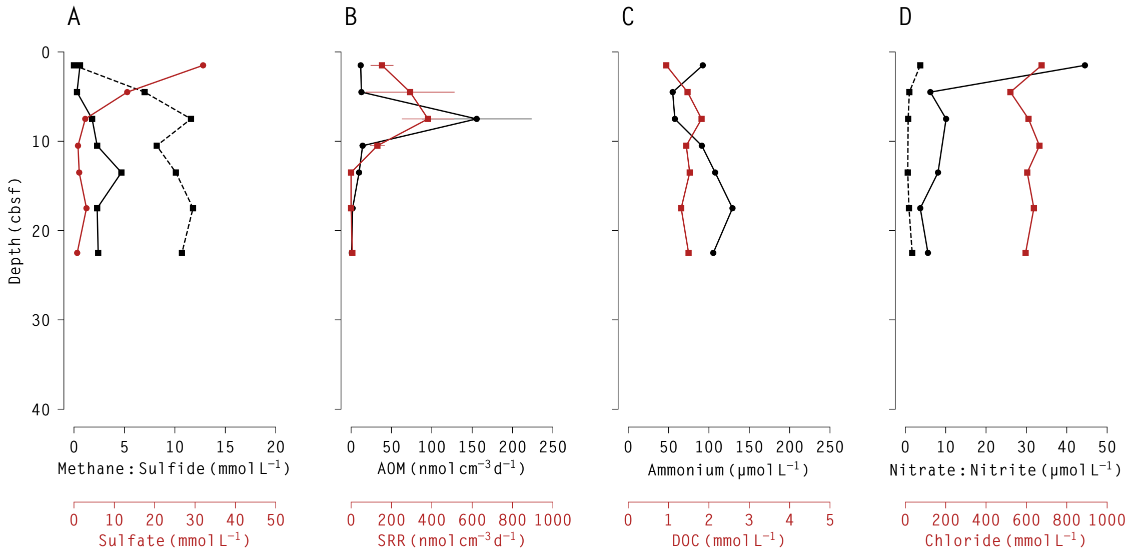

Figure 4.7: Geochemistry and rates for GC600, core AT26-13–S05.E14. (A) methane (solid black), sulfate (red), sulfide (dashed black), (B) AOM, SRR, (C) ammonium, DOC, and (D) nitrate (solid black), nitrite (dashed black), and chloride.

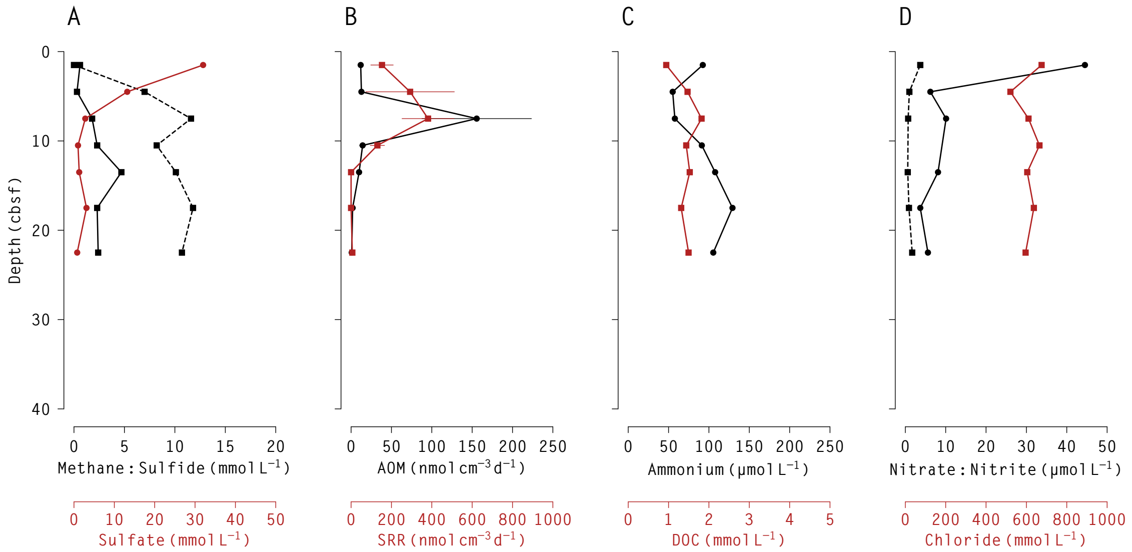

Figure 4.8: Geochemistry and rates for GC600, core AT26-13–S05.E14. (A) methane (solid black), sulfate (red), sulfide (dashed black), (B) AOM, SRR, (C) ammonium, DOC, and (D) nitrate (solid black), nitrite (dashed black), and chloride.

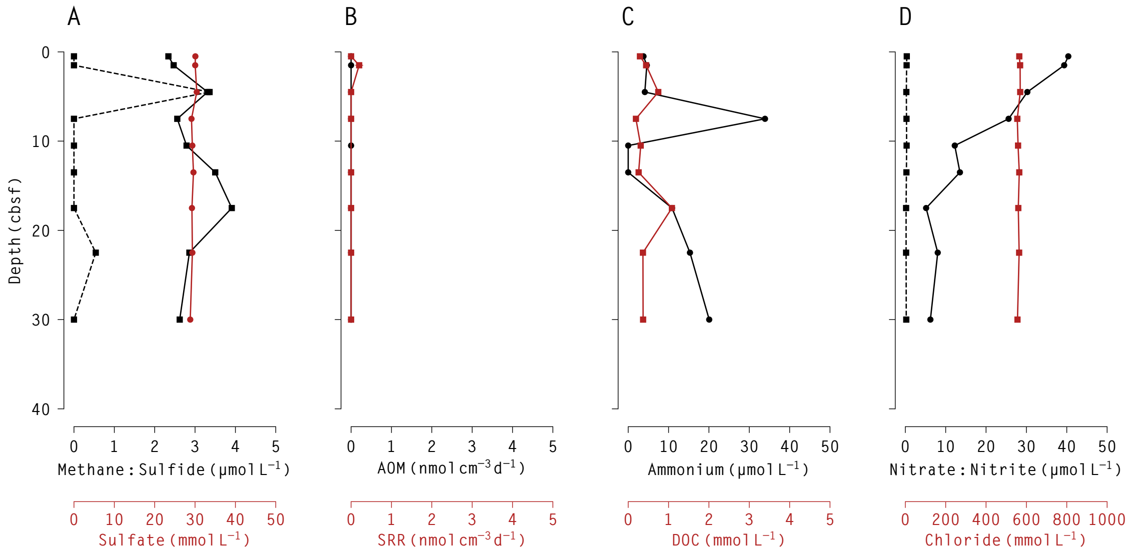

Figure 4.9: Geochemistry and rates for GC767, core EN586–S06.E09. (A) methane (solid black), sulfate (red), sulfide (dashed black), (B) AOM, SRR, (C) ammonium, DOC, and (D) nitrate (solid black), nitrite (dashed black), and chloride.

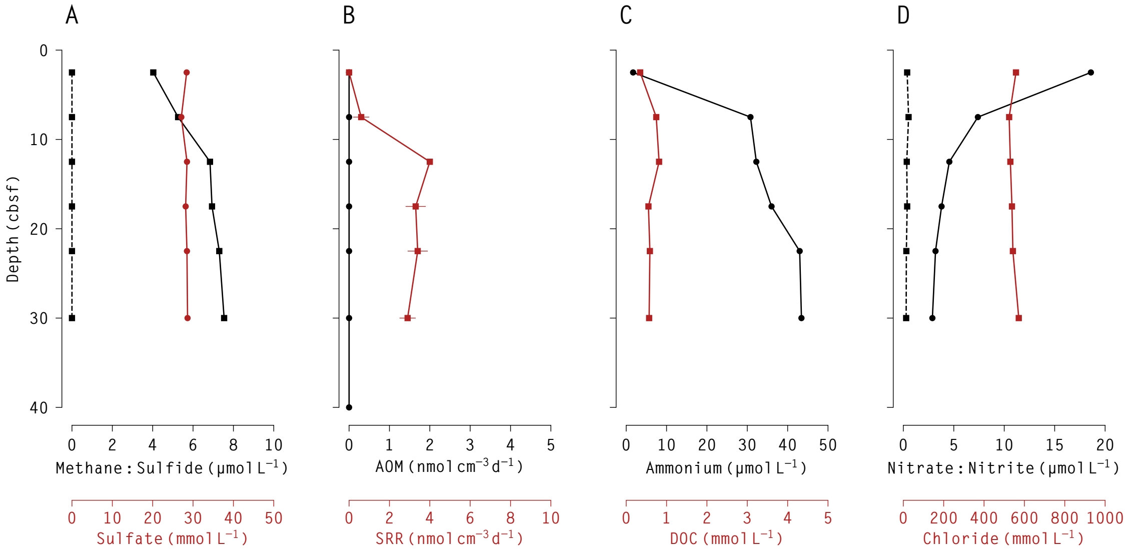

Figure 4.10: Geochemistry and rates for GC185, core EN528–S29.E06. (A) methane (solid black), sulfate (red), sulfide (dashed black), (B) AOM, SRR, (C) ammonium, DOC, and (D) nitrate (solid black), nitrite (dashed black), and chloride.

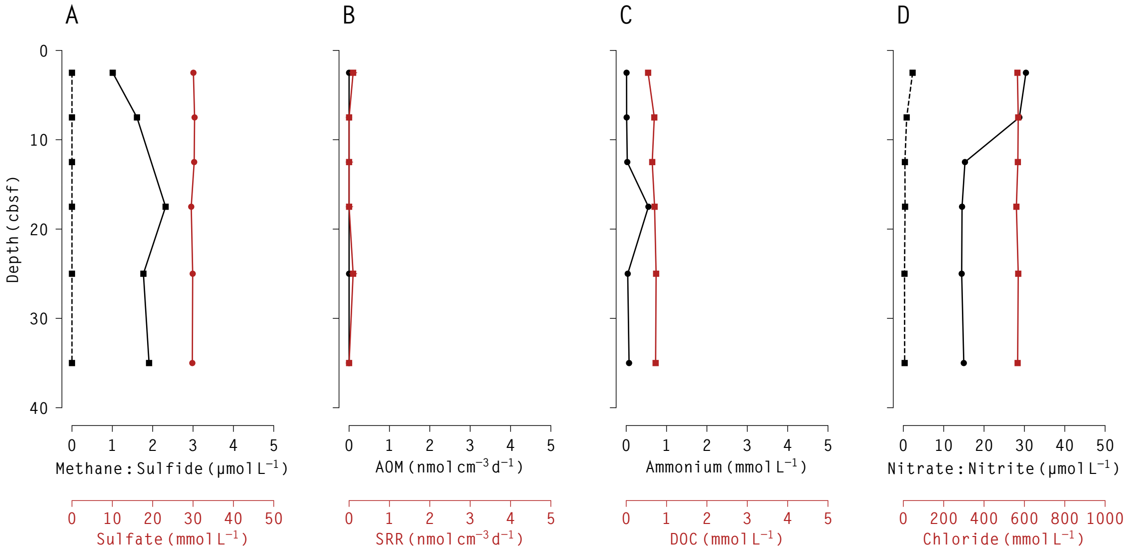

Figure 4.11: Geochemistry and rates for GC186, core EN559–S06.E05. (A) methane (solid black), sulfate (red), sulfide (dashed black), (B) AOM, SRR, (C) ammonium, DOC, and (D) nitrate (solid black), nitrite (dashed black), and chloride.

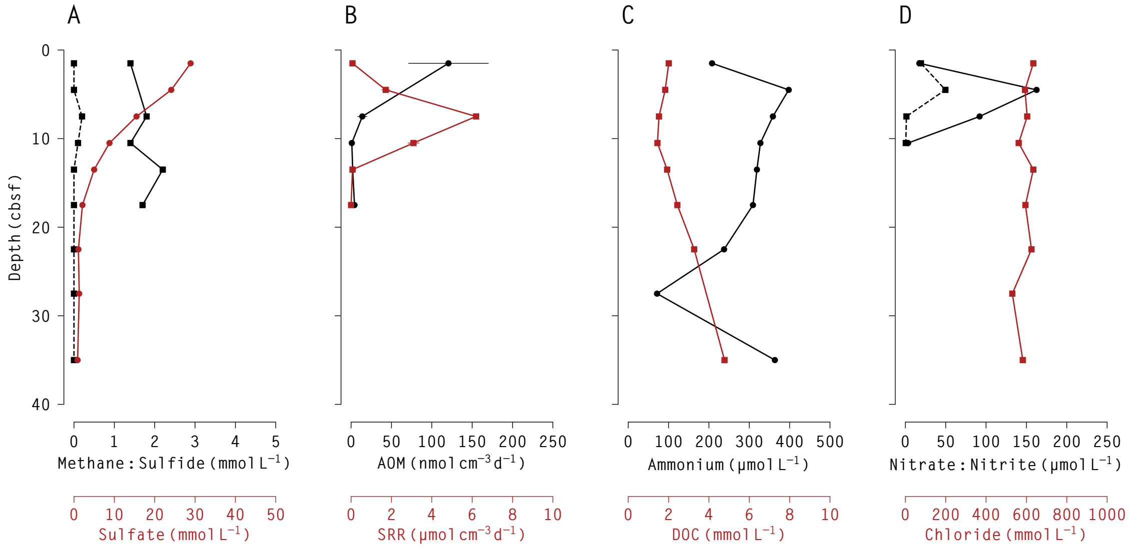

Figure 4.12: Geochemistry and rates for GC415, core EN528–S27.E07. (A) methane (solid black), sulfate (red), sulfide (dashed black), (B) AOM, SRR, (C) ammonium, DOC, and (D) nitrate (solid black), nitrite (dashed black), and chloride.

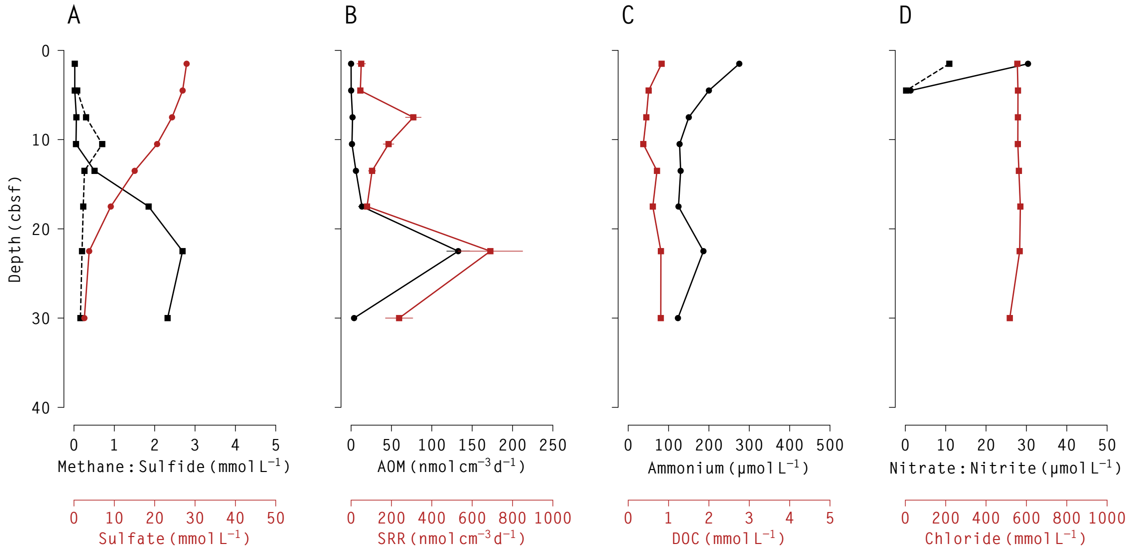

Figure 4.13: Geochemistry and rates for MC118, core EN586–S20.E02. (A) methane (solid black), sulfate (red), sulfide (dashed black), (B) AOM, SRR, (C) ammonium, DOC, and (D) nitrate (solid black), nitrite (dashed black), and chloride.

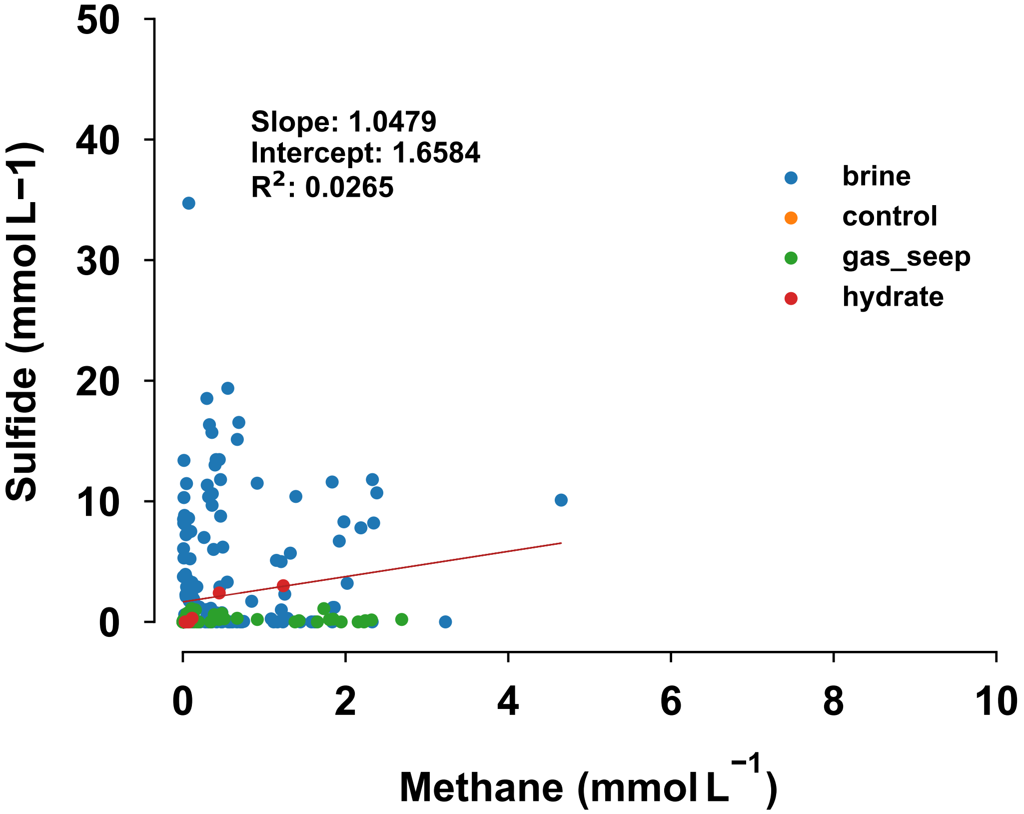

Figure 4.14: Regression between sulfide and methane at all sites and for all depths.

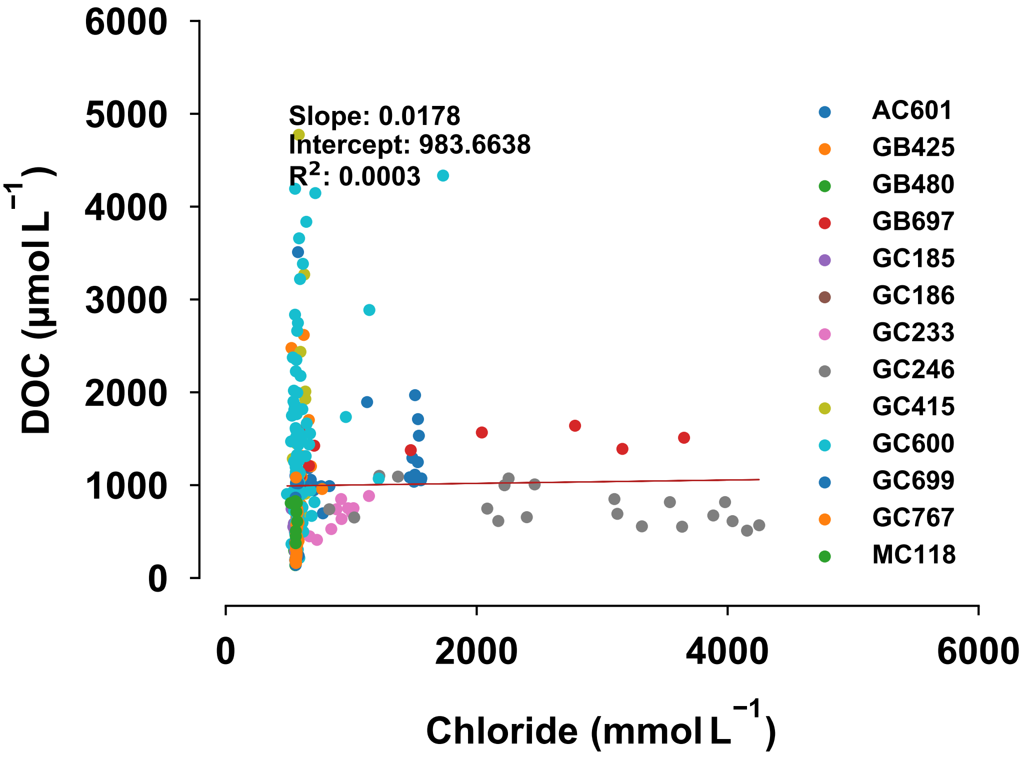

Figure 4.15: Regression between chloride and DOC concentrations for all samples, divided by lease block.

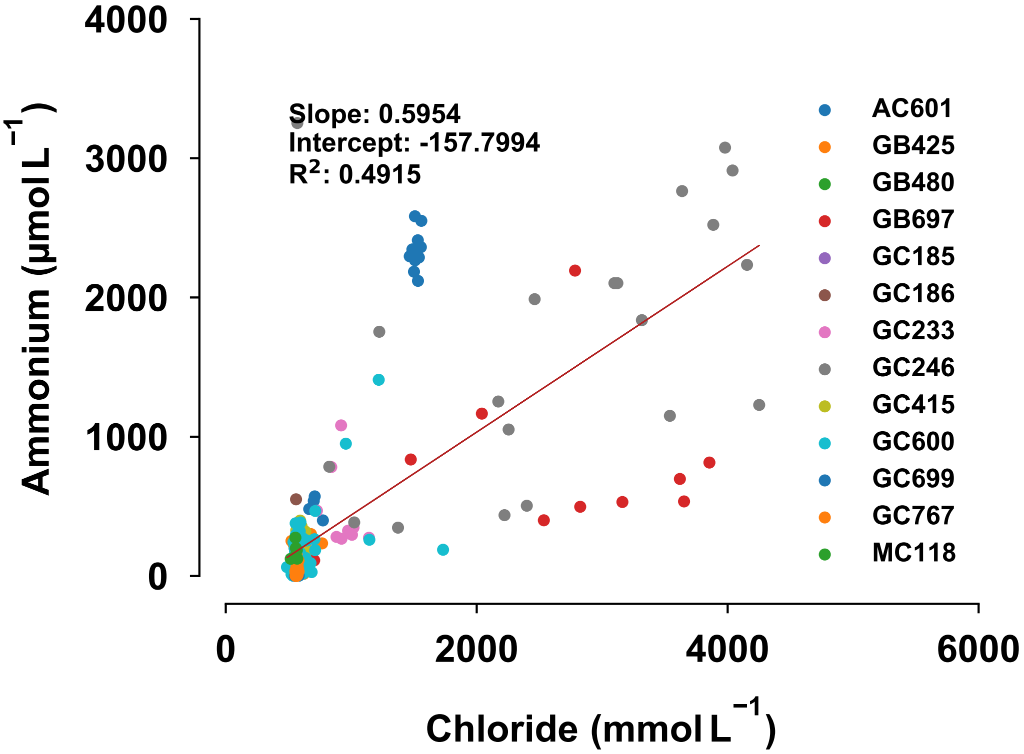

Figure 4.16: Regression between chloride and ammonium concentrations for all samples, divided by lease block.

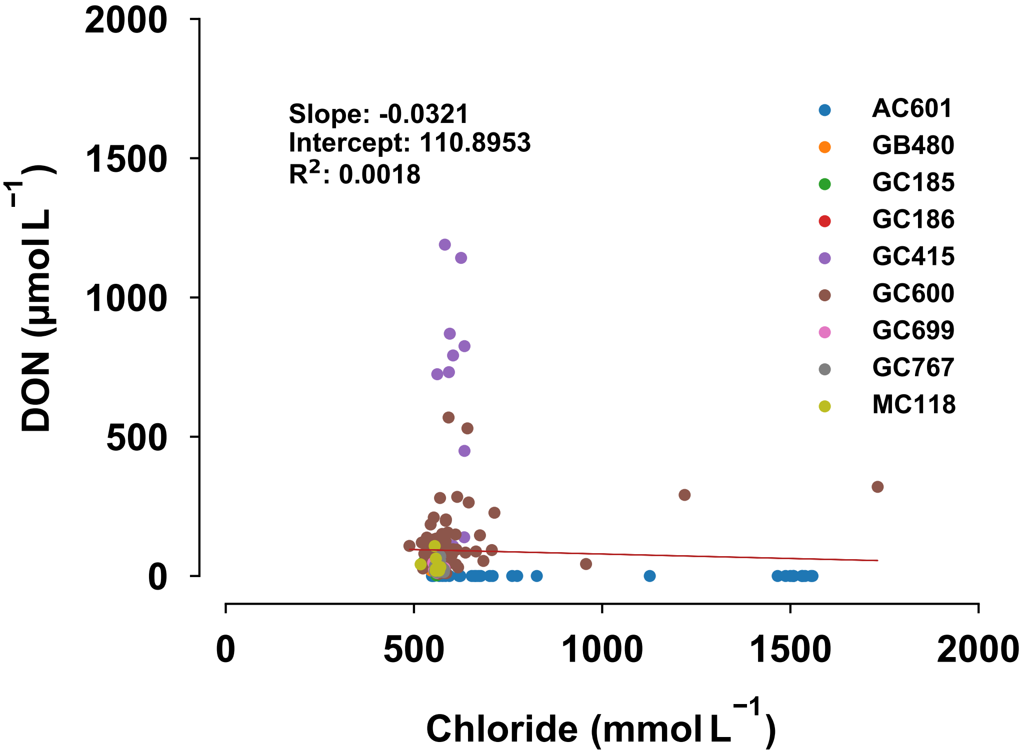

Figure 4.17: Regression between chloride and dissolved organic nitrogen concentrations for all samples, divided by lease block.

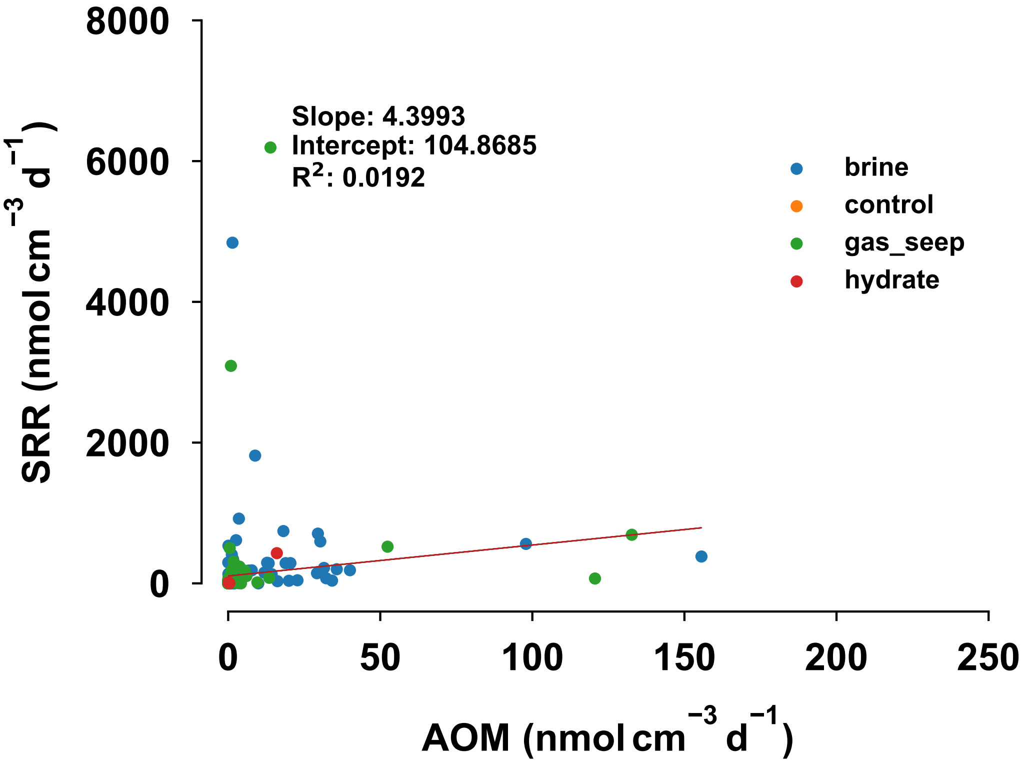

Figure 4.18: Regression between the anaerobic oxidation of methane and sulfate reduction rates concentrations for all samples, divided by lease block.

BIBLIOGRAPHY

1. Huerta, A. D. & Harry, D. L. Wilson cycles, tectonic inheritance, and rifting of the North American Gulf of Mexico continental margin. *Geosphere* **8,** 374–385 (2012).
2. Locker, S. & Hine, A. in, 60–74 (2020). ISBN: 978-3-030-12962-0.
3. Galloway, W. Chapter 15 Depositional Evolution of the Gulf of Mexico Sedimentary Basin. *Sedimentary Basins of the World* **5** (2008).
4. Hudec, M., Jackson, M. & Peel, F. Influence of deep Louann structure on the evolution of the northern Gulf of Mexico. *AAPG Bulletin* **97,** 1711–1735 (2013).
5. Kennicutt, M., McDonald, T., Comet, P., Denoux, G. & Brooks, J. The origins of petroleum in the northern Gulf of Mexico. *Geochimica et Cosmochimica Acta* **56,** 1259–1280 (1992).
6. Macdonald, I. *et al.* Natural and unnatural oil slicks in the Gulf of Mexico. *Journal of Geophysical Research* **120** (2015).
7. Joye, S. B. The Geology and Biogeochemistry of Hydrocarbon Seeps. *Annual Review of Earth and Planetary Sciences* **48,** 205–231 (2020).
8. Macdonald, I. R. *et al.* Asphalt Volcanism and Chemosynthetic Life in the Campeche Knolls, Gulf of Mexico. *Science* **304,** 1002–999 (2004).
9. Lloyd, K. *et al.* Spatial Structure and Activity of Sedimentary Microbial Communities Underlying a Beggiatoa spp. Mat in a Gulf of Mexico Hydrocarbon Seep. *PloS one* **5,** e8738 (2010).
10. Paull, C. K. *et al.* Biological communities at the Florida Escarpment resemble hydrothermal vent taxa. *Science* **226,** 965–967 (1984).

11. Orcutt, B. *et al.* Life at the edge of methane ice: Microbial cycling of carbon and sulfur in Gulf of Mexico gas hydrates. *Chemical Geology* **205,** 239–251 (2004).

12. Orcutt, B., Boetius, A., Elvert, M., Samarkin, V. & Joye, S. B. Molecular biogeochemistry of sulfate reduction, methanogenesis and the anaerobic oxidation of methane at Gulf of Mexico cold seeps. *Geochimica et Cosmochimica Acta* **69,** 4267–4281 (2005).

13. Cordes, E. E. *et al.* Alternate unstable states: Convergent paths of succession in hydrocarbon-seep tubeworm-associated communities. *Journal of Experimental Marine Biology and Ecology* **339,** 159–176 (2006).

14. Joye, S. B., Bowles, M. W., Samarkin, V. A., Hunter, K. S. & Niemann, H. Biogeochemical signatures and microbial activity of different cold-seep habitats along the Gulf of Mexico deep slope. *Deep Sea Research Part II: Topical Studies in Oceanography* **57,** 1990–2001 (2010).

15. Bowles, M., Hunter, K. S., Samarkin, V. & Joye, S. Patterns and variability in geochemical signatures and microbial activity within and between diverse cold seep habitats along the lower continental slope, Northern Gulf of Mexico. *Deep Sea Research Part II: Topical Studies in Oceanography* **129,** 31–40 (2016).

16. Fisher, C., Roberts, H., Cordes, E. & Bernard, B. Cold Seeps and Associated Communities of the Gulf of Mexico. *Oceanography* (2007).

17. Joye, S. B. *et al.* The anaerobic oxidation of methane and sulfate reduction in sediments from Gulf of Mexico cold seeps. *Chemical Geology* **205,** 219–238 (2004).

18. Bowles, M. W., Samarkin, V. A., Bowles, K. M. & Joye, S. B. Weak coupling between sulfate reduction and the anaerobic oxidation of methane in methane-rich seafloor sediments during ex situ incubation. *Geochimica et Cosmochimica Acta* **75,** 500–519 (2011).

19. Bowles, M. *et al.* Remarkable Capacity for Anaerobic Oxidation of Methane at High Methane Concentration. *Geophysical Research Letters* **46,** 12192–12201 (2019).

20. Teske, A. P. & Joye, S. B. in *Marine Hydrocarbon Seeps* 69–100 (Springer Nature, Switzerland, 2019).

21. Razaz, M., Di Iorio, D., Wang, B., Asl, S. D. & Thurnherr, A. M. Variability of a natural hydrocarbon seep and its connection to the ocean surface. *Scientific Reports* **10,** 1–13 (2020).

22. Garcia-Pineda, O. *et al.* Transience and persistence of natural hydrocarbon seepage in Mississippi Canyon, Gulf of Mexico. *Deep Sea Research Part II: Topical Studies in Oceanography* **129,** 119–129 (2016).

23. Johansen, C., Todd, A. C. & MacDonald, I. R. Time series video analysis of bubble release processes at natural hydrocarbon seeps in the Northern Gulf of Mexico. *Marine and Petroleum Geology* **82,** 21–34 (2017).

24. Johansen, C. *et al.* Hydrocarbon migration pathway and methane budget for a Gulf of Mexico natural seep site: Green Canyon 600. *Earth and Planetary Science Letters* **545** (2020).

25. Dickens, G., O'Niel, J., Rea, D. & Owen, R. Dissociation of oceanic methane hydrate as a cause of the carbon isotope excursion at the end of the Paleocene. *Paleoceanography* **10,** 965–971 (1995).

26. Dickens, G. Rethinking the global carbon cycle with large, dynamic and microbially mediated gas hydrate capacitor. *Earth and Planetary Science Letters* **213,** 169–183 (2003).

27. Brooks, J., Kennicutt, M., Fay, R., McDonald, T. & Sassen, R. Thermogenic gas hydrates in the Gulf of Mexico. *Science* **225,** 409–411 (1984).

28. MacDonald, I. R. *et al.* Chemosynthetic mussels at a brine-filled pockmark in the northern Gulf of Mexico. *Science* **248,** 1096–1099 (1990).

29. Joye, S. B., MacDonald, I. R., Montoya, J. P. & Peccini, M. Geophysical and geochemical signatures of Gulf of Mexico seafloor brines. *Biogeosciences* **2,** 295–309 (2005).

30. Joye, S. B. *et al.* Metabolic variability in seafloor brines revealed by carbon and sulphur dynamics. *Nature Geoscience* **2,** 349 (2009).

31. Wankel, S. *et al.* New constraints on methane fluxes and rates of anaerobic methane oxidation in a Gulf of Mexico brine pool via in situ mass spectrometry. *Deep Sea Research Part II: Topical Studies in Oceanography* **57,** 2022–2029 (2010).

32. Starinsky, A. & Katz, A. The formation of natural cryogenic brines. *Geochimica et Cosmochimica Acta* **67,** 1475–1484 (2003).

33. Cordes, E., Becker, E., Hourdez, S. & Fisher, C. *Deep-Sea Research Part II: Topical Studies in Oceanography* **57,** 1870–1881 (2010).

34. Nauhaus, K., Treude, T., Boetius, A. & Krüger, M. Environmental regulation of the anaerobic oxidation of methane: a comparison of ANME-I and ANME-II communities. *Environmental Microbiology* **7,** 98–106 (2005).

35. Dekas, A. E., Poretsky, R. S. & Orphan, V. J. Deep-sea archaea fix and share nitrogen in methane-consuming microbial consortia. *Science* **326,** 422–426 (2009).

36. Duan, Z. & Mao, S. Thermodynamic model for calculating methane solubility, density and gas phase composition of methane-bearing aqueous fluids from 273 to 523 K and from 1 to 2000 bar. *Geochimica et Cosmochimica Acta* **70,** 3369–3386 (2006).

37. Lapham, L., Wilson, R., Riedel, M., Paull, C. K. & Holmes, M. E. Temporal variability of in situ methane concentrations in gas hydrate-bearing sediments near Bullseye Vent, Northern Cascadia Margin. *Geochemistry, Geophysics, Geosystems* **14,** 2445–2459 (2013).

38. Roberts, H. *et al.* Alvin explores the deep northern Gulf of Mexico Slope. *Eos, Transactions American Geophysical Union* **88,** 341–342 (2007).

39. Reitz, A., Haeckel, M., Wallmann, K., Hensen, C. & Heeschen, K. Origin of salt-enriched pore fluids in the northern Gulf of Mexico. *Earth and Planetary Science Letters* **259,** 266–282 (2007).

40. Roberts, H. H., Feng, D. & Joye, S. B. Cold-seep carbonates of the middle and lower continental slope, northern Gulf of Mexico. *Deep Sea Research Part II: Topical Studies in Oceanography* **57,** 2040–2054 (2010).

41. Reeburgh, W. S. An improved insterstitial water sampler. *Limnology and Oceanography* **12,** 163–165 (1967).

42. Cline, J. D. Spectrophotometric Determination of Hydrogen Sulfide in Natural Waters. *Limnology and Oceanography* **14,** 454–458 (1969).

43. Soloranzo, L. Determination of ammonia in natural waters by the phenolhypochlorite method. *Limnology and Oceanography* **14,** 799–801 (1969).

44. Álvarez-Salgado, X. A. & Miller, A. E. Simultaneous determination of dissolved organic carbon and total dissolved nitrogen in seawater by high temperature catalytic oxidation: conditions for precise shipboard measurements. *Marine Chemistry* **62,** 325–333 (1998).

45. Monaghan, E. J. & Ruttenberg, K. C. Dissolved organic phosphorus in the coastal ocean: Reassessment of available methods and seasonal phosphorus profiles from the Eel River Shelf. *Limnology and Oceanography* **44,** 1702–1714 (1999).

46. Lin, Y.-S. *et al.* Towards constraining H2 concentration in subseafloor sediment: A proposal for combined analysis by two distinct approaches. *Geochimica et Cosmochimica Acta* **77,** 186–201 (2012).

47. Crozier, T. E. & Yamamoto, S. Solubility of hydrogen in water, sea water, and sodium chloride solutions. *Journal of Chemical & Engineering Data* **19,** 242–244 (1974).

48. Hoehler, T. M., Alperin, M. J., Albert, D. B. & Martens, C. S. Thermodynamic control on hydrogen concentrations in anoxic sediments. *Geochimica et Cosmochimica Acta* **62,** 1745–1756 (1998).

49. Fossing, H. & Jørgensen, B. B. Measurement of bacterial sulfate reduction in sediments: evaluation of a single-step chromium reduction method. *Biogeochemistry* **8,** 205–222 (1989).

50. Sibert, R., Samarkin, V. & Joye, S. in *Hydrocarbon and Lipid Microbiology Protocols* (ed McGenity T. Timmis K., N. B.) (Springer, Berlin Heidelberg, 2016).

51. Jørgensen, B. B. A comparison of methods for the quantification of bacterial sulfate reduction in coastal marine sediments. *Geomicrobiology Journal* **1,** 11–27 (1978).

52. Alperin, M., Reeburgh, W. & Whiticar, M. Carbon and hydrogen isotope fractionation resulting from anaerobic methane oxidation. *Global biogeochemical cycles* **2,** 279–288 (1988).

53. Cordes, E. E., Bergquist, D. C. & Fisher, C. R. Macro-ecology of Gulf of Mexico cold seeps. *Annual Review of Marine Science* **1,** 143–168 (2009).

54. Crespo-Medina, M., Bowles, M., Samarkin, V., Hunter, K. & Joye, S. Microbial diversity and activity in seafloor brine lake sediments (Alaminos Canyon block 601, Gulf of Mexico). *Geobiology* **14** (2016).

55. Hourdez, S., Weber, R. E., Green, B. N., Kenney, J. M. & Fisher, C. R. Respiratory adaptations in a deep-sea orbiniid polychaete from Gulf of Mexico brine pool NR-1: metabolic rates and hemoglobin structure/function relationships. **205,** 1669–1681 (2002).

56. Smith, E. B., Scott, K. M., Nix, E. R., Korte, C. & Fisher, C. R. Growth and Condition of Seep Mussels (Bathymodiolus Childressi) at a Gulf of Mexico Brine Pool. *Ecology* **81,** 2392–2403 (2000).

57. Orcutt, B. N., Sylvan, J. B., Knab, N. J. & Edwards, K. J. Microbial Ecology of the Dark Ocean above, at, and below the Seafloor. **75,** 361–422 (2011).

58. McClain, M. *et al.* Biogeochemical Hot Spots and Hot Moments at the Interface of Terrestrial and Aquatic Ecosystems. *Ecosystems* **6,** 301–312 (2003).

59. Bernhardt, E. *et al.* Control Points in Ecosystems: Moving Beyond the Hot Spot Hot Moment Concept. *Ecosystems* **20** (2017).

60. Corinaldesi, C. New perspectives in benthic deep-sea microbial ecology. *Frontiers in Marine Science* **2,** 17 (2015).

61. Kalanetra, K., Joye, S., Sunseri, N. & Nelson, D. Novel vacuolate sulfur bacteria from the Gulf of Mexico reproduce by reductive division in three dimensions. *Environmental microbiology* **7,** 1451–60 (2005).

62. Dekas, A. E., Chadwick, G. L., Bowles, M. W., Joye, S. B. & Orphan, V. J. Spatial distribution of nitrogen fixation in methane seep sediment and the role of the ANME archaea. *Environmental Microbiology* **16,** 3012–3029 (2014).

63. Orcutt, B. N. *et al.* Impact of natural oil and higher hydrocarbons on microbial diversity, distribution, and activity in Gulf of Mexico cold-seep sediments. *Deep Sea Research Part II: Topical Studies in Oceanography* **57,** 2008–2021 (2010).

64. Macdonald, I. *et al.* Gulf of Mexico hydrocarbon seep communities: VI. Patterns in community structure and habitat. *Geo-Marine Letters* **10,** 244–252 (1990).

65. Schutte, C. A. *et al.* Vertical stratification and stability of biogeochemical processes in the deep saline waters of Lake Vanda, Antarctica. *Limnology and Oceanography* **65,** 569–581 (2019).

66. Saxton, M. A. *et al.* Biogeochemical and 16S rRNA gene sequence evidence supports a novel mode of anaerobic methanotrophy in permanently ice-covered Lake Fryxell, Antarctica. *Limnology and Oceanography* **61,** S119–S130 (2016).

Chapter 5

Conclusions

5.1 Dynamics and diversity of methanotrophy across the chemocline of the deep hypersaline Orca Basin.

This chapter reported the first rates of microbial methane oxidation and sulfate reduction across the chemocline of Orca basin, Gulf of Mexico, one of the world's largest submarine brine basins. Three potential modes of methane oxidation were documented, each taking advantage of a different redox niche and creating an effective sink for methane in this environment. We hypothesized that (1) anaerobic methanotrophy would predominantly control methane flux from the gas-charged brine (2) sulfate reduction would co-occur with anaerobic methanotrophy and be a dominant terminal metabolism across the chemocline as in other deep marine hypersaline systems, and (3) microbial metabolism would be salinity-inhibited within the core of the brine.

Our results indicated that both aerobic and anaerobic methanotrophy occur along the chemocline, and sulfate reduction was either completely absent, or below our ability to detect with conventional radiotracer assays. Anaerobic methane oxidation was likely more important than aerobic methanotrophy but rapid uptake of methane tracer along a suboxic, mildly salty horizon indicates a robust community of aerobic methanotrophic scavengers. Not only was AOM active within the brine, but experimental additions of oxidized iron minerals stimulated AOM rates at full brine salinity ($>250\,\mathrm{g\,kg^{-1}}$). Iron-coupled AOM has been demonstrated in sediments, but this study reports the first occurrence of this in brine fluids and work with additional electron acceptors such as nitrite suggests a dynamic community of anaerobic hydrocarbon degraders.

I recommend that future work at this basin expand upon the iron and nitrogen experiments and include other potential electron acceptors such as birnessite (a Mn oxide) or artificial humic substances. The possibility that the methanotrophy in a deep-sea basin is influenced by atmospheric deposition of iron-rich dust is intriguing and would expand our view on potential drivers of local biogeochemistry. Additionally, an adequate description of the sulfur cycle at Orca basin remains elusive. Sulfide oxidation may play a larger role here than previously thought.

5.2 Microbial Hydrocarbon Oxidation in Sediments from Across the Northern Gulf of Mexico

Chapter 3 reports naphthalene and hexadecane oxidation rates in Gulf sediments across nine sites of different water depth and hydrocarbon loading rates in the context of datasets describing porewater and solid phase geochemistry, microbial sulfate reduction and AOM, and extractable hydrocarbons. We hypothesized that (1) sulfate reduction rates would be a good predictor for presence and magnitude of alkane and PAH degradation, (2) that the relative magnitude of oil oxidation would follow thermodynamic predictions, *i.e., n*-alkanes would be oxidized before PAHs, and (3) exposure to oil would prime the sediment microbial community for hydrocarbon metabolism and further predict the magnitude of hydrocarbon oxidation rates at a given site.

The hypotheses that rates of hydrocarbon oxidation would correlate to rates of sulfate reduction was disproven. Sulfate reduction rates did not broadly correlate to either hexadecane or naphthalene oxidation across site types, in general, though the site with the highest rates of sulfate reduction (MC118) also exhibited the highest rates of oil oxidation. The second hypothesis, that n-alkanes would be degraded faster than PAHs, was also disproven. Though alkane degradation yields more energy than PAH degradation, the inherent insolubility of n-alkanes like hexadecane limits their biodegradation substantially. The idea that sites impacted by oil and gas would express the highest rates of activity was proven correct. While oil loading did correlate with the potential for oil degradation (see Figure 3.5 and Table 3.6), this relationship was not robust. Finally, we discovered a surprising connection between sedimented oil and microbial activity at the seabed at sites impacted by both natural oil and anthropogenic oil sedimentation. The amount and relative reactivity of sedimented oil determines the relative extent to which the material stimulates anaerobic terminal metabolism. Finally, some of these data (GC767) provides tantalizing evidence of the importance of fermentative (methanogenic) metabolism of oil, even in the presence of sulfate.

I recommend that future work be focused on the role of methanogenesis from hexadecane and naphthalene. It is not at all clear what percentage of the labile alkane fraction of crude oil is oxidized directly to carbon dioxide and what fraction is converted to methane. New tracer methods will have to be developed or modified to explore the possibility that linear alkanes are used by deep-sea microbes as methanogenic substrate. This work would have broad appeal to both industry and the scientific community.

5.3 A Survey of Anaerobic Oxidation of Methane and Sulfate Reduction in the Gulf of Mexico.

In chapter 4 I presented the first systematic assessment of microbial activity under quasi in situ conditions in sediments of mixed hydrocarbon and brine impact along the northern continental slope of the Gulf of Mexico. The northern continental slope of the Gulf of Mexico is host to thousands of cold seeps each with unique sedimentary biogeochemical signatures driven in some part by variable inputs of oil, gas and brine. Sulfate reduction and anaerobic methanotrophy (AOM) were used to assess variability between four different kinds of sites: i) sites containing quiescent abyssal sediments, ii) sites impacted by oil and gas, iii) sites in proximity to methane hydrates, and iv) sites influenced by brine seepage. The purpose of this study was to (1) compile one of the most expansive spatial-temporal datasets of biogeochemistry and microbial activity within Gulf of Mexico cold seep sediments, (2) to expand the availability of rate data collected under an improved method that approximates conditions found at the sea floor, and (3) to highlight the variability inherent in cold seep systems.

This study reveals that the highest cumulative rates of AOM were found predominantly at oil and gas seeps. However, high cumulative rates of AOM were also documented at the GC233 and GB425 brine sites, suggesting a larger role for anaerobic methanotrophy in high salinity environments. Two of the three highest rates of SR were documented at the GC233 and GC246 brine sites, yet both the highest maximum and cumulative rates of SR were recorded at the GC415 seep sites. This dataset is large and offers numerous lines of research moving forward. Two of the most enticing are: 1) sulfur availability at brine sites may drive the microbial ecology of these sites, which influences the benthic community around them, 2) anaerobic methanotrophy may be more important at brine sites than previously thought, and 3) the limited availability of sulfur at brine sites may promote new and interesting modes of methanotrophy.

APPENDIX A

SUPPLEMENTAL DATA

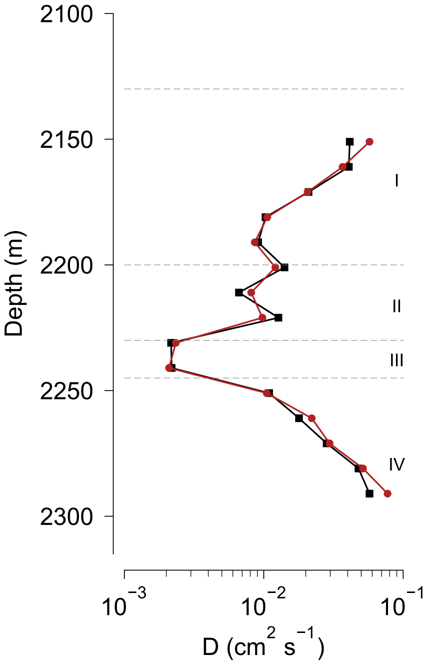

Figure A.1: Diffusion coefficients D across the chemocline of Orca Basin, N (black squares) and S (red circles), calculated from EN586 CTD profiles. Horizon abbreviations: I = oxycline, II = suboxic, III = halocline, and IV = brine. Data from cruise EN600.

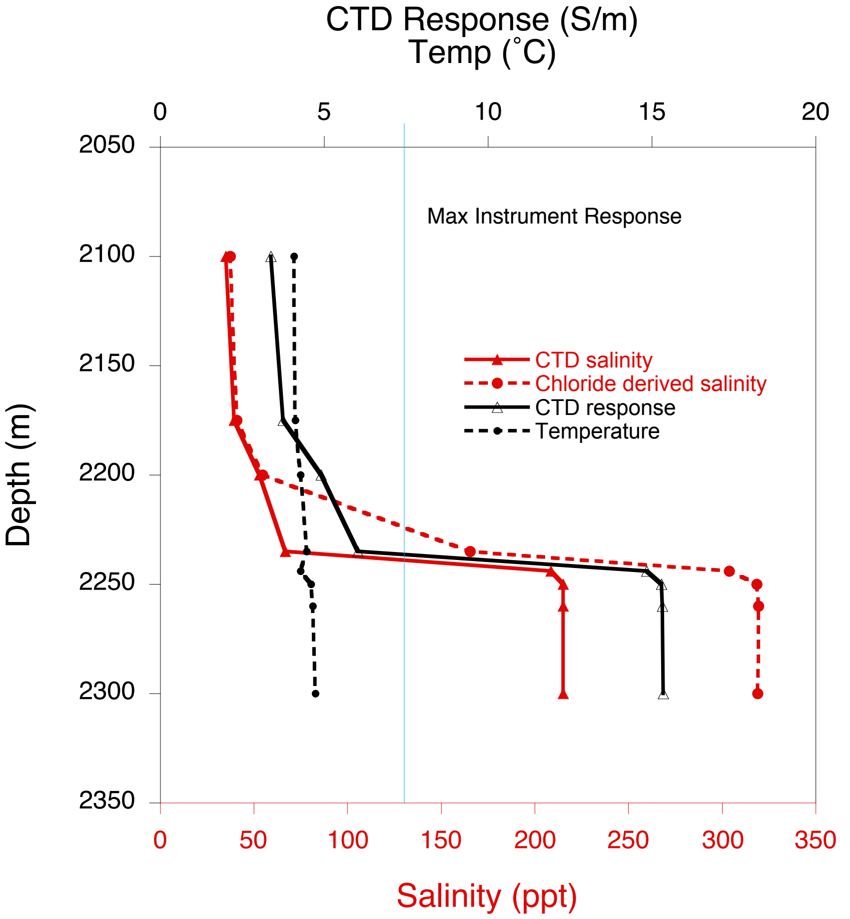

Figure A.2: CTD salinity vs. salinity calculated from major ions. Blue vertical line is the reported manufacturer (SBE) response limit.

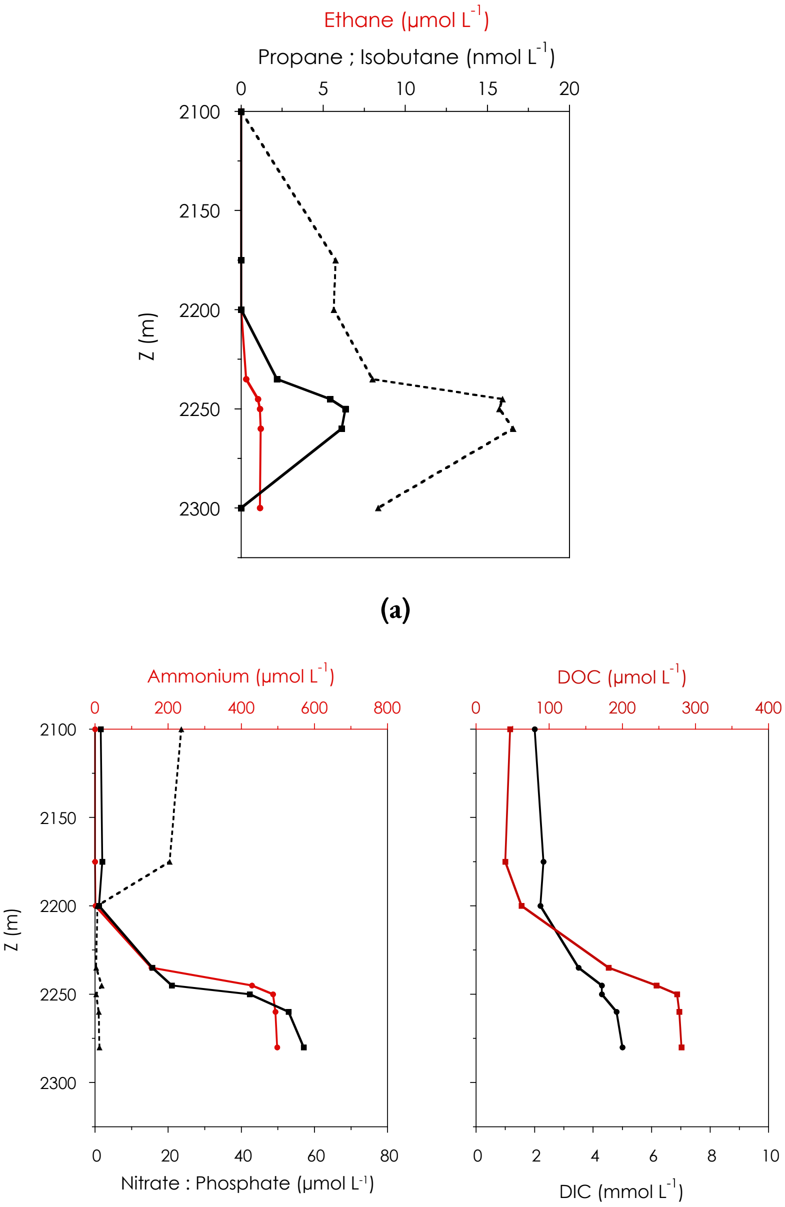

(a)

(b) (c)

Figure A.3: Orca N basin profiles of (a) alkanes (ethane: red, propane: solid black, and butane: dashed) (b) ammonium (red), phosphate (solid black), and nitrate (dashed black), and (c) DIC (black) and DOC (red). Alkane data from cruise EN586, S05.E03. Nutrient and carbon data from EN600.

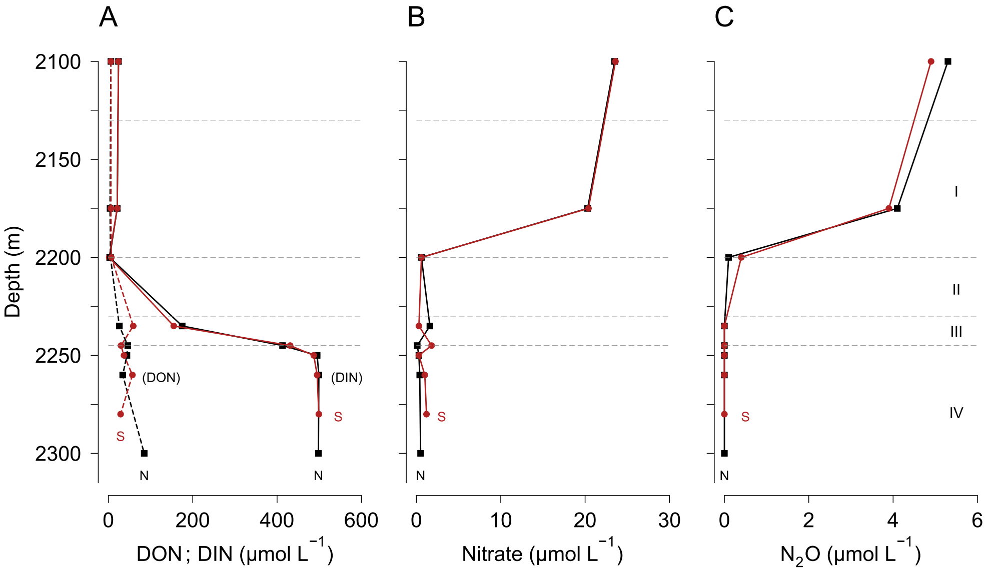

Figure A.4: Profiles of dissolved organic and inorganic nitrogen (DON and DIN, respectively) (A), nitrate (B), and nitrous oxide (C) for both Orca N and S basins. Horizon abbreviations: I = oxycline, II = suboxic, III = halocline, and IV = brine. Data from cruise EN600.

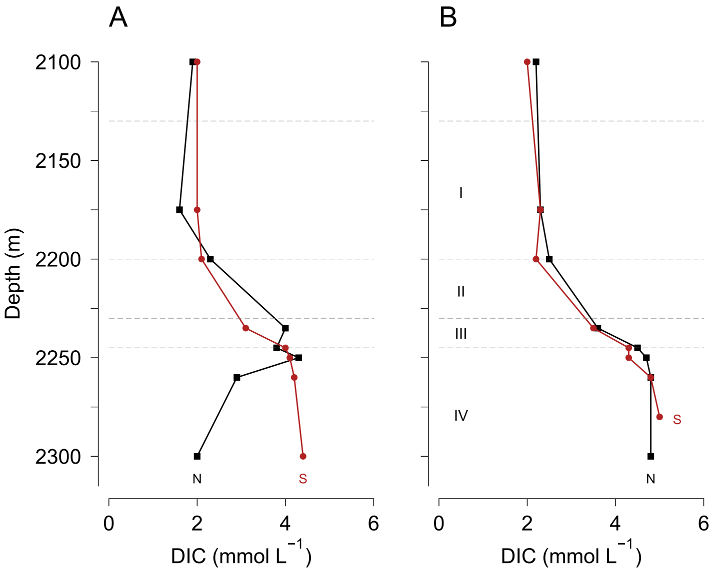

Figure A.5: Profiles of dissolved inorganic carbon (DIC) across the chemocline of Orca N and S. Horizon abbreviations: I = oxycline, II = suboxic, III = halocline, and IV = brine. Data from cruises EN586 (A) and EN600 (B).

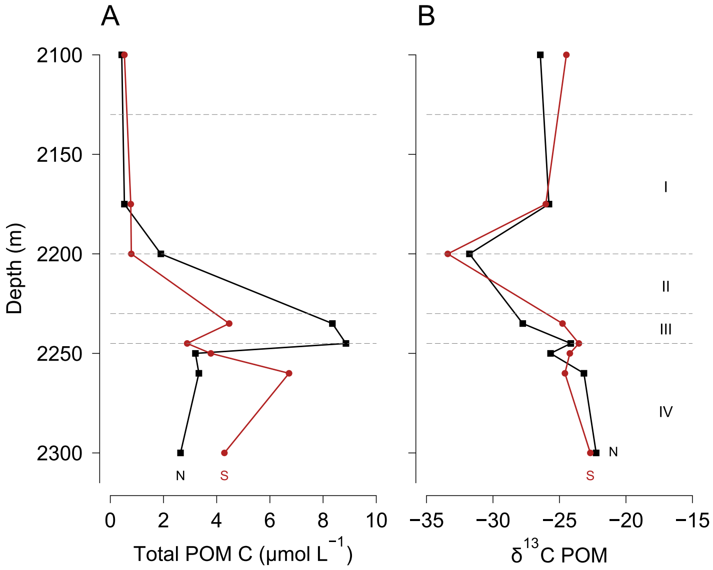

Figure A.6: Profiles of particulate organic matter (POM) (A), and δ^{13}C stable isotopes of POM carbon (B) for both Orca N and S basins. Horizon abbreviations: I = oxycline, II = suboxic, III = halocline, and IV = brine. Data from cruise EN586.

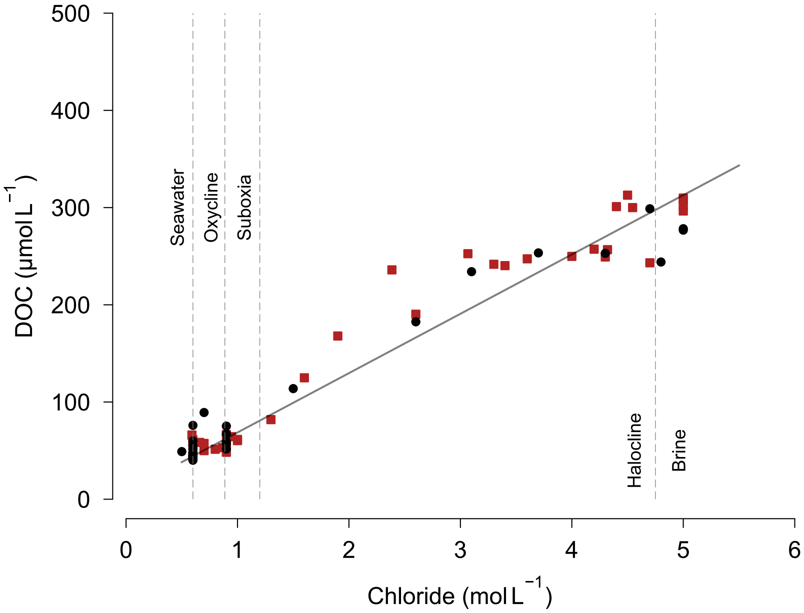

Figure A.7: DOC mixing diagram. Black circles for Orca N, red circles for Orca S. Data from AT26–13, EN586, and EN600.

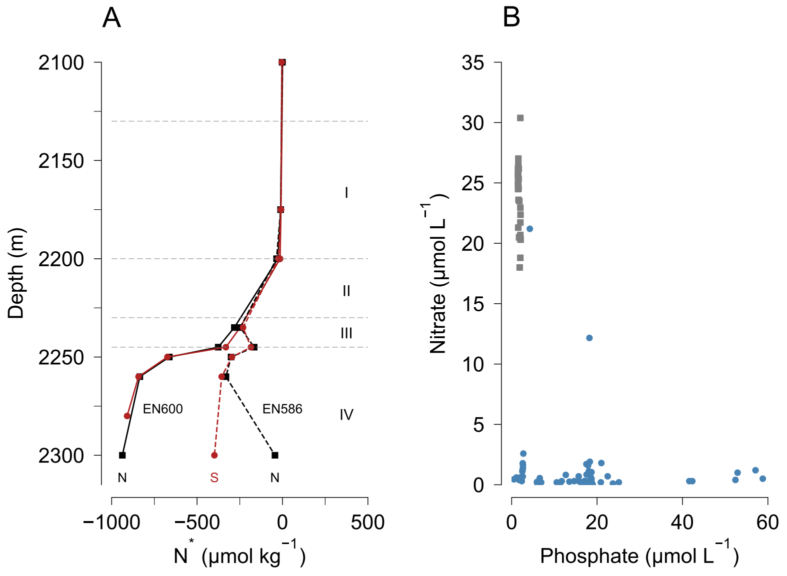

Figure A.8: Calculated values of N-star (A) and comparison of phosphorus to nitrate (B) in seawater ($z < 2200$ m) and brine ($z \geq 2200$ m). Horizon abbreviations: I = oxycline, II = suboxic, III = halocline, and IV = brine. Data from cruises EN600 and EN586.

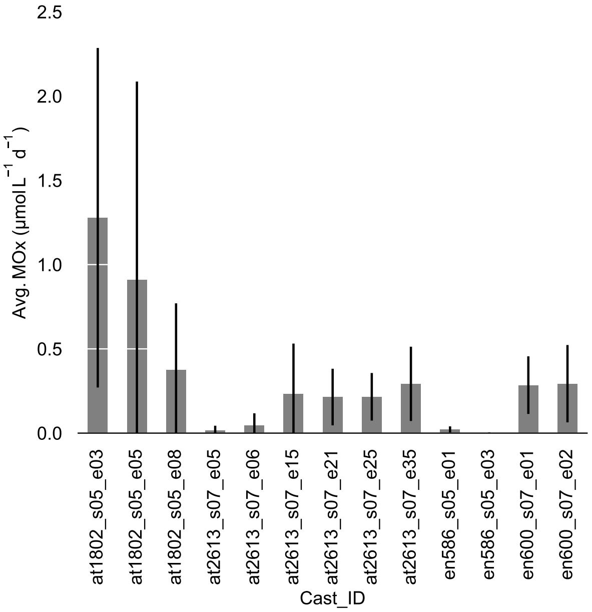

Figure A.9: Average methane oxidation rates over time.

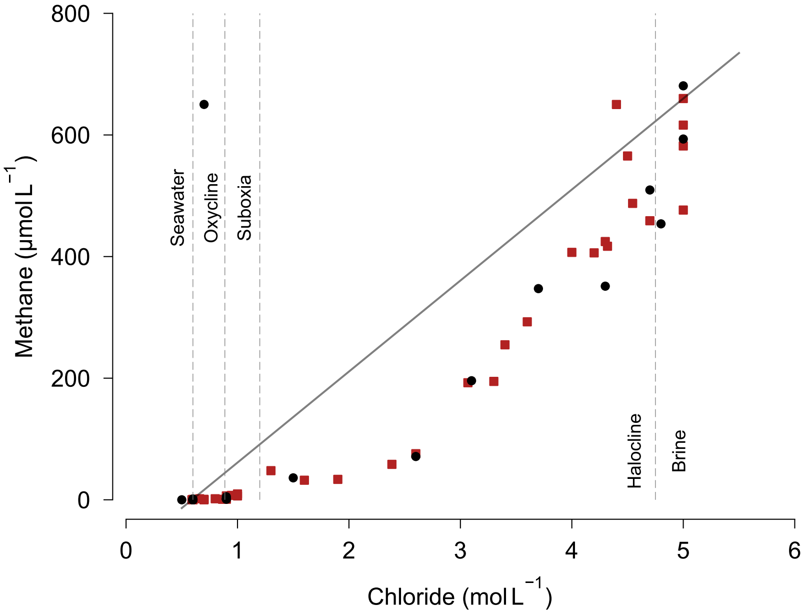

Figure A.10: Methane mixing diagram. Black circles for Orca N, red circles for Orca S. Data from AT26–13, EN586, and EN600.

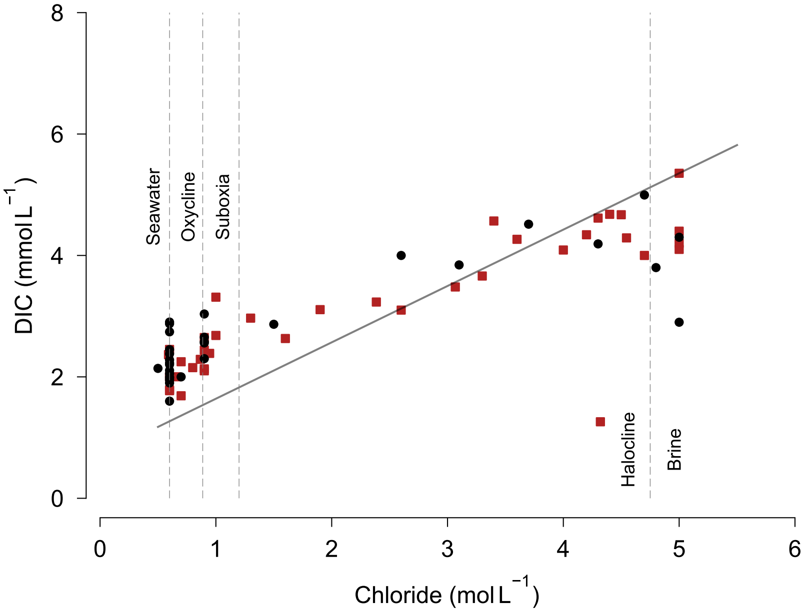

Figure A.11: DIC mixing diagram. Black circles for Orca N, red circles for Orca S. Data from AT26–13, EN586, and EN600.

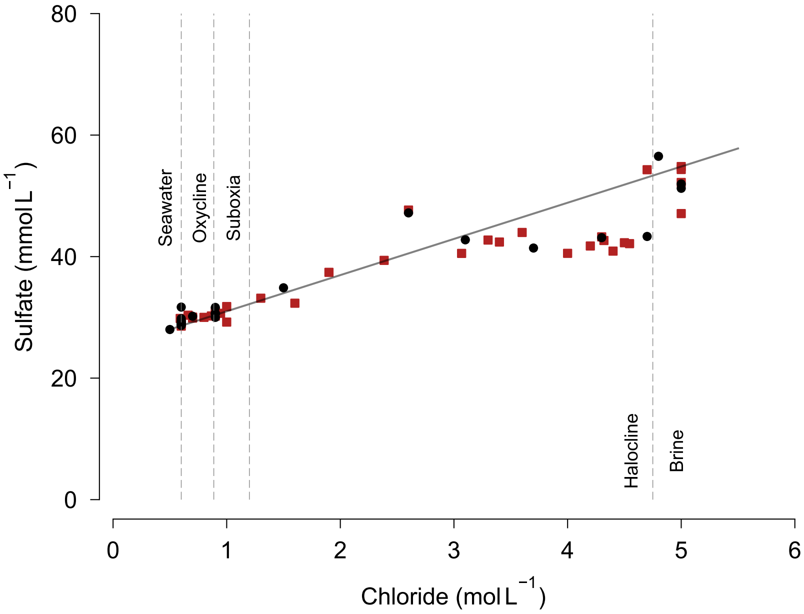

Figure A.12: Sulfate mixing diagram. Black circles for Orca N, red circles for Orca S. Data from AT26–13, EN586, and EN600.

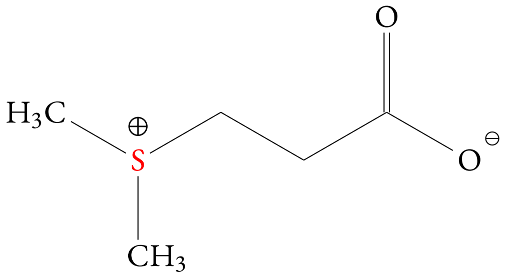

Figure A.13: Chemical structure of dimehtylsufoniopropionate (DMSP)

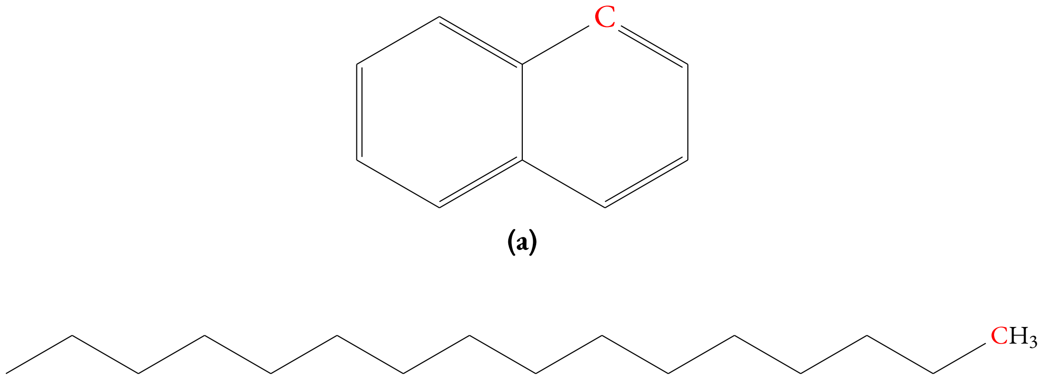

Figure A.14: Structure and label position of *n*-[1-14C]Hexadecane and [1-14C]Naphthalene.

Year	Basin	Host Waters	Salinity $g\,kg^{-1}$	Temp °C
1948	Albatross	Red Sea	n.a.	n.a.
1958	Vema	Red Sea	–	–
1964[1,2]	Atlantis II	Red Sea	261	56
1965[3,4]	Discovery	Red Sea	271	44
1967	Shagara	Red Sea	–	–
1967[5]	Chain	Red Sea	74.2	34
1967[6]	Oceanographer	Red Sea	–	24.9
1969[7]	Wando	Red Sea	–	29.3
1970[6,7]	Nereus	Red Sea	–	30.2
1972[7]	Valdivia	Red Sea	–	29.5
1972[7]	Gypsum	Red Sea	–	–
1972[7]	Kebrit	Red Sea	–	23.3
1972[6,7]	Saukin	Red Sea	–	23.7
1972[7]	Port Sudan	Red Sea	–	36.2
1972[7]	Erba	Red Sea	–	27.9
1972[7]	Thetis	Red Sea	–	22.6
1977[8,9]	Orca	Gulf of Mexico	260	5
1983[10,11]	Tyro	Mediterranean	n.a.	14
1983[10]	Kretheus	Mediterranean	n.a.	n.a.
1984[12]	Jean Charcot	Red Sea	310	24.8
1985[11,13]	Bannock	Mediterranean	325	15
1986[6,14]	Conrad	Red Sea	n.a.	23
1990[15]	NR1	Gulf of Mexico	121	8.7
1995[16]	Urania	Mediterranean	–	16.7
1995[16,17]	L'Atalante	Mediterranean	365	14.06
1995[6,16]	Discovery	Mediterranean	–	45
2003[18]	GC205	Gulf of Mexico	–	–
2007[19,20]	AC601	Gulf of Mexico	90	4

Table A.1: A timeline of DHAB discoveries. Abbreviations: n.a., no data.

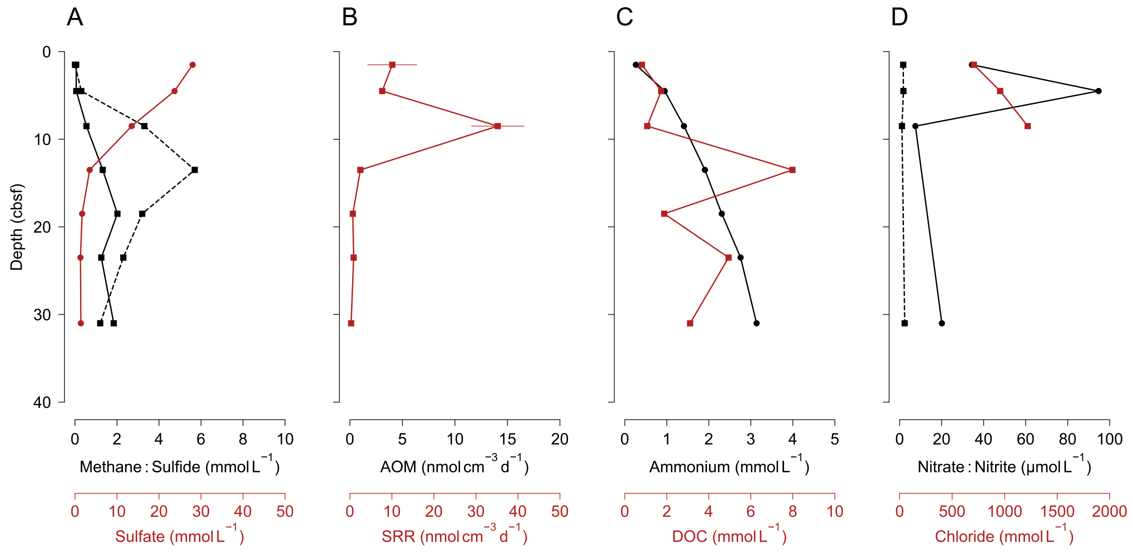

Figure A.15: Geochemistry and rates for GC600, core AT26.13-S05.E24. (A) methane (solid black), sulfate (red), sulfide (dashed black), (B) AOM, SRR, (C) ammonium, DOC, and (D) nitrate (solid black), nitrite (dashed black), and chloride.

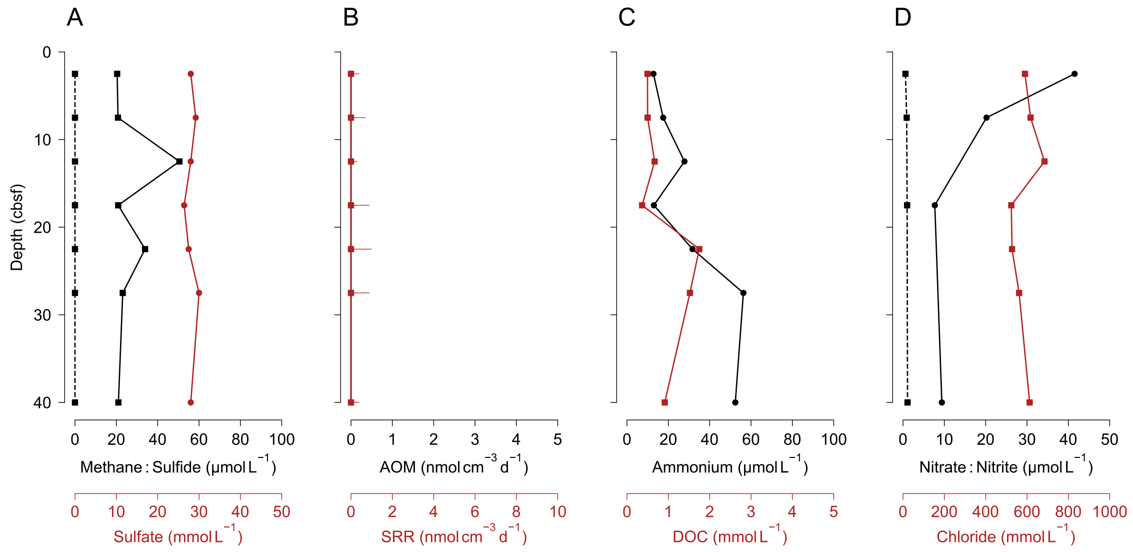

Figure A.16: Geochemistry and rates for GC600, core AT26.13-S05.E25. (A) methane (solid black), sulfate (red), sulfide (dashed black), (B) AOM, SRR, (C) ammonium, DOC, and (D) nitrate (solid black), nitrite (dashed black), and chloride.

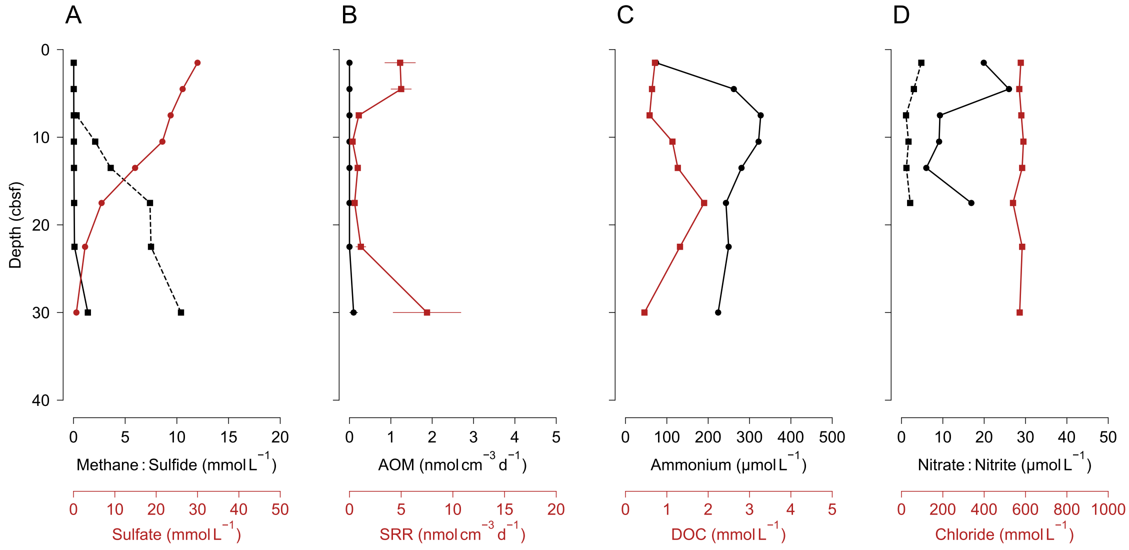

Figure A.17: Geochemistry and rates for GC600, core AT26.13-S05.E33. (A) methane (solid black), sulfate (red), sulfide (dashed black), (B) AOM, SRR, (C) ammonium, DOC, and (D) nitrate (solid black), nitrite (dashed black), and chloride.

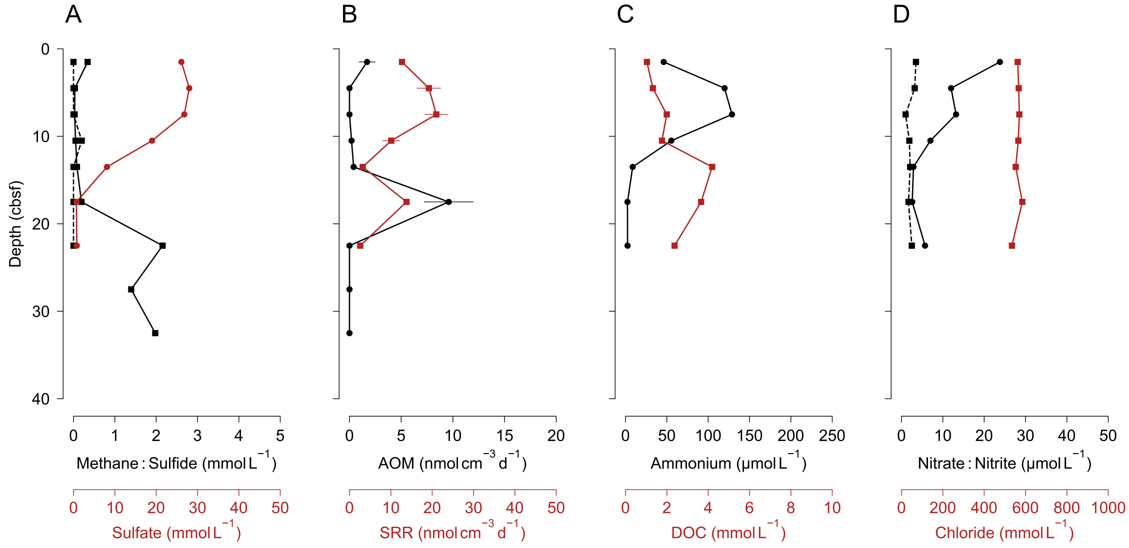

Figure A.18: Geochemistry and rates for GC600, core EN527-S01.E05. (A) methane (solid black), sulfate (red), sulfide (dashed black), (B) AOM, SRR, (C) ammonium, DOC, and (D) nitrate (solid black), nitrite (dashed black), and chloride.

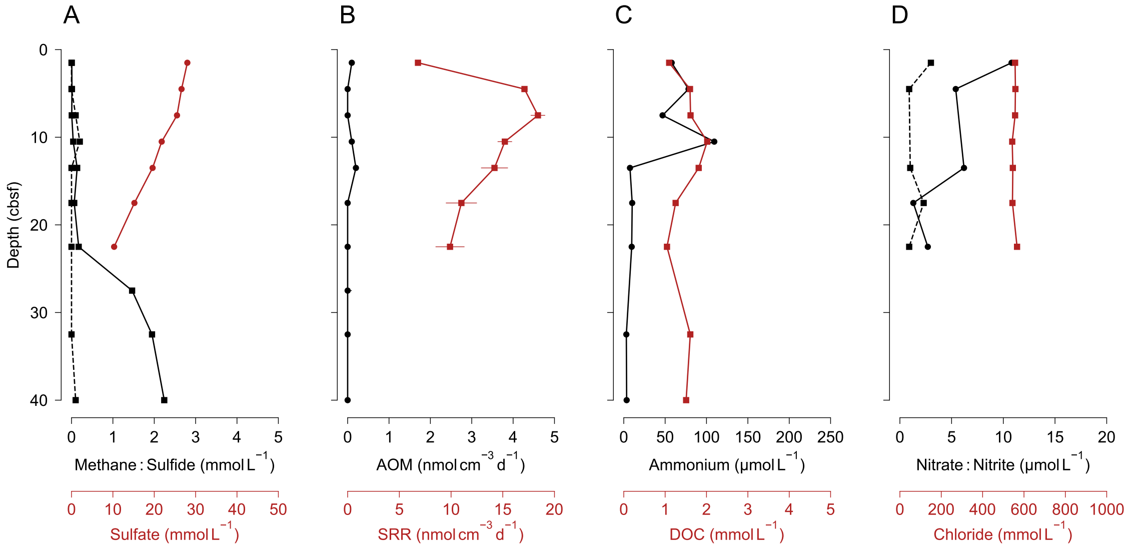

Figure A.19: Geochemistry and rates for GC600, core EN527-S01.E07. (A) methane (solid black), sulfate (red), sulfide (dashed black), (B) AOM, SRR, (C) ammonium, DOC, and (D) nitrate (solid black), nitrite (dashed black), and chloride.

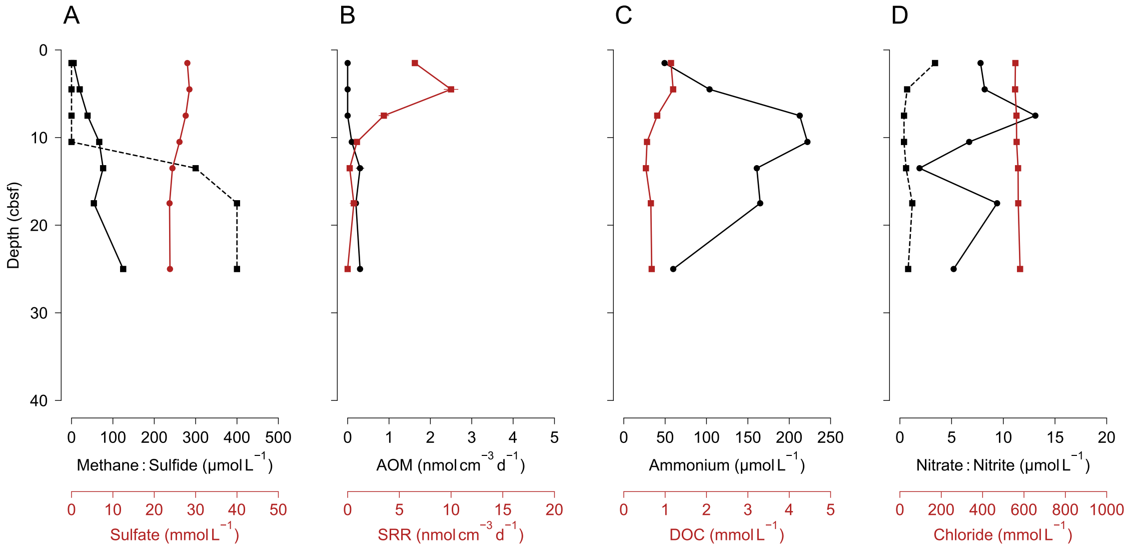

Figure A.20: Geochemistry and rates for GC600, core EN559-S02.E06. (A) methane (solid black), sulfate (red), sulfide (dashed black), (B) AOM, SRR, (C) ammonium, DOC, and (D) nitrate (solid black), nitrite (dashed black), and chloride.

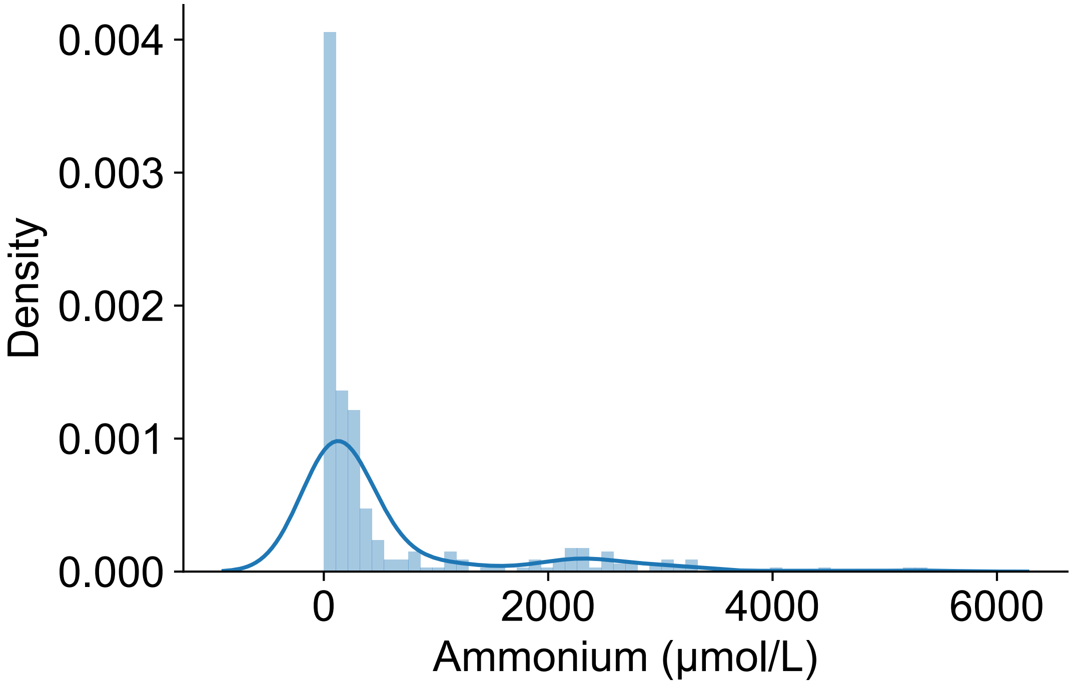

Figure A.21: Distribution of Chapter 4 ammonium dataset.

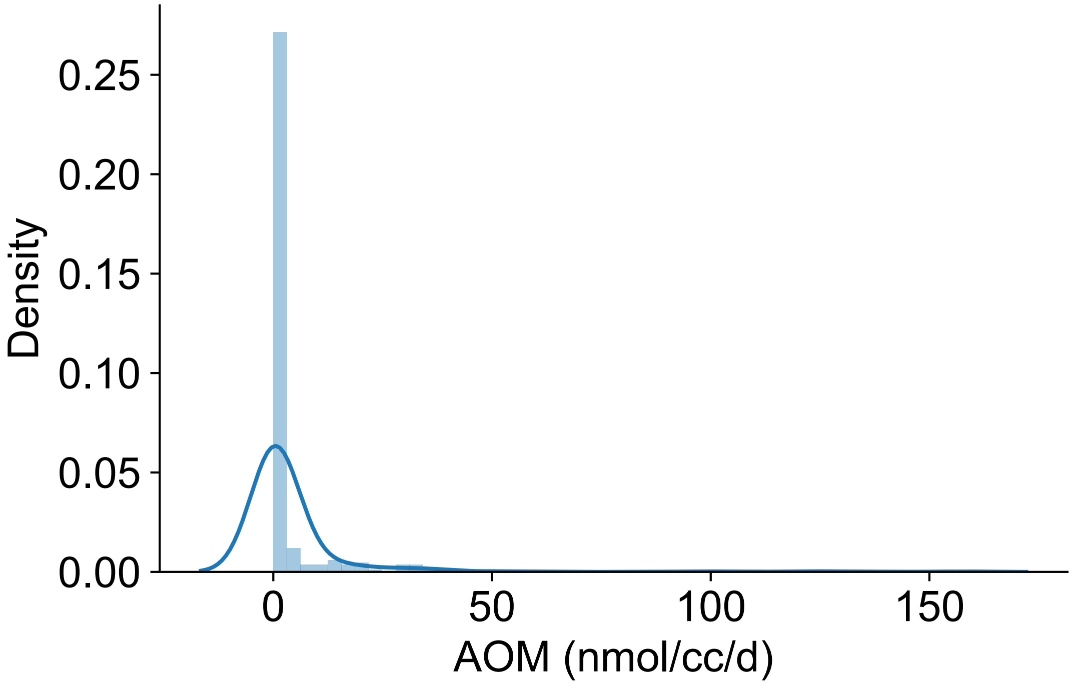

Figure A.22: Distribution of Chapter 4 anaerobic oxidation of methane dataset.

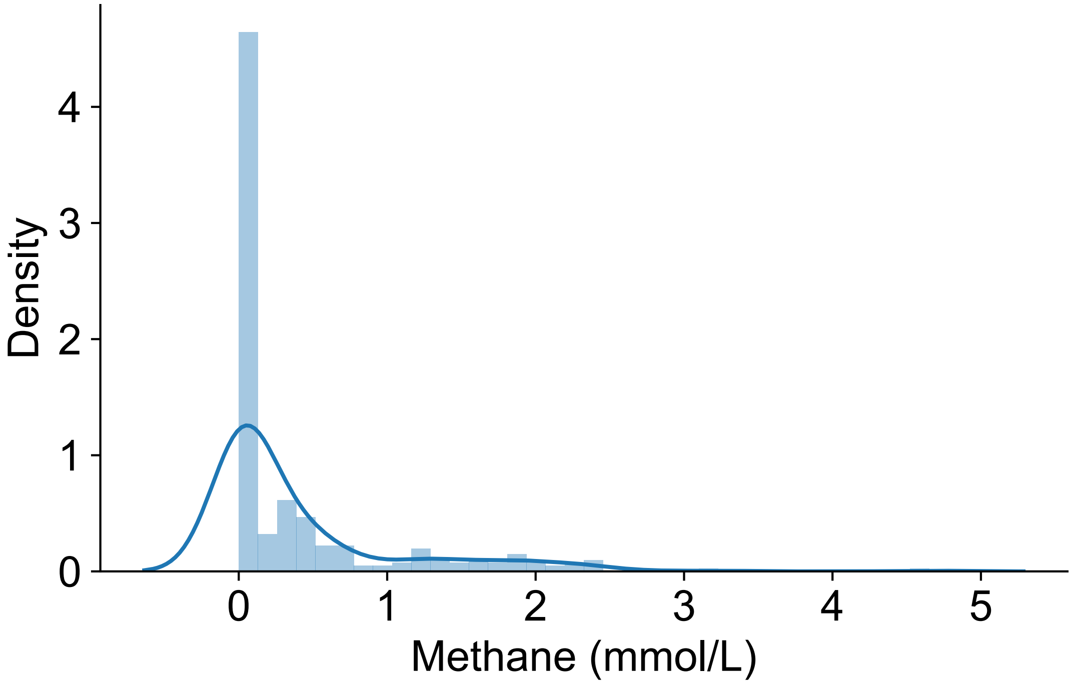

Figure A.23: Distribution of Chapter 4 methane dataset.

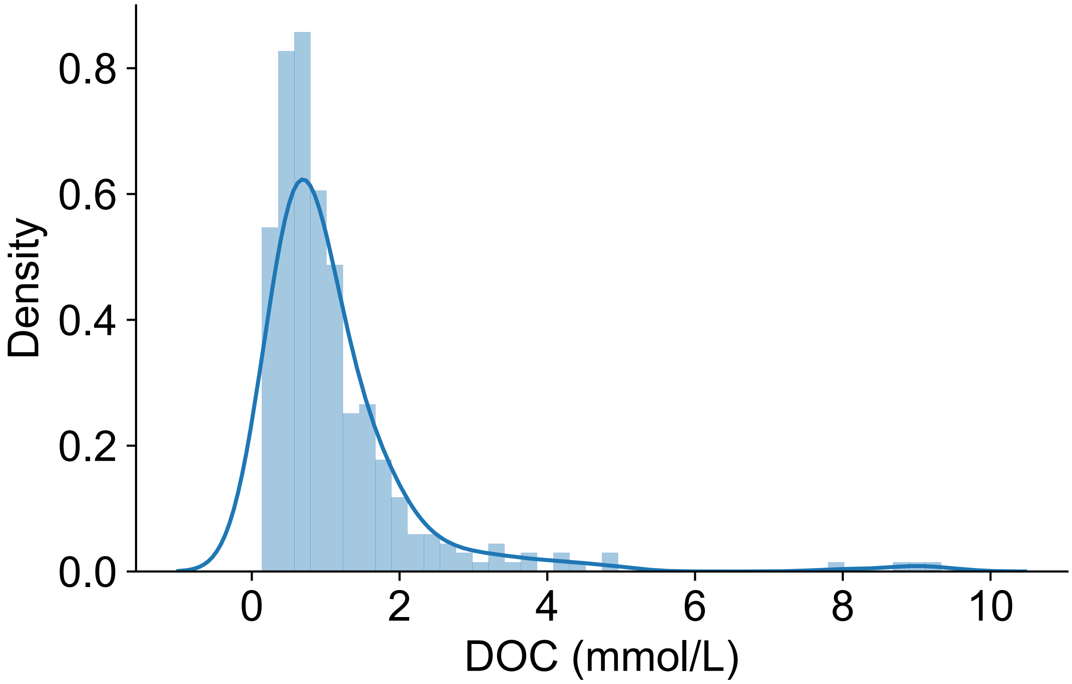

Figure A.24: Distribution of Chapter 4 DOC dataset.

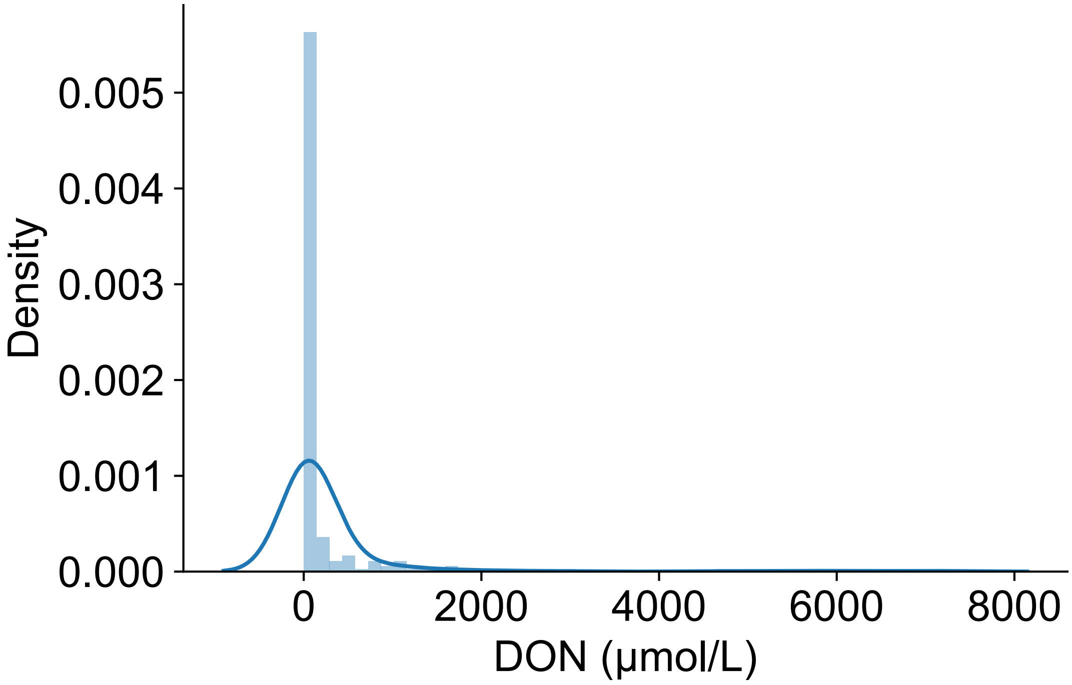

Figure A.25: Distribution of Chapter 4 DON dataset.

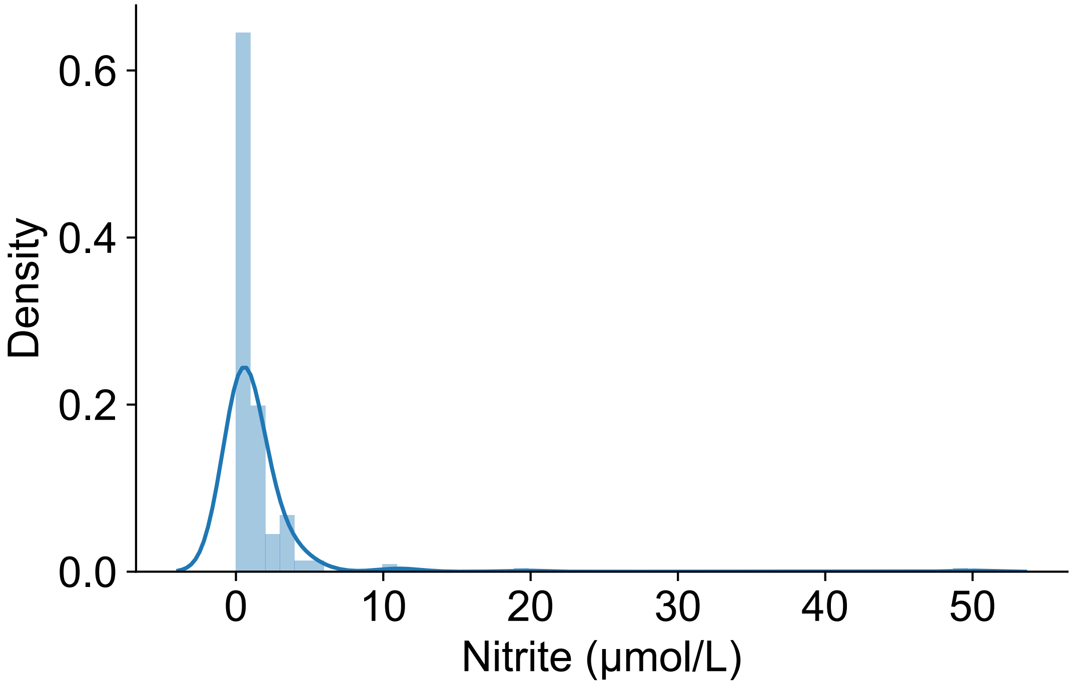

Figure A.26: Distribution of Chapter 4 nitrite dataset.

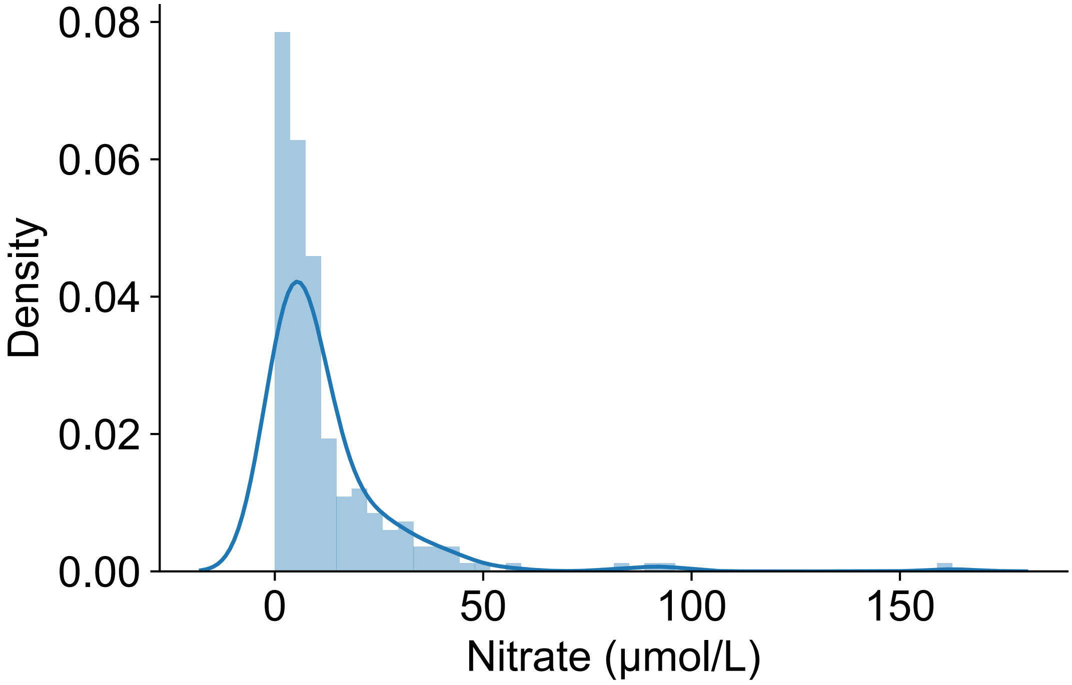

Figure A.27: Distribution of Chapter 4 nitrate dataset.

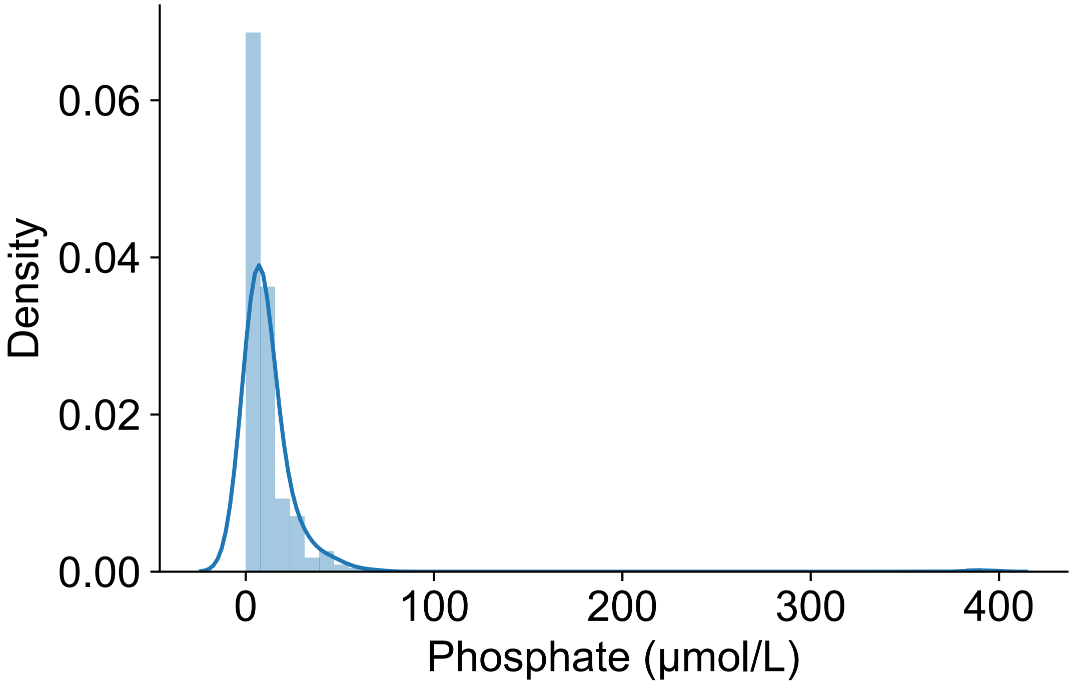

Figure A.28: Distribution of Chapter 4 phosphate dataset.

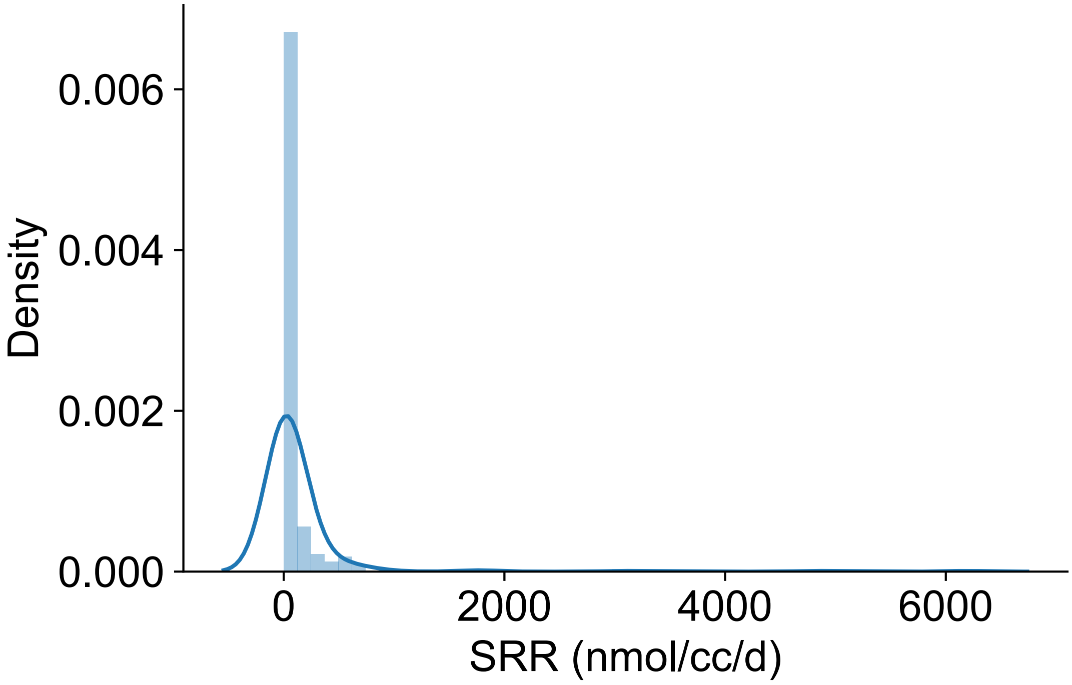

Figure A.29: Distribution of Chapter 4 sulfate reduction rate dataset.

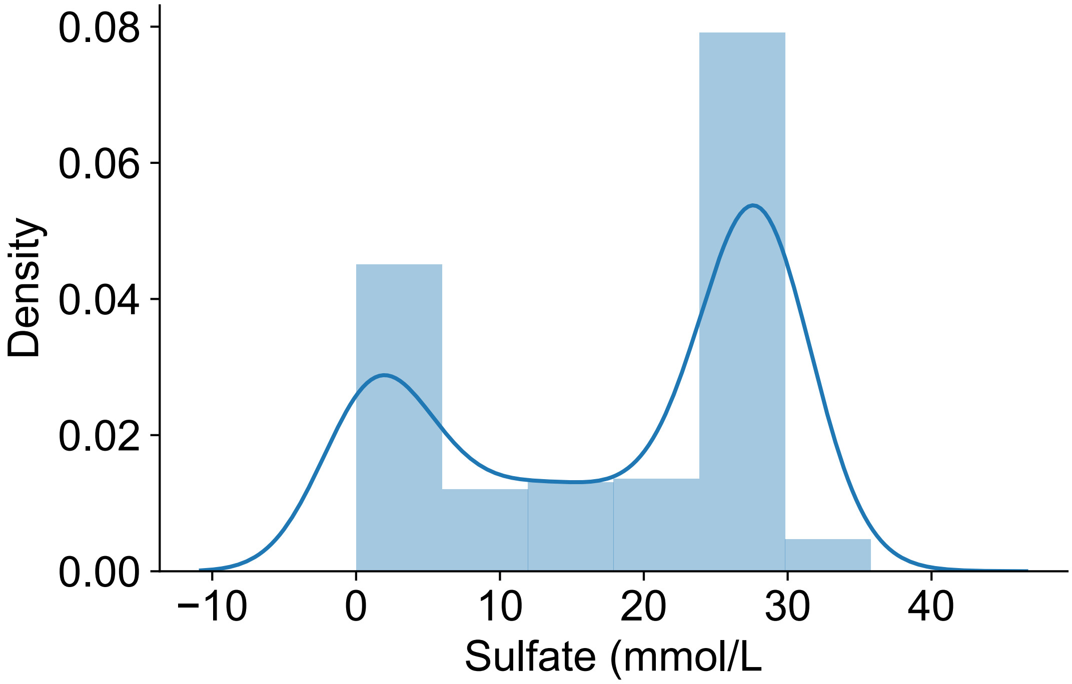

Figure A.30: Distribution of Chapter 4 sulfate dataset.

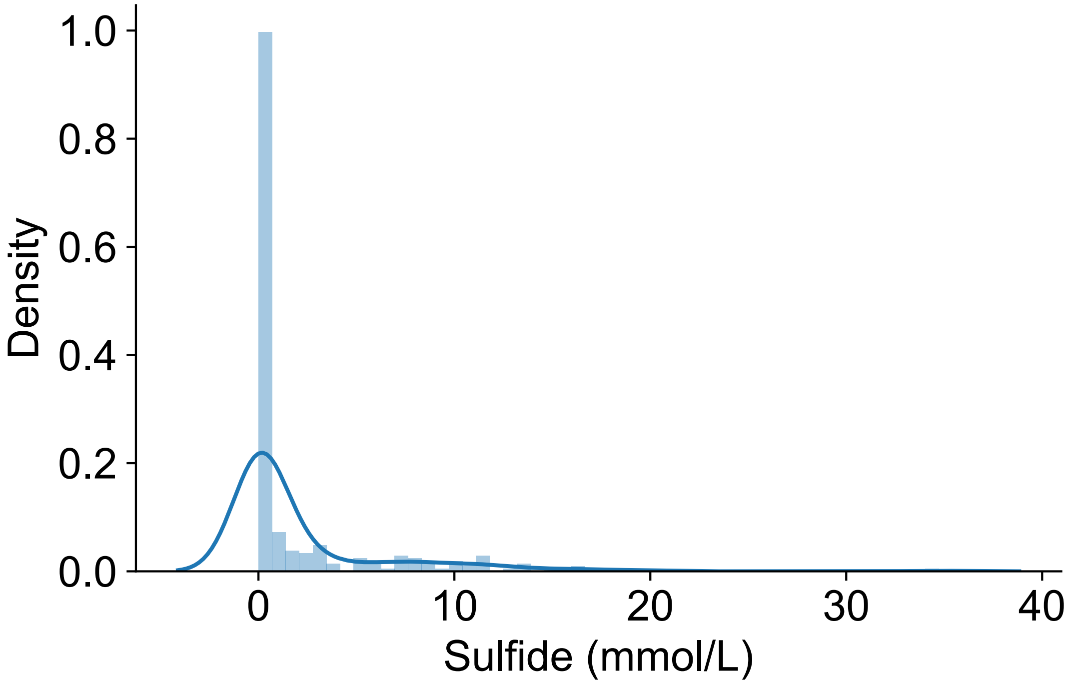

Figure A.31: Distribution of Chapter 4 sulfide dataset.

Bibliography

1. Miller, A. R. High salinity in sea water. *Nature* **203,** 590–591 (1964).
2. Miller, A. R. *et al.* Hot brines and recent iron deposits in deeps of the Red Sea. *Geochimica et Cosmochimica Acta* **30,** 341–359 (1966).
3. Swallow, J. C. & Crease, J. Hot salty water at the bottom of the Red Sea. *Nature* **205,** 165–166 (1965).
4. Brewer, P., Riley, J. & Culkin, F. *The chemical composition of the hot salty water from the bottom of the Red Sea* in *Deep Sea Research and Oceanographic Abstracts* **12** (1965), 497–503.
5. Ross, D. & Hunt, J. Third brine pool in the red sea. *Nature* **213,** 687–688 (1967).
6. Schmidt, M., Al-Farawati, R. & Botz, R. in *The Red Sea* (eds Rasul, N. M. & Stewart, I. C.) 219–233 (Springer, Berlin, Heidelberg, 2015).
7. Backer, H. & Schoell, M. New deeps with brines and metalliferous sediments in the Red Sea. *Nature Physical Science* **240,** 153–158 (1972).
8. Shokes, R. F., Trabant, P. K., Presley, B. J. & Reid, D. F. Anoxic, hypersaline basin in the northern Gulf of Mexico. *Science* **196,** 1443–1446 (1977).
9. LaRock, P. A., Lauer, R. D., Schwarz, J. R., Watanabe, K. K. & Wiesenburg, D. A. Microbial biomass and activity distribution in an anoxic, hypersaline basin. *Appl. Environ. Microbiol.* **37,** 466–470 (1979).
10. Jongsma, D. *et al.* Discovery of an anoxic basin within the Strabo Trench, eastern Mediterranean. *Nature* **305,** 795 (1983).

11. Bregant, D., Catalano, G., Civitarese, G. & Luchetta, A. Some chemical characteristics of the brines in Bannock and Tyro Basins: salinity, sulphur compounds, Ca2+, F-, pH, At, PO3- 4, SiO2, NH3. *Marine chemistry* **31,** 35–62 (1990).

12. Pautot, G., Guennoc, P., Coutelle, A. & Lyberis, N. Discovery of a large brine deep in the northern Red Sea. *Nature* **310,** 133–136 (1984).

13. Cita, M. B. *et al.* Gypsum precipitation from cold brines in an anoxic basin in the eastern Mediterranean. *Nature* **314,** 152 (1985).

14. Cochran, J. R., Martinez, F., Steckler, M. S. & Hobart, M. A. Conrad Deep: a new northern Red Sea deep. Origin and implications for continental rifting. *Earth and Planetary Science Letters* **78,** 18–32 (1986).

15. MacDonald, I. R. *et al.* Chemosynthetic mussels at a brine-filled pockmark in the northern Gulf of Mexico. *Science* **248,** 1096–1099 (1990).

16. Consortium, M. Three brine lakes discovered in the seafloor of the eastern Mediterranean. *Eos, Transactions American Geophysical Union* **76,** 313–318 (1995).

17. Yakimov, M. M. *et al.* Primary producing prokaryotic communities of brine, interface and seawater above the halocline of deep anoxic lake L'Atalante, Eastern Mediterranean Sea. *The ISME journal* **1,** 743–755 (2007).

18. Lloyd, K. G., Lapham, L. & Teske, A. An Anaerobic Methane-Oxidizing Community of ANME-1b Archaea in Hypersaline Gulf of Mexico Sediments. *Applied and Environmental Microbiology* **72,** 7218–7230 (2006).

19. Roberts, H. *et al.* Alvin explores the deep northern Gulf of Mexico Slope. *Eos, Transactions American Geophysical Union* **88,** 341–342 (2007).

20. Wankel, S. *et al.* New constraints on methane fluxes and rates of anaerobic methane oxidation in a Gulf of Mexico brine pool via in situ mass spectrometry. *Deep Sea Research Part II: Topical Studies in Oceanography* **57,** 2022–2029 (2010).